Integration of ferrimagnetic $CoFe_2O_4$ epitaxial films with silicon

Patricia de Coux González

PhD Thesis

Supervisors: Dr. Bénédicte Warot-Fonrose
Dr. Florencio Sánchez Barrera

2013

Integration of ferrimagnetic $CoFe_2O_4$ epitaxial films with silicon

Patricia de Coux González

PhD Thesis

Supervisors: Dr. Bénédicte Warot-Fonrose
Dr. Florencio Sánchez Barrera

Tutor: Javier Rodríguez Viejo

Members of the jury:

Luis A. Morellón Alquézar	Presidente
Jaume Gázquez Alabart	Secretario
Francesca Peiró Martínez	Vocal
Yves Dumont	Vocal
Michel Goiran	Vocal
Guillaume Saint-Girons	Vocal
Bénédicte Warot-Fonrose	Directora de tesis
Florencio Sánchez Barrera	Director de tesis

Programa de Doctorado en Ciencias de Materiales- Departamento de Física (UAB)
Memoria presentada para la obtención de la titulación de Doctor

Barcelona, 30 September 2013

To J.P.

Abstract

Microelectronics is progressing continuously by the exponential growth with time of the number of transistors per integrated circuit, the popularly known as “Moore’s Law”. This law is still valid but it is approaching intrinsic limits. The “More than Moore” is a complementary approach based on the use of radically new concepts as well as on the use of new materials in existing devices to improve performance. In particular, functional complex oxides represent an opportunity to extend and develop new devices functionalities with a wide range of applications.

This thesis presents a study on the integration of $CoFe_2O_4$ thin films with silicon. $CoFe_2O_4$ is ferromagnetic and electrically insulating at room temperature, the properties required to be used as tunnel barrier in a spin filter device. This device could permit the injection of spin polarized currents in silicon, as an alternative to the injection using ferromagnetic electrodes and passive tunnel barriers. However the spin filter requires a nanometric $CoFe_2O_4$ film, thinner than 4-5 nm to allow tunneling, and has to be epitaxial with high crystalline quality to preserve the ferromagnetism and tunneling transport. The thermodynamical instability between $CoFe_2O_4$ and silicon imposes the use of a buffer layer for its epitaxial integration. The challenging goal is therefore fabricating ultrathin epitaxial $CoFe_2O_4$/buffer bilayers on silicon. Investigating the possibility to achieve such goal has been the main objective of this thesis.

The buffer layer is critical. Thus we have followed a strategy based on investigating in parallel several candidates. $SrTiO_3$, which can be grown epitaxially on Si(001) with sharp interface and that has been already used as single crystal to deposited $CoFe_2O_4$, has been a natural option. We have used thick (around 17 nm) $SrTiO_3$ buffers fabricated by collaborators at INL-Lyon to grow by pulsed laser deposition (PLD) $CoFe_2O_4$, which is epitaxial and ferromagnetic. However, there is diffusion of Ti into $CoFe_2O_4$ and the $SrTiO_3$/Si(001) interface could be unstable.

Yttria-stabilized-zirconia (YSZ) has been other investigated material. It is widely used to grow oxides on Si(001), but having the YSZ buffershigh thickness of tens of nm and presence of interfacial SiO_x. Here we have investigated the mechanisms of YSZ epitaxy to determine the limits reducing the YSZ thickness and the interfacial layer. Ultrathin buffers around 2 nm thick, with less than 1 nm thick SiO_x layer, can be fabricated by reflection high energy electron diffraction (RHEED) assisted PLD. Ultrathin $CoFe_2O_4$ films subsequently

grown were epitaxial, although (111) oriented and with the SiO_x layers more than 2 nm thick. The result is remarkable, but the total thickness of CFO/YSZ/SiO_x is excessive for a tunnel device.

We have used also Sc_2O_3 and Y_2O_3 buffers on Si(111), provided by collaborators at IHP-Frankfurt Oder. They are original candidates never combined with $CoFe_2O_4$. In spite of the huge lattice mismatch of around 15 and 20% $CoFe_2O_4$ grows epitaxially. Detailed transmission electron microscopy (TEM) has showed a mechanism of domain matching epitaxy. The films present magnetization close to the bulk value and without interfacial SiO_x layer in the $CoFe_2O_4$/Y_2O_3/Si(111) sample. Thus Y_2O_3 appear as very promising buffer layer and maybe convenient for the nanometric structure required in a spin filter. We have demonstrated that ultrathin Y_2O_3 buffers, less than 2 nm thick, permit epitaxial growth of $CoFe_2O_4$, although the investigation of the interface stability has not been conclusive.

Résumé

Le progrès continu en microélectronique est dû à la croissance exponentielle avec le temps du nombre de transistors par circuit intégré, relation connue comme la loi de Moore. Cette loi reste vraie mais approche ses limites intrinsèques. C'est pourquoi est apparu la loi de "More tan Moore" qui est une approche complémentaire basée sur de nouveaux concepts et l'introduction de nouveaux matériaux pour améliorer les performances dans les dispositifs actuels. En particulier, les oxydes fonctionnels représentent une bonne opportunité pour accroître et développer les réponses des dispositifs d'intérêt pour une large gamme d'applications.

Cette thèse présente une étude sur l'intégration de couches minces de $CoFe_2O_4$ sur silicium. $CoFe_2O_4$ est ferromagnétique et isolant électrique à température ambiante, qui sont les propriétés requises pour être utilisé en tant que barrière tunnel dans un dispositif de filtre à spin. Ce dispositif pourrait permettre l'injection de courants de spin polarisés dans le silicium, comme alternative à l'injection utilisant des électrodes ferromagnétiques et des barrières tunnel passives. Cependant, un filtre à spin nécessite une couche mince de $CoFe_2O_4$ avec une épaisseur nanométrique, inférieure à 4-5 nm pour permettre l'effet tunnel, et une épitaxie de très bonne qualité afin de préserver le ferromagnétisme et le transport par effet tunnel. L'instabilité thermodynamique entre $CoFe_2O_4$ et le silicium impose l'utilisation d'une couche tampon pour son intégration épitaxiale. L'exigeant défi est donc de fabriquer des bicouches épitaxiées et ultrafines de $CoFe_2O_4$/couche tampon sur silicium. Le principal objectif de cette thèse a été d'étudier la possibilité d'accomplir cet objectif.

La couche tampon est essentielle. Nous avons donc adopté une stratégie de recherche en parallèle considérant différents candidats. $SrTiO_3$, pouvant croître épitaxié sur Si(001) avec une interface nette et ayant déjà été utilisé sous forme de substrat monocristallin pour déposer $CoFe_2O_4$, a été une option naturelle. Nous avons utilisé des couches tampon de $SrTiO_3$ épaisses (environ 17 nm) fabriquées par des collaborateurs de l'INL-Lyon pour déposer des couches de $CoFe_2O_4$ épitaxiées et ferromagnétiques par dépôt par laser pulsé (*pulsed laser deposition,* PLD). Nous avons décelé une diffusion de Ti dans $CoFe_2O_4$, et une possible instabilité de l'interface $SrTiO_3$/Si(001).

L'Yttrium stabilisé avec de la zircone (*yttria-stabilized zirconia*, YSZ) est un autre oxyde largement utilisé comme couche tampon pour intégrer des oxydes sur Si(001). Cependant, il est utilisé avec des épaisseurs de dizaines de nanomètres et présentant une

couche interfaciale de SiO_x. C'est pourquoi nous avons étudié les mécanismes de croissance épitaxiale d'YSZ afin de déterminer les limites de réduction d'épaisseur d'YSZ et de la couche interfaciale. Nous avons obtenu des couches ultrafines de buffer d'environ 2 nm d'épaisseur avec moins d'1 nm de SiO_x par PLD monitorisé par RHEED (*reflection high energy electron diffraction*). En utilisant ces couches tampon, les couches ultrafines de $CoFe_2O_4$ épitaxiées présentent une orientation (111) et des couches interfaciales de SiO_x supérieures à 2 nm d'épaisseur. Bien que le résultat soit remarquable, l'épaisseur totale de CFO/YSZ/SiO_x est excessive pour un dispositif de filtre à spin.

Nous avons aussi utilisé des buffers de Sc_2O_3 et Y_2O_3 sur Si(111), fournis par des collaborateurs de l'IHP-Frankfurt Oder. Ce sont des candidats originaux qui n'ont jamais été combinés avec $CoFe_2O_4$. En dépit de leur grand désaccord paramétrique avec $CoFe_2O_4$, entre 15 et 20%, la croissance de $CoFe_2O_4$ est épitaxiale. La caractérisation par microscopie électronique en transmission a montré le mécanisme de croissance epitaxiale par domaines. Les films présentent une magnétisation proche de celle du matériau massif et sans couche interfaciale de de SiO_x dans des hétérostructures des échantillons de $CoFe_2O_4/Y_2O_3/Si(111)$. Les buffers d'Y_2O_3 sont donc très prometteurs pour la structure nanométrique requise dans un filtre à spin. Nous avons démontré que des buffers ultrafins d'Y_2O_3, avec une épaisseur inférieure à 2 nm, permettent la croissance épitaxiale de $CoFe_2O_4$, même si les recherches sur la stabilité de l'interface n'ont pas été concluantes.

Resumen

El continuo progreso en microelectrónica se debe al crecimiento exponencial con el tiempo del número de transistores por circuito integrado, dependencia conocida como ley de Moore. Esta ley se sigue cumpliendo, pero se va acercando a límites intrínsecos. Por ello ha emergido la alternativa “More tan Moore”, un enfoque complementario basado en conceptos radicalmente nuevos y en la introducción de nuevos materiales que mejoren las prestaciones de dispositivos. En particular, los óxidos funcionales representan una buena oportunidad para incrementar y desarrollar las respuestas de dispositivos de interés para una gran gama de aplicaciones.

Esta tesis presenta un estudio sobre la integración de capas delgadas de $CoFe_2O_4$ sobre silicio. $CoFe_2O_4$ es ferromagnético y un aislante eléctrico a temperatura ambiente, que son las propiedades requeridas para ser utilizado como barrera túnel en un dispositivo de filtro de espín. Dicho dispositivo podría permitir la inyección de corrientes de espines polarizados en silicio, como alternativa a la inyección usando electrodos ferromagnéticos y barreras túneles pasivas. Sin obstante, un filtro de espín necesita una capa fina de $CoFe_2O_4$ de espesor nanométrico, inferior a 4-5 nm para permitir el efecto túnel, y una epitaxia de muy buena calidad para conservar el ferromagnetismo y el transporte por efecto túnel. La instabilidad termodinámica de $CoFe_2O_4$ con el silicio impone el uso de una capa barrera para su integración epitaxial. El mayor desafío reside en fabricar bicapas epitaxiales y extrafinas de $CoFe_2O_4$/barrera sobre silicio. El principal objetivo de esta tesis ha sido estudiar la posibilidad de realizar este objetivo.

La capa barrera es crucial. Hemos llevado a cabo una estrategia de investigación en paralelo considerando varios candidatos. $SrTiO_3$, pudiendo crecer de forma epitaxial sobre Si(001) y ya usado como substrato monocristalino para el depósito de $CoFe_2O_4$, ha sido una opción evidente. Hemos usado capas búfer de $SrTiO_3$ gruesas (alrededor de 17 nm) fabricadas por colaboradores del INL-Lyon para crecer capas de $CoFe_2O_4$ epitaxiales y ferromagnéticas mediante depósito con láser pulsado (*pulsed laser deposition*, PLD). Sin embargo hemos encontrado difusión detitanio en el $CoFe_2O_4$, y que la intercara de $SrTiO_3$/Si(001) podría ser inestable.

Zirconia estabilizada con ítria (*yttria-stabilized zirconia*, YSZ) es otro óxido ampliamente usado como lámina barrera para la integración de óxidos sobre Si(001). Sin

embargo siempre se usa siendo una barrera gruesa, con espesores de decenas de nanómetros y presentando una capa de SiO_x en la intercara. Por ello hemos invesigado los mecanismos de crecimiento epitaxial de YSZ, con el fin de determinar los límites en la reducción de espesor de YSZ y de SiO_x. Como resultado podemos obtener láminas barrera ultrafinas, de aproximadamente 2 nm de espesor y con menos de 1 nm de SiO_x Ha sido posible usando PLD monitorizado con RHEED (*reflection high energy electron diffraction*). Usando estas láminas barrera, capas ultrafinas de $CoFe_2O_4$ epitaxiales presentan una orientación (111) y capas interfaciales de SiO_x superiores a 2 nm de espesor. Aunque el resultado es remarcable, el espesor total de CFO/YSZ/SiO_x es excesivo para un dispositivo de filtro de espín.

También hemos utilizado barreras de Sc_2O_3 y Y_2O_3 sobre Si(111), proporcionadas por colaboradores del IHP-Frankfurt Oder. Son candidatos originales que no se habían combinado nunca con $CoFe_2O_4$. A pesar del gran desajuste estructural con el $CoFe_2O_4$, de entre 15 y 20%, el crecimiento de $CoFe_2O_4$ es epitaxial. La caracterización por microscopia electrónica en transmisión ha mostrado un mecanismo de crecimiento epitaxial por ajuste dominios. Las capas presentan una magnetización cercana a la del material masivo y sin capa interfacial de SiO_x en las heteroestructuras de $CoFe_2O_4$/Y_2O_3/Si(111). Las barreras de Y_2O_3 son por tanto prometedoras para la estructura nanométrica requerida en un filtro de espín. Hemos demostrado que barreras ultrafinas de Y_2O_3, con un espesor inferior a 2 nm, permiten el crecimiento epitaxial de $CoFe_2O_4$, aunque las investigaciones sobre la estabilidad de la intercara no han sido concluyentes.

Table of contents

Chapter I: General introduction ... 1

I.1 Context and objectives ... 1
I.1.1 Complex oxides ... 1
I.1.2 Multiferroics and magnetoelectric oxides: a paradigm of functional oxides ... 3
I.1.3 Integration of functional oxides on silicon ... 4
I.1.4 Objectives of the thesis ... 5
I.2 $CoFe_2O_3$ ... 5
I.3 Oxides on silicon ... 7
I.3.1 Metal oxide/Silicon interface: thermodynamics ... 8
I.3.2 Incompatibility of $CoFe_2O_4$ with silicon ... 9
I.4 Outline of the thesis ... 10

Chapter II: Experimental techniques ... 11

II.1 Elaboration techniques ... 11
II.1.1 Molecular Beam Epitaxy (MBE) ... 11
II.1.2 Pulsed Laser Deposition (PLD) ... 11
II.2 Diffraction techniques ... 13
II.2.1 Theory of diffraction ... 14
II.2.2 X-Ray diffraction ... 15
II.2.3 Electron diffraction ... 16
II.2.3.1 Reflection High-Energy Electron Diffraction (RHEED) ... 16
II.2.3.2 Transmission electron diffraction by TEM ... 17
II.3 Transmission Electron Microscopy (TEM) ... 19
II.3.1 Interface contrast ... 21
II.3.2 TEM sample preparation methods ... 21
II.3.2.1 Planar view and cross-section ... 21
II.3.2.2 Conventional TEM sample preparation ... 22
II.3.2.3 Wedge technique: totally mechanical TEM sample preparation ... 23
II.3.3 Particular TEM sample preparations ... 26
II.3.3.1 TEM sample preparation for the oxide/silicon interface characterization ... 26
II.3.3.2 Improving TEM preparation for ultrathin oxide films integrated on silicon ... 27

Chapter III: Integration of $CoFe_2O_4$ with Si(001) using $SrTiO_3$ buffer layers ... 31

III.1 Introduction ... 31
III.2 $SrTiO_3$ on Si(001) ... 32
III.3 $CoFe_2O_4$ on Si(001) buffered with $SrTiO_3$ ... 35
III.3.1. In-situ RHEED, AFM and XRD characterization ... 35
III.3.2 Structural characterization by TEM ... 36
III.3.3 EELS characterization ... 40

III.3.3.1 EELS in a direction perpendicular to the interface 40
III.3.3.2 EELS along a direction parallel to the interface 43
III.4 Summary 47

Chapter IV: Integration of $CoFe_2O_4$ with Si(001) using YSZ buffer layers 49

IV.1 Introduction 49
IV.2 $CoFe_2O_4$ on Si(001) using CeO_2/YSZ double buffers 50
IV.3 Growth mechanisms of yttria stabilized zirconia on Si(001) 52
IV.4 Integration of ultrathin $CoFe_2O_4$/YSZ with Si(001) 59
IV.5 Summary 62

Chapter V: Integration of $CoFe_2O_4$ with Si(111) using A_2O_3 (A=Sc, Y) buffer layers .. 65

V.1 Introduction 65
V.1.1 Materials 66
V.1.2 Domain Matching Epitaxy 67
V.1.2.1 Description of the mechanism 67
V.1.2.2 $CoFe_2O_4$ on A_2O_3: possibilities of domain matching epitaxy 69
V.2 $CoFe_2O_4$ on Sc_2O_3 buffered Si(111) 70
V.2.1 Introduction 70
V.2.2 Thin film growth and in-situ characterization by RHEED 71
V.2.3 AFM and XRD of $CoFe_2O_4$ and Sc_2O_3 films on Si(111) 72
V.2.4 HRTEM characterization 73
V.2.5 Magnetic properties 76
V.3 $CoFe_2O_4$ on Y_2O_3 buffered Si(001) 77
V.3.1 Introduction 77
V.3.2 Thin film growth and in-situ characterization by RHEED 78
V.3.3 AFM and XRD of $CoFe_2O_4$ and Y_2O_3 films on Si(111) 80
V.3.4 HRTEM characterization 81
V.3.4.1 $CoFe_2O_4$/Y_2O_3 interface 81
V.3.4.2 Y_2O_3/Si interface 83
V.3.5 Magnetic properties 86
V.3.6 Ultrathin films of $CoFe_2O_4$ and Y_2O_3 on Si(111) 86
V.4 Summary 90

VI Conclusions and perspectives 91

Appendix A: Transmission Electron Microscopy (TEM) 93

A.1 Generalities 93
A.2 Image contrast for structure analysis 95
A.3 Some concepts definition 99
A.4 Incoherent imaging: Z-contrast by High Angular Annular Dark Field (HAADF) 100
A.5 Scanning TEM (STEM) 101
A.6 Effects of the sample preparation for TEM analysis 102

Appendix B: Spectroscopies: EDXS and EELS 105

B.1 Physical principle: Diffusion 105
B.2 Energy Dispersive X-ray Spectroscopy (EDXS) 106
B.3 Electron Energy-Loss Spectroscopy (EELS) 108
B.4 EELS/ EDXS comparison 111

Appendix C: Other characterization techniques 113

C.1 Atomic Force Microscope (AFM) 113
C.2 SQUID 113

Appendix D: Thin film growth modes and interface 114

D.1 Thin film growth 115
D.1.1 Epitaxial growth 115
D.1.2 Elastic deformation 117
D.1.3 Plastic deformation 117
D.1.4 Critical thickness h_c 117
D.2 Interfaces microstructure 118
D.3 Dislocations 119

Scientific contributions 121

Publications list 121
Oral communications 121
Posters list 123

Acknowledgements 125

References 127

Chapter I

General introduction

I.1 Context and objectives

In 1965 Gordon Moore stated that continuous increase in the performance to cost ratio in electronic products could be achieved through transistor scaling. Popularly known as "Moore's Law", the exponential growth in the number of transistors per integrated circuit (the functionality per chip doubles every 1.5 to 2 years), is still valid. However, we are arriving to limits in the reduction of the transistor size. The ITRS (International Technology Roadmap for Semiconductors, http://www.itrs.net) identifies problems and provides guides to maintain the constant progress in microelectronics. On one hand it is still possible to reduce sizes in order to increase density (reduction of cost per function) and performance (increase of memory speed). This is called the "More Moore" scaling. On the other hand, it is necessary to develop new concepts as well as use new materials in existing devices to improve performances without necessity of size reduction. This is the "More than Moore" approach.

Amorphous SiO_2, with its nearly electrically perfect interface with silicon, has been the most technologically important oxide until its physical limitations were revealed by the miniaturisation of transistors. SiO_2 layer loses its effective insulator property when thickness is below 1 nm. Higher dielectric constant materials (high-k oxides) are an alternative [WIL01]. Today HfO_2 and other oxides are being used as gate oxide in high performance field effect transistors (FET). This example illustrates that the "More than Moore" approach can provide effective alternatives when the "More Moore" approaches a limit.

Beyond high-k oxides, functional complex oxides represent an opportunity to extend and develop new devices functionalities with a wide range of applications. For instance, replacement on a gate oxide in a FET by a ferroelectric would result in a non-volatile device. This device, the ferroelectric FET, is not yet in the marked in spite of the strong efforts for its development [INI10]. Ferroelectric oxides are already used in commercial devices (Ferroelectric Random Access Memories, FeRAM) [seehttp://www.fujitsu.com/global/services/microelectronics/product/memory/fram/for example]. But the role of ferroelectric oxides in microelectronics is still low, and other functional oxides (ferromagnets, for instance) are still far to be used in commercial devices. This is mainly due to its difficult integration with silicon.

I.1.1 Complex oxides

Complex oxides represent a vast class of materials with a wide range of crystal structures and functionalities. Even simple binary oxide materials (MO, MO_2, M_2O_3, M= metal cation) including crystal structures as rocksalt, wurzite, fluorite, rutile and corundum present a wide range of properties from insulating to metallic, magnetic (FM, AF) and even ferroelectric. The variety of materials and properties extends enormously in ternary oxides, including ilmenite, spinel, perovskite, and other derived structures. Perovskites (ABO_3) is the most relevant family, where A and B cations of different size are permitted, with different valence combinations and partial substitutions. In spite of the complexity of these materials, the development of thin film growth techniques has allowed the production of high-quality films. Epitaxy is also exploited to obtain metastable phases, and to control properties through lattice strain. Reviews in references:[DEK10, REI10, ZUB11]detail recent advances in the growth and characterization of functional oxides, mainly ferroelectric, magnetic and multiferroics. They are complex materials, with physical properties arising from the strong coupling between the electron, spin, lattice and orbital orderings as summarised in figure I.1.

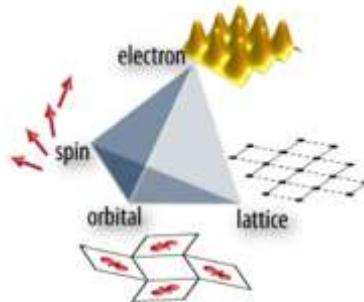

Figure I.1: The strong coupling between lattice, orbital, spin and charge givesrise to the diverse functionalities of transition metal oxides, such as ferroelectricity, colossal magnetoresistence, and superconductivity[RON11].

The complexity of these oxides that permits the variety of functional properties is in turn a difficulty since the control of thin films growth is very challenging, and slight changes in the nanostructure can have a huge impact on their properties. Degradation of properties in thin films is widely reported [ZUB11, LU_96, BIB01, SIM04],and in addition toextrinsic factors favoured by the difficult growth, other causes much more subtle, including off-stoichiometry to relieve epitaxial stress, have been proved [EST08]. In addition, structural distortions induced by the epitaxy can be highly significant and influence the electronic properties. The ideal simple cubic ABO_3 perovskite structure consists of octahedrally coordinated B-site cations with three dimensionally corner-connected BO_6 oxygen octahedral resulting in O-B-O chains with 180° bonds angles. In perovskites, the most frequent distortions are rotations or tilts of oxygen microscopy around one or more high symmetry axes (figure I.2). In addition to these octahedral rotations driven by geometric and electrostatic considerations, there are electronically driven distortions caused by Jahn-Teller (J-T) effects. The J-T effect is an electronic degeneracy usually associated to the d electrons on the B-site cation and is manifested by a change of B-O bonds length. All these distortions critically determine the functional properties, and structural changes caused by the epitaxial stress can cause degradation. However, if the effects are understood and controlled they offer the opportunity to tune the properties.

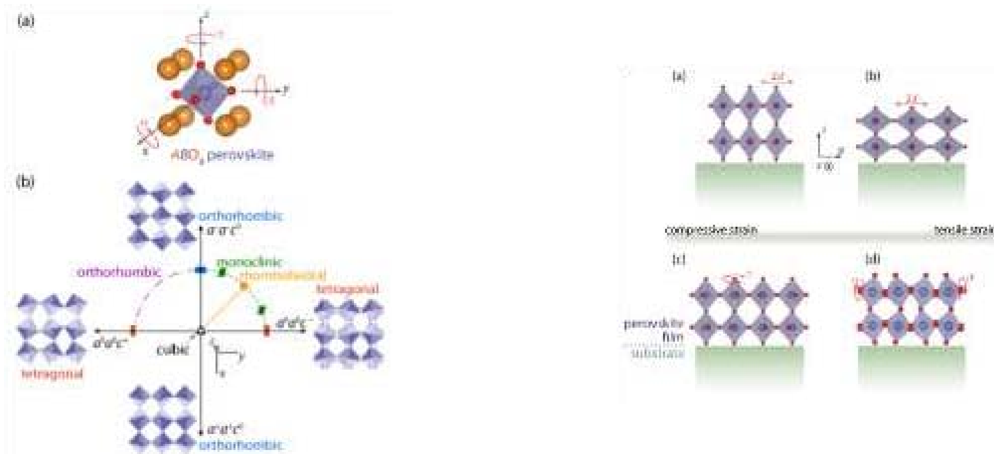

Figure I.2: (1a) Ideal octahedral in perovskite transition metal oxide and (1b) Small rotations from the ideal perovskite structure results in symmetry lowering structural distortions.(2) In coherently strained perovskite films, the BO_6 octahedra can distord through contraction (a) or elongation (b) of the equatorial B_O bonds due to compressive or tensile strain respectively. Simultaneously or alternatively, the film can accommodate the substrate induced change of the in-plane lattice parameters by rotation perpendicular to the substrate (c) and/or about an axis parallel to the substrate plane (d) [RON11].

I.1.2 <u>Multiferroics and magnetoelectric oxides: a paradigm of functional oxides</u>

In ferroic materials, the electric field E, magnetic field H, and stress σ control the electric polarization P, magnetization M, and strain ε respectively (figure I.3.a). Ferromagnetism, ferroelectricity, and ferroelasticity are main properties used for many decades in devices.

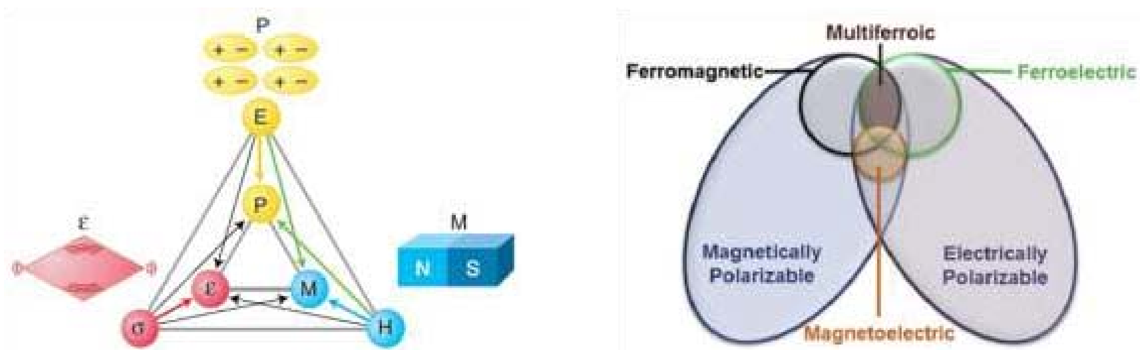

Figure I.3:(a) Control of P, M, and in ferroics and εmultiferroics[SPA05]and (b) Sketch of the relationship between multiferroic and magnetoelectric materials [MAR12].

Materials presenting simultaneously two or more “ferroic” properties such as ferroelectricity, ferromagnetism and ferroelasticity (figure I.3.b) are known as multiferroics[MAR10-12]. Magnetoelectric coupling typically refers to the magnetoelectric effect manifested as induction of magnetization by an electric field or of polarization by a magnetic field. But single-phase multiferroic materials are uncommon, particularly at room temperature. Then, magnetoelectricity can be obtained by combining single phase materials (figure I.4).As an example, two-phase multiferroic composites can combine two materials with ferroelectric and ferromagnetic property, with magnetoelectric effect arising from the elastic interaction of both constituents. An electric field induces a strain in the ferroelectric, which is transmitted to the ferromagnet, causing magnetization, and viceversa.

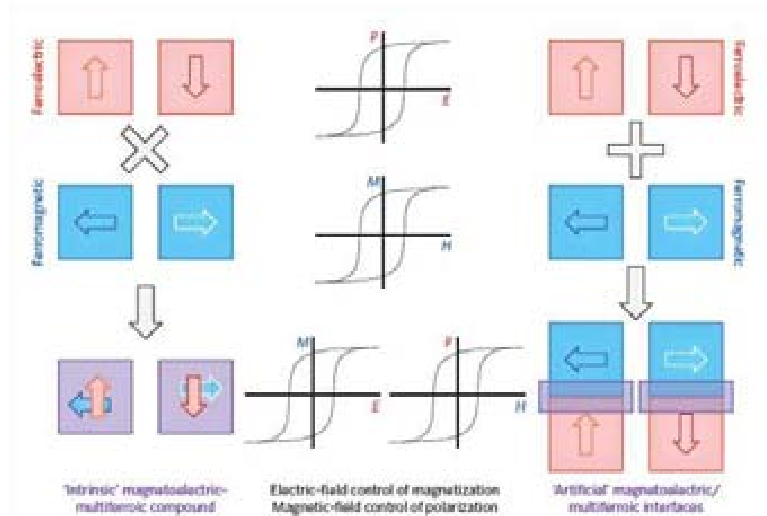

Figure I.4: Sketch presenting the intrinsic (single phase) and artificial (two phase) magnetoelectric-multiferroic compounds[BIB12].

I.1.3 <u>Integration of functional oxides on silicon</u>

A technological revolution, using complex oxides for microelectronics, was envisaged after the discovery of the high-Tc superconductivity in 1986. Superconducting $Yba_2Cu_3O_7$ films were used to fabricate complex devices as SQUIDS on oxide single crystals [LEE91]. More simple devices as bolometers were obtained on silicon platforms with YSZ buffers [Li_93]. Unfortunately, $Yba_2Cu_3O_7$ films on silicon presented aging problems, most probably due to cracks that formed by the stress originated by the thermal mismatch. Today, the interest of high-Tc superconductors appear more focused on applications such as energy transport and not on microelectronics.

The research on high Tc superconductivity also stimulated in the 90's a huge interest in colossal magnetoresistence (CMR) and ferroelectric oxides. Contrary to the case of superconductors, some CMR and ferroelectric oxides were integrated with silicon having properties comparable to films on perovskite substrates. Examples include $La_{0.65}Sr_{0.33}MnO_3/Bi_4Ti_3O_{12}$/YSZ/Si(001) with bulk-like magnetization M(T) and $La_{0.5}Sr_{0.5}CoO_3/PbZr_{0.53}Ti_{0.47}O_3/La_{0.5}Sr_{0.5}CoO_3$/Pt/Si(001) with no fatigue ($< 10^{10}$ cycles) [TRA96, DAT94].

Although perovskite oxides received most of the attention, spinels are also of high interest for spintronics. Some of them, including $CoFe_2O_4$ and $NiFe_2O_4$, are ferromagnetic at room temperature with high magnetization, and contrary to most ferromagnetic materials they are electrically insulators. Thus they offer new opportunities for spintronics. In particular, they can be used as active tunnel barrier in spin filter devices, where the tunnel probability depends on the spin of the electrons, see a sketch in figure I.5.

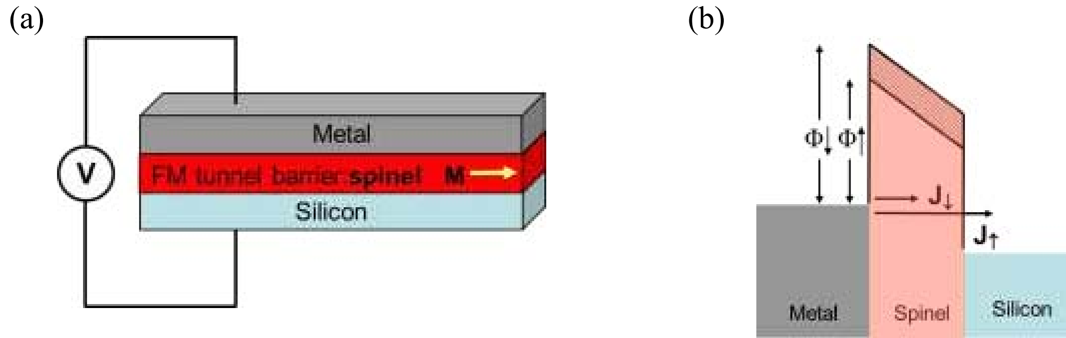

Figure I.5: Sketch of a spin filter device, where $CoFe_2O_4$ is used as active tunnel barrier (a), and of the spin injection in silicon through the spinel barrier (b).

Pioneering work with $NiFe_2O_4$ as ferromagnetic barrier demonstrated a spin-filtering efficiency of 23% at low temperatures [LUD06], and more recently it has been reported room temperature spin filtering in magnetic tunnel junctions (MTJs) containing $CoFe_2O_4$ tunnel barriers with tunnel magnetoresistence(TMR) values of 18% and 3% at 2 and 290 K, respectively[RAM07]. The use of functional oxides as CFO in electronics critically depends on the epitaxial integration with silicon, which requires a buffer layer to avoid chemical interaction and allows lattice matching.The use of yttria-stabilized zirconia (YSZ) as buffer layer, which was early investigated [KEE98],allows for a direct crystallization after reduction of the native silica, and become the most common buffer used to integrate functional oxides on silicon. For example, ferroelectrics as $Pb(Zr, Ti)O_3$[GUE01, DEK 10], or $Bi_{3.25}La_{0.75}Ti_3O_{12}$[LEE02], and $Bi_{3.15}Nd_{0.85}Ti_3O_{12}$[ZHA10] as well as ferromagnetic $La_{2/3}Sr_{1/3}MnO_3$ and related manganites [FON99, KIM03, TRA96, PER09] and spinel oxides [WAK02-04]can grow epitaxially on YSZ buffered Si(001).It can be noted that YSZ films are epitaxially grown by pulsed laser deposition (PLD) [AGU97, FOR90]and do not require removal of the native silicon oxide. Indeed, their crystalline quality is enhanced compared to YSZ deposited on bare silicon [COP00, KIG02-03, WAN00-01].Other oxides as γ-Al_2O_3 and $SrTiO_3$ that can be used as buffers are usually grown by molecular beam epitaxy (MBE) on a SiO_x-free silicon surface[MAR06, MI_8].

I.1.4 Objectives of the thesis

The thesis aims at integrating CFO with silicon using different buffer layers. The ultimate goal being the fabrication of ultrathin CFO/buffer structures that could permit the fabrication of a spin filter device for spin injection in silicon.
The selection of the buffer layer is critical, since it has to allow the growth of high quality epitaxial layers of CFO and display high stability with silicon under the conditions used to deposit CFO. In a parallel study we have used $SrTiO_3$, Sc_2O_3 and Y_2O_3 buffer layers fabricated by molecular beam epitaxy (MBE) by collaborators, as well as pulsed laser deposition (PLD)-grown ultrathin YSZ layers, developed during this thesis.

I.2 $CoFe_2O_4$

The spinel $CoFe_2O_4$ is an electrical insulator that shows ferromagnetic order at room temperature with high magnetocrystalline anisotropy. In addition, it is a low cost and highly stable material.

The ideal spinel structure is sketched in figure I.6(the unit cell is formed by 8 cubes as the one shown). Oxygen atoms form a fcc lattice, and cations occupy interstitial tetrahedral and octahedral sites.

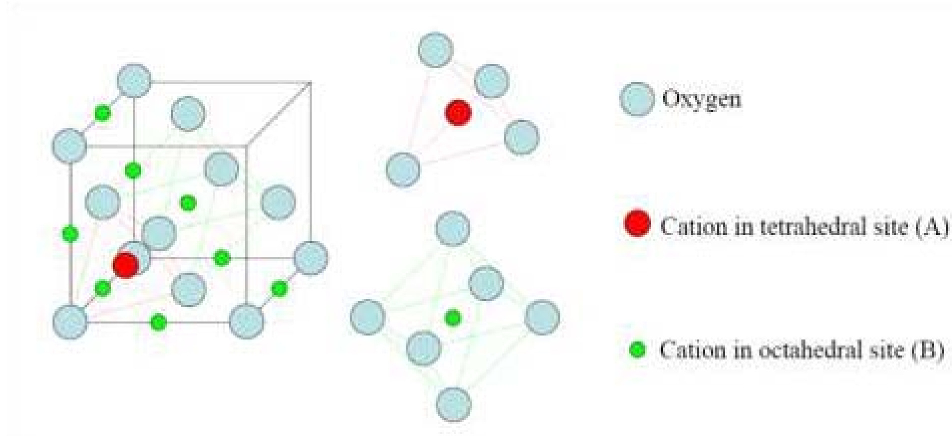

Figure I.6: Schematic representation of the spinel crystal structure[RIG10].

In the unit cell there are 8 divalent cations and 16 trivalent cations. There are three different structures of spinels: "normal", "inverse" and "mixed", which are distinguished in function of the cations position distribution on tetrahedral (A) and octahedral (B) positions.In the normal spinel type, divalent cations only occupy A-sites, while the trivalent cations are only presentin B-sites (e.g. $MgAl_2O_4$, $CoCr_2O_4$ and other chromites). In the inverse spinel structure, divalent cation occupiesB-sites, and trivalent cations equally distributed over A- and B- sites (e.g. $NiFe_2O_4$ and Fe_3O_4). The mixed structure is a combination between the normal and the inverse structure (e.g. $(Mn,Zn)Fe_2O_4$).The respective general formula of these type of spinel are: $(M^{2+})^A[N^{3+}]_2^B O_4$, $(N^{3+})^A[M^{2+}N^{3+}]^B O_4$, and $(M_{1-x}^{2+}N_x^{3+})^A[M_x^{2+}N_{2-x}^{3+}]^B O_4$ where $0<x<1$.

In their bulk form, most of spinel ferrites are electrical insulators, and thus ultrathin films of spinel ferrites could be ideally used as insulator layer for spin polarized tunnel transport. The spin filter efficiency of an ideal ferrite barrier depends on its thickness, and it is predicted that a barrier thickness of less than 2nm is large enough to ensure a full polarization (negative) of the tunnelling current[MOO88-10].

$CoFe_2O_4$has an inverse spinel structure, assimilated to a CFC structure with a Fd-3m symmetry group and a lattice parameter of 0.839 nm.The unit cell contains 32 oxygen atoms, 64 tetrahedral sites (A) and 32 octahedral (B) sites with respective occupation fractions of 1/8 and 1/2. The tetrahedral (A) sites are occupied exclusively by Fe^{3+} cations and octahedral (B) sites by both Fe^{3+} and Co^{2+}. The A or B-site position of the cation defines the number of nearest neighbours, which is 4 in the A-site position and 6 in the case of B-site occupancy. The distance between cations varies from 0.297 nm for B-B neighbours, to 0.348 nm for A-B neighbours, and 0.365 nm for A-A neighbours (considering a 0.84 nm unit cell).
The atomic stacking sequence in the [001] direction are A-planes of Fe^{3+} alternated with B-planes of Fe^{3+} and Co^{2+}, while in the [111] direction oxygen planes are intercalated with A and B planes (OBOABAOBO).

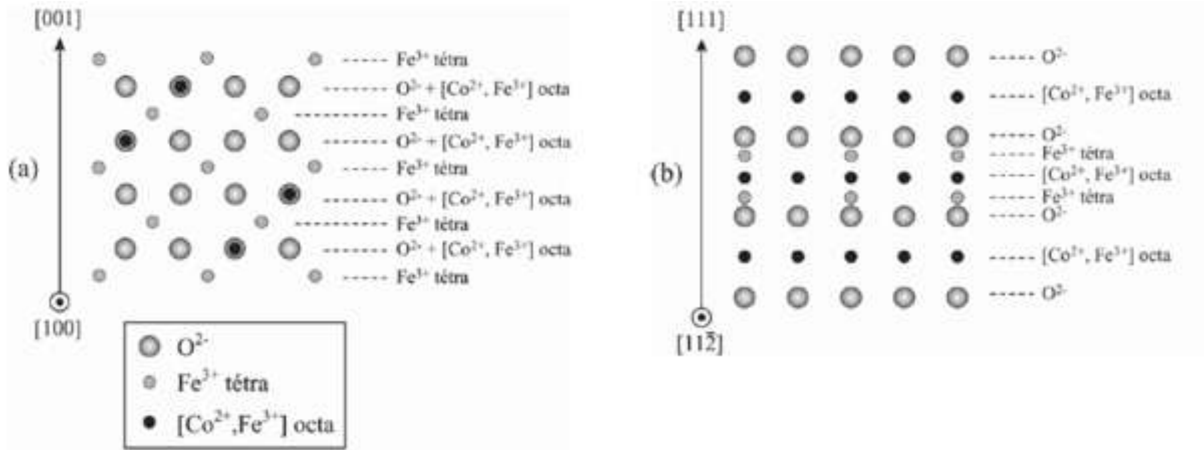

Figure I.7: Sketch of the atomic stacking along [001] and [111] directions[GAT04].

CFO is an electrical insulator and ferromagnetic at room temperature with a Curie temperature of T_c= 793K [KIN00]. It has very high magnetocrystalline anisotropy and very high magnetostrictive coefficients (λ_{100}= -590.10^{-6} and λ_{111}=120.10^{-6}) [BOZ55, STU69].
Magnetic properties can be modified by ion substitutions[BOZ55, TAC60] or epitaxial strain [HU_00].
The resistivity ρof a 100 nm CFO thin film at room temperature is 2.66 × 10^4Ω·cm [RAI11]. The insulating character for epitaxial thin films (t ≈15 nm) was demonstrated to be preserved, although with highly reduced resistivity values (around of 10^2Ω·cm at room temperature and around 10^6Ω·cm at 150 K)[RAM07-08].Integrating ultrathin films of CFO on silicon, with the total thickness of the system a few nm, could allow a magnetic tunnelling barrier for spin polarized electron injection on silicon although the low resistivity and room temperature could be a serious limitation.

Considering the growth of CFO film, the surface energy is a main parameter. Surface energy values for CFO are not reported, but data of related spinels as Fe_3O_4 and $NiFe_2O_4$[MIS77]can be taken as a reference. The surface energy is highly anisotropic, with {111} planes having a surface energy factor 4 lower than the {001} ones.

I.3 Oxides on silicon

Silicon has a cubic diamond structure, with lattice parameter a= 5.43088 Å. The atomic interspacing along the diagonal of a face, $a/\sqrt{2}$ = 3.84 Å, is close to perovskites lattice parameter (a_{STO}= 3.905 Å). It has a low thermal expansion coefficient of 2.3.10^{-6} K^{-1} generally smaller than complex oxides[FUK11].The growth of oxide thin films on silicon has been extensively studied, mainly for the development of high-k materials, and many of them can be successfully integrated[KIN00, MI_08, REI10]. In contrast, most of complex functional oxides cannot be grown directly on silicon due to the structural mismatch and/or chemical interaction, and then the use of a buffer layer is required. It represents a difficulty, but even for applications ideally requiring direct complex oxide/Si interface, the use of ultrathin buffer can maybe permit epitaxy being compatible with the application.

The silicon wafers are covered by amorphous SiO_2 which could hinder the epitaxial growth.The native amorphous silica can be removed by chemical etching (HF), thermal treatment in UHV, or if can be reduced by depositing atoms with strong affinity to oxygen. The growth of a crystalline oxide typically requires high temperature and presence of oxygen

in the vacuum chamber. There is interaction between silicon, oxygen and the oxide cations, and thus different chemical reactions are possible. Thermodynamics, comparing the Gibbs energy in the reaction causing formation of the desired oxide with others reactions forming silicides or silicates, is to be considered to rationalize the growth. However kinetics and limitation in the amount of oxygen or cations can be highly relevant opening the possibility to develop growth strategies to avoid formation of energetically-favoured interfacial compounds. Temperature and oxygen pressure are crucial parameters. As an example, the Motorola method, developed to grow epitaxially $SrTiO_3$ by molecular beam epitaxy, includes several steps that are critical to obtain an atomically sharp interface.Indeed, $SrTiO_3$ is thermodynamically unstable in contact with silicon at 1000K: $3Si + SrTiO_3 \rightarrow SrSiO_3 + TiSi_2$ (ΔG= - 19.133 kcal/mol) [HUN96], but extensive experimental studies have reveled that an intermediate epitaxial SrO monolayer permits epitaxial integration of $SrTiO_3$with Si ($SrTiO_3$/ SrO/ Si) [KEE98, Li_93, MOR91, YU_00].

The optimal method of preparation is different for other oxides and moreovercan depend on the specific deposition technique used, but there are some common trends. In particular, the excess of oxygen may lead to interface oxidation creating SiO_x or silicate phases by diffusion through the oxide layer, while an oxygen-deficient environment could lead to silicides and oxygen vacancies in the thin film. The sketch presented in figure I.8shows possible binary oxide/silicon interfaces.

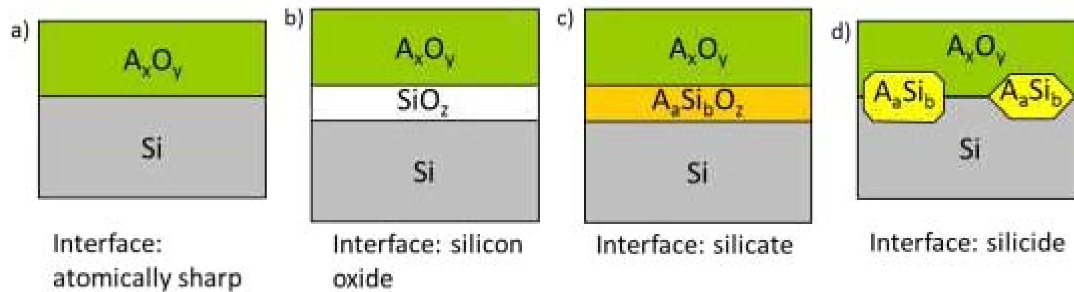

Figure I.8: Sketch representing the possible silicon interfaces with oxides: (a) atomically sharp, (b) silicon oxide, (c) silicate, (d) silicide, adapted from[STE04].

I.3.1 Metal oxide/Silicon interface: thermodynamics

In 1998 , before the experimental demonstration of an atomically sharp interface between Si and $SrTiO_3$[KEE98], Schlom and co-workers[HUB96]analysed tabulated thermodynamic data (Gibbs energy changes) of possible reactions between Si, O, and different metals. They reported additional information in a latter paper [SCH02]. Most metal oxides are not thermodynamically stable in contact with silicon, giving a failed balance reaction of the type: $Si + MO_x \rightarrow M + SiO_2$ ($\Delta G<0$), unless a few on them including ZrO_2. In some cases the lack of tabulated ΔG data did not permit a prediction.

Moreover in a M-Si-O system, further reactions are possible, in particular those causing silicide and/or silicate formation:

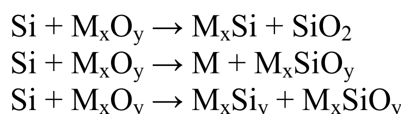

$$Si + M_xO_y \rightarrow M_xSi + SiO_2$$
$$Si + M_xO_y \rightarrow M + M_xSiO_y$$
$$Si + M_xO_y \rightarrow M_xSi_y + M_xSiO_y$$

As mentioned above, the thermodynamic analysis indicates, as pointed out in the pioneering work of Hubbard and Schlom [HUB96], a driving force for reaction, but kinetic barriers can prevent it. The analysis only included volume free energies, neglecting interface energies and reaction involving gaseous species. A discussion on their role can be found in the reviews [LOC06, STE04].

Functional oxide films, usually with complex stoichiometry, rarely will be stable with silicon. Also, lattice mismatch can be high causing high interface energy in case of sharp interface, which would add other driving force for decomposition or reaction. Thus, a buffer layer is generally required. Candidates are in principle all oxides that can be grown epitaxially on silicon. One of the most popular, used from the early 90's, is yttria-stabilized zirconia (YSZ). Later, the research on high-k oxides demonstrated the epitaxial growth of other oxides, being $SrTiO_3$ the best example. $SrTiO_3$ is moreover, as single crystal, the most popular substrate to deposit functional perovskites. But the list of candidates is longer, including for example CeO_2, ZrO_2, HfO_2, Y_2O_3, Al_2O_3, Gd_2O_3,..[HUB96, LOC06, SCH02, STE04]. Within the candidates, the choice of the material to be used as buffer layer to deposit a specific functional oxide has to consider the crystal compatibility (structure and lattice mismatch), eventual chemical interaction, and thermal expansion mismatch. The buffer role is to act as a nonreactive diffusion barrier and a stable nucleation template for the epitaxial growth of the functional oxide. Thermal expansion mismatch arises because most of the oxides have much higher thermal expansion coefficients than silicon. It must be minimized to prevent cracking due to induced tensile stress upon cooling. On the other hand, for some applications the buffer layer must be stable not only at the temperature of its growth, but also at the temperatures used for the growth of additional layers. In many cases, functional oxides are deposited at temperatures higher than 800 ºC. This can result in formation of interfacial SiO_x or silicate layers that probably will not impede epitaxial growth of the functional film. However, this can be a serious limitation if the application requires very close proximity between silicon and the functional layer.

III.3.2 <u>Incompatibility of $CoFe_2O_4$ with silicon</u>

In the case of the ternary oxide$CoFe_2O_4$, as for binary oxides, the analysis of thermodynamic stability is not so straightforward. It has to include the binary oxides that can be formed with the present metals, Co and Fe ($CoFe_2O_4$ is deposited from vapor phase, and thus atomic Fe and Co arrive to the Si surface).

Considering Fe, there are three binary oxides that are solid at 1000K: FeO, Fe_3O_4 and Fe_2O_3[SCH02]. Possible reactions between these oxides and Si are:

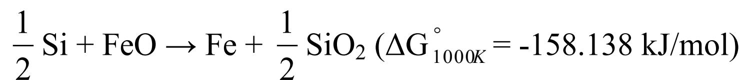

$$\frac{1}{2}\,Si + FeO \rightarrow Fe + \frac{1}{2}\,SiO_2\ (\Delta G^{\circ}_{1000K} = -158.138\ kJ/mol)$$

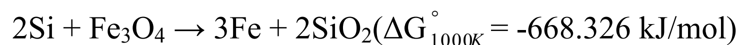

$$2Si + Fe_3O_4 \rightarrow 3Fe + 2SiO_2 (\Delta G^{\circ}_{1000K} = -668.326\ kJ/mol)$$

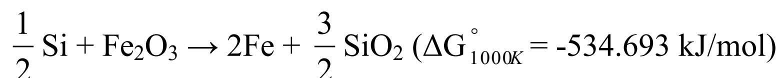

$$\frac{1}{2}\,Si + Fe_2O_3 \rightarrow 2Fe + \frac{3}{2}\,SiO_2\ (\Delta G^{\circ}_{1000K} = -534.693\ kJ/mol)$$

The high value and $\Delta G<0$ indicates that all these binary oxides are highly unstable with silicon. Cobalt oxidesare also highly unstable. For example, cobalt silicide formation can occur by$Co + 2Si \rightarrow CoSi_2$at 500°C. These data are in agreement with the low structural quality reported for CFO films directly grown on silicon [ZHO07]. The need to use of a buffer layer to integrate CFO on silicon is then clear.

I.4 Outline of the thesis

First of all, the principal experimental techniques used in this work are presented in chapter II. Physical thin film deposition methods are introduced, with a special attention to pulsed laser deposition, the technique used to integrate CFO on silicon with different buffers layers: STO, YSZ, Sc_2O_3 and Y_2O_3.The in-situ RHEED monitoring is introduced, and a quick review of the ex-situ characterization techniques is presented(XRD and Φ-scan) with a brief comparison of X-rays and electron diffraction.
The description of transmission electron microscope is presented in annex A with its different modes and techniques.The image mode is detailed for low and high resolution, and EELS and EDXS spectroscopies are described and compared in annex B. The TEM experimental part aims to understand the origin of image contrasts and artefacts leading to a coherent interpretation. A detailed part is dedicated to the TEM sample preparation, with its challenges and alternative variations to overcome the sample degradation.

Chapter III presents the study of the STO buffer use to integrate CFO with Si(001). The STO film grown by MBE at INL-Lyon was structurally characterized at ICMAB, previously to the CFO integration. Both films grown in a two-step elaboration process are epitaxial. Detailed HRTEM analysis is presented as well as a chemical analysis by EELS, which shows Ti diffusion into the CFO layer.

Yttria-stabilized-zirconia (YSZ) as alternative buffer for the integration of CFO with Si(001) is studied in chapter IV.The mechanisms of epitaxy of YSZ were investigated and ultrathin films (~2 nm) were fabricated with very small amount of SiO_x (<1 nm) at the interface. CFO grows epitaxially on YSZ, with (111) out-of-plane orientation. Extremely thin CFO/YSZ bilayers were fabricated, being the SiO_x interfacial layer around 2 nm.

Sc_2O_3 and Y_2O_3 films deposited on Si(111) by MBE at IHP-Frankfurt, have been also used and are studied in chapter V. They present huge lattice mismatch with CFO, but domain matching epitaxy permits high structural quality of CFO. Highly relevant, the Y_2O_3/Si(111) interface is stable after CFO growth. We show that ultrathin (t< 2 nm) Y_2O_3 buffers permit epitaxy of CFO.

Other characterization techniques used in this work are presented (AFM, SQUID) in annex C, and growth generalities and concepts definition about interfaces and dislocations are detailed in annex D.

Chapter II

Experimental techniques

II.1 Elaboration techniques

Techniques of fabrication of thin films are usually categorized in two groups: CVD (Chemical Vapour Deposition) and PVD (Physical Vapour Deposition). The first one uses materials reacting in their vapour phase, and the second uses a physical process to extract atoms from a solid. The physical techniques used in this work are molecular beam epitaxy (MBE) for some buffers layers ($SrTiO_3$, Sc_2O_3 and Y_2O_3 buffers), and pulsed laser deposition (PLD) to grow YSZ buffers layers and thin films of $CoFe_2O_4$.
In this chapter, the MBE technique is briefly introduced, and PLD is described in more details.

II.1.1 Molecular beam deposition (MBE)

MBE is an ultrahigh vacuum deposition technique consisting on molecular evaporation of the constituent elements from one or more effusion cells to a heated substrate. MBE growth is carried under conditions out of the thermodynamic equilibrium and is conditioned by the kinetics of the surface processes. The thin film crystallisation is low enough to allow surface migration of species. The growth rate is typically less than 1ML/s and the surface of the grown film can be very smooth. MBE is applicable to the epitaxial growth of a wide variety of materials and in this thesis we have used some MBE deposited oxides as buffers layers. In particular, collaborators at IHP (Frankfurt-Oder, Germany) have provided Sc_2O_3 and Y_2O_3 films, and collaborators at INL (Lyon, France) $SrTiO_3$ films.

II.1.2 Pulsed Laser Deposition (PLD)

The technique of PLD is illustrated schematically in figure II.1.

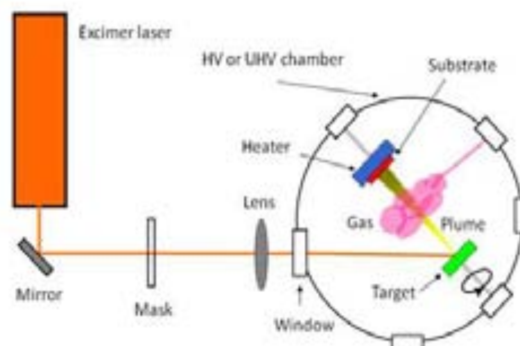

Figure II.1: (a) Schematic illustration of the PLD technique [HER04].

It is based on the use of proper laser radiation directed through a window on a ceramic target placed in a vacuum chamber, to create a plasma that will be deposited on a substrate. A main characteristic of the technique is that the stoichiometry of the target, excluding highly volatile species, will be transferred to the substrate. This requires however some characteristics of the radiation arriving to the target: wavelength in the ultraviolet, pulsed (tens of ns or shorter), and high energy density. In general excimer lasers are used, the most common ones being those using KrF. The wavelength is 248 nm (photon energy around 5 eV), and the repetition rate and pulse length are typically 1-10 Hz and 10-40 ns, respectively. Other excimer lasers, as the ArF (λ = 193 nm), Nd:YAG lasers, or ultra-fast lasers are much unusual. Ultraviolet radiation is necessary because optical absorption length (typically below 1 micron) is very high for most of materials, and then the radiation will be absorbed in the volume closest to the target surface. It is also necessary that the heat caused by the absorption stays confined very close to the irradiated area and very close to the surface. It implies that the thermal diffusion length has to be very short, and then the laser pulse has to be very short (tens of nanoseconds). The third requirement is that the energy exceeds a threshold that will cause that the atoms will be in a state totally out of the equilibrium, forming a plasma quickly [WIL00]. Typical energy density (usually known as laser fluence) is 1-3 J/cm^2, which is achieved by focusing the beam with a lens placed out of the deposition chamber. In addition the target needs to be moved during the process to reduce its erosion, otherwise its morphology will be finally non-uniform, with typical formation of cone-like structures that would result in non-stoichiometric evaporation [EAS07]. The process of irradiation under these conditions is usually known as ablation, and causes congruent etching of the atoms in the target. It is important to mention that the technique is not efficient for all classes of materials. For example, when metals or semiconductors are irradiated under the mentioned conditions they tend to eject liquid droplets. Detailed information on the mechanisms of laser-matter interaction for different classes of materials can be found at reference [EAS07]. PLD is particularly efficient to deposit oxides, and because ablation is congruent results particularly convenient to grow oxide films having more than one cation.

As mentioned, the target is inside a high or ultra-high vacuum chamber, and thus the plasma will expand quickly towards the substrate that usually is at a distance of 4-7 cm from to the target. The substrate holder permits heating it and it is usual to introduce oxygen in the vacuum chamber (typically from 10^{-4} to 0.5 mbar). It is necessary because although oxygen is present in the target (as example, stoichiometric ceramic targets of $CoFe_2O_4$ are used to deposit $CoFe_2O_4$ films), its high vapour pressure would cause loss in both target and substrate/film surface. On the other hand, the oxygen pressure permits to reduce the huge energy (up to hundreds of eV) that atoms and ions have when are ablated. Under vacuum the plasma would expand very quickly along the direction normal to the target (due to characteristic shape revealed by the emitted photons the plasma is known as “plume”). Increasing the pressure the front of the plasma is decelerated (see in figure II.2 the effect of the pressure on CeO_2 plumes).

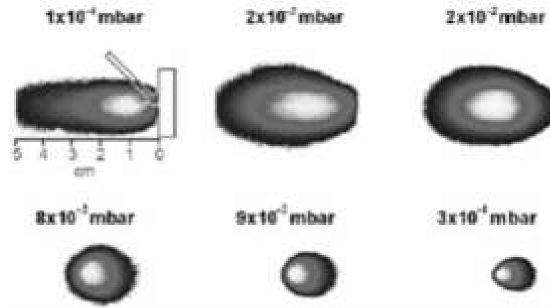

Figure II.2: (a) Pictures of a PLD plume taken 4.5 μs after ablation of CeO_2 for different oxygen pressures [TRT99].

The kinetic energy of the particles that arrive on the substrate will depend on the specific deposition condition, particularly the pressure, target-substrate distance, and laser fluence, but usually will be above the eV. This high energy is believed to enhance crystal growth compared to low-energy techniques [CHR08]. A distinctive characteristic of PLD is the pulsed deposition: after each laser pulse, atoms arrive on the substrate during few microseconds, with no additional arrival for a time of 1/f (f the laser frequency). This results in two different parameters, instantaneous and average growth rate, that can have different influence on the growth. A further advantage of PLD is that different deposition parameters (as oxygen pressure, temperature, and both instantaneous and average deposition rate) can be modified independently. Finally, PLD is compatible with the use of reflection high-energy electron diffraction (RHEED), thus permitting deposition with real time control. Indeed, sometimes PLD done with RHEED control is called as “laser molecular beam epitaxy”.

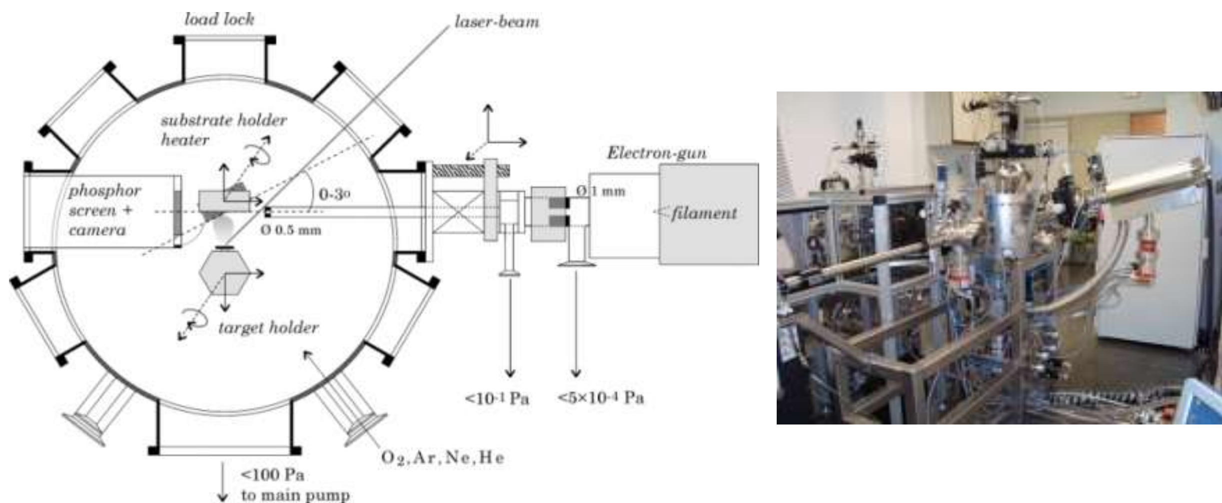

Figure II.3: (a) Schematic illustration of a PLD system with RHEED [RIJ07-1], and (b) picture of the used experimental set up at ICMAB.

Experiments were carried out in the thin film laboratory of the ICMAB laboratory (figure II .3).The laboratory owns two PLD deposition systems and the beam of an KrF excimer laser (wavelength of 248 nm, pulse duration around 30 ns, repetition rate up to 10 Hz, maximum energy per pulse 700 mJ) can be directed to each of them. They were fabricated by Twente Solid State Technology. The two systems dispose of load lock chamber and a multiple target holder to allow fabrication of multilayers in a single process. Both substrates and targets can be loaded via the load lock. The base pressure in both PLD systems is below 10^{-8} mbar, and the substrate heaters permit high deposition temperature (above 850 ºC) under oxygen and/or argon pressures.

One of the chambers integrates a RHEED system for growth dynamic studies and real-time control of the deposition. It uses an electron gun operated at 30 kV (in the experiments here reported) and two-differential vacuum stages that allow monitoring the growth under high-pressure oxygen up to 0.5 mbar.

II.2 Diffraction techniques

Diffraction by crystalline materials corresponds to the coherent scattering of radiation by a periodic structure of atoms. It only occurs if the wavelength has the same order of magnitude than the periodicity of the structure probed. The radiations used here are X-rays and electrons. After a description of the reciprocal space, we summarize the basics of diffraction and describe the particularities of diffraction by X-rays and electrons, in the latter for both reflection and transmission cases.

II.2.1 Theory of diffraction

A crystal is defined by its long order periodicity, with a repetition of its unit cell. This elementary volume "v" is defined in the real space by the base of vectors $\overrightarrow{a_1}, \overrightarrow{a_2},$ and $\overrightarrow{a_3}$, as $\nu = \overrightarrow{a_1}(\overrightarrow{a_2} \wedge \overrightarrow{a_3})$. And atom positions can be described by: $\vec{R} = m_1\overrightarrow{a_1} + m_2\overrightarrow{a_2} + m_3\overrightarrow{a_3}$.

The reciprocal lattice is described with another vector base $\overrightarrow{b_1}, \overrightarrow{b_2},$ and $\overrightarrow{b_3}$. Where each vector is defined by par $\vec{b}_i = \frac{\overrightarrow{a_j}.\overrightarrow{a_k}}{\overrightarrow{a_i}(\overrightarrow{a_j} \wedge \overrightarrow{a_k})}$, with i, j and k= 1, 2 or 3, and is orthogonal to two vectors of the direct base: $\overrightarrow{a_i}.\overrightarrow{b_j} = 1$ if $i = j, = 0$ if $i \neq j$. $\vec{K}$ is then defined by $\vec{K} = h\overrightarrow{b_1} + k\overrightarrow{b_2} + l\overrightarrow{b_3}$, and more generally in the reciprocal lattice: $\overrightarrow{r^*} = n_1\overrightarrow{b_1} + n_2\overrightarrow{b_2} + n_3\overrightarrow{b_3}$.

A family of lattice planes are determined by the integers (hkl) called Miller indexes. Equivalently, (hkl) denotes a plane that intercepts the three points $a_1/h, a_2/k$ et a_3/l in the direct lattice. The vector $\vec{K}$ is orthogonal to the hkl plans, and its length is the inverse of the interplanar distance.

The radiation interaction with atomic planes of a crystal is shown in figure II.4, where the incident rays are diffracted with an angle of θ. In the real lattice, the condition of constructive interference is given by the Bragg law: $2d\sin\theta = n\lambda$.

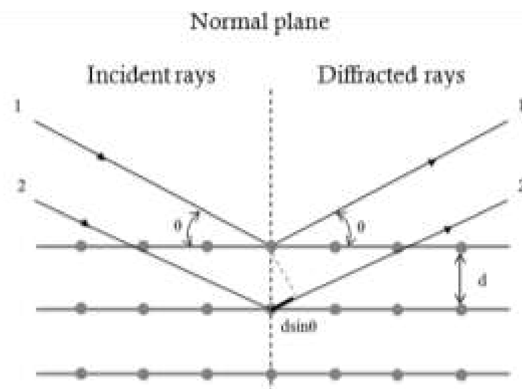

Figure II.4: Diffraction of X-rays by atomic planes of a crystal.

II.2.2 X-Ray diffraction

X-rays are electromagnetic waves interacting weakly with matter (at the considered energies).
Their wavelength has the same order of magnitude that the interatomic plane distances. Then, interplanar distances can be detected from the theta angle (Bragg law), at which there is diffraction, and this permits to identify crystalline phases, orientation, and lattice strain in the analysed materials. Most of the X-ray diffraction (XRD) analyses presented here have been performed at ICMAB using a 3-circles diffractometers Siemens D500, Rigaku Rotaflex RU-200B, and a 4-circle Bruker D8 equipped with a 2D detector. These diffractometers use Cu X-ray sources, which emission presents two lines called $K_{\alpha 1}$ (λ = 1.540562 Å) and $K_{\alpha 2}$ (λ= 1.544390 Å). Their relative intensity is 2/1, and because they are very close in wavelength is usual that their contribution to diffraction peaks from films is not resolved, and then an effective wavelength λ* = 1.541838 Å can be used for the analysis.

For an X-ray beam irradiating a set of crystallographic planes (hkl) the maximum intensity of the scattered beam occurs at an incidence angle according the Bragg law:

$$2d_{(hkl)}\sin\theta = \lambda$$

Where d_{hkl} is the interplanar spacing, and λ is the wavelength of the used source of X-rays.

Two measurements geometries are presented in figure II.5: symmetric and asymmetric. In the symmetric configuration the diffraction planes are parallel to the sample surface, and in the asymmetric configuration the sample is oriented in order to obtain diffraction conditions for different planes non parallel to the sample surface.

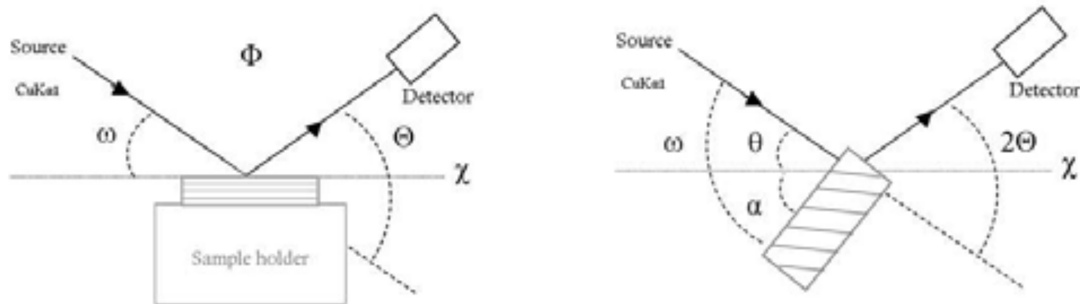

Figure II.5: Sketches of the diffractometer used on symmetric (a), and asymmetric (b) configurations.

The symmetric configuration θ-2θ adjustment is done with respect to the substrate. χ and ω are adjusted to obtain a substrate symmetrical reflection. The experimental substrate and film spectra in the symmetric configuration present different peaks corresponding to atomic planes parallel to the surface. The substrate, being typically perfectly crystalline and thick, shows high intensity and narrow peaks, while the width of the film peaks is inversely proportional to the number of diffracting plans in the thin film. The angular location of the peaks in the spectra allows measuring the distance of the atomic planes in the direction perpendicular to the sample surface. In the case of textured films, a single family of planes is oriented perpendicular to the sample surface. In polycrystalline samples, different orientations can be observed in the spectra.
Other family planes tilted with respect to the sample surface can be measured with an asymmetric configuration of the system: ($\omega \neq \frac{2\theta}{2}$, or tilting χ) and orienting properly the sample along the in-plane direction.

The Φ-scans allow exploring the in-plane texture of the film by a sample rotation around the azimuthal angle Φ. In order to satisfy the Bragg condition for a certain asymmetrical reflection, the sample is tilted in the χ angle while keeping the ω= θ condition. This procedure allows determining the relative in-plane orientation between the film and the substrate and their epitaxial relationship. The combination of different phi-scans taken with different values of ω leads to a pole figure which is a 2-dimensional Φ-ω map.

II.2.3 Electron diffraction

Both elastic and inelastic scattering are involved in electron diffraction techniques. Two theories, the kinematic one and the dynamical one, describe these processes. The kinematic theory considers that the incident beam is not attenuated after the diffraction phenomenon, and that its intensity is largely higher than the diffracted beams. Furthermore, the diffracted beams do not diffract themselves again, and their interaction with the incident beam is neglected. This theory is applied in most of the analysis of crystals such X-ray or neutron diffraction.
In the case of electron diffraction, the huge interaction with matter does not respect the kinematic approximation. Indeed, the incident beam can be attenuated by diffraction due to a higher thickness of the sample probed, presence of defects, etc, and multiple diffraction and interferences with other beams cannot be neglected. The diffracted beam can then have a higher intensity than the incident one, as in Bragg condition. A dynamic theory, taken into account these effects, is then described [COW81, REI84].

The kinetic approximation can be used to describe Bragg spots in electron diffraction patterns, but other features as Kikuchi lines require the dynamical theory.

II.2.3.1 Reflection High-Energy Electron Diffraction (RHEED)

Reflection High-Energy Electron Diffraction (RHEED) consists in sending an accelerated electron beam (10-100kV) in grazing incidence in the probed surface (up to 2°), and detecting the diffracted beams. This characterization technique allows checking the crystallinity and roughness of the surface. In-situ RHEED can be combined with a deposition technique, controlling the evolution of the thin film growth, from the first steps of the process. This is critical information to understand the growth mechanisms.

One of the chambers of the PLD systems at ICMAB integrates a RHEED system with two-differential vacuum stages that allow monitoring the growth under high-pressure up to 0.5 mbar. It used a 30 kV electron gun, and the substrate is up-side down, but the geometry is equivalent as the sketched below (figure II.6). The electron wavelength λ (Å) can be estimated by $\lambda = \sqrt{\frac{150}{E}}$, with E in eV. The distance sample-phosphor screen is usually less than 30 cm, the incident angle ~ 0.5º <θ_i< 3º, and the azimuth (in-plane) angle is adjusted to the desired axis zone.

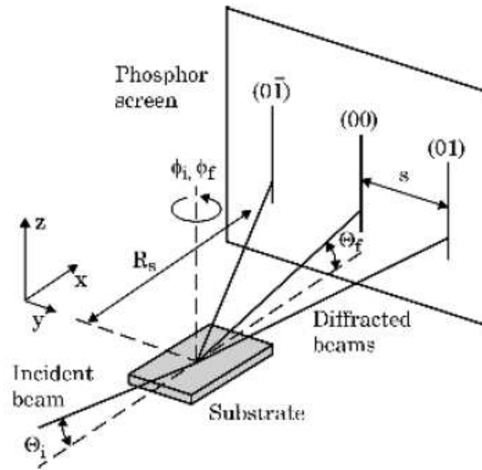

Figure II.6: Schematic illustration of RHEED geometry. Θ_I (Θ_F) and ϕ_I (ϕ_F) are the incident and azimuthal angles of the incident (diffracted) beam. R_S is the distance between substrate and phosphor screen and S the distance between the diffraction spots or streaks. Sketch from [RIJ07-2].

RHEED provides information about the periodic arrangement of the surface atoms, resulting in different types of patterns (figure II.7) depending on the crystallinity and the surface morphology.

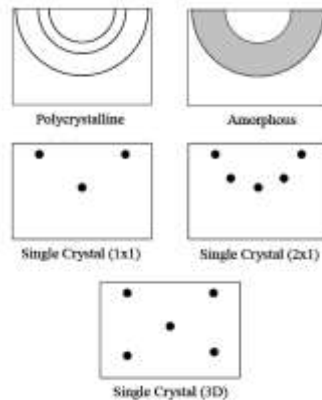

Figure II.7: RHEED schematic patterns of different crystalline states of the surface [HYD06].

A diffuse halo is observed for amorphous surfaces, concentric rings for a polycrystalline state. For a single crystalline surface there is a pattern of Bragg spots along Laue circles. With moderate surface roughness they transform to vertical streaks, but with high roughness arrays of spots characteristics of 3D diffractions appear.

II.2.3.2 Transmission electron diffraction by TEM

The electron-matter interaction is very strong, as the electron beam interacts with the electrostatic potential of matter probed. Then, even using accelerated electron beams, the sample needs to be thinned down to several hundreds of nanometres for a transmission study.

Considering an electron beam of 300 kV, the wavelength is 0.002nm and the Ewald sphere diameter is 1000 nm^{-1}that can be considerated as a plane. In the particular case of transmission electron microscopy, the samples are so thin that the diffraction condition relaxes along the normal of the surface foil. This relaxation of the diffraction condition transforms the diffraction spots in relrods.

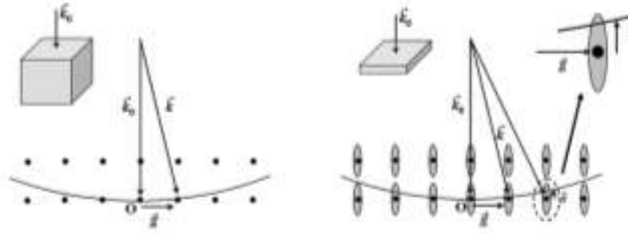

Figure II.8: Sketch of the intersection of the Ewald sphere with the reciprocal lattice showing the relaxation of the diffraction spots for thin samples.

The diffraction domains are reduced to fine sticks of 2/t length, where "t" is the sample thickness. Then, an excitation of a selective reflection hkl of non null intensity can occur when the Ewald sphere intersects with the correspondent diffraction domain, without necessarily passing by a node. $\vec{K} = \vec{k} - \vec{k}_0 = \vec{r}* + \vec{s}$, where $\vec{s}$ is the deviation of the Bragg position.
Ewald sphere intersect simultaneously several reciprocal planes, leading to circular and concentric Laue zones.

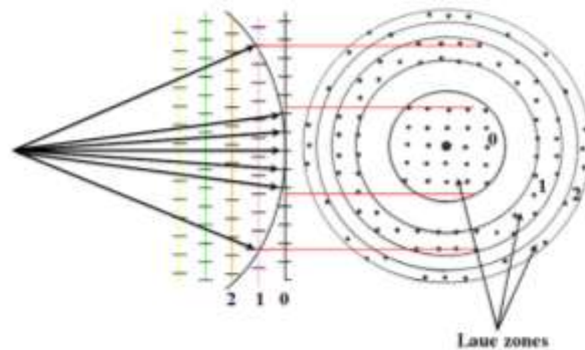

Figure II.9: Sketch of the Laue zones witch thickness depends on the relaxation conditions.

The most frequent diffraction mode used in TEM is the selected area of electron diffraction (SAED). A diaphragm inserted in the image plane of the objective lens is used to select a particular zone of the object in the image mode. Then, the diffraction diagram of this zone can be observed in diffraction mode. Electron diffraction phenomenon in TEM is really important to understand the high resolution contrast detailed in part III.2.2.

Radiation	X-rays		Electron beam	
Technique	XRD	Φ-scan	RHEED	XS-TEM
Orientation (incident beam/sample)	θ°/ atomic planes parallel to sample surface.	θ°/ atomic planes not parallel to sample surface.	Grazing incidence (0-2°)/ surface	Orthogonal to the thin film, the substrate and their interface
Sounded atomic planes	Out-of-plane	Non- parallel to the interface	Out-of-plane	In-plane & Out-of-plane
λ (nm)	0.15406 (Cu)		0.0086 (20 kV)	0.00197 (300 kV)
Resolution	0.01°		5% precision	0.1 nm
Range	0-360°		10-100 kV	200-300 kV
Quantitative analysis	$2d_{hkl}\sin\theta = \lambda$		a= λD/e	Direct measure (/ substrate)

Table II.1: Characteristics of the different diffraction techniques.

d_{hkl}: interplanar distance for the respective (kkl) family planes.
D: distance between the substrate and the RHEED screen
e: distance between two consecutives rods of the RHEED pattern
a: parametter

II.3 Transmission Electron Microscopy (TEM)

The essential characterization technique used in this work is high resolution transmission electron microscopy (HRTEM). The microscope components and techniques are detailed in several books [CAR96, EGE96, REI84, WIL96]. Some TEM generalities and concepts are approached in appendix Aandspectroscopies (EDXS and EELS) are compared in appendix B.
In this study of the CFO integration with silicon, we dedicated a particular attention to the interfacial microstructure and arrangement which is critical for the thin film growth, structure and properties. Thin film growth mechanisms and different types of interfaces are described in appendix D.
In this part, the particular contrast of TEM pictures is introduced, and the conventional TEM sample preparation is described. The consideration of the damages suffered by specimen lead to try different TEM sample preparations detailed here.

II.3.1 Interface contrast

In this work, we have noticed that different interfacial contrasts were observed in low magnification (LM) and HRTEM pictures for the same observed zone. Special attention has to be paid on the characterization of the interfacial contrast and structure.

The low resolution pictureshows the thickness homogeneity of the films and the roughness at interfaces. The white contrast observed at the silicon interface so commonly interpreted or related to the presence of an amorphous interfacial layer (AIL) is revealed to be commensurately crystalline in some cases. The HRTEM picture confirms in these cases that interfaces are abrupt and do not exhibit any trace of amorphous layer or additional phases. Then the white contrast observed in LM is not always related to the presence of an amorphous interfacial layer (AIL).

The formation of the contrast at interfaces does not result from the same phenomenon in conventional and high resolution imaging (appendix A.2). The interfacial white contrast observed in LM could be originated by a preferential thinning of the interface during the sample preparation. The image intensity described is express in function of the phase shift introduced by the objective lens $X(\vec{v})$ which depends on the spherical aberration C_s. Then, the spherical corrector in a microscope prevents the delocalisation at interfaces in their resulting pictures. The interface characterization has to be done imperatively in high resolution. Interface imaging change in function of the sample thickness, defocus, and other parameters detail below.

Amorphous interfacial layer:
Amorphous material does not diffract the electron beam as crystalline compounds, then the part of transmitted beam is higher, and the contrast is brighter. The white contrast at the interface can result from the presence of an amorphous interfacial layer.

Fresnel contrast:
Fresnel fringes are seen at the interface of every crystal. Then, the Fresnel method was used to study interfacial properties, by obtaining a series of images at different defocuses [ROS91]. The central Fresnel fringe contrast gives qualitative information of the mean inner potential of the layer respect to the surrounding material. If the fringe is bright underfocus, then the mean inner potential of the layer is lower than the surrounding material (and higher for a dark fringe). The analysis and interpretation of Fresnel contrast at interfaces was studied in detail by R.E. Dunin-Borkowski [DUN00].

Sample thickness:
Lattice fringes in HRTEM appear at interfaces, and rough interfaces can appear smooth changing the defocus conditions. The sample thickness seems to be a major factor contributing to the interface contrast. Indeed, a black contrast at the interface is observed for thickness superior to 30 nm. The sample thickness effect must be reduced by decreasing the sample thickness (6 nm)[BAU00, DIE03].
However, as the materials studied on cross-section geometry have different thinning down rates, the thickness effect cannot be reduced for all the different materials in the same region (Part III.4, figure II.15).

Delocalisation:
The top silicon layer is not always the last layer of dots in the image. This image delocalisation arose in uncorrected microscopes and will result in errors in the measured thicknesses. The amount of delocalisation can vary in function of the microscope and the imaging conditions used. Exit wave reconstruction can quantitatively correct this problem. Muller and Neaton have proposed that uncorrected HRTEM consistently underestimates the thickness by 1.9 Å [MUL01].

Sample tilt:
The observed interfacial thicknesses can be affected by a sample tilt. Ross and Stobbs have discussed the impact of the sample tilt on the interface observations. For a sample of a 10 nm thickness, a tilt angle of 1° will result in 0.17 nm observed extension of the crystalline region into the amorphous region [ROS91].

Residual strain in silicon substrate:
Thermally-induced strains in single crystalline wafers was studied by M. Herms et al [HER00]. An internal strain can remain if there are structural defects or changes of lattice parameters after cooling the sample. A survey of papers have stated that temperature gradients in a range of 1 and 100 $K.cm^{-1}$ causes stresses in a range of 1 and 100 MPa.

Oxygen interfacial layer:
G.Y Yang et al. have reported the epitaxy of a 10 nm STO layer on Si without AIL. They proposed a model for the atomically sharp interface based on HRTEM experimental results and simulations. And they evidence from the simulated images that the oxygen layer at the interface has little influence on the contrast variation along the interface [YAN02].

Delhaye et al have studied the HRTEM contrast at the STO/Si interface. They had systematically observed a dark layer on the silicon side of the AIL, and they carefully checked that it does not correspond to Fresnel fringes resulting from defocusing. Then, they had interpreted this interfacial contrast as a different electron beam absorption in function of the

material. (The amorphous layer appears bright). This tends to indicate that the very thin darker layer contains predominantly Sr (Z_{Sr}=38, Z_{Si}=14, Z_{Ti}=22) [DEL06].

Local misorientation at the interface:
Local small misorientations at the interface resulting in local deviation from the Bragg conditions can change the contrast at the interface.
Interfacial contrast in LM and HRTEM pictures is originated by different phenomenon and provides complementary information. Interfacial imaging and interpretation by HRTEM is not obvious, as the thickness and defocus variation changes the interfacial contrast. The Fresnel method was widely used before the electron exit wave reconstruction and the widespread availability of HAADF atomically resolved.

Finally, it may be relevant to note that the thickness of native silicon oxide on Si(001) characterised previously to thin film growth was 2.4 nm. The same amorphous interfacial layer (IL) thickness was founded for other buffers layers grown on silicon.

II.3.2 TEM sample preparation methods

The heavy interaction between electrons and matter explain the imposition of a previous sample preparation for a TEM characterization. The thickness of the sample transparent to the electron beam can increase with the high tension of the microscope, but is typically inferior to 100 nm. In addition, each different TEM technique needs specific sample preparation conditions leading to a particular thickness (HRTEM), surface homogeneity, smooth surfaces and constant thicknesses over a large area (chemical analysis using STEM imaging to lower magnifications and holography), and very thin area (EELS) (usually < 500 Å). Then, the studied material and the characterization technique have to be considered in order to choose the correct sample preparation strategy. A compromise is often needed when studying several materials (with different properties) by multiple techniques.

II.3.2.1 Planar view and cross-section

There are two different preparations possible for specimen: planar view (PV) and cross-section (CS or XS) with different polishing orientations and observation direction [CAR09, MAR94].
The planar view is prepared by thinning only the substrate side of the specimen, parallel to the thin film interface. It provides a relatively large view area of a thin film normal to its surface, which gives information about grain size, distribution of defect or precipitates.

For cross-section geometries, the specimen is cut to the desired dimensions. (1.7 mm wide, 5-10 mm long and 0.2-1 mm thick), and two pieces of the specimen are embedded face to face, and the sandwich specimen is cross-sectioned (figures II.10 from 1 to 3). Contrary to the planar view, achieving a cross section allows the observation of the interface separating the thin films and the substrate. Then, the film thickness can be extracted, and particular information can be studied as the step coverage, implant damage, etch profile interface contamination…. It also allows multiplying the observable material quantity in the same object, and to protect the material surface. But the different milling rate for different species can be a problem, especially in interfacial zones.
The principal TEM sample preparation techniques are presented and compared, and then sample damage and artifacts induced are review. Finally, the preparation procedure used in this thesis is detailed.

II.3.2.2 Conventional TEM sample preparation

The conventional TEM sample preparation consist on a first mechanical thinning down process (grinder + concave or tripod), and a precision ion polishing system (PIPS) or ion milling to reach the electron transparency around the small hole. The preparation steps are shown for cross-section geometry in figure II.10, and described successively.

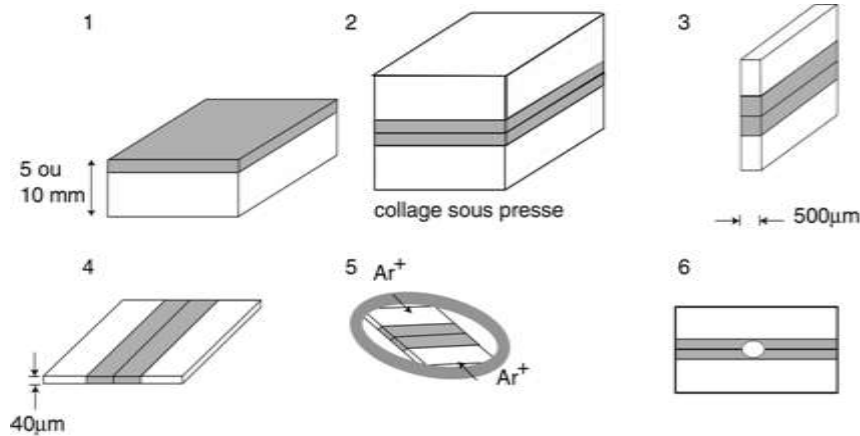

Figure II.10: Sketch of the conventional TEM sample procedure [WAR01].

1: The specimen surface is carefully cleaned with solvent in order to obtain perfectly clean surfaces.

2: A thin glue film of epoxy bond (Gatan) is spread over a surface, and a specimen-glue-specimen sandwich is formed when the two surfaces are put together face to face. This sandwich is introduced in a press in order to obtain a very thin glue film. The whole mounting is placed in a furnace at 80°C to ensure a proper glue polymerization. After polymerization the glue should resist mechanical polishing and ion bombardment.

3: The sandwich or sample bock is then sliced into pieces around 500 µm in thickness using a diamond abrasive saw.

4: The slice is glued on the sample holder and is wet polished using progressively finer lapping films until the scratches lines disappear. Then, the sample piece is turned the side, and is thinned down mechanically with progressively finer films until a thickness of around tens of microns, and then a copper grid (3 nm) is glued on it (with araldite or platinum).

5: An ion bombardment focused on the middle of the sample thin it down to electron transparency.

6: At the edge of the hole, the sample is thin enough to be cross by accelerated electrons, and observable by TEM. At the electron microscope scale, the thin edges of the hole produced by the ion bombardment have parallel faces.

During these successive stages and especially during the final processing, a binocular or an optical microscope is used to check the polish quality (and to locate residual scratches from the preceding polishing step).

The thinning down of the sample can be done manually with a grinder and carbon discs, or mechanically with a tripod and a rotary polisher and diamond discs. Both uses water over the

plate in order to eliminate wastes and to reduce heat produced by friction, and begin with a coarse abrasive and carries on progressively with a finer abrasive grain. The grinder thinning down process is usually followed by a concave polishing resulting in a local thinner area. The thin slice obtained by mechanical polishing with a tripod is homogeneous but very fragile. However, it gives a larger area transparent to electrons and better surface smoothness.
In that preparation stage, the colour of the silicon substrate observed by transparency is a good indicator for its thickness.

Lab bench

Polisher & Tripod

Precision Ion Polishing System (PIPS)

Tripod

Figure II.11: Sample preparation equipment.

Then, an ion milling step can be operated in a chamber under secondary vacuum (10^{-5} Torr). It consists on bombarding the sample with argon ions accelerated from a few volts to several kV (typically 5 keV). The perforation of the sample is detected by an optical microscope and ensues to electron transparent zones characterized by fringes.

The ion-milling procedure is applicable for most Ar^+ ions mills, which allows simultaneously milling from both sides of a TEM sample (top and bottom) in an azimuthally restricted sector perpendicular to the central epoxy line of that cross-sectional TEM sample. This last polishing step by interaction of accelerated ions with the sample removes the surface atoms and suppress the possible damages induced during the mechanical polishing (strain hardening in hard materials, mechanical damage in soft and ductile materials, and thermal effects due to friction, and some matter transport). But the ion milling process can also introduce others artefacts as amorphisation, phase transformation, structure and chemical composition modifications. In order to minimise this effects, it is possible to decrease the incident angle and the ion beam energy and to cool down the sample with liquid nitrogen.

II.3.2.3 Wedge technique: totally mechanical TEM sample preparation

The tripod polisher can thin the sample down to less than 1 µm by pure mechanical polish. The wedge technique was originally developed at IBM [BEN90], and provides the highest flexibility over the other techniques. The real challenge of doing precision TEM samples by wedge technique is the first side polish. The preparation steps from 1 to 4 (figure

II.10) are similar for conventional and wedge technique. Contrary to the conventional preparation where the final thinning down is done by ion milling, the wedge technique consists on introducing a polishing angle to reach electron transparency thickness.

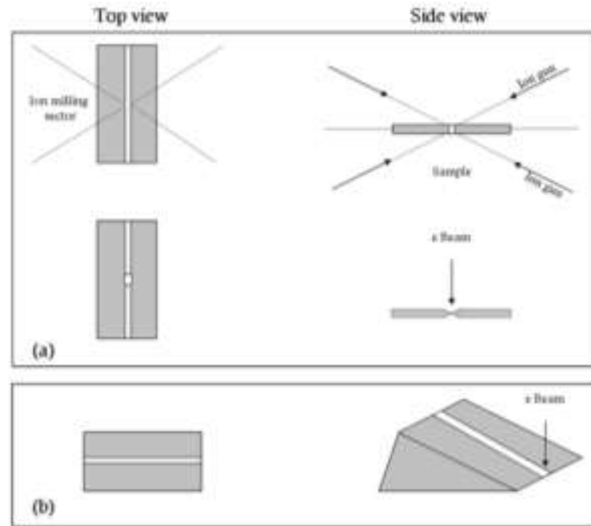

Figure II.12: Schematic view of the sample prepared by mechanical polishing and ion milling (a); and only with mechanical polishing by tripod to bevel (b).

The detailed procedure differing from the conventional preparation is principally the last steps of the mechanical polishing for the planar first side, and the edge second side. The specimen is wet polished using progressively finer diamond lapping films (30, 15, 6, 3 and 0.5 µm), and scratches lines are inspected by optical microscope. The thickness of damage layers formed during the mechanical polishing can reach up to three times the size of the diamond grit. Then, a final polishing is performed using chemical mechanical polishing (CMP) colloidal silica slurry. This step is very important to eliminate all the undesired damages on the specimen. For the first side polishing, the specimen thickness is reduced just to remove the scratch lines implied by the coarser polishing, but as it is the remaining part of the sample, the surface state is crucial. For the second side, attentive inspection of the sample edge is needed because the sample can scrape away. This step is quite difficult, and to protect the sample from cracking, the turning conditions such as speed, direction and loading weight are very important. Furthermore, the necessary conditions are slightly different depending on the form, thickness and composition of samples. During this last step, interference fringes appear under the optical microscope, and are revealed by the chemical mechanical polishing indicating the electron transparency [CAF98].

Figure II.13: Picture of the sample prepared by mechanical polishing by tripod to bevel. The glue joint is visible in the zoom, and the fringes attest the transparency to electrons of the sample.

Finally, the advantages and drawbacks of the polishing techniques are summarized on the following table.

Polishing techniques		Advantages	Drawbacks
Mechanical	**Grinder + Concave**	-Robust sample -Easy to polish the specimen planarly	-Small thin area -Carbon waste from disc can pollute the sample -The ion milling step is needed to arise the electron transparency -Different thinning down rate for different hardness materials -Difficult to target special feature
Mechanical	**Tripod**	-Homogeneous and large atomically flat area with constant thickness/ region of interest (ROI) -Good surface smoothness -Diamond films does not pollute the sample -Possibility to lead the electron transparency without ion milling step (Wedge technique) - Thickness variation depending on the position to apply different analyses techniques with the same sample (Wedge technique) -Possible to target special feature	-Fragile -Heat produced by friction -Difficult to conserve the planar polishing sample - Thickness gradient perpendicular to the wedge angle (Wedge technique)
Ion beam	**PIPS** (Precision Ion Polishing System)	-leads to electron transparency - removes the surface atoms and suppress the possible damages induced during the mechanical polishing	-Different thinning down rate for different hardness materials -Structure and chemical composition modifications: Amorphisation Phase transformation

Table II.2: Comparison of the different manual polishing techniques with their respective effects on the sample.

There are other preparation techniques more or less commonly used as cleaving, focused ion beam (FIB) and ion slicer not detail here. Cleaving is the simplest TEM preparation technique for semi-conductors and single-crystal materials, and it produces atomically flat surfaces with no initial amorphous layer. But this preparation technique does not provide constant thickness samples, and difficult the TEM observation [TEO09, SUD97, CAF91]. FIB sample preparation provides particular specificities that are not available by any other technique including parallel-sided, electron transparent membranes and site specific positional accuracy on the sub-micron scale. But FIB produces the most extensive surface amorphisation (20-35 nm), and provides very limited view area [CAF91, GIA99, MAY07]. The newly developed technique called ion slicer facilitates a very wide area homogeneously thinned [TAT09].

The choice of TEM sample preparation technique is dependent on the information desired, and it is important to minimize the extent of surface amorphisation with all techniques.
Transmission electron microscopy (TEM) is a very useful technique to characterize structural, physical and chemical properties at an atomic scale, and with the realization of aberration corrected high resolution TEMs, the quality of the TEM specimens becomes a limitation factor of interest [DIE03, ZHA98]. Thus, it is crucial that the preparation does not deteriorate the TEM study of the specimen, or in the worst case, know how the sample preparation affects the specimen in order to extract its inherent properties. This is a main issue for obtaining and interprets TEM results which leads to the development of different sample

preparation techniques and studies concerning the artifacts induced [KIM01]. Effects of sample preparation are review in appendix A.6 in order to understand the damage origin. In this thesis conventional sample preparation was first used and it was really important to understand the effects and artifacts caused in order to found a specific preparation procedure adapted to our materials and interpret the experimental results from TEM analysis.

II.3.3 Particular TEM sample preparations

In this study of integration of functional oxides on silicon for a spin filter application, two principal challenges of TEM sample preparation were confronted. The first one consisted on the characterization of the silicon/oxide interface, and the second one on the ultrathin film observation due to preparation damage of the sample.

II.3.3.1 TEM sample preparation for the oxide/silicon interface characterization

The HRTEM characterization of oxide interfaces with silicon was not possible with a classical TEM preparation by grinder or tripod mechanical thinning down and an ion milling process at 5 keV. It was possible to observe the thin film or the substrate separately one from each other, but not simultaneously.
Considering that the ion milling (PIPS) thins down faster the silicon than the oxide film, resulting in zones where the silicon is amorphised and others where the thin film is too thick to be observed by HRTEM. Then, to characterize the thin film/silicon interface, special conditions of sample preparation were needed. The mechanical thinning down was favour and proceed up to 8 μm, and the PIPS tension was reduced to 3 keV.

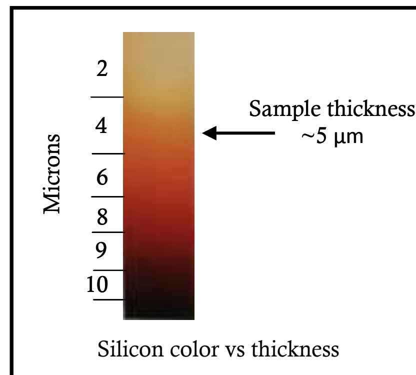

Figure II.14: Silicon colour vs thickness, adapted from [CAF97].

This sample preparation protocol allows the observation of interfaces between materials having different hardness and sputtering yields. But the specimen thickness is not constant across the interface and can affect the contrast of the image.

Preferential thinning down at the interface/ Thicknesses and Contrast:
As in thinner parts of the sample the silicon interface is amorphised by the ion milling process, it is not excluded that the silicon could be thinner next to the interface. The same preferential thinning down can be considered at the CFO/Y_2O_3 interface.

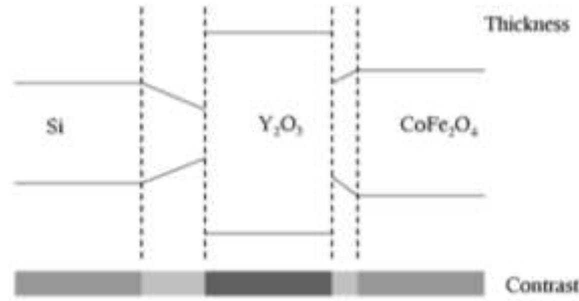

Figure II.15: Sketch of the thickness profile across the interface.

In conventional microscopy, the amplitude contrast depends on the selected beam (transmitted or diffracted) resulting in an amplitude contrast, while in high resolution electron microscopy, the contrast is related to the phase difference between the diffracted beams (phase contrast) (appendix A.2).
The white interfacial contrast observed in LM pictures could be originated by the gain of transmitted beam through the thinner part of the sample. But as the interaction of the electron beam with the sample is very high it is difficult to consider it. The analisis and interpretation of Fresnel contrast at interfaces was studied by R.E. Dunin-Borkowski [DUN00].

II.3.3.2 Improving TEM preparation for ultrathin oxide films integrated on silicon

Ultrathin films (1-3 nm) are easily damaged during the sample preparation process, and more precautions were needed. CFO, Y_2O_3 and silicon are not observed simultaneously in the HRTEM pictures. It seems that these different materials have a different thinning down behavior during the TEM sample preparation step. The CFO degradation was particularly noted and studied.

Here we tried to define the critical preparation step responsible of the degradation of the top film (CFO), and to find a way to avoid this degradation.

The methodology adopted here to lighten this problem was to prepare tree samples by different ways from the classical one (1) (figure II.16.a):
(2) Classical preparation + cooling the ion milling process.
(3) Total mechanical thinning down by tripod (without ion milling)
(4) Depositing a platinum protective film on CFO before the preparation of the cross section. Then a mechanical polishing and cold ion milling stage was proceed.

The PIPS can be used at very low tension on a sample cooled down to -170°C, to reduce its disorder effect related to the heating (2). Then, a preparation totally done mechanically by tripod thinned down to bevel was tried (3). The tripod allows to prepare a sample exclusively by thinning it down mechanically. The tripod preparation will let us determine the effect of the PIPS on the silicon interface and films. Another strategy has been considered for the preparation (4), consisting on growing a coating film to protect the ultrathin films. A platinum film was deposited on the ultrathin films in order to protect them during the sample preparation for tem characterization. This deposition takes place just before the cross-section assembling.

In addition, we can note that these different materials were observed easily for thicker films. This suggests that it should be a problem related to the reduced scale of the ultrathin films.

The platinum recovered sample will attempt to protect the thin films and determine the effect of the mechanical thinning.

<u>Description of preparation methods</u>:
(1) The classical sample preparation method consists on preparing a cross section slice and thinning it mechanically down to ~8µm. Then an ion milling step consists on bombarding the centre of the sample with Ar^+ in order to obtain a hole surrounded by electron transparent zones. This last step, done at room temperature at 3keV, can damage the order of the materials (figure II.16.1).
(2) The preparation method presented here is only differentiated from the (1) in the fact that the ion milling process is proceed at a cooled temperature (-170°C) in order to limit the rise of temperature and disorder in this step.
(3) The tripod allows preparing a sample exclusively by thinning it down mechanically (without the ion milling step). In fact the polishing id done with an angle and results in a bevel. (figure II.16.2). The quality of the bevel and its electron transparency can be characterized by the presence of fringes in the zone of observation (figure II.16.3).
(4) A platinum film was deposited on the ultrathin films in order to protect them during the sample preparation for tem characterization. This deposition takes place just before the cross-section assembling. Here the platinum film was deposited at room temperature and a base pressure of 4.10^{-7} Torr. The thickness deposited was controlled by a quartz balance and was around 10 nm. Then, a cold ion milling step was proceed.

The HRTEM pictures for the same hétérostructures of CFO/Y_2O_3/Si(111) after the four different preparation processes are presented in figure II.16.
The thickness of the CFO top layer is constant in all the samples presented here: 1.5 nm; while the Y_2O_3 buffer layer has a thickness of 3 nm for (1; 2 and 3) and a 1.8 nm thickness in the last case (4). As the CFO layer is the one must affected in the degradation, this slight difference on the buffer thickness can be neglected.

<u>Preparation analysis from figure presented below:</u>
Observing the Si interface, the first observation is that independently of the sample preparation used, the same 2.0 nm amorphous interfacial layer (AIL) is present. This comparison allows to discard the ion milling degradation of the silicon at the interface. Then the classical sample preparation (mechanical polishing + ion milling) is not excluded in our study of the integration of thin films on silicon. Then, the AIL is representative of the sample and it can be concluded that the interfacial structure is formed during the thin films deposition.

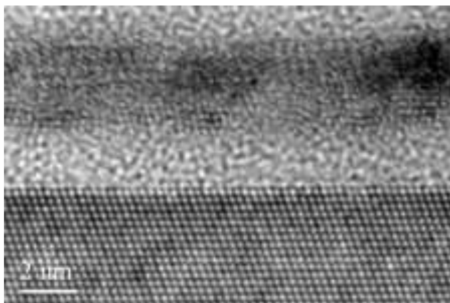

(1) Classical thinning down + PIPS

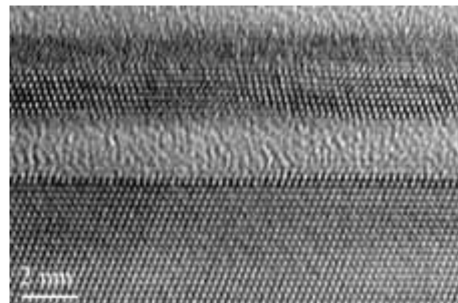

(2) Classical thinning down + Cooled down PIPS

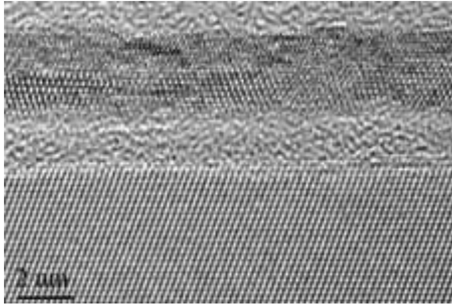

(3) Mechanical thinning down, without PIPS

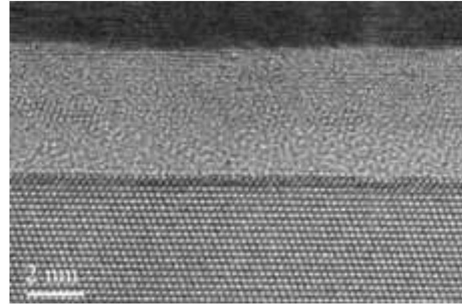

(4) Classical thinning down + a Pt protective film + cold PIPS

Figure II.16: Pictures of ultrathin films of CFO/Y_2O_3 on silicon prepared with different approaches.

Comparing the crystalline quality of the films, we can see that the top film (CFO) is the most affected in the degradation during the preparation. Furthermore, it can be seen that even if the limits of the film can be distinguish in almost all cases, the quality of its crystallinity is improved by reducing the effect of the ion milling (figures II.16. 1, 2 and 3). Finally, it is clear that removing the ion milling step is not sufficient to succeed on the structural characterization of all the ultrathin multilayer system. This suggests that the origin of the degradation is partially due to the mechanical polishing or that the CFO film was not monocrystalline. Indeed, no previous analysis of the crystallinity of the film was done due to the ultrathin thickness of the films. Then, it could be thought that even if the best elaboration condition were used to grow the films, the ultrathin films could be amorphous or polycrystalline.

Finally, the effect of the platinum coating film was not the expected one. Indeed, as this sample preparation problem was not found for thicker films, the platinum film could protect the ultrathin films from damage induced by preparation. But it seems to have accentuated the damage problem, the ultrathin films being preferentially thinned down with respect to platinum.

In addition, it could be relevant to consider that the interfacial oxidation could be possible after the TEM sample preparation. The natural silicon oxide appearing with a direct contact with air (previously to the introduction in the TEM) is known to have a thickness of around 1 nm. And considering further lateral oxidation of the prepared thin foil, it cannot be excluded that the silicon interface with thin films could be damaged. As the preparation is performed in air, a thin layer of amorphous SiO_2 is spontaneously formed on the surface before the sample is examined in the TEM (1-1.5 nm [CAF01]).

A particular sample of Pt/Si(001) is included in this study as a point of reference for the amount of native silica.

Chapter III

Integration of $CoFe_2O_4$ with Si(001) using $SrTiO_3$ buffer layers

III.1 Introduction

$SrTiO_3$ (STO) presents a cubic perovskite cell (Pm3m) with lattice parameter a_{STO}= 3.905Å. The unit cell (figure III.1) contains Sr atoms at the corners, one Ti atom at the center, and oxygen atoms in the centers of all faces. STO crystals have, along <100> directions, alternating SrO and TiO_2 atomic planes.

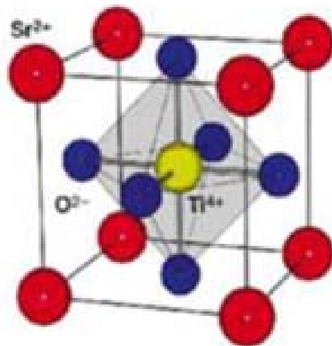

FigureIII.1: Sketch of the $SrTiO_3$ unit cell.

STO has a high dielectric constant around 300, a band gap of 3.3 eV and its conduction and valence bandoffsets with respect to Si are -0.14 eV and 2.4 eV[BER90]. It was a candidate as high-k oxide to replace SiO_x as dielectric, but epitaxial growth on Si(001) was elusive until McKee et al. proved in 1998 that it is possible, and more over they showed that the STO/Si(001) interface can be free of SiOx interfacial layer [KEE98]. Very soon researchers at Motorola described in detail the process required to grow high quality STO films on Si(001) using molecular beam epitaxy [Li_03], and today the method is recurrently followed with little variations by all as a recipe [BHU03, HU_03, Li_03, MI_08, NOR06, TAM98, TIA06, YU_00]. The method is effective but it is not simple, and the reproducible growth of high quality STO/Si(001) is difficult.

Single crystalline STO(001) has been the most used substrate to deposit functional oxide films, and thus it is natural to integrate these oxides with Si(001) using a STO buffer layer [MEC99, NIU11-1, PRA05,-08, TOK95]. CFO has moderately good matching with STO, with mismatch of 7.5% for cube-on-cube epitaxial relationship with STO (figure III.2). Epitaxial CFO film on STO(001) substrate with semicoherent interface and saturation magnetization (350 emu/cm^3) close to the bulk has been reported [XIE08]. The integration of CFO on STO buffered Si(001) has been an objective of this thesis. We have used STO buffers fabricated by MBE by collaborators at INL were used to deposit CFO by PLD at ICMAB.

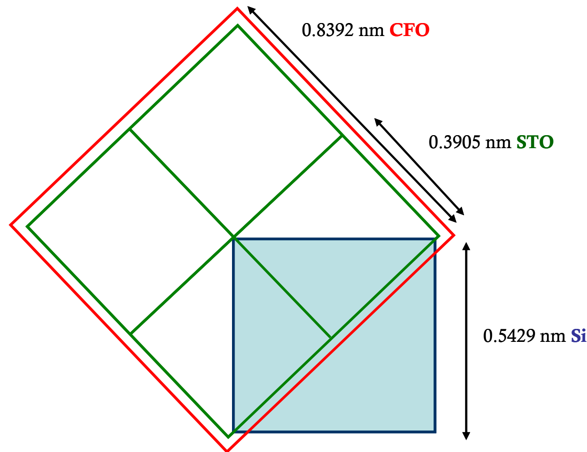

FigureIII.2: Sketch of the epitaxial matching between (001) surfaces of CFO, STO and Si unit cells.

III.2 $SrTiO_3$ on Si(001)

$SrTiO_3$ was deposited at INL on p-type Si(001) substrates deoxidized by annealing under Sr partial pressure. This mechanism leading to a reconstructed surface was described by Wei et al [WEI02]. After Sr coverage of half a monolayer, 1 min annealing at 360°C and $P(O_2)= 6\times10^{-8}$ Torr was done to oxidize the Sr layer. Then, 2-3 monolayers of STO were deposited before ramping the oxygen pressure up to 10^{-6} Torr for the rest of the growth. The optimisation of the elaboration conditions, using Sr and Ti effusion cells is detailed in the thesis of G. Niu [NIU09]. The $P(O_2)$/T diagram shows a very small window of appropriate elaboration conditions; the optimal T is 360 °C with initial oxygen partial pressure of 5×10^{-8} Torr. This permits to achieve a high-quality single crystalline $SrTiO_3$ film andflat interface between STOand Si [NIU11]. The STO buffer layers provided by INL were t= 17.5 nm thick.

Figure III.3 shows RHEED patterns along $[100]_{STO}$ and $[110]_{STO}$. The observation of intense streaks indicates good crystallinity of the STO film. The surface exhibits a 1×1 pattern characteristic of an unreconstructed epitaxial surface. The intensity modulation of the rods in the pattern taken along $[100]_{STO}$ could be due to a certain surface roughness.

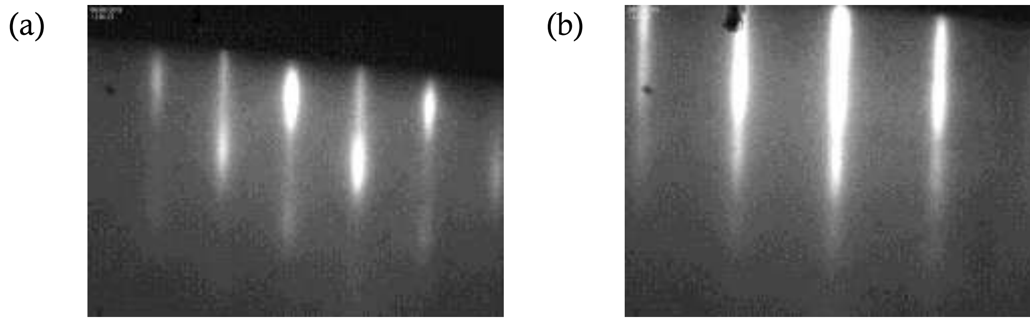

FigureIII.3: RHEED patterns of STO/ Si(001) along (a) [100]STO, and (b) [110]STO.

Figure III.4 presents the STO surface topology obtained by AFM. The surface is flat, with a root means square (rms) roughness of 0.5 nm and with islands having 20 nm lateral size. The bright spots could be due to contamination of the sample during its ambient air exposure.

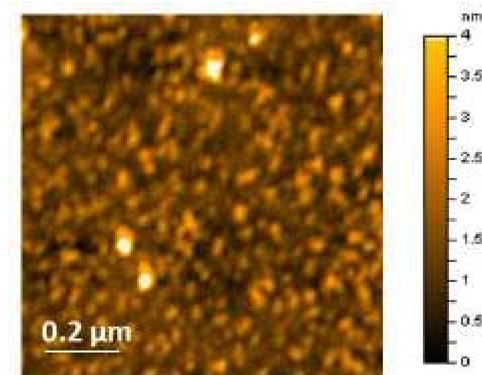

FigureIII.4: AFM topographic image of STO/Si(001).

The sample was cut along $[110]_{Si}$ direction for cross-section TEM sample preparation. The low resolution (LR) picture presented in figure III.5 shows that the STO film on Si(001) has an homogeneous thickness of 17.5 nm. The contrast variations of the film and the inhomogeneous thickness of the bright region of the STO/Si interface is function of the specimen thickness and indicates a degradation effect of the TEM sample preparation. Observing the intensity profiles (figure III.5.b) extracted from the LRTEM pictures (figure III.5.a), it can be seen that the bright contrast at the STO/Si interface increases when decreasing the specimen thickness. The IL thickness measured varies from 2.4 nm in thin specimen zones of the sample to 1.5 nm in thicker ones. The higher brightness at the interfacial layer in comparison with Si and STO can be due to the lower atomic order and/or to the smaller quantity of material. Figure III.5 shows clearly the degradation effect of the sample preparation at interfaces, and confirms that special attention has to be paid on the choice of a representative part of the foil (the effect of the sample preparation is detailed and discussed in chap II).

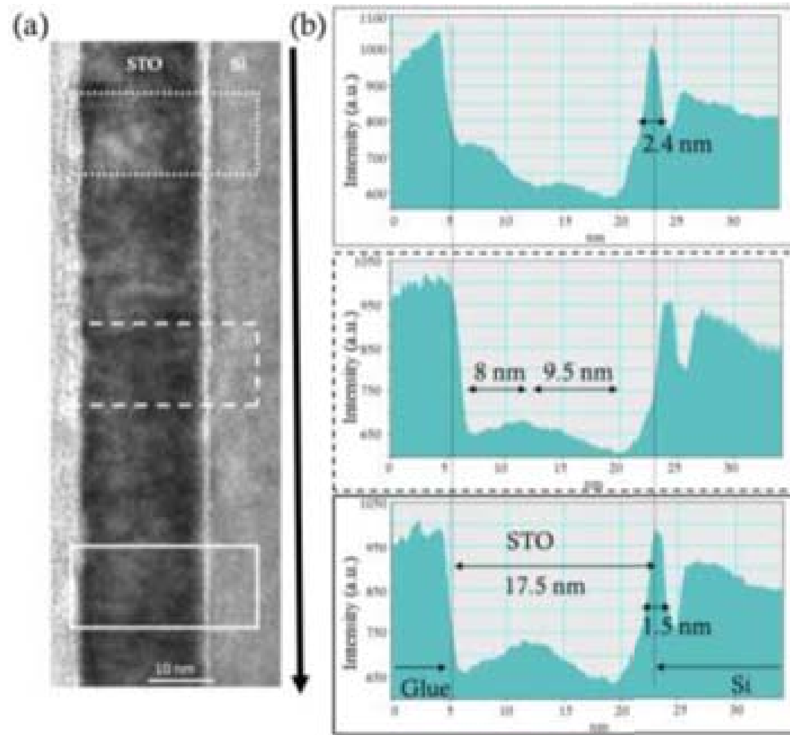

Figure III.5: (a) LRTEM cross-sectional view of STO/Si(001), and (b) intensity profile along the corresponding marked zones, showing the effects of the TEM specimen preparation.

Different information can be extracted from different zones of the cross-section sample. The thinner part of the specimenis more convenient to characterize the STO structure, and the thicker parts to study the interface. This is evident in high resolution images. The thinnest zone of the sample presents interfacial disorder of around 2 nm width (not presented here). On the contrary, the STO/Si interface appears crystalline in thicker parts of the sample (figure III.6), although the STO thin film was not enough electron transparent, and its structural analysis was impossible.

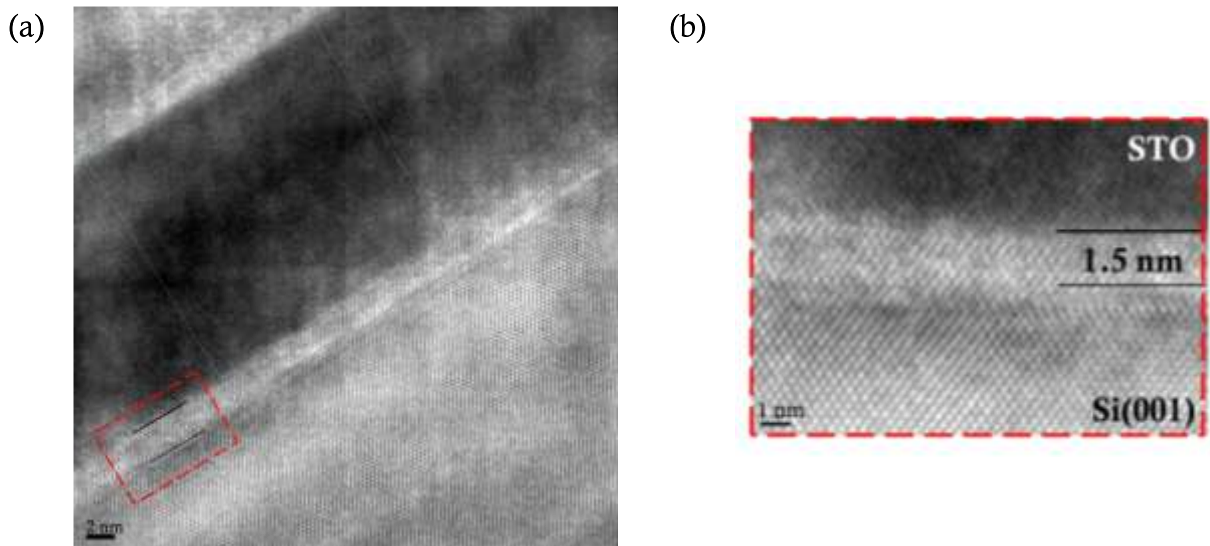

FigureIII.6: (a) HRTEM cross-sectional view of STO/Si(001) in $[100]_{Si}$ zone axis and (b) zoom of the interfacial zone indicated by a rectangle in (a).

The HRTEM characterization of high-quality epitaxial STO thin films directly on Si, with sharp and commensurately crystalline interface, was already reported [KEE98, LI_03, Mi_08]. However, the presence of an amorphous or transition interfacial layer of few nanometres is very usual [HE_05, YU_00-04], being apparently very sensitive to the pressure and temperature during deposition [NIU11-1,-2,-3, YON10].

III.3 $CoFe_2O_4$ on $SrTiO_3$/ Si(001)

A CFO thin film was grown on STO/Si(001) by pulsed laser deposition at ICMAB. The CFO thin film, 18.5 nm thick, was deposited at 550°C at an initial oxygen pressure 10^{-4} mbar for the first 40 laser pulses, and 0.1 mbar for the rest of the pulses (up to 5000).

III.3.1 In-situ RHEED, AFM and XRD characterization

A RHEED system installed in the PLD chamber allowed to check in-situ the crystallinity of the surface of the STO buffer layer, and to monitor in real time the growth of the CFO film. Figure III.7 shows the evolution of the RHEED patterns during the CFO growth. The pattern of the STO buffer (figure III.7.a) quickly changes when CFO growth starts. After 40 laser pulses (nominal thickness 1.5 nm) Bragg spots corresponding to both STO buffer and CFO film are observed (figure III.7.b).With additional laser pulses the pattern changes (figure III.7.c) and remains stable until deposition ends.

FigureIII.7: RHEED patterns taken at 1.2° along [100]STO: before CFO growth (a), after 40p of CFO deposited under an oxygen partial pressure of 10^{-4} mbar (b), and (c) under 0.1 mbar of oxygen and 250p of CFO.

Figure III.8 presents RHEED patterns of the deposited CFO film, taken along $[100]_{STO}$ and $[110]_{STO}$. They show spots with different spacing characteristics of the periodicity of the specific crystal directions. The patterns are more spotty than streaky, particularly along [100]STO, signalling significant surface roughness.

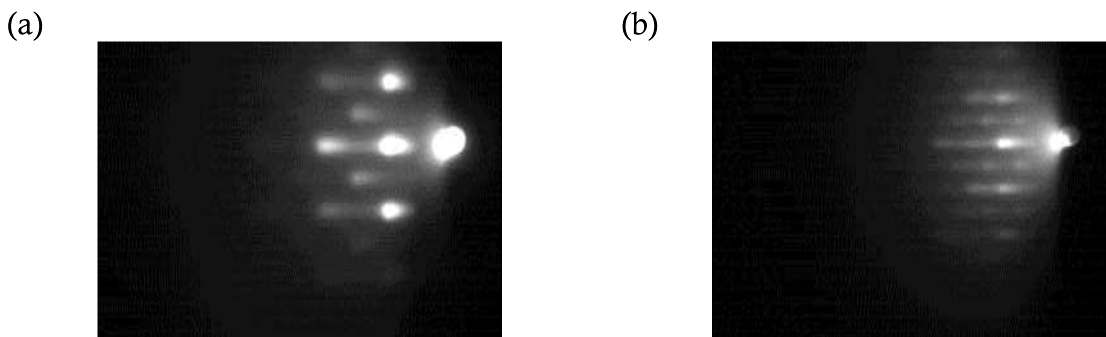

FigureIII.8: RHEED patterns of the deposited CFO film along [100]STO (a), and [110]STO (b).

The CFO surface morphology is presented in figure III.9. The surface is homogeneous and moderately flat with a measured roughness of 0.5 nm.The white spots are probably particles due to contamination during the ambient air exposure.

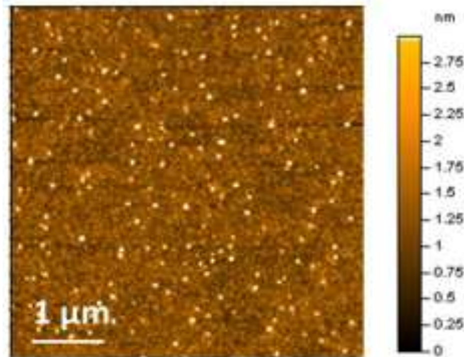

FigureIII.9: AFM topography of the CFO/STO/Si(001) sample.

The crystallinity of the structure was characterized by XRD. Figures III.10.a and b show the θ-2θ scans around symmetrical and Φ–scans around asymmetrical reflections, respectively. The diffraction peaks in the symmetrical θ-2θ scan (figure III.10.a) correspond to (001) reflections of CFO, STO and Si, indicating that CFO is fully (001) oriented along the out-of-plane. This is in agreement with the epitaxial growth of the bilayer indicated by RHEED, and the absence of additional peaks signal the presence of a single phase spinel.The Φ-scans around asymmetrical Si(111), $SrTiO_3$(111) and CFO(222) reflections are presented in figure III.10.b. The four $SrTiO_3$(111) peaks, 45° apart from the Si(111) ones, indicate that the STO unit cell is rotated in-plane by 45° respect the Si cell. The Φ-scan around CFO(222) reflections confirms epitaxial growth, with four peaks at the same angles that the STO ones indicating cube-on-cube growth of CFO on STO. The epitaxial relationshipsare [100]$CoFe_2O_4$(001) // [100]$SrTiO_3$(001) // [110]Si(001).

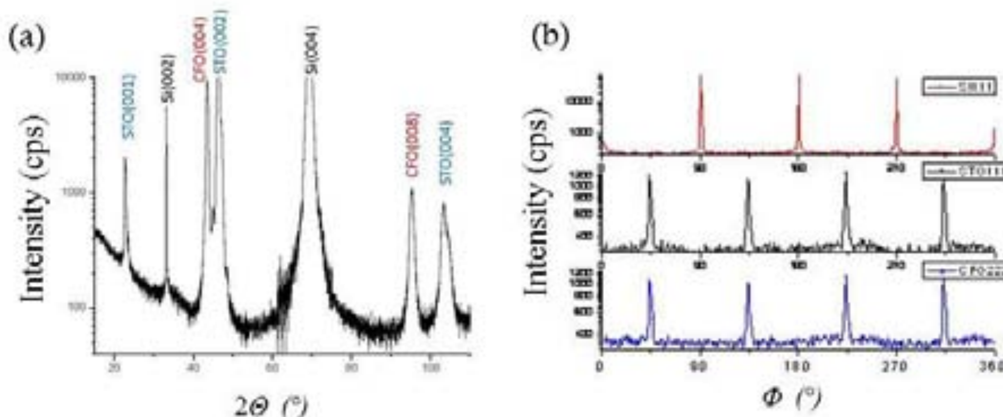

FigureIII.10: XRD θ/2θ (a) and Φ (b) scans of the CFO/STO/Si(001) sample.

III.3.2 Structural characterization by TEM

A cross-section of the sample was prepared by tripod and the TEM observation of the bilayer is presented below. Figure III.11.a shows a low-resolution picture of CFO/STO/Si(001) sample.

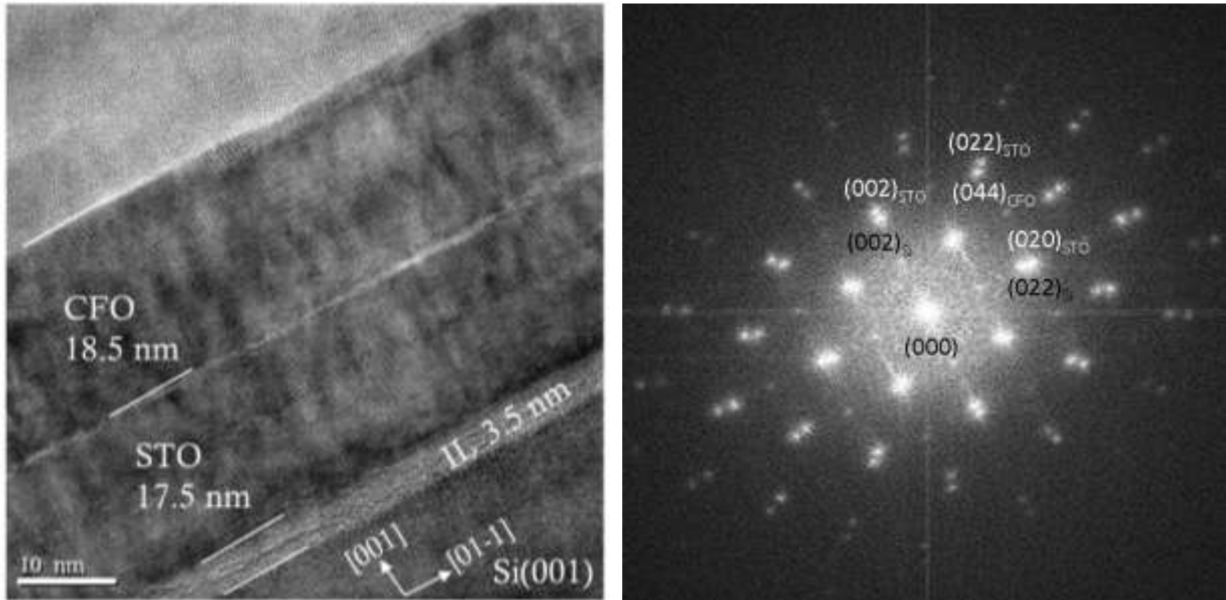

Figure III.11:LRTEM cross-sectional view (a) and FFT (b) of the CFO/STO/Si(001)sample along the $[011]_{Si}$ zone axis.

The CFO surface and the CFO/ STO interface are regular and quite sharp. An amorphous interfacial layer (AIL) of 3.5 nm is observed at the STO/Si interface, hindering an STO deformation analysis. This AIL could be due to oxygen diffusion through STO during the CFO deposition, but it could be due to sample degradation during TEM specimen preparation as discussed above (figure III.5). The STO film presents contrast variation dividing the film in two horizontal regions: a 9.5 nm layer close to the AIL, and a second 8 nm thick. Our collaborators at Lyonhad reported the presence of a double layer on a thick STO film consisting on a STO phase coherently strained on Si up to 24 ML (9 nm), and above this thickness, plastic relaxation leads to a fully relaxed STO at 118 ML [NIU11]. The quality of the prepared specimen has not permitted verify if this inhomogeneous strain state is present in the CFO/STO/Si(001) sample.

Observing the FFT of the picture (figure III.11.b), we can see two close patterns of spots at positions reflecting that the LRTEM image was taken in $<011>_{Si}$ zone axis, and that the epitaxy of the system is [100]CFO(001) // [100]STO(001) // [110]Si(001), ie, the orientation of both thin films is rotated of 45° with respect to the silicon substrate. The spot splitting resulting from the 7% latticemismatch between CFO and STO indicates that CFO is relaxed.

High-resolution pictures presented in figure III.12 show the excellent crystalline order of CFO and STO films, and the sharp and commensurately crystalline CFO/STO interface with slight roughness within ~0.5 nm. Observing closely the atomic columns, the correspondence between a CFO unit cell (uc) with 2 STO uc is confirmed. The in-plane and out-of plane interplanar distances measured for STO and CFO layers correspond to the bulk ones, and dislocations formed by half-atomic planes of CFO are detected at the interface with a spacing around 2.5 nm.

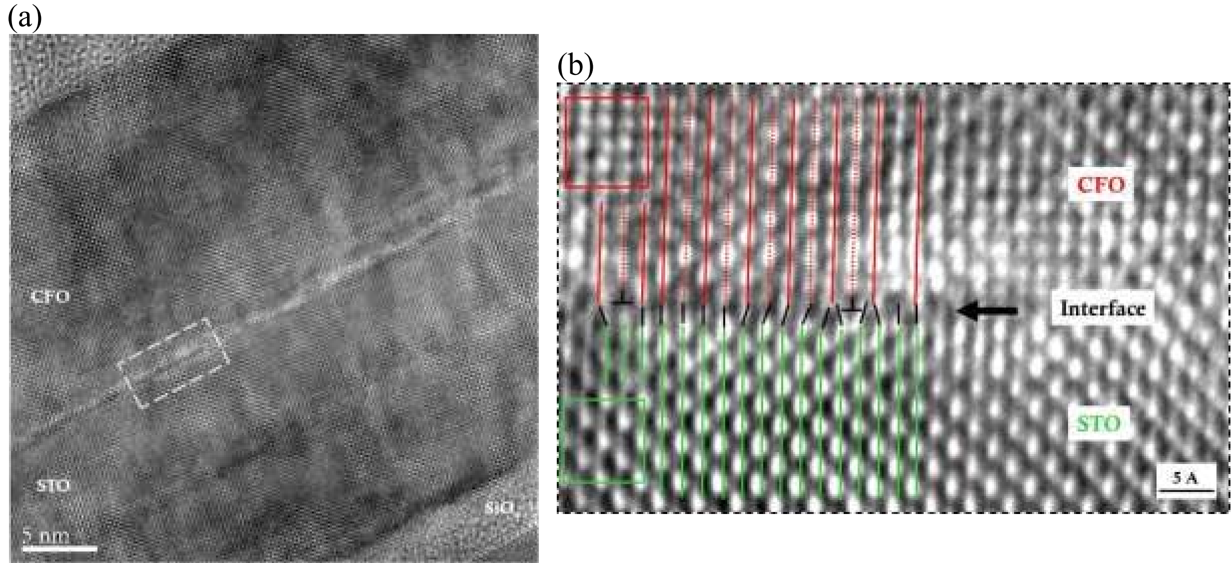

Figure III.12: (a) HRTEM cross-sectional view of the CFO/STO interface, (b) zoom of the region marked in (a).

The GPA a nalysis is appropriate to study the strain of the CFO thin film. The stra in is determined here relative to the STO film. Figure III.13.a shows the map of in-plane strain ε_{xx} of C FO. The stra in profile through the int erface (figure II I.13.b), averaged ove r 15 nm (marked r ectangle in the map), re veals a d eformation of ~7%. This de formation c losely corresponds to the theoretical mismatch between CFO and STO. The out-of-plane strain map shows a sim ilar relative stra in map (not shown here) confirming th at the C FO thin film is relaxed on STO.

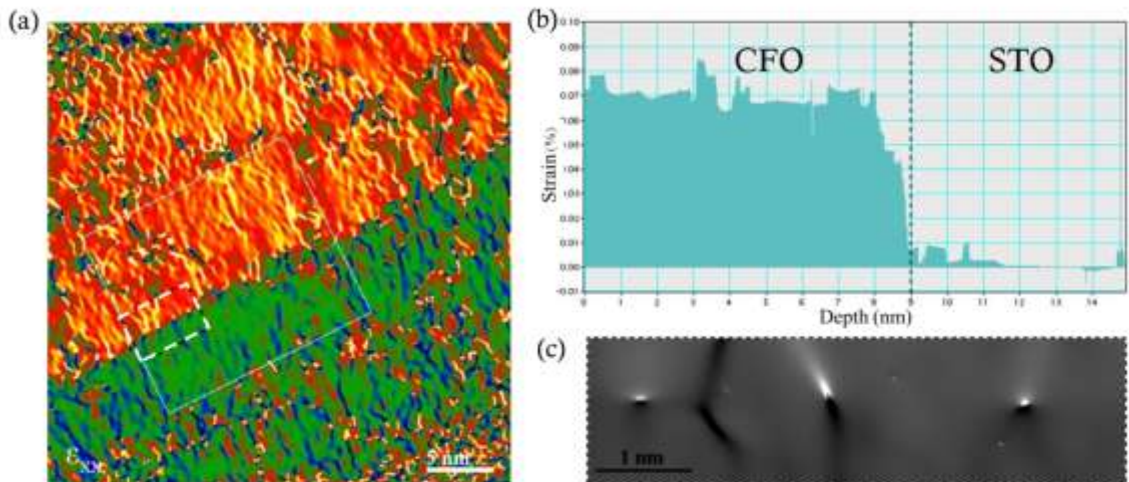

Figure III.13:(a) In-plane strainε_{xx} of CFO relative to STO, (b)ε_{xx} profile through the interface, (c) zoom around the interface of (a)showing misfit dislocations.

Figure III.13.c shows the presence of misfit dislocations at the interface that permit the strain accommodation. We also show in figure III.14 the Fourier filtered reconstructed image from (020) spot s which a llows to identify the interfacial disl ocations. The CFO/STO interface presents coherent zones separated by misfit dislocations (signalled by arrows), thus reflecting a se mi-coherent interface.The C FO and S TO (001) plane s are c ontinuous a cross the interfacebetween these mi sfit dislocations as observed in figure II I.14.b. The int erplanar

distance measured along the interface is d= 0.2 nm. It corresponds to the smaller interplanar distances of CFO and STO along <100> directions, which are the quarter of the lattice spacing for CFO and the half of the lattice spacing for STO: d_{CFO}= 0.21 nm and d_{STO}= 0.19 nm.

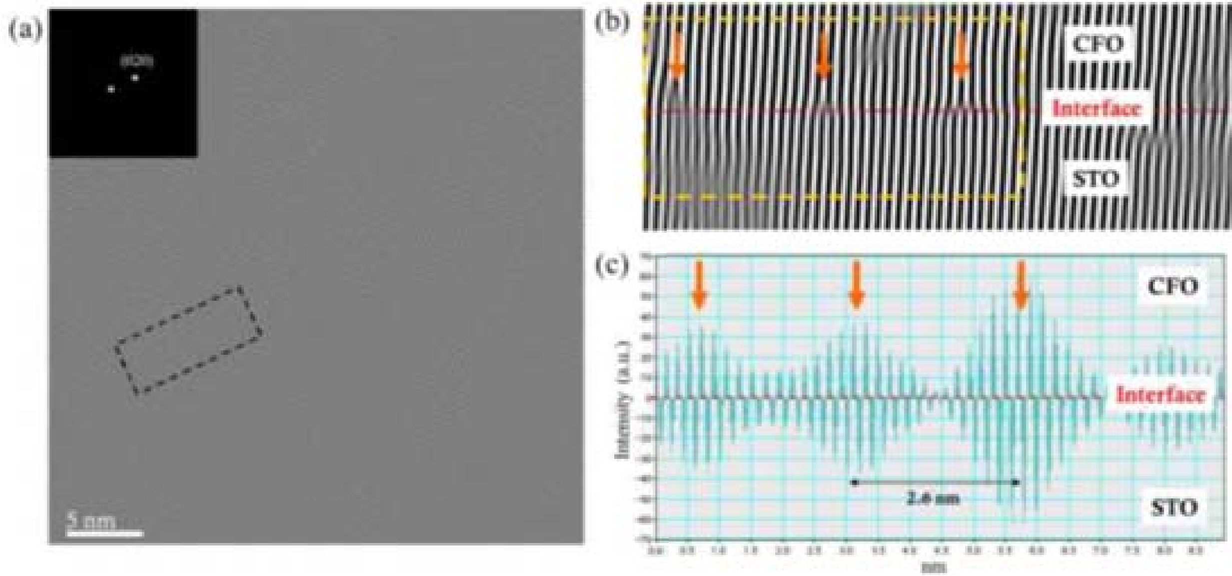

FigureIII.14:(a) Reconstructed HR TEM image (original shown in figure III. 12) from (020) spots of the corresponding FFT, and (b) zoom of the marked rectangle in (a), and (c) intensity profile extracted from the rectangular marked zone in (b), signalling the periodic pattern of misfit dislocations.

Oscillations are observed in the intensity profile (figure III.14.c), taken from figure III.14.b, around the CFO/STO interface. The maxima of the oscillations correspond to the dislocation position, while the minima correspond to the coherent zone between two consecutives dislocations. The intensity modulation of the Fourier filtered image reconstructed directly depends on atomic planes diffraction conditions. In coherent zones, the atomic planes are slightly deformed in order to match the CFO atom columns with the STO ones, changing the diffraction conditions and resulting in a diminution of the diffracted intensity.

The misfit interfacial dislocations have a Burgers vector: $\vec{b} = \frac{1}{2}\vec{a}[110]$. The intensity modulation allows to determine accurately the position of the interfacial dislocations. The averaged distance between two misfit dislocations is 2.6 nm. The expected average distance D between two misfit dislocations for a fully relaxed system can be calculated according to:

$$D = (d_A \times d_B) / |d_A - d_B|$$

Where d_A and d_B are the smaller in-plane interplanar spacing (along the interface) for each materials respectively. In this case, the smaller interplanar distances are:

$$d_{CFO} = \frac{1}{4} a_{CFO} = 0.21nm \text{ and } d_{STO} = \frac{1}{2} a_{STO} = 0.195nm$$

The expected distance between two misfit dislocations D_{Th} is 2.73 nm, closely matching with the distance measured. In conclusion, the study by HRTEM, GPA analysis and FFT-reconstructed image confirms the CFO film relaxation with misfit dislocations at the CFO/STO interface.

The CFO/STO interface is structurally sharp, but a chemical analysis across the interfaces is needed to evaluate possible atomic diffusion. In particular, Ti diffusion in $NiFe_2O_4$ films on

STO(001) substrates was already observed [FOE11]. Here we study chemical composition across the interfaces using EELS, and possible correlation between structural defects and Ti diffusion is investigated.

III.3.3 EELS characterization

In a first part, the chemical composition of the CFO film along the direction perpendicular to the interface is studied by EELS. The study provide information about the stoichiometry of the films, the diffusion depth of titanium in CFO, and the possible diffusion of iron or cobalt in STO.

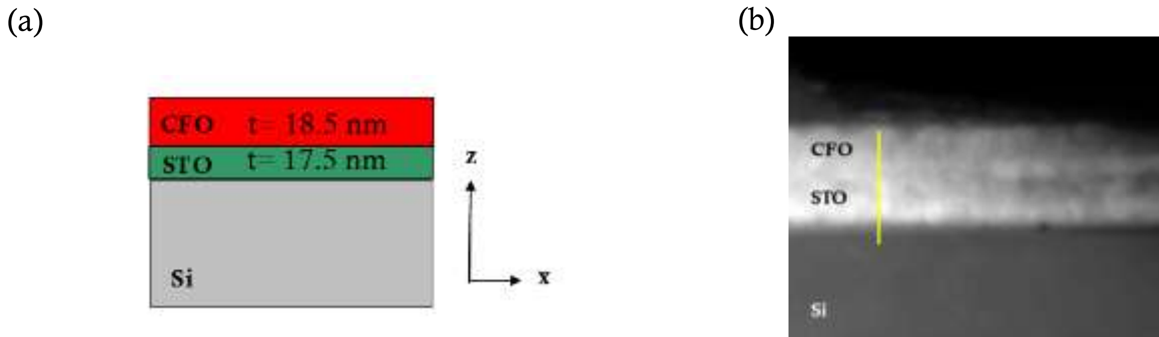

FigureIII.15: (a) Sketch and (b) STEM image in dark contrast of the transversal view of the sample.

In a second part, EELS profiles were recorded in two CFO zones. The two zones were selected considering the structural quality of the bottom STO. One presented high quality and the other appeared defective. We aimed to study if there is a correlation between the titanium diffusion through the CFO film and the presence of structural defects in STO as grain boundaries.

In the STEM-EELS measurements, the probe size was 1.5 nm and spectra were recorded with a step of around 0.9 nm. The accuracy in the position can be considered 2 nm. The recorded energy window (300-900 eV) includes edges of Ti, O, Fe and Co. $L_{2,3}$ edges of Ti are at 462 and 456 eV, K_1 edge of O is at 532 eV, $L_{2,3}$ edges of Fe are at 721 and 708 eV and, $L_{2,3}$ edges of Co are at 794 and 779 eV. However there are neither Sr nor Si edges in the recorded energy window.

III.3.3.1 EELS in a direction perpendicular to the interface

The EELS were taken in a region without evidence of structural defects, at different positions along the vertical solid line marked in figure III.15.b. The line extends from the Si substrate to close to the CFO surface. Figure III.16 shows a 3D view of the individual spectra. Three regions are distinguished, corresponding to the CFO and STO films and the silicon substrate. The spectra do not show asharp CFO/STO interface. The dashed line marking the interface in figure III.16 is positioned with a precision around 2 nm. Effects of the probe size, intermixing or diffusion, and interface roughness can contribute to the observation of a broad interface. However, a small amount of Ti is present in the CFO film. The Ti signal decreases from the interface to the CFO film, and is detectable 10 ±2 nm from the interface, indicated by a double arrow in figure III.16.

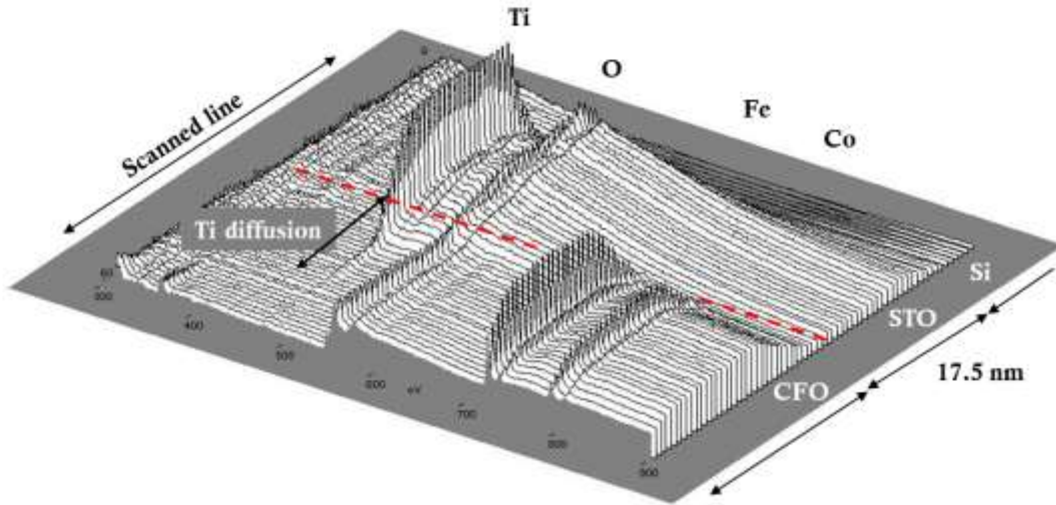

Figure III.16: 3D view of the individual EELS spectra acquired along the line marked in figure III.15.b.

The energies of the cobalt and iron edges are close, and the integration of the area below the cobalt peak can contain the decreasing part of the Fe signal.Then, the quantification extraction and interpretation of the iron and cobalt composition in the CFO film has to be studied carefully, and it has to be taken into account that the Co quantification could be overestimatedor underestimated after a background (containing some Fe signal) substraction. We note also the presence of low intensity undefined peaks at around 300 and 350 eV in the top part of the CFO film.

Individual spectra of CFO and STO films far from interfaces are showed in figure III.17, and the characteristic peaks of each element is labelled: Ti(L_3-L_2) at 456-462 eV, O(K_1) at 532 eV, Fe(L_3-L_2) at 708-721 eV, and Co(L_3-L_2) at 779-794 eV. The background window in the energy range previous to the element edge is marked in red.

(a) (b)

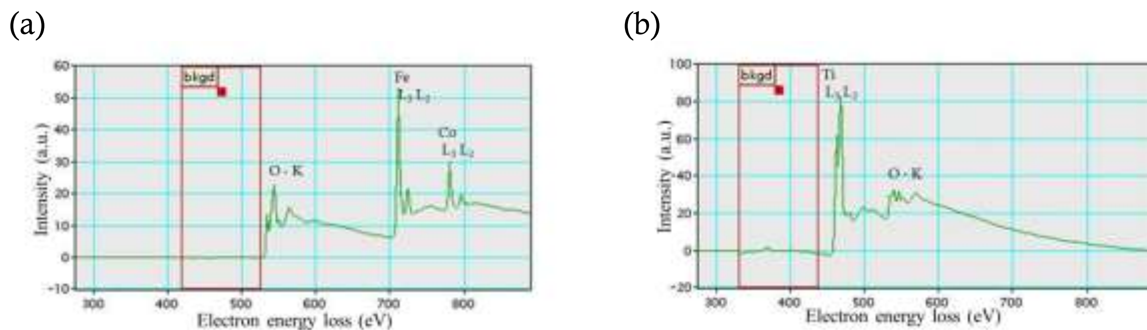

FigureIII.17: Representative EEL spectra of the CFO film (a) and the STO film (b).

Figure III.18.a shows the presence of all the elements at the interface that could be due to probe size, intermixing, diffusion or interfacial roughness. Figure III.18.b shows the spectrum recorded in the CFO film at 6.5 nm from the interface. The low intensity peak of Ti indicates a Ti diffusion in CFO.

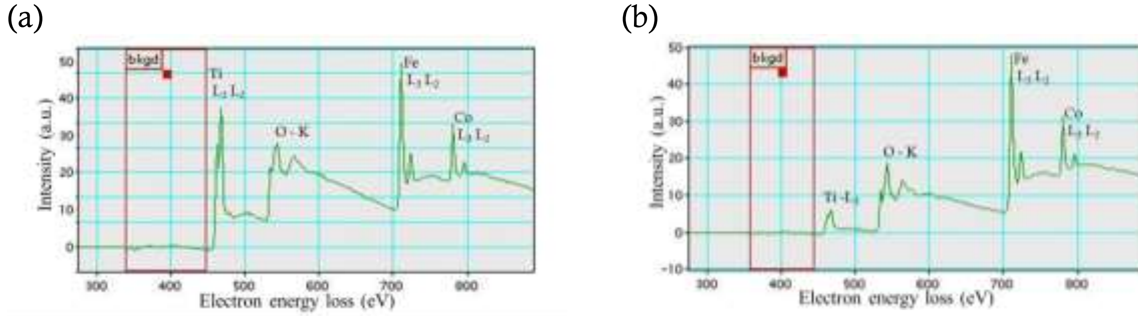

Figure III.18: EEL spectra around the CFO/STO interface (a), and in the CFO film at 6.5 nm of the interface (b).

Figure III.19 shows a chemical composition profile, extracted taking into account the convergence and collection angle, here 7.8 and 19.5 mrad respectively. The element peak positions are corrected in function of the zero loss peak, and the background was removed (power law and 25 eV window) individually for each element in order to reduce the overlapping problem. The cross-section model used was the Hartree-Slater and the width of the integration window for each element was 70 eV. Finally, the MSA filter was applied in order to decrease the noise of the signal.

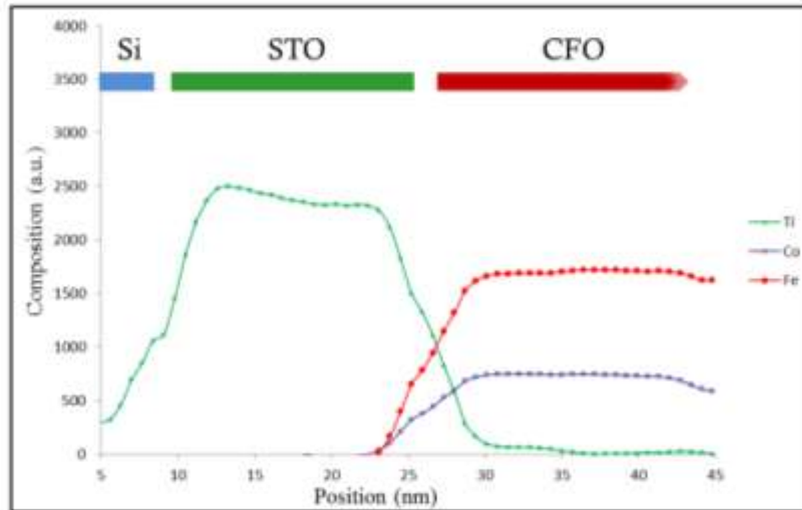

FigureIII.19: Composition vs position scannedperpendicularly to the interface. The plateau in the Ti content between around 30 and 35 signals diffusion into CFO film.

The $CoFe_2O_4$ stoichiometry is apparently the nominal one. A slight Ti diffusion in the CFO film can be observed. The quantitative composition of $CoFe_2O_4$ and $SrTiO_3$ is presented below, and their interface is described.
In order to quantify the CFO stoichiometry, the Fe/O and Co/O ratios are plotted in figure III.20.a. The data represented below have the same x-scale than the profile presented infigure III.19.

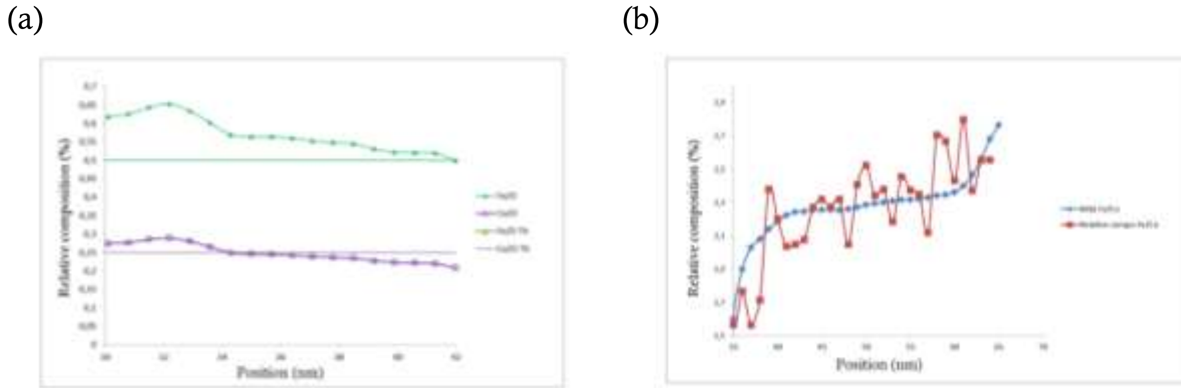

FigureIII.20: (a) Fe/O and Co/O ratio along the CFO thickness, (b) Fe/Co relative composition plotted from raw data (red squares) and after MSA filtering (blue diamonds).

The graphs in figure III.20.a show that the Co/O ratio is close to the stoichiometric value (0.25), and that the Fe/O ratio is slightly higher than the expected one (0.5). Previous structural analysis by XRD, RHEED, and TEM, showed high crystalline quality, lattice parameter of bulk CFO and absence of traces of other phases. The discrepancy in the Fe/O ratio respect the nominal is within the error bar of the EELS measurement, which is estimated to be around 10%.

Moreover, the iron peak just before the cobalt edge makes difficult the quantification of cobalt, which can be underestimated when the integration window is too large (70 eV). Edge windows of 40 and 50 eV were tested. We also plot the Fe/Co ratio in figure III.20.b. The Fe/Co ratio of 2.27 in average, which is in agreement with the nominal value of 2 considering an accuracy of measure of around 10%. It can be noted that the MSA filter smooth the relative composition curve. Below we see in part III.3.2, the CFO stoichiometric composition determined along a line parallel to the interface.

III.3.3.2 <u>EELS along a direction parallel to the interface</u>

Two profiles were taken in CFO along a direction parallel to the interface (//x) at a distance of 7.5 nm to it. The objective is to determine the homogeneity of the CFO stoichiometry and of Ti diffusion in CFO, and a possible correlation between stoichiometry and structural defects in the STO layer. First, a region without structural defect was studied, and second, another region with defects. In particular, we aim to determine if there is correlation between Ti diffusion and the presence of grain boundaries.

<u>EELS profiles in a region without structural defects</u>

In a region without structural defect in the CFO or STO layer (figure III.21.a), EEL spectra were recorded in the CFO film at 7.5 nm from the STO interface. Two selected EEL spectra, taken at positions 1 and 2, are plotted in figure III.21.b. All spectra are shown in a 3D graph in figure III.21.c.

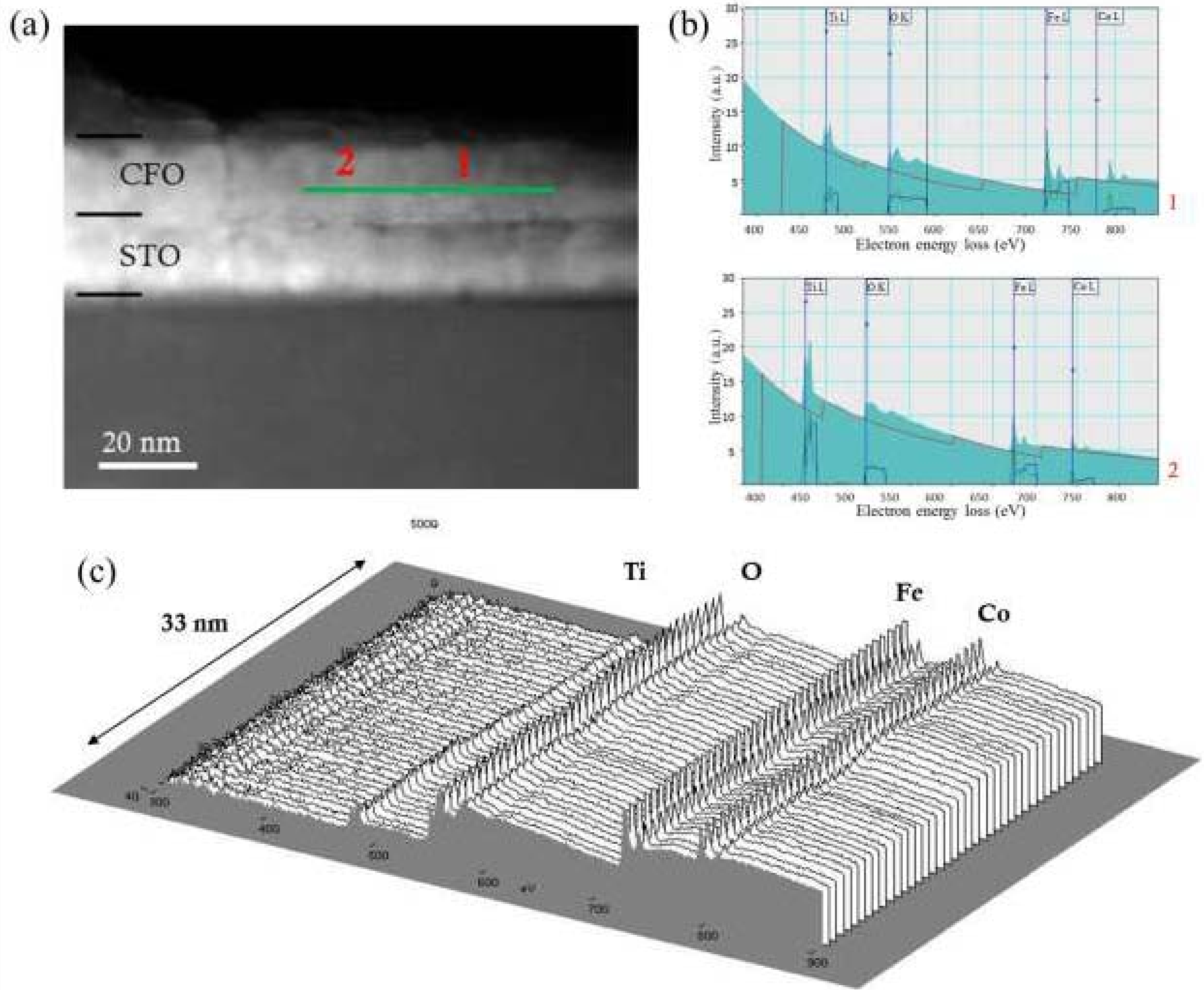

Figure III.21: (a) Dark contrast TEM image. The spectra were recorded along the marked line, (b) EEL spectra recorded at positions 1 and 2, (c) three dimensional graph of the spectra recorded along the line.

The chemical analysis presented in figure III.22 shows that the content of Fe and Co film is homogeneous. The presence of Ti in CFO, at 7.5 nm from the STO interface, is consistent with the previous study where the Ti diffusion depth found was 10 ±2 nm. Its amount increases in some regions, indicating a preferential diffusion of Ti in CFO in particular zones.

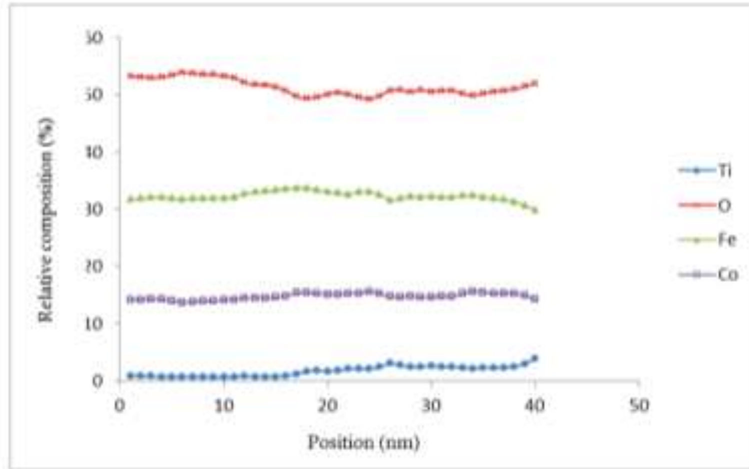

FigureIII.22: Quantification of the present elements in CFO at 7.5 nm from its interface with STO.

The Fe/Co ratio is plotted in figure III.23. The Fe/Co ratio is around 2.32 in average for its relative composition, and 2.19 after the application of the MSA filter, which is very close to the expected value 2 with an error inferior to 10%.

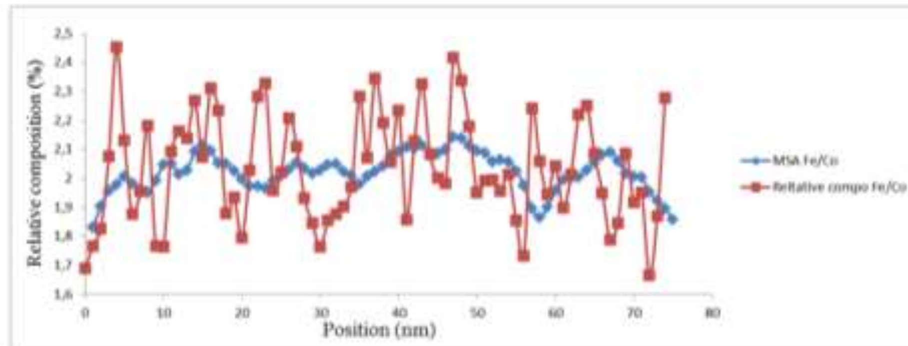

FigureIII.23:Fe/Co relative composition plotted from raw data (red squares) and after MSA filter (blue diamonds).

<u>EELS profiles in a region with structural defects</u>

The significant variation of Ti along a direction parallel to the interface suggests that microstructural defects could enhance Ti diffusion. In order to investigate the possible correlation between the Ti diffusion and the presence of structural defects or grain boundaries (GB) in the STO thin film, a high resolution picture of the sample was taken in the region studied by EELS. A zoom of the grain boundary present in the STO film is shown here, and the reported green line on the CFO film is the distance scanned for the chemical analysis (figure III.24).

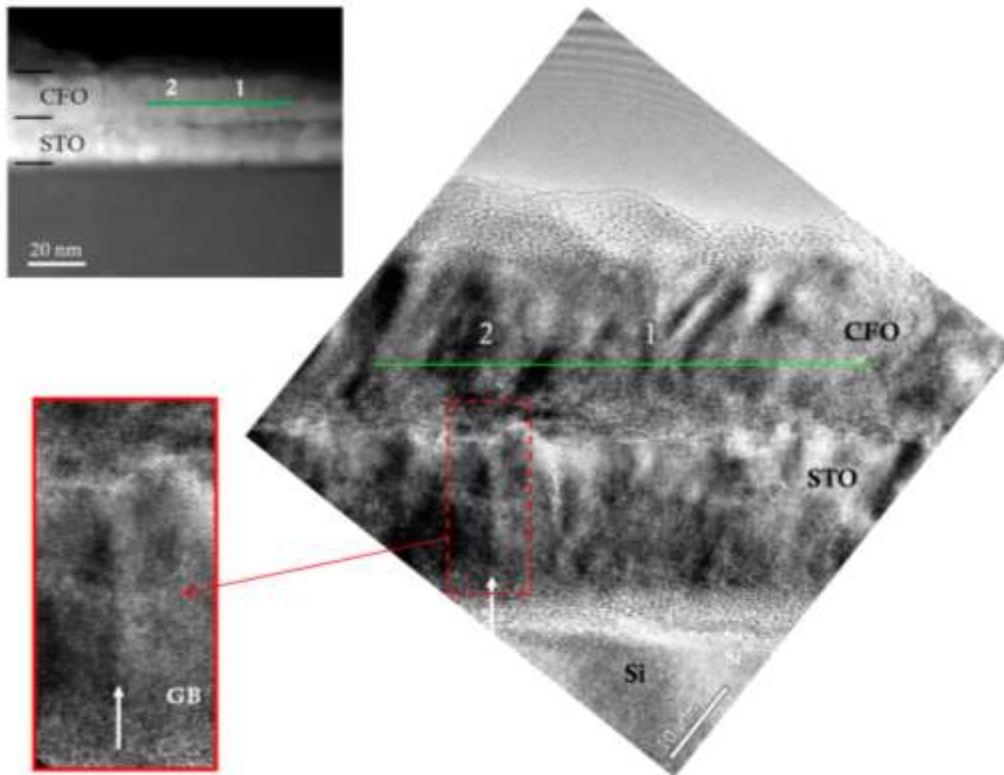

FigureIII.24: HREM picture of the sample studied by EELS. Individual spectra recorded at regions 1 and 2 are presented below.

In the HRTEM picture it can be seen that the CFO/STO interface is rough. The roughness would be the main cause of the not abrupt composition profiles across the interface (figure III. 19). The three dimensional graph in figure III.25.a signals that the thickness of the specimen is homogeneous in the CFO film as the Fe and Co intensity is constant along the profile.The oxygen signal displays a certain variation across the profile, but the most noticeable observation is the strong changes in the titanium peak. In particular, there is a very high increase of titanium in zone 2 respect to zone 1. The first one does not present evident defects whereas the second shows a GB in the bottom STO layer.

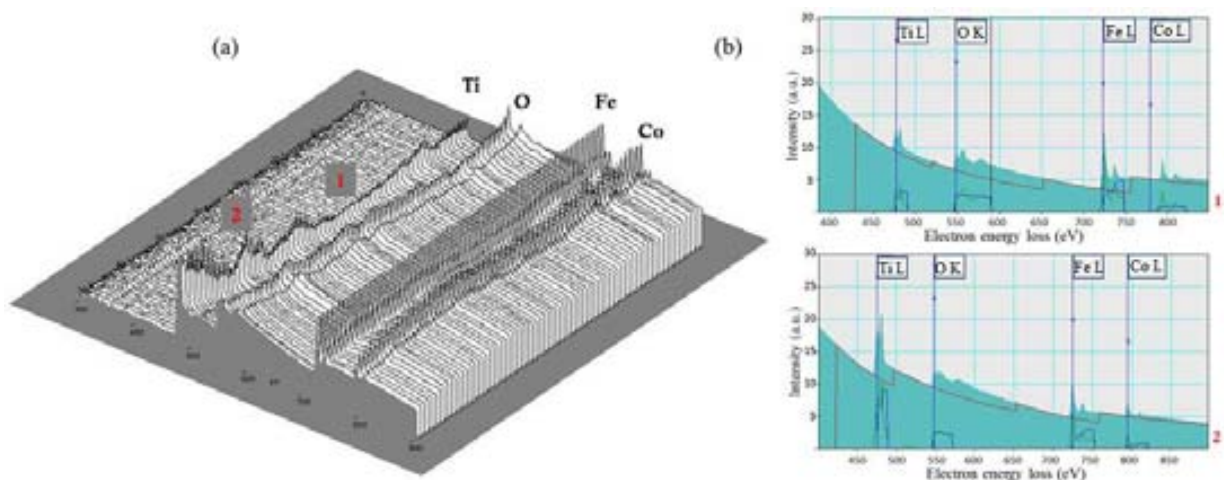

FigureIII.25: Three dimensional view of the EEL spectra recorded in the CFO thin film, along the line at 7 nm to the CFO/STO interface (a).Representative EEL spectra (b)extracted from (a) and recorded in a region without structural defects (1), and in a region with structural defects in the bottom STO layer (2).

Two characteristic spectra of two regions (1 and 2) are shown in figure III.25.b. The higher Ti content is evident in the spectra recorded in region 2 (bottom panel).This signals that microstructural defects could enhance Ti diffusion in CFO.

III.4 Summary

In summary,epitaxial CFO films were grownon STO buffered Si(001) with an epitaxial relationship [100]$CoFe_2O_4$(001) // [100]$SrTiO_3$(001) // [110]Si(001). The amorphous interfacial layer (AIL) of 3.5 nm observed at the STO/Si interface could be due to oxygen diffusion through STO during the CFO deposition, or result by sample degradation during TEM specimen preparation. The CFO surface is homogeneous and moderately flat with a roughness of 0.5 nm.The CFO/ STO interface is sharp with slight roughness within ~0.5 nm and is commensurately crystalline. The atomic columns correspondence between a CFO unit cell (uc) with 2 STO uc was confirmed, and dislocations formed by half-atomic planes of CFO are 2.5 nm spaced. Direct HRTEM measurements, GPA analysis and reconstructed HRTEM image confirmed that CFO is relaxed on STO with presence of misfit dislocations.
A chemical analysis by EELS across the interfaces revealed a 10 nm depth Ti diffusion in CFO film. The quantitative composition of CFO was found to be the nominal, considering the accuracy of measure, in zones far from the interface (>10 nm). In addition, the inhomogeneous Ti diffusion in CFO near the CFO/Ti interface and the structural correlation, suggests that microstructural defects could enhance its diffusion.

Chapter IV

Integration of $CoFe_2O_4$ with Si(001) using YSZ buffer layers

IV.1 Introduction

The crystal structure of yttria-stabilized zirconia (YSZ) depends on the stoichiometry. It has a cubic fluorite structure (figure IV.1) for a Y_2O_3molar content higher than around 12 %, with lattice parameter that increases linearly and slightly with the Y_2O_3 content (the most recently reported measurements [KRO11] are a_{YSZ}= 5.136 Å for 11.7% of Y_2O_3 and 5.146 Å for 18%). The PLD target used to grow the films studied in this thesis is nominally below 15%, being thus YSZ cubic and having a lattice parameter around 5.14 Å.

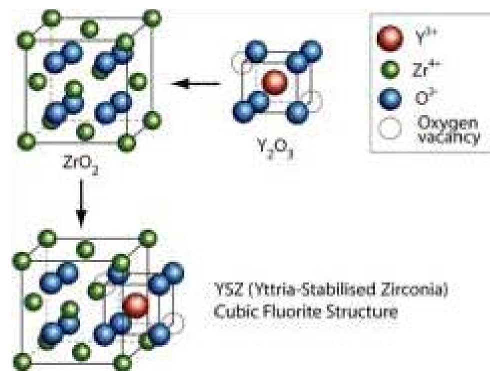

Figure IV.1: Fluorite structureof the cubic yttria –stabilized zirconia [VAR06].

YSZ, with static permittivityclose to 30 [SAM90], is a candidate as dielectric in capacitors for dynamic random access memories[LOC06].The lattice mismatch between YSZ and Si(001) is -5.36%. Although is a high mismatch, YSZ grows epitaxially with cube-on-cube epitaxial relationship on Si(001), even without removing the amorphous native silica[AGU97, BAR94, FOR90]. This has been probably the main reason of its wide use as buffer layer to integrate functional oxides with silicon. For example, it permits epitaxial growth of ferromagnetic manganites [FON99-1-2, PER09, TRA96] and spinels [WAK02-04], and ferroelectric oxides [DEK09, SCI13, ZHA10]. YSZ films used as buffer are typically tens of nanometerthick. Thinner buffers, required for applications based on heterostructures with ultrathin films [LUD06], have been scarcely investigated [BAR94, WAK00].In such ultrathin heterostructures the stability of the YSZ/Si interface is a critical issue, since YSZ is highly permeable to oxygen and the usual reactive oxygen atmosphere during deposition of YSZ (or during deposition of functional films when YSZ is used as buffer) causes SiOx regrowth [BAC11, HUB96, PER09].

The possibilities of YSZ as suitable buffer layer for epitaxy of CFO are *a priori* not evident considering the lattice parameters (a_{YSZ} = 5.14 Å and a_{CFO} = 8.392 Å, with $a_{CFO}/2$ = 4.196 Å). YSZ is (001) oriented on Si(001) and the mismatch *f* between CFO and YSZ, assuming (001) growth of CFO, is -18.4% for cube-on-cube matching, and slightly lower (f = +15.4%) when there is a 45º in-plane rotation of CFO. To reduce the huge mismatch there is the possibility to incorporate other buffer layer for a progressive accommodation of the lattices. A good candidate is CeO_2, with cubic fluorite structure and lattice parameter of 5.41 Å, and that grows epitaxially with cube-on-cube epitaxial relationship on YSZ/Si(001) [TRT98]. Matching of CFO on CeO_2/YSZ/Si(001) with 45º in-plane rotation of CFO implies still a very high mismatch of 9.6%, but it is much lower than the corresponding value in case of direct growth on YSZ.

In a first part of this chapter we will show that CFO grows epitaxially on Si(001) using the double CeO_2/YSZ buffer. We will see however that it grows with (111) out-of-plane orientation, which suggests that it can be deposited directly on single YSZ buffers. This is a relevant point because spin filter devices require an ultrathin heterostructure (< 5 nm). Thus we have studied the early stages of YSZ epitaxy on Si(001) in order to determine the lowest YSZ thickness having well-ordered crystalline structure, suitable as buffer layer. Finally we use the ultrathin YSZ buffer layers to deposit also ultrathin CFO films, being the bilayers CFO/YSZ few nanometer thick.

IV.2 $CoFe_2O_4$ on Si(001) using CeO_2/YSZ double buffers

CFO/CeO_2/YSZ heterostructures were deposited by pulsed laser deposition in a single process. The oxygen partial pressure and the substrate temperature during deposition were 3×10^{-4} mbar and 800 °C for YSZ and CeO_2 buffer layers, and0.1 mbar and 550 °C for CFO. The beam of a KrF excimer laser (λ=248 nm), operating at a repetition rate of 5 Hz, was focused sequentially on stoichiometric ceramic targets at a fluence~1.2 J/cm2. The target-substrate distance was around 50 mm. The Si(001) substrates, used without removing the native oxide, were heated to the deposition temperature of YSZ under vacuum (~10^{-6} mbar at 800 °C). YSZ deposition started at the base pressure and oxygen was introduced after ~8 s [AGU97]. Layer thickness "t" and growth rate were~160 nmand 0.32 Å/pulse for YSZ, ~110 nmand 0.55 Å/pulse for CeO_2, and from~30 to~75 nm and~0.08 Å/pulse for CFO.

The time dependence of the intensity of the RHEED specular spot is plotted in figure IV.2 for the early and the last growth stages of YSZ, CeO_2 and CFO. The intensity dropswhen the YSZ deposition starts (marked by the horizontal arrow in figure IV.2.a), and it decreases more after introduction of oxygen (vertical arrow). Then, with constant oxygen pressure, the intensity increases progressively during the growth of around 10 nm of YSZ, and later the intensity remains basically constant. This suggests enhancement of crystalline ordering up to this thickness, which agrees with the higher crystal disorder reported for very thin YSZ films respect to thicker ones [AGU97]. Although periodic variations of the RHEED intensity cannot be observed, the significant intensity recovery (figure IV.2.b) occurring during a long time of few tens of seconds at the end of the YSZ deposition (t=160 nm) suggests two-dimensional growth. In the sequential deposition of CeO_2(figure IV.2.c) on the YSZ buffer, two complete periodic intensity oscillations signal layer-by-layer growth.After, a slightmonotonous increase of intensity is observed up to 25 nm but the oscillations are barely distinguishable; at the end of the deposition (t=110 nm) there is a clear recovery of the

intensity (figure IV.2.d).To subsequently deposit the CFOfilm, the substrate temperature was decreased to 550 °C and the pressure increased to 0.1 mbar. The increase of oxygen partial pressure in the chamber yields a decrease of collected RHEED intensity. During the initial growth stage (up to~1nmof CFO) intensity varies as shown infigure. IV.2.e. After, intensity decreases up to~2 nm and remains constant straight afterwards up to the endof the deposition (t=30 nm). No periodic intensity variation can be appreciated after the early stage although, as occurred with the buffer layers, there is intensity recovery at the end (figure IV.2.f) indicating an overall two-dimensional growth.

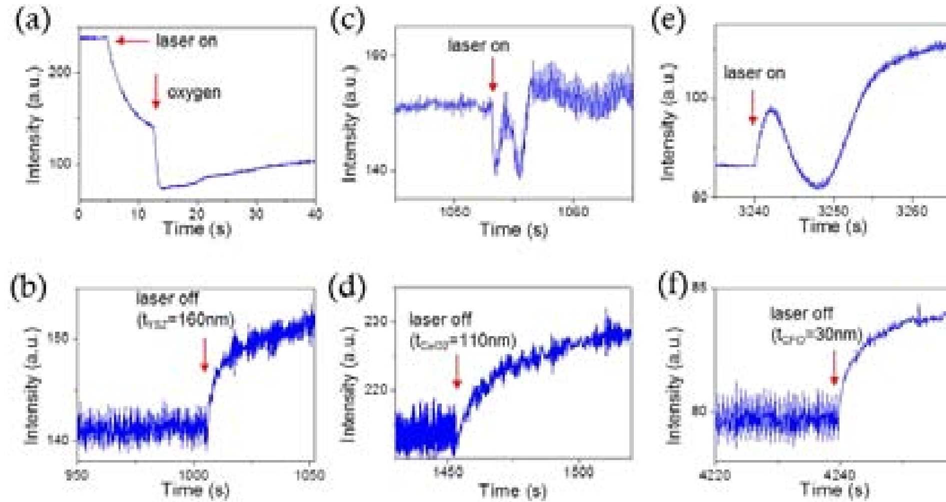

Figure IV.2: Time dependence of the intensity of the RHEED specular spot during the early growth stages of YSZ (a), CeO_2 (c), and CFO (c). The last stage of the corresponding depositions are in panels (b), (d) and (f), respectively.

Figure IV.3.a shows the RHEED pattern recorded at the end of the deposition along the Si[100] azimuth. The pattern shows streaks signalling smooth CFO surface and confirming the two-dimensional epitaxial growth of the heterostructure expected from the observed recovery of the specular spot intensity at the end of the deposition of each layer. The same RHEED pattern is observed rotating the sample azimuthally (around the Si[001] axis) every 30°. This symmetry suggests that CFO grows (111)-oriented as confirms the XRD characterization presented below.

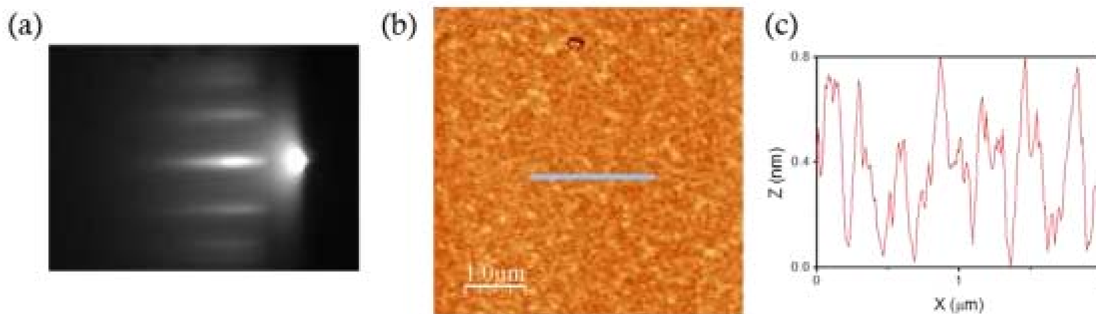

Figure IV.3: (a) RHEED pattern taken along the Si[100] direction at the end of the growth of CFO/CeO_2/YSZ/Si(001). (b) Topographic AFM image of the CFO film. (c) Height profile along the line marked in (b).

The smoothness of the surface is confirmed by the AFM topographic image in figure IV.3.b. The surface is very flat and homogeneous, pinhole-free, with a root means square (rms) roughness of 0.26 nm. The height profile in figure IV.3.c along the line marked in the image shows height variation in a short range of 0.8 nm (less than two consecutive (111) atomic planes).

The XRD θ–2θ scan in figure IV.4.a shows that YSZ and CeO_2 are (00l) textured, and confirms that CFO is (111) textured. The out-of-plane lattice parameters of YSZ and CeO_2, determined from the position of the corresponding diffraction peaks, are 5.14 Å and 5.41 Å, respectively, matching the bulk values. Both YSZ and CeO_2 are thus fully relaxed. In contrast, CFO with out-of-plane lattice parameter of 8.363 Å, presents a strain of -0.34%.

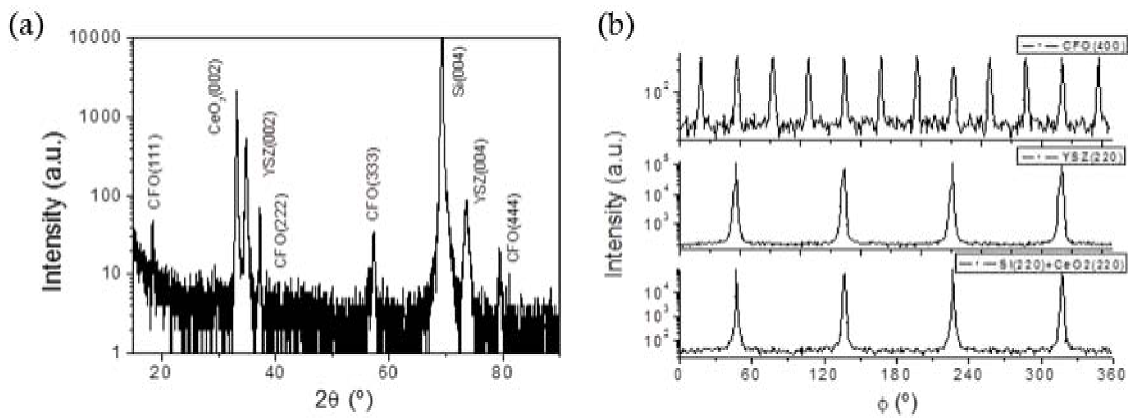

Figure IV.4: XRD characterization of a t~45 nm CFO film on CeO_2/YSZ/Si(001). (a) θ–2θ scan, (b) Φ-scans around Si(220), CeO_2(220), YSZ(220) and CFO(400) reflections.

Figure IV.4.b shows the Φ–scans performed around Si(220), CeO_2 (220), YSZ(220) and CFO(400) asymmetrical reflections. The Φ–scans around Si(220) and YSZ(220) display four peaks 90 °C apart;with the peaks located in the same positionsin both scans, indicating cube-on-cube epitaxial relationship. In the case of the second buffer, CeO_2, its lattice parameter is almost identical to that of Si and the CeO_2(220) reflections overlap the four high intensitySi(220) peaks. Finally, the Φ–scan around CFO(400) shows twelve peaks 30 °C apart, corresponding to four sets of three peaks that signal the presence of four crystal domains.

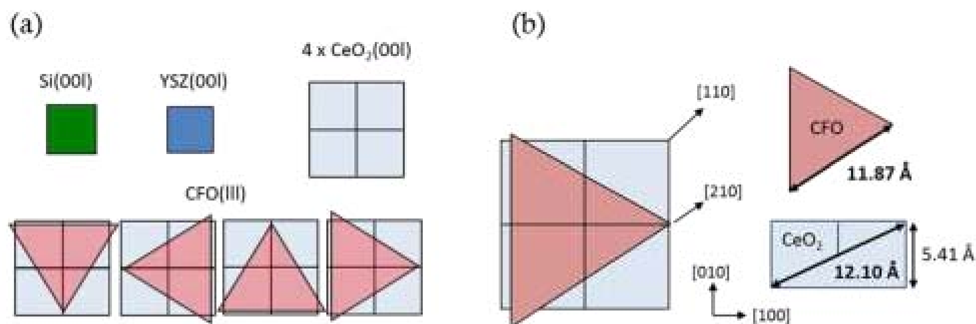

Figure IV.5: (a)Sketch of thefour crystal variants, (b) detail of a crystal variant, showing the alignment of the CFO triangle sides of the CFO in-plane triangular lattice to the [010], [210], and [2-10] directions of CeO_2.

The sketch in figure IV.5.a explains the (111) texture of CFO and the presence of four crystal domains.The bulk lattice parameters of Si, YSZ and CeO_2 are 5.43 Å, ~5.14 Å and 5.41 Å, respectively. They are similar and the epitaxial relationship is cube-on-cube. In contrast, the lattice parameter of CFO, 8.392 Å, is much larger. It grows (111) -oriented and remarkablyepitaxially in spite of this high mismatch. On the other hand, the CFO(111) has four possible alignments on the four-fold symmetry CeO_2(00l) lattice, which causes the formation of the crystal domains. The same domains structure was found by Wakiya et al. in (Ni,Zn)Fe_2O_4(111) films on CeO_2/YSZ/Si(001) [WAK02-04].

In figure IV.5.b one of the crystal variants is sketched to illustrate the matching of the triangular CFO(111) lattice with four unit cells of the square CeO_2(001) lattice. The triangular CFO(111) lattice, with 11.87 Å parameter, is aligned along [010], [210] and [2-10] CeO_2 directions. Considering the four CeO_2(001) cells, the distance along [010] and < 210> directions is 10.8 Å and 12.1 Å, respectively.The mismatch between CFO(111) and CeO_2(001)is then 9.7% along [010] CeO_2, and -1.9% along the two other directions. On the other hand, calculating the equivalent lattice mismatch between CFO and YSZ we obtain slightly higher values, 15.4% and 3.1%, which suggest possibility of epitaxy of CFO on YSZ, as we will demonstrate in the last part of this chapter.
The low magnification cross-section TEM image along the Si[100] zone axis in figure IV.6.a shows a general view of the YSZ and CeO_2 buffer layers and the CFO film.The films are homogeneous, with flat interfaces in the whole observed area. There is sharp contrast across the interfaces that suggest absence of interdiffusion, and the CFO top surface is very flat in agreement with the AFM topographic images. Figure IV.6.b shows a high resolution micrograph of the CFO/CeO_2 interface. There is a certain disorder extended around 0.8 nm, and coherency of atomic planes across the interface is not easily observed. This disorder during the first steps of CFO growth occurs due to the high mismatch with CeO_2. Interestingly, we do not observe defects in the rest of the film, suggesting that the disordered interface reduces the epitaxial stress thatwould be huge due to the high lattice mismatch and the lack of structural symmetry between spinel CFO(111) and fluorite CeO_2(001).

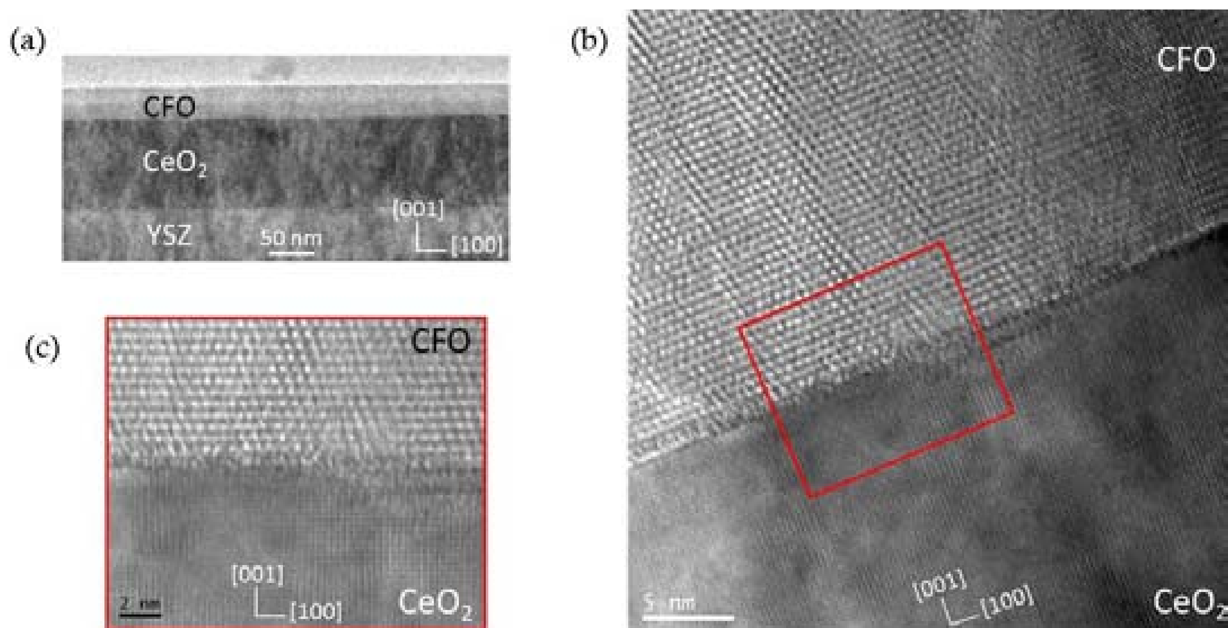

FigureIV.6: Cross section TEM analysis of a t~45 nm CFO film on CeO_2/YSZ/Si(001) viewed in the Si[010] zone axis. (a) Low magnification image. (b) High magnification image around the CFO/CeO_2 interface. (c) Detailed view of the marked area in (b).

The magnetization loop of a 75 nm thick film, measured at 10 K with magnetic field applied along a Si[110] in-plane direction, is presented in figure IV.7. The estimated saturation magnetization of about 300 emu/cm^3 is close to the bulk value and the coercivity amounts to1.4 T.

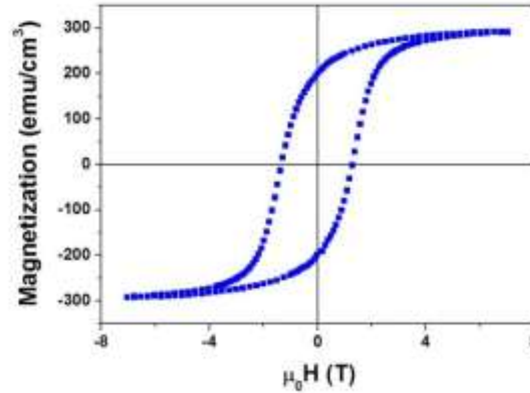

Figure IV.7: Magnetization loop of a t~75 nm CFO film measured at 10 K with magnetic field applied within the plane (along a Si[110] direction).

In summary, CFOfilms have been grownon CeO_2/YSZ buffered Si(001) with RHEED assisted pulsed laser deposition. The films are epitaxial with (111) out-of-plane orientation and present four in-plane crystal domains. They grow two-dimensionally and CFO presents flat interface with CeO_2 and very flat surface with roughness below 0.3 nm. The saturation magnetization, around 300 emu/cm^3, is close to the bulk value.

However, the fabrication as spin filter devices requires an ultrathin heterostructure. Here we have used a thick double buffer layer, but the analysis of the epitaxial relationship has suggested that a single YSZ buffer is also suitable. Improvements of growth of YSZ buffer could allow to use a single buffer minimising its thickness with a controlled interface with silicon. We have investigated the growth mechanisms of YSZ on Si(001) aiming to fabricate ultrathin buffer layers. This study is presented below.

IV.3 Growth mechanisms of yttria stabilized zirconia on Si(001)

A distinctive feature of the epitaxial growth of YSZ on Sirespect to other oxidesis thatremoval of the native silicon oxide is not 54equired, and indeed its crystalline quality is enhanced compared to YSZ films deposited on bare silicon[COP00, KIG02-03, WAN00-01]. The crystallization of YSZ above a critical thickness around 1 nm [BAC11, BAR94] signals that epitaxy occurs by reduction of SiO_x by Zr and Y atoms and subsequent crystallization of YSZ at the Si(001) surface.

Two alternative mechanisms of epitaxial growth of YSZ on SiO_x/Si(001) can be considered: i) complete reduction of SiO_x along the entire interface and YSZ crystallization progressing perpendicularly from the reduced interface, and ii) local reduction of SiO_x and local YSZ crystallization that would then expand laterally over the remnant SiO_x interfacial layer (figure IV.8). The latter case shows similarities with the so-called processes of lateral

epitaxial overgrowth of semiconductors on amorphous SiO_x[LI_04, ZHE97]. In the case of lateral crystallization of YSZ, further YSZ deposition under ultrahigh vacuum (UHV) will promote complete SiO_x reduction and the formation of an interface between existing crystalline YSZ and Si. Due to the lattice mismatch and the different specific volume of SiO_x and YSZ, the formation of the new interface would generate a high stress. Indeed, in experiments of thermal crystallization of thick amorphous YSZ films it was observed that interfacial SiO_x relaxes stress[KIG02-03, KIG05].

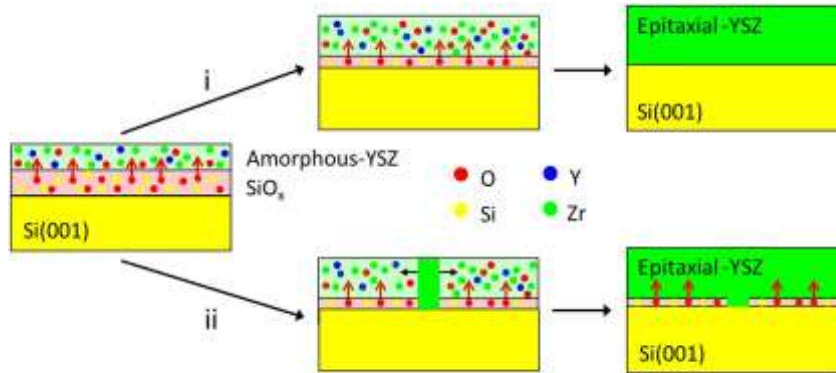

FigureIV.8: Sketch of two alternative mechanisms of epitaxial growth of YSZ on SiO_x/Si(001): i) complete reduction of SiO_x along the entire interface and YSZ crystallisation progressing perpendicularly to the interface, and ii) local reduction of SiO_x and local YSZ crystallisation that would then expand laterally over the SiO_x interfacial layer.

To investigate the YSZ epitaxy mechanisms and to discern the possible formation of defects associated to the complete reduction of native SiO_x, we have characterized the interface between ultrathin YSZ films and Si(001) using aberration corrected high resolution transmission electron (HRTEM).
YSZ films were deposited on Si(001) substrates without chemical etching to remove the native oxide. A substrate was characterized by TEM to determine the native silicon oxide thickness. Before the preparation of the sample for TEM, it was coated with Pt. The cross-section in figure IV.9 shows that SiO_x presents an homogeneous thickness around 2.3 nm.

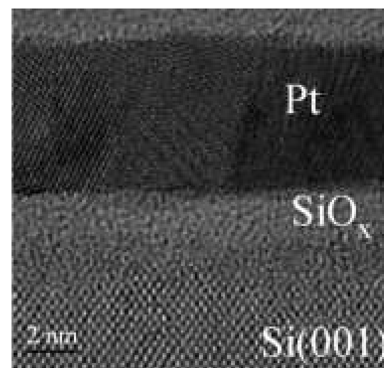

Figure IV.9: Cross-section HRTEM image of a platinum film on Si(001) showing a thickness of 2.3 nm of native silica.

Because our objective is epitaxial growth of YSZ with the lowest thickness, we deposit the films under base pressure (around 10^{-6} mbar at 800 °C) to favour fast reduction of SiO_x. The laser frequency was 2 Hz. The RHEED patterns presented in (figure IV.10) were taken along the Si[100] direction of the Si(001) substrate at 800 °C during the YSZ growth. Bragg

diffraction spots and Kikuchi lines are clearly observed in spite of the native SiO_x. Absence of 2×1 reconstruction in the pattern along Si[110] (not shown here) confirmed the oxidation of Si(001). The pattern changed with YSZ deposition and a halo characteristic for an amorphous film was observed during the first 50 laser pulses, corresponding to a nominal YSZ thickness of ~1 nm (figure.IV.10.b). With further increase of the thickness, diffraction spots become visible (see in figure.IV.10.c)the pattern acquired after 60 laser pulses). The intensity of the Bragg spots increased with additional laser pulses defining the RHEED pattern characteristic of an epitaxial film (see figure.IV.10.d). It is concluded that a minimum amount of Y and Zr atoms has to be deposited on SiO_x to reduce it and then to form a crystalline YSZ epilayer on the bare Si(001) surface[BAR94].The time dependence of the RHEED line profiles plotted in figure. IV.10.e reflects these stages. Remarkably, the film is flat (signaled by the streaky pattern).

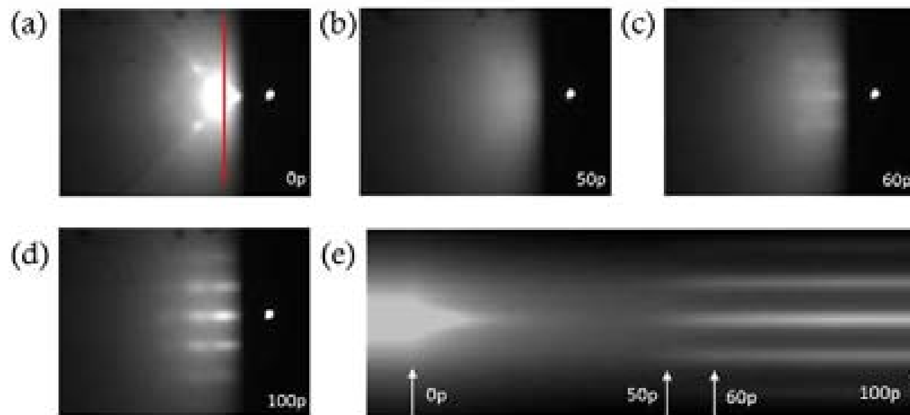

Figure IV.10: RHEED patterns taken along Si[100] (a) of the Si(001) substrate and during the deposition of YSZ, after (b) 50, (c) 60, and (d) 100 laser pulses. The respective grazing angles were 1.6° in (a), (b), and (c), and 0.9° in (d). (c) RHEED intensity profiles along the line in the Si[010] direction marked in (a) plotted as a function of deposition time. The grazing angle was 1.6°. Arrows in the bottom indicate the start of the deposition (0 laser pulses), 50, 60 and 100 laser pulses (end of the deposition).

This observation was confirmed by AFM, revealing a low surface roughness of 0.1 nm (see figures IV.11.a and IV.11.b). Inhomogeneous YSZ crystallization on Si(001) had been earlier reported [BAR94].In contrast, the homogeneous crystallization reported here results in ultrathin YSZ films that are atomically flat and epitaxial from thickness of about 1.5 nm as detected by in situ RHEED.

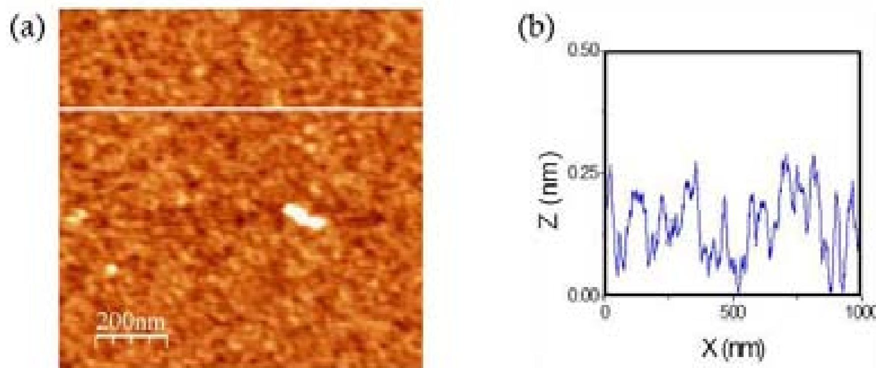

Figure IV.11: AFM topographic image of the YSZ buffer (a), with (b) the corresponding height profile along the marked line in (a).

The cross-section low-magnification TEM image of the t = 2.2 nm sampleshows that the YSZ film is continuous and flat over the large field of view. The HRTEM picture in figure IV.12 confirms the crystallisation with YSZ (001)[100]//Si(001)[100] epitaxial relationship in agreement with X-ray diffractometry characterization of thicker films. It can be appreciated that there is a SiO_x interfacial layer of about 1 nm thick, less than half the thickness of the native oxide.

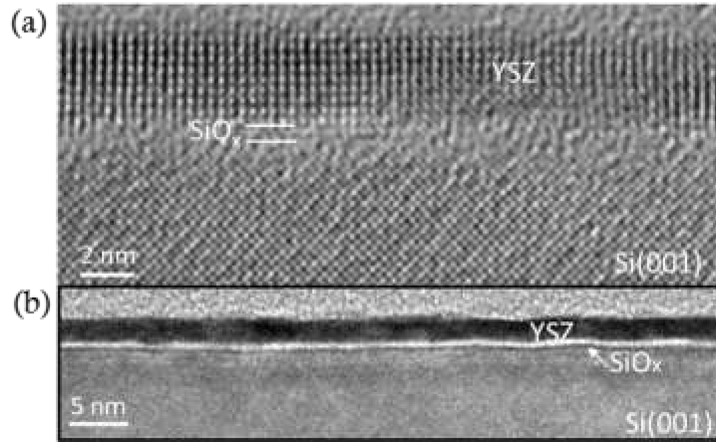

Figure IV.12: Cross-section HRTEM picture (a) with its low resolution (b) of the 2.2 nm thick YSZ film deposited at 800°C and 2Hz.

Oxygen permeability is very high in YSZ. The films are cooled down under UHV after growth, but they are exposed to ambient pressure at room temperature. To confirm that these conditions do not cause oxidation of the interface, an ultrathin YSZ film was capped in-situ with CeO_2, at T_s= 110 °C and under base pressure (3×10^{-8} mbar).

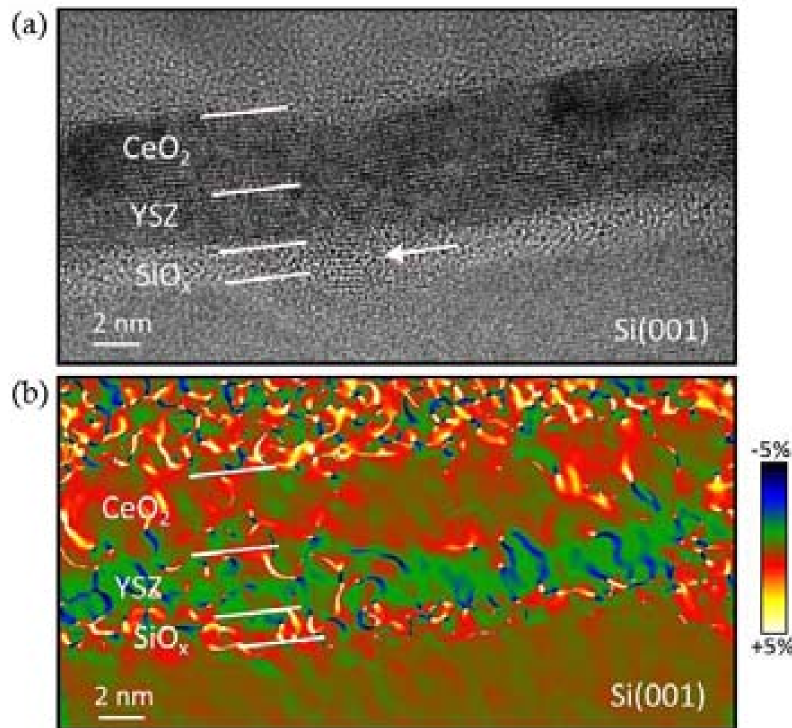

Figure IV.13: (a) HRTEM cross-sectional view of the t = 2.2 nm YSZ film capped with 4.2 nm of CeO_2 along the [110] zone axis, and its corresponding in-plane deformation map (b). Interfacial SiO_x is not uniform in thickness, being thicker than 1 nm in some zones whereas in others there is an atomic continuity as shown by an arrow.

It can be appreciated in figure IV.13 that there is a SiO_x interfacial layer of about 1 nm thick, which is also present in the equivalent film uncapped with CeO_2(figure IV.12). The HRTEM picture also shows that CeO_2 grows epitaxially in spite of the low deposition temperature. The CeO_2/YSZ as well as the YSZ/SiO_x/Si interfaces are well resolved in the corresponding in-plane deformation map presented in figure IV.13.b. Detailed views of the interfacial layer between YSZ and Si in both uncapped film (figure IV.12) and capped film (figure IV.13) shows that SiO_x is not uniform in thickness, being thicker than 1 nm in some zones whereas in others (marked by arrows) there is continuity of atomic columns between Si and YSZ. These observations suggest that YSZ can grow on SiO_x/Si(001) by a lateral epitaxial overgrowth process as schematically shown in figure IV.8. We note that local reduction of SiO_x here caused by YSZ deposition (figure IV.13), is reported to occur after thermal annealing of oxidized silicon under UHV, causing random formation of voids where SiO_x is locally decomposed.

Two other ultrathin YSZ films were deposited at the same conditions (100 laser pulses, base pressure) that the previous sample, but one with lower temperature (750 °C) and the same laser frequency (2 Hz); and the other with lower laser frequency (0.5 Hz) and same temperature (800 °C).

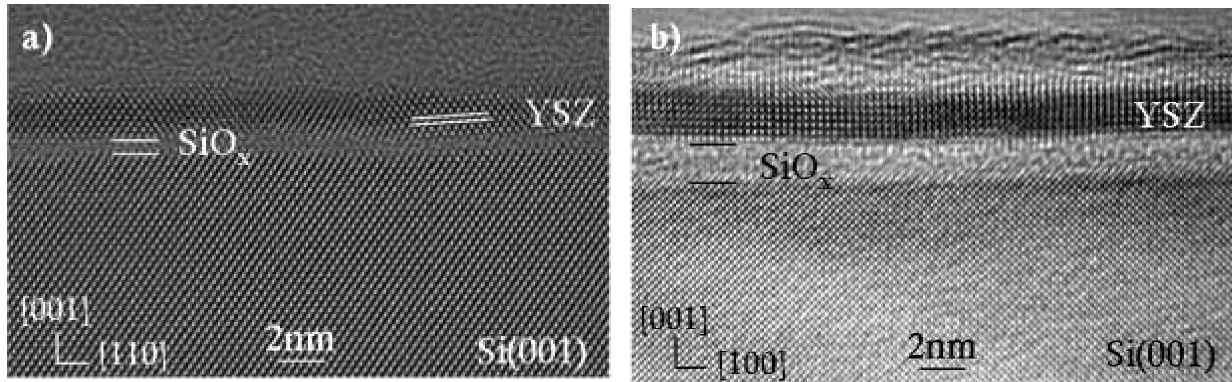

Figure IV.14: Cross-section HRTEM picture of YSZ thin film deposited at (a) 750°C and 2Hz, and (b) 800 °C and 0.5 Hz.

Comparing figures IV.12 and IV.14.a, it can be seen that decreasing the temperature growth of YSZ from 800°C to 750°C gives rise to a decrease of crystalline quality of the film. Figure IV.14.a shows the presence of different YSZ regions with atomic planes misaligned respect to the silicon planes. There is a similar amorphous interfacial layer with no relevant difference in thickness. On the other hand, comparing the TEM images of the samples deposited at 800 °C and 2 Hz and 0.5 Hz (figures IV.12 and IV.14.b), respectively, no qualitative changes of the YSZ quality are found, but the interfacial SiO_x thickness is increased from less than 1 nm to around 1.5 nm with the deposition time.

A sample was prepared with 300 laser pulses to increase the thickness to 6.6 nm. The RHEED pattern evolution with thickness was similar to that of the t = 2.2nm sample (figure IV.10). There are not qualitative changes in the patterns when thickness increases to 6.6 nm (figure IV.10.e) and the pattern recorded at the end under optimized beam incidence angle shows very sharp streaks (figure IV.10.f). The flatness the film was confirmed by atomic force microscopy (not shown here), revealing homogeneous surface similar to that shown in figure IV.11 and very low rms roughness around 1 Å. The cross-section TEM images of this sample are shown in figures IV.15.a and IV.16.a. There is not a SiO_x interfacial layer,

indicating that the SiO_x present in thinner YSZ is finally reduced with further YSZ deposition under UHV conditions.
The YSZ film shows high crystal quality, except close to the interface where two alternating distinct types of defects (shown in figures IV.15 and IV.16) are observed. In figure IV.15.a coexistence of commensurate crystalline regions with small residual amorphous areas can be appreciated.

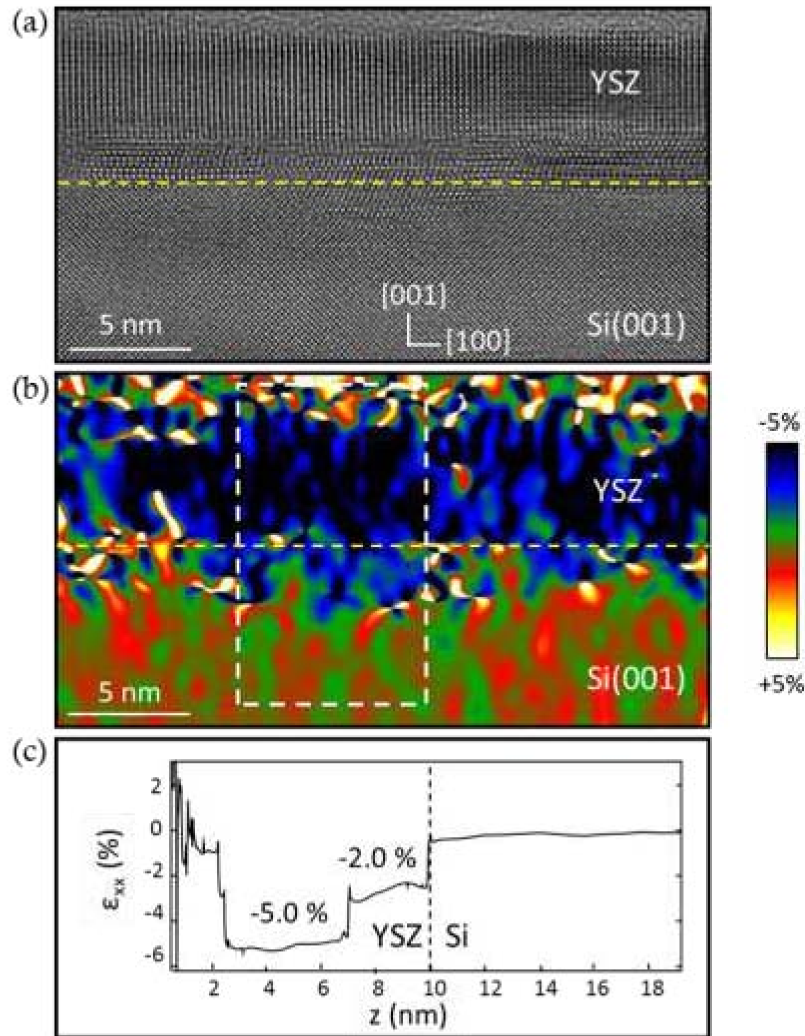

Figure IV.15: (a) HRTEM cross-sectional view along the [001] zone axis of the t = 6.6 nm film. The dashed line marks the interface; (b) Strain map calculated by the geometrical phase analysis of the same interface (marked by the dashed line) region shown in (a). (c) Profile of the in-plane deformation along the direction perpendicular to interface. The profile is averaged over the width of the rectangular region marked in (b). Due to the filtering in the Fourier space of the picture, the spatial resolution of the map is 1 nm.

The defective YSZ film extends along about 2 nm away from the interface, with high crystal quality in the top region of the film. To quantify locally the lattice strain we have applied the geometric phase analysis method, analysing the shifts of the crystalline planes with respect to an unstrained reference zone. The deformation along the in-plane [100] direction (figure IV.15.b) was obtained using a reference zone in the Si substrate at a distance of 20 nm from the interface (far from interfacial defects). The line profile of the deformation, $\varepsilon_x = 100 \times (\delta u_x/\delta_x)$, averaged over 4 nm along the direction parallel to the interface, is shown in figure IV.15.c. The deformation of the lower part of the YSZ film is around -2% respect Si, whereas

the upper part of the YSZ film is around -5%, corresponding to a lattice parameter of 5.2 Å. Deformation maps along the out-of-plane direction (not shown here) indicated similar deformation of around -5% in the upper part, thus implying that this part of the YSZ film, with the highest crystalline quality, is basically relaxed.

Interface regions as shown in figure IV.15.a alternate with others characterized by inclusions within the Si substrate (figure IV.16.a). Similar inclusions, observed in Pr_2O_3[SCH09] and Nd_2O_3[FIS06] films on silicon, were proposed to be silicides that tend to form under reducing atmosphere deposition [FIS06, SCH09] or annealing [STE04]. The inclusions shown in figure 16.a, likely silicides formed by Zr or Y diffusion into Si(001), extend around 10 nm along the interface and around 3 nm in depth, are faceted and appear to be monocrystalline.

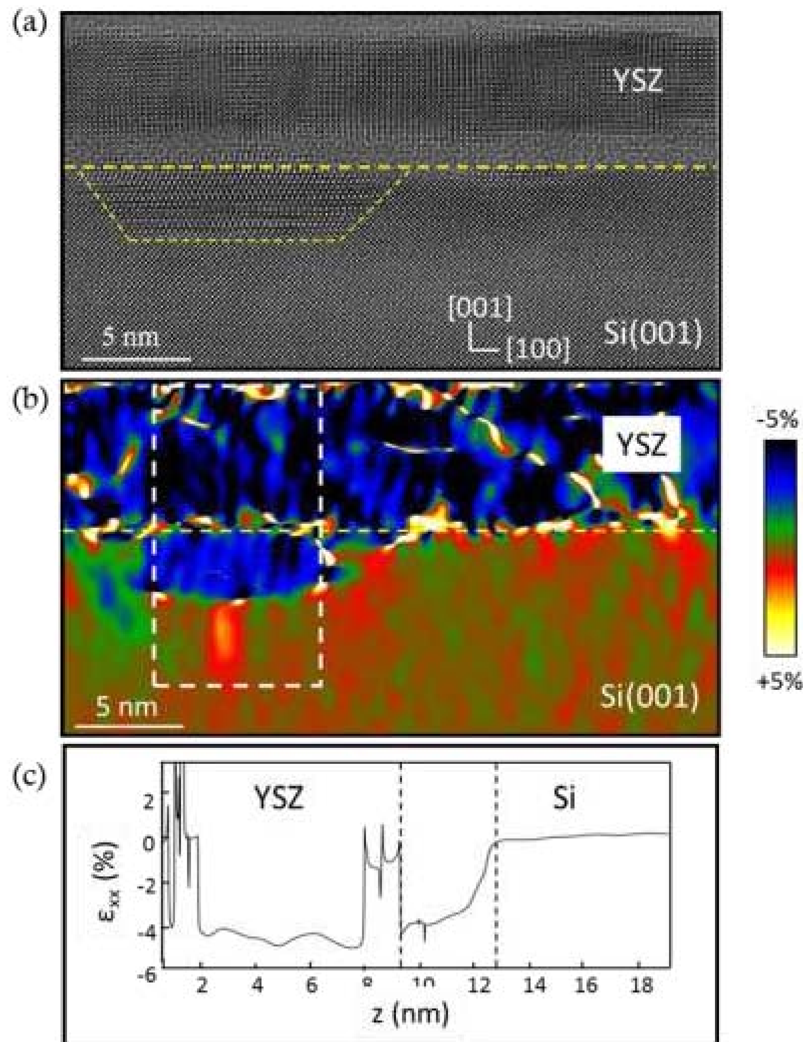

Figure IV.16: (a) HRTEM cross-sectional view along the [001] zone axis of the t = 6.6 nm film. The dashed line marks the interface. The interface of this sample shows regions as this one alternating with others as the one shown in figure IV.3 (see the text for details); (b) Strain map (b) and profile of the in-plane deformation along the direction perpendicular to interface (c).

The interface with silicon is sharp, whereas YSZ is disordered close to the inclusions. The corresponding in-plane deformation map is shown in figure IV.16.b, with the average line profile plotted in figure IV.16.c. The in-plane lattice parameter in the inclusion is smaller in around -3.8% respect silicon, whereas the YSZ film is relaxed as indicates the deformation of around -5% (note that close to the interface cannot be accurately calculated). The lattice

parameter in the inclusions, similarly to the bottom part of the film shown in figure IV.15, is thus intermediate between substrate and film and likely helps to accommodate the large lattice mismatch of around -5% between relaxed YSZ and Si.

In summary, we have shown that epitaxy of YSZ on oxidized Si(001) can occur by local reduction of SiO_x and then YSZ crystallization. Ultra-thin YSZ films with the presence of the SiO_x interfacial layer present high crystalline quality, whereas complete reduction of this layer in thicker YSZ films causes generation of defects close to the interface. The defective regions present in-plane lattice parameter intermediate between Si and the rest of the YSZ film, and thus can help to relief the stress associated to the interface between crystalline YSZ and Si(001).

IV.4 Integration of ultrathin $CoFe_2O_4$/YSZ with Si(001)

We have shown that ultrathin YSZ films, around 2 nm thick, present high crystal quality and thus they can be used as buffer layer. The total thickness is around 3 nm including the SiO_x interfacial layer. Deposition of a ultrathin CFO film on this buffer could result in a heterostructure with thickness around 5 nm, potentially suitable to develop monolithic spin filters. It remains to demonstrate that such ultrathin buffers permit epitaxy of CFO, and that the interface with Si is stable under the conditions required for CFO deposition. To determine it, CFO films were grown at 500-550 °C with different number of laser pulses to control the thickness (at ~0.007 nm/pulse growth rate). CFO deposition started under base pressure in order to avoid the silicon oxidation through the ultrathin YSZ at the first stages of CFO growth. An oxygen pressure of ~ 5×10^{-4} mbar was introduced after 40 laser pulses, and increased after 90 additional laser pulses until 0.1 mbar.

First, we prepared CFO films, around 50 nm thick, on ultrathin (~2 nm) YSZ buffers. Such high CFO thickness permits characterization by XRD and SQUID. The θ-2θ XRD scan around symmetrical reflections only shows substrate and CFO(111) reflections (figure IV.17.a), attesting that CFO grows (111) oriented. Pole figures of Si(220) and CFO(400) asymmetrical reflections are in figure IV.17.b.The twelve CFO(400) peaks, 30º apart in ϕ, signal the presence of four (111)-oriented crystal domains. Spinel (Ni,Zn)Fe_2O_4 films were reported to form the same crystal variants on YSZ(001) buffers,and the same kind of epitaxy was found for CFO grown on double CeO_2/YSZ(001) buffers(figure IV.4)[BAC11, WAK02]. The AFM topographic image (figure IV.17.c) shows that the CFO surface is flat, with rms roughness of 0.3 nm.

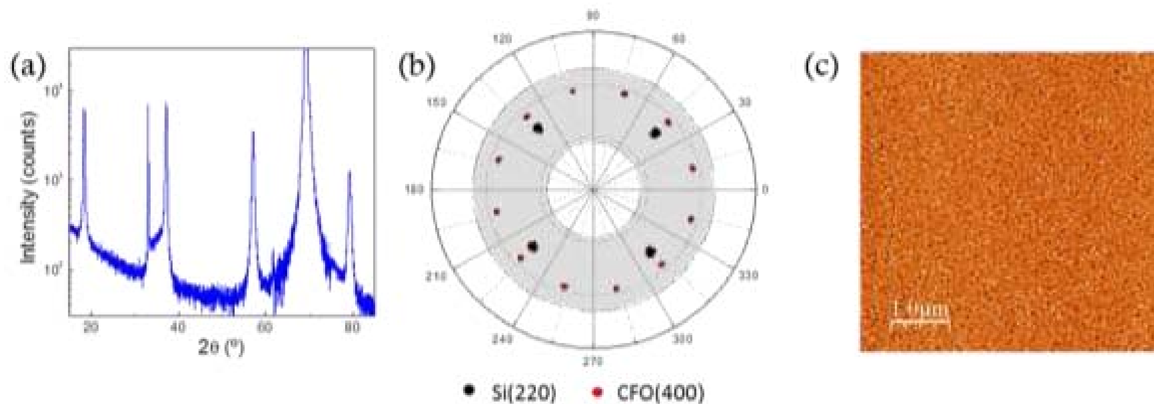

Figure IV.17: XRD measurements of thick CFO on ultrathin YSZ/Si(001): θ-2θ scan (a) and pole figures of Si(220) and CFO(400) (b). (c) AFM topographic image.

The cross-section TEM picture of the heterostructure(figure IV.18) shows high contrast between the Si substrate and the CFO/YSZ heterostructure. The low resolution image (figure IV.18.a) reveals that thickness is very uniform, as well as a bright region parallel to the interface that corresponds to the SiO_x interfacial layer. In the high resolution image (figure IV.18.b), a SiO_x thickness around 2.8 nm is determined.

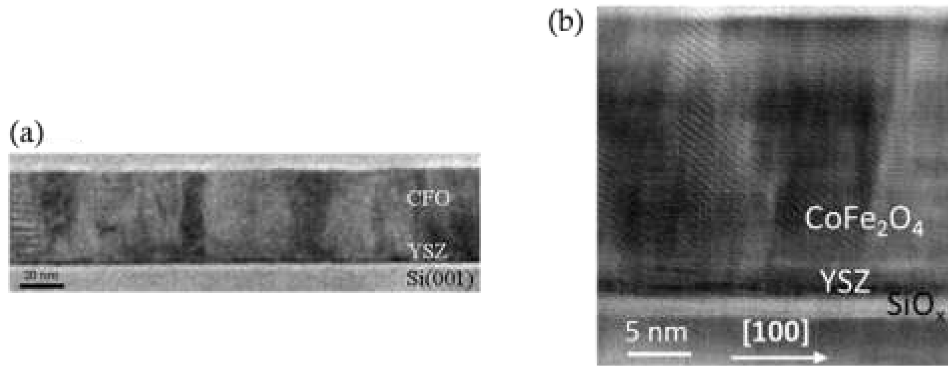

FigureIV.18: Cross-section TEM pictures of the CFO (~50 nm) thin film on YSZ (~2nm)/Si(001): in low magnification (a) and in high resolution (b).

Finally, the magnetic hysteresis loop of this sample is present in figure IV.19. The coercive field is ~1.5 T, and the saturation magnetization ~ 350 emu/cm^3, close to the bulk value. It has to be remarked that the good magnetic properties and the surface flatness of CFO films grown on ultrathin YSZ buffers are very similar to those grown on thick buffer layers(figure IV.7) [BAC11].

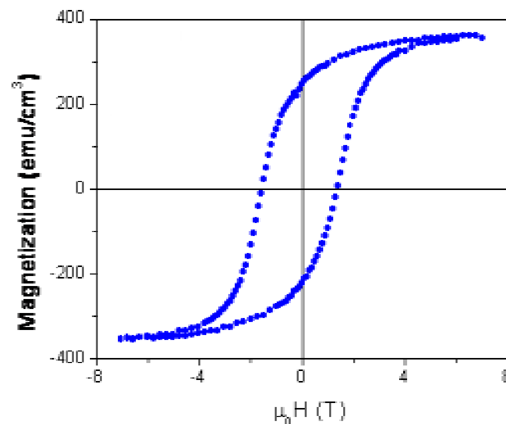

Figure IV.19: Magnetization hysteresis loop measured at 10 K with the field applied in-plane along the Si[110] direction.

The high magnetization value is strongly dependent on the thin film and interface microstructrure, and seems to be improved for slight mismatch heterostructures. However, the magnetization was enhanced in CFO integrated in single YSZ buffered in comparison with the double buffered CeO_2/YSZ buffered Si(001) (350/300 emu/cm^3) (figures IV.7 and IV.19).

Thus, the CFO thin film (~50 nm) integrated directly on an ultrathin YSZ buffer presents good structural and magnetic properties, although the interfacial SiO_x layer becomes thicker (close to 3 nm). This thickness, certainly small comparing with the CFO thickness, is probably excessive in case of an ultrathin CFO/YSZ bilayers used as tunnel barriers. It is then necessary to determine if the increase in SiO_x thickness occurs mainly during the early

deposition stages, which would make difficult the use of CFO/YSZ bilayer for monolithic spin filters. Thus, we have fabricated ultrathin CFO/YSZ bilayers and analyse them by TEM. We show first figure IV.20 the in-situ characterization by RHEED. When CFO starts to grow diffraction rings start to appear in the pattern, signalling a polycrystalline growth. The first CFO layers were deposited under base pressure, and introduction of relatively low pressure of oxygen ($\sim 5\times10^{-4}$ mbar) oxidizes the deposited CFO and enhances the crystalline ordering. The diffraction patterns after 50 (figure IV .20.a) and 100 laser pulses (figure IV.20.b)evidences quick change from rings to streaks that remain stable during the rest of the deposition. The streaky pattern at the end of the deposition (figure IV.20.c) signals epitaxial growth and flat surface.

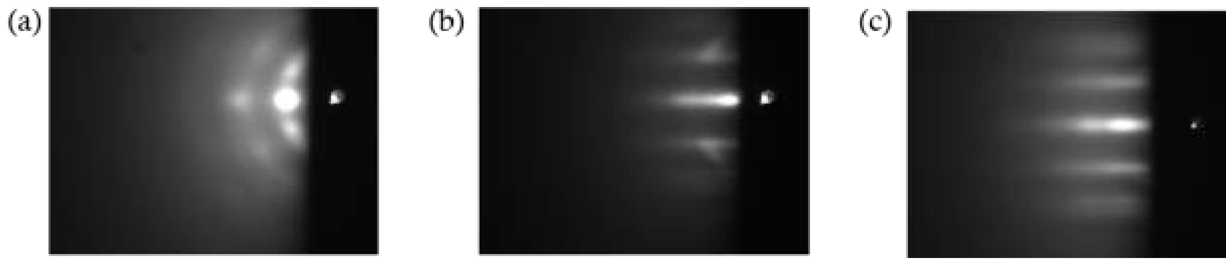

Figure IV.20: RHEED patterns taken along Si[100] during growth of CFO at 500 ºC acquired at a grazing angle of 1.0º after deposition of 50 (a) and 100 laser pulses (b). (c) Pattern taken at the end of the growth (400 laser pulses) at a grazing angle of 1.6º.

Ex-situ AFM (see a topographic image and the corresponding height profile in figures IV.21.a and b, respectively) confirms two-dimensional growth with very low roughness (rms = 0.1 nm).

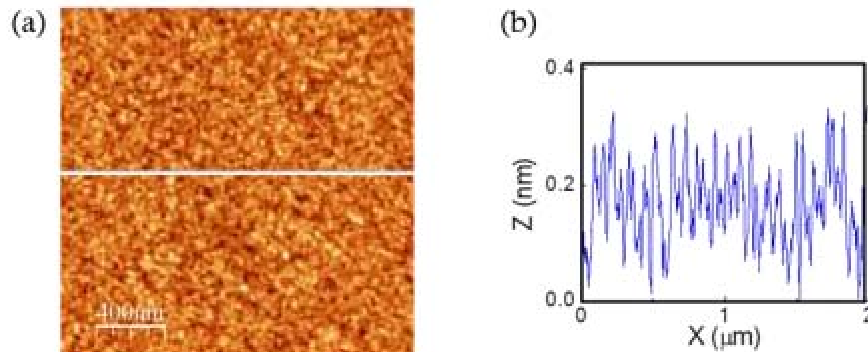

Figure IV.21: Topographic AFM image of the CFO film, with (a) the height profile along the marked line in (b).

In figure IV.22 we show a cross-section TEM image of the ultrathin heterostructure. The high quality of the epitaxy of both CFO and YSZ layers (with respective thicknesses of 2.9 and 1.9 nm) can be appreciated. The narrow white band along the interface indicates the presence of an interfacial SiO_x layer 2.4 nm thick. The SiO_x layer in single YSZ buffer on Si(001) was thinner than 1.0 nm (figure IV.12), and therefore it is concluded that the interfacial layer became thicker during CFO growth due to oxygen diffusion through the YSZ buffer, although slightly thinner that when a thicker CFO was grown (figure IV.18). Total thickness of CFO/YSZ/SiO_x is around 7 nm, probably too thick for tunnelling transport.

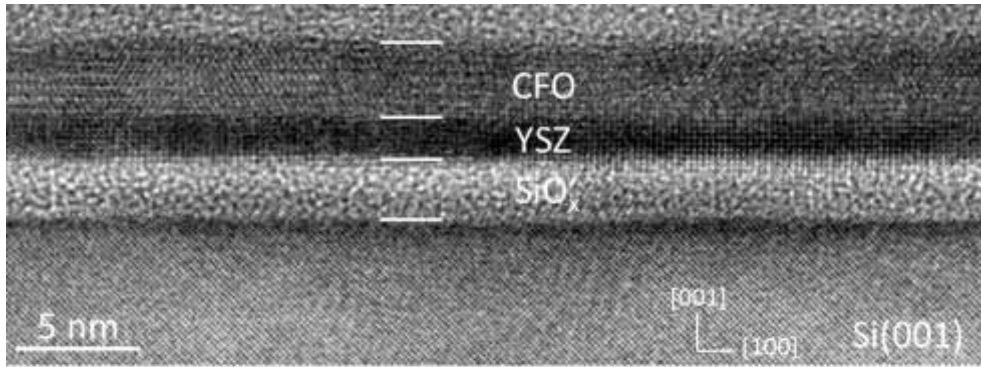

Figure IV.22: Cross-section TEM showing the ultrathin epitaxial heterostructure.

IV.5 Summary

In summary,epitaxial CFOfilms have been grownon CeO_2/YSZ buffered Si(001) with (111) out-of-plane orientation and present four in-plane crystal domains. They grow two-dimensionally and CFO presents flat interface with CeO_2 and very flat surface with roughness below 0.3 nm. The saturation magnetization, around 300 emu/cm^3, is close to the bulk value.
The mechanism of epitaxy of YSZ on oxidized Si(001) can occur by local reduction of SiO_x and then YSZ crystallization. Ultrathin YSZ films with presence of around 1 nm of SiO_x interfacial layer present high crystalline quality, whereas complete reduction of this layer in thicker YSZ films causes generation of defects close to the interface. The defective regions present in-plane lattice parameter intermediate between Si and the rest of the YSZ film, and thus can help to relief the stress associated to the interface between crystalline YSZ and Si(001).
Finally, epitaxial CFO films with thicknesses in the 2-50 nm range were grown on Si(001) buffered with ultrathin YSZ buffers in a single process. Properties were similar to those of CFO on double CeO_2/YSZ thick buffer layers.Ultrathin CFO/YSZ heterostructures with a total thickness of 5 nm were fabricated, being the SiO_x interface layer 2.4 nm. The total thickness above 7 nm appears to be excessive for their use in spin filter devices.

Chapter V

Integration of $CoFe_2O_4$ with Si(111) using A_2O_3 (A=Sc, Y) buffer layers

V.1 Introduction

The epitaxial integration of CFO with Si has been achieved on Si(001) using yttria-stabilized zirconia (YSZ) as buffer layer [see chap IV]. (111) faces of spinels have typically the lowest surface energy and thus spinel films tend to form (111) facetted islands when they grow (001)-oriented [LUD04-06]. Alternatively they can grow (111)-oriented and thus flat, as occurs on YSZ/Si(001) [WAK04, chap IV]. In this case, the change from four-fold to three-fold in-plane symmetry at the interface causes formation of four in-plane CFO crystal variants. Si(111) wafers can thus be a better choice as substrate to grow spinel films, ideally flat and monocrystalline (free of crystal variants).

Growth of CFO on Si(111) requires a suitable buffer layer. Although oxides on Si(111) have been much less investigated than with Si(001), direct epitaxial growth of some oxides is demonstrated. Examples include $LaYO_3$ and $PrYO_3$, generally usedin silicon or germanium on-insulator heterostructures [BOJ03, GIU10], orSc_2O_3 and Y_2O_3as buffer layer for integration of GaN or oxides as ZnO and $YMnO_3$[TAR10, GUO09, ITO03, LIU08]. Also, other oxides as γ-Al_2O_3 have been grown epitaxially on Si(111), and have been used to integrate functional complex oxides [KUM03, AKA05].

In addition of the above mentioned oxides, Sc_2O_3 and Y_2O_3 grow epitaxially on Si(111) with high crystal quality [KLE05, NIE08]. They are thus candidates as buffer layer for the integration of functional oxides with Si(111). However, epitaxial growth of $CoFe_2O_4$ on Sc_2O_3 and Y_2O_3 is *a priori* very challenging due to the huge lattice mismatch ($f = (a_f-a_s)/a_s$) of -14.7% and -20.9%, respectively. Nevertheless, a large difference of lattice parameters does not prevent necessarily epitaxial growth. For example, it has been reported epitaxy of TiN on Si(001)[NAR92], having a lattice mismatch of 22% in the direct 1/1 unit cell matching.Other examples include AlN on Al_2O_3 [VIS95], $SrTiO_3$/TiN on Si(001)[VIS96], and ZnO/α-$Al_2O_3$with mismatches of 11.1%, 13.2% and 16.6%, respectively. Such cases of epitaxy occur when there is good matching of *m* unit cells of the film with *n* unit cells of the substrate, or even simpler *m* lattice planes of the film with *n* lattice planes of the substrate. This particular type of epitaxy is known as domain matching epitaxy (DME) [NAR03]. This particular matching occurs immediately as the film nucleates, and thus differs respect to semi-coherent interfaces where misfit dislocations appear when the film relaxes plastically. Below we describe the DME mechanism in more detail.

V.1.1 **Materials**

Sc_2O_3 and Y_2O_3 present a cubic bixbyite structure, which is a particular group of Mn_2O_3 fluorite with a Ia3 space group. The basic fluorite structure (figure V.1) has a stoichiometry of AX_2, and is described as a stacking of empty and full cubes with anions at their corners. At the centre of the cube there is a cation A with a coordination of eight, and the coordination of the anions is four.

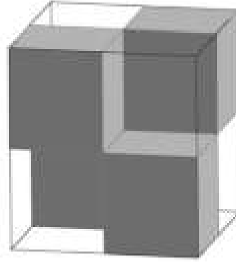

FigureV.1: Basic fluorite structure[NAV10].

However, there are several ways of producing more energetically favourable configurations with anion vacancies. In either case, the position of cations and anions near the defect distort from the parent cubic arrangement, leading to a long range order and new structure. The bixbyite structure (figure V.2, corresponding to Y_2O_3), typical of lanthanide oxides, has an ordering of oxygen vacancies in the [111] direction. These oxygen vacancies are alternated with cations and are separated by a ½ <111> lattice vector.

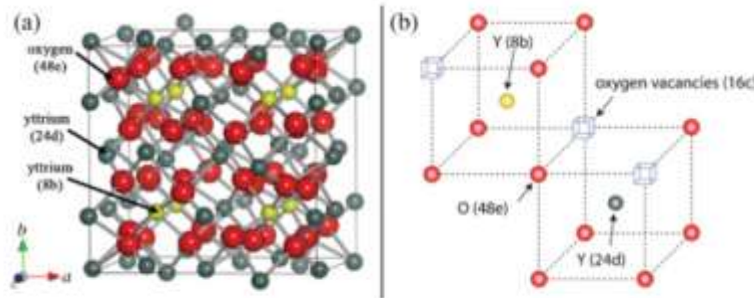

Figure V.2 : Y_2O_3 structure[LAC11].

In the particular case of Y_2O_3, the Y-O bond length ranges from 2.25 to 2.34 Å. In a simple consideration of the structure, the Y atom is in a highly distorted octahedral environment while the O atom has a distorted tetrahedral coordination [CHI90-1].Sc_2O_3 and Y_2O_3 have lattice parameter a_{Sc2O3}= 9.854 Å and a_{Y2O3}= 10.604Å, and respective lattice mismatch with silicon of $f_{Sc2O3/Si}$= -9.36% and $f_{Y2O3/Si}$= -2.37% [f= $(a_{A2O3}-2a_{Si})/2a_{Si}$)].

The lattice mismatch with $CoFe_2O_4$ (a_{CFO}= 8.3919Å) is $f_{CFO/Sc2O3}$= -14.7% and $f_{CFO/Y2O3}$= -20.9% [f=$(a_{CFO}-a_{A2O3})/a_{A2O3}$)]. These huge lattice mismatches make the epitaxial growth of $CoFe_2O_4$on these buffers impossible considering a single unit cell matching. However, matching of m/n atomic planes by DME, could be maybe a mechanism to allow epitaxy. As the materials are cubic, the spacing between successive (hkl) planes is: $d_{hkl} = \frac{a}{(h^2+k^2+l^2)^{1/2}}$

A_2O_3 and CFO are expected to grow (111) oriented on Si(111), being the inter-plane spacings along the [1-10] in-plane direction: $d_{[1-10]}$(Si)= 3.84 Å, $d_{[1-10]}$(Sc_2O_3)= 6.96 Å, $d_{[1-10]}$(Y_2O_3)= 7.48 Å and $d_{[1-10]}$(CFO)= 5.92 Å. The number of atomic planes along the $d_{[1-10]}$ distance is two

for Si and four for Sc_2O_3, Y_2O_3, and $CoFe_2O_4$. Thus, the spacing between atomic planes for Si, Sc_2O_3, Y_2O_3 and CFO are d(Si)= 1.92Å, d(Sc_2O_3)= 1.74 Å, d(Y_2O_3)= 1.87 Å and d(CFO)= 1.48 Å, respectively(Table V.1).

	a(Å)	d_{1-10}(Å)	Atomic planes spacing (Å)
Si	5.431	3.840	1.920
Sc_2O_3	9.854	6.968	1.742
Y_2O_3	10.604	7.498	1.874
CFO	8.392	5.933	1.483

Table V.1: Lattice parameters, $d_{[1-10]}$ distances, and spacing between atomic planes along [1-10].

V.1.2 Domain Matching Epitaxy

V.1.2.1 Description of the mechanism

It is conventionally assumed that lattice matching epitaxy LME (one to one matching of lattice constants across the interface) during thin film growth is only possible for systems with mismatch lower than 7-8%. However, exceptions have been found [NAR92-95, VIS95], and Narayan and Larson [NAR03] introduced the concept of domain matching epitaxy (DME) to describe epitaxy between film and substrate having compatible crystal symmetry but very high lattice mismatch.

In domain matching epitaxy *m* atomic planes of the film accommodate on *n* atomic planes of the substrate with low overall strain, and the size of the domain equals integral multiples of planar spacing. There is matching of atomic planes across the interface, with extra planes (dislocations) corresponding to the additional atomic planes in the film (if m > n) or in the substrate (if m < n). If the film and the substrate have similar crystal structures, and mismatch below ~7%, then the matching of planes becomes equivalent to the matching of lattice constants (LME). In conventional lattice matching epitaxy (LME), the growth matches one to one lattice constants across the interface, and the correspondent misfit strain energy is relaxed by the introduction of dislocations when the film is above the critical thickness.

In the matching of lattice planes (interatomic distances along the interface) of the film d_f with those of the substrate d_s can occur even if the initial mismatch $f = \frac{d_f - d_s}{d_s}$ is very large. This matching of integral multiples (m, n) of lattice planes leaves to a residual mismatch $f_r = \frac{md_f - nd_s}{nd_s}$. In the ideal case of a perfect coincidence, $md_f = nd_s$, the residual mismatch f_r is zero. A domain is defined by the perfect continuity of *m* or *n* consecutive atomic planes through the interface and it ends in additional half-planes (dislocations). In the case of d_f>d_s, n= m+1, and the additional half-plane forming the interfacial dislocation will be on the substrate ⊤. On the contrary, if d_s>d_f, then m= n+1 and the dislocation is formed in the film ⊥.
In conventional LME with ideal full plastic relaxation at the interface, the distance between dislocations in the semi-coherent interface can be calculated from the in-plane interplanar distance of the thin film (d_f) and substrate (d_s) with the formula:

$$D = \frac{(d_f \times d_s)}{|d_f - d_s|}$$

Dislocations in DME are not due to plastic relaxation, but are inherent to the particular mechanism of epitaxy. They are separated by a distance D between n consecutive atomic substrate planes through the interface if n<m (m film planes, if n>m). The size of a m/n domain, and thus the spacing D between dislocations, can be estimated as nd_s if n<m, or md_f, if n>m (here d_s and d_f are the spacing between atomic planes).

If the domain matching is not perfect, $nd_s \neq md_f$, there would be a residual mismatch that can be avoided by changing the domain size. Two domains m/n and m'/n'(= m-1/n-1 or m+1/n+1) may alternate with a certain frequencyto provide a perfect matching:
$\alpha_{m/n} md_f + \alpha_{m'/n'} m'd_f = \alpha_{m/n} nd_s + \alpha_{m'/n'} n'd_s$ or $(1-\alpha)md_f + \alpha m'd_f = (1-\alpha)nd_s + \alpha n'd_s$
considering $\alpha_{m'/n'} = \alpha$ and $\alpha_{m/n} = (1-\alpha)$.
Then, $(m \pm \alpha)d_f = (n \pm \alpha)d_s$, $and\ \alpha = \alpha_{m'/n'} = \left|\frac{md_f - nd_s}{d_s - d_f}\right|$

For example, if α=0.5, then m/n and m'/n' domains alternate with an equal frequency $\alpha_{m'/n'} = \alpha_{m/n}$. In general two alternated domains will alternate with respectively frequencies $\alpha_{m'/n'}$ and$\alpha_{m/n}$, being $\alpha_{m/n} = 1 - \alpha_{m'/n'}$. The alternation of tensile and compressive domains leads to an interface without residual strain. The sketch in figure V.3 shows an example with perfect matching by DME with75% of m/n domains and 25% of m'/n' domains.

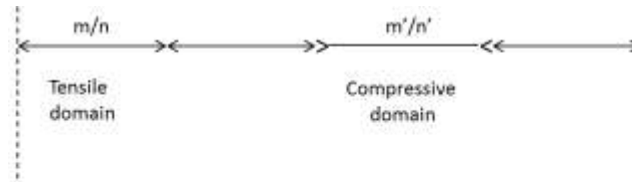

Figure V.3: Interface with local tensile and compressive domains alternated leading to a null global residual strain.

It is important to note that the high lattice mismatch in DME imposes that most of the strain is relieved immediately as the film nucleates. Then, the thin film can be grown relaxed and free of defects. This epitaxial growth process provides a critical advantage over small-misfit lattice matching epitaxy (LME), where most of the dislocations are generated on the surface beyond the critical thickness and then glide to the interface as half loops degrading the structure [MAT70]. Also, epitaxial stress in LME can be also relieved by changes in stoichiometry [EST08] or transition to 3D growth (Stranski-Krastanov mechanism) [EAG90]. Films with low or negligible strain grown by DME would be thus more robust against formation of such effects.

	Considered parameter	Initial misfit strain	Critical thickness	Dislocation step D	Dislocation formation	Quality of the film
LME	a	≤7-8%	h_c	$\frac{(d_f \times d_s)}{\lvert d_f - d_s \rvert}$	Relaxation	+
DME	d	≥10%	-	$nd_s \approx md_f$	With film nucleation	++

Table V.2: Comparison between LME and DME. Table elaborated from data collected in [MAT74, NAR03].

V.1.2.2 $CoFe_2O_4$ on A_2O_3: possibilities of domain matching epitaxy

As it was indicated in the introduction of this chapter, the lattice mismatch of CFO respect to Sc_2O_3 and Y_2O_3 is -14.76% and -20.86%, respectively. This huge lattice mismatch discards epitaxy by conventional lattice matching, and thus the mechanism of domain matching epitaxy has to be considered. As calculated in section I.1.2, the atomic planes spacing along [1-10] are d(CFO) = 1.48Å, d(Sc_2O_3) = 1.74Å and d(Y_2O_3) = 1.87Å. For both A_2O_3 compounds, $d_{CFO} < d_{A2O3}$, and then the matching of md_f on nd_s imposes $m>n$.

The residual mismatch $f_r = \frac{md_f - nd_s}{nd_s}$ of different m/n possible domains can be calculated to predict the domain configuration in case of this type of epitaxy. For the combination of CFO with Sc_2O_3 or Y_2O_3, the data of residual lattice mismatch corresponding to different values of m and n are presented in table V.3. It can be seen that a minimum residual mismatch f_r = -0.55% would be obtained for a 7/6 DME for the CFO/SC_2O_3 system, and that a 5/4 DME for the CFO/Y_2O_3 would lead to a minimum residual mismatch of f_r = -1.07%. The minimum residual mismatch is negative, and thus, alternation with domains presenting positive residual mismatch could lead to a perfect matching. Considering the values presented in table V.1, it can be seen that 6/5 and 4/3 respective domains for the SC_2O_3 and Y_2O_3 buffers systems could provide a positive strain. As the amplitude of the respective positive residual mismatch of 6/5 and 4/3 domains is much higher than the respective negative residual mismatch, it can be anticipated that the 7/6 domain will be more frequent than the 6/5 domain forthe CFO/Sc_2O_3 heterostructure, and similarly the 5/4 domain will be more frequent than the 4/3 domain for the CFO/ Y_2O_3 system in order to obtain a perfect matching epitaxy without residual strain.

M=n+1		$f_r = (md_{CFO} - nd_{A2O3})/nd_{A2O3}$ (%)	
CFO m	A_2O_3 n	$A_2O_3 = Sc_2O_3$	$A_2O_3 = Y_2O_3$
1	1	-14.759	-20.860
2	1	70.480	58.278
3	2	27.860	18.708
4	3	13.653	5.518
5	4	6.550	**-1.076**
6	5	2.288	-5.033
7	6	**-0.553**	-7.671
8	7	-2.582	-9.555
9	8	-4.104	-10.968
10	9	-5.288	-12.067

Table V.3: Table of the residual mismatch f_r calculated for different domain matching systems of md_{CFO} with nd_s.

Comparing with previous studies [NAR92-03, VIS95], it can be seen that the interplane spacing ratio of the CFO/Sc_2O_3 system (0.85) falls between values corresponding to the α-Al_2O_3/ZnO (0001) system (0.83) and the Cu/TiN(100) system (0.857), which shows alternation of 5/6 and 6/7 domains [NAR03]. Similarly, for the CFO/Y_2O_3 system, the interplane spacing ratio (0.79) is between the planar spacing ratio of TiN/Si(100) (0.75) and AlN/Si(111) (0.8). The domains experimentally observed in these systems were alternation of 3/4 and 4/5 [NAR03, VIS95].

The frequency factor of presence of each domain can be predicted by $\alpha_{m'/n'} = \left|\frac{md_f - nd_s}{d_s - d_f}\right|$. Considering the CFO/$Sc_2O_3$ system, perfect matching would occur with 7/6 and 6/5 domains with respective frequency factors of $\alpha_{7/6}$=0.73 and $\alpha_{6/5}$=0.27. Then, the 7/6 domain is expected to be more than two times more often than the 6/5 domain being the respective percentages 73% and 27%. For the CFO/Y_2O_3 system, perfect matching would occur for $\alpha_{5/4}$=0.79and $\alpha_{4/3}$ = 0.21. Thus, the CFO/Y_2O_3 interfacewould be ideally accommodated by 79% of 5/4 domains and 21% of 4/3 domains. In both DME interfaces of CFO/A_2O_3, dislocations are formed by CFO extra half-plane.

The 7/6 and 6/5 domains in the CFO/Sc_2O_3 interface have respectively 6 or 5 consecutive planes matching across the interface, and the size of the domains are 10.4 Å (7d_{CFO}), and 8.9 Å (6d_{CFO}). Considering the domain size variation of around 72.6% of 7/6 domains with 27.4% 6/5 domains, the average size of the domainsis 9.89Å.

In the CFO/Y_2O_3 interface, the size of the 5/4 domain is around 7.4 Å (5d_{CFO}) and the size of the 4/3 domain around 5.9Å (4d_{CFO}). In average, dislocationswill be7.09Å apart.

Interface	Plane spacing ratio	Variation of domain	Residual mismatch	Frequency factor	Percentage of domain	Total residual mismatch	Domain size (Å)	Pondered average of D(Å)
	x	m/n	f_r (%)	$\alpha_{m/n}$	%	f_r (%)	md_f	<D>
CFO/Sc_2O_3	0.85	7/6	-0.55	0.73	73	0.29	10.3	9.89
		6/5	2.29	0.27	27		8.8	
CFO/Y_2O_3	0.79	5/4	-1.08	0.79	79	0.24	7.4	7.14
		4/3	5.51	0.21	21		5.9	

Table V.4: Summarised DME parameters calculated for CFO/Sc_2O_3 and CFO/Y_2O_3.

V.2 $CoFe_2O_4$ on Sc_2O_3 buffered Si(111)

V.2.1 Introduction

The integration of Sc_2O_3 on silicon has been investigated due to its potential use as an alternative gate dielectric for Si, since it has a relatively high dielectric constant, large band gap, and thermodynamic stability with Si at moderated temperatures [AFA07, CHE05, COP10]. However, Sc_2O_3 and Si have very different lattice constants leading to a high mismatch of 9.2% (1u.c. Sc_2O_3/ 2u.c. Si). Then, it was unexpected to observe that Sc_2O_3 thin films grow epitaxially on Si(111) [CHE05, HON05, KLE05]. Films are typically deposited by MBE on (7×7) reconstructed Si(111), and the resulting epitaxial relationship is $(111)_{Sc2O3}[1\text{-}10]_{Sc2O3}//(111)_{Si}[1\text{-}10]_{Si}$. It was reported, for relatively thick (t = 35 nm) Sc_2O_3 films, formation of edge-type misfit dislocations with the line direction parallel to $[11\text{-}2]_{Si}$ and exhibiting a regular spaced network around 1.8 ±0.1 nm, in good agreement with the nominal spacing of 1.9 nm for a dislocations fully accommodated mismatch system [KLE05]. In contrast, the absence of a regular dislocation network was evidenced for ultrathin films [HON05], signalling epitaxy by LME in spite of the high mismatch (>9%).

Epitaxy of CFO on Sc_2O_3 is even more difficult considering the existing lattice mismatch. The lattice parameters of CFO and $Sc_2O_3$are 8.392 Å and 9.85 Å, respectively, resulting in a mismatch of -14.76% $((a_{CFO}- a_{Sc2O3})/a_{Sc2O3})$. This excludes standard epitaxy but

the mismatch can be reduced to-0.553% by domain matching epitaxy of CFO on $Sc_2O_3$with periodicity 7/6 (table V.3).

Here we will show that CFO films grow epitaxially on Sc_2O_3(111)/ Si(111) by a mechanism of domain matching. The $CoFe_2O_4$ thin films were grown by RHEED-assisted PLD (at ICMAB) on Si(111) with an epitaxial Sc_2O_3 buffer layer grown by MBE (at IHP).

V.2.2 Thin film growth and in-situ characterization by RHEED

A sketch of the elaboration process is in figure V.4. Before Sc_2O_3 deposition, the Si(111) wafer was chemically etched and thermally treated, leading to a (7×7) Si(111) surface reconstruction. The treatment and the subsequent deposition of Sc_2O_3 by MBE was done at IHP Frankfurt-Oder (Germany), and the growth conditions are reported elsewhere [TAR10]. The Sc_2O_3 thin film deposited on a 4' wafer was 39 nm thick. Then, pieces around 10x5 mm in size were cut and used to deposit CFO.

Figure V.4: Sketch of the elaboration of the CFO/Sc_2O_3 films on Si(111).

CFO thin films, 24 nm and 36 nm thick, were depositedon the Sc_2O_3/Si(111) chips by PLD(λ=248 nm, repetition rate of 5 Hz, fluence ~1.5J/cm^2) at 550 ºC. The deposition started under base pressure (~10^{-7} mbar) aiming to minimize formation of a SiO_x interfacial layer at the Sc_2O_3/Si(111) interface. Then, around 5×10^{-4} mbar of oxygen was introduced after 40 laser pulses (corresponding to a nominal thickness of 0.20 nm), and the pressure was increased to 0.1 mbar after additional 90 pulses (corresponding to a nominal thickness of 0.65 nm). The process is summarized in figure V.5, where we include RHEED patterns of the initial Sc_2O_3 surface and the CFO surface at several growth stages.

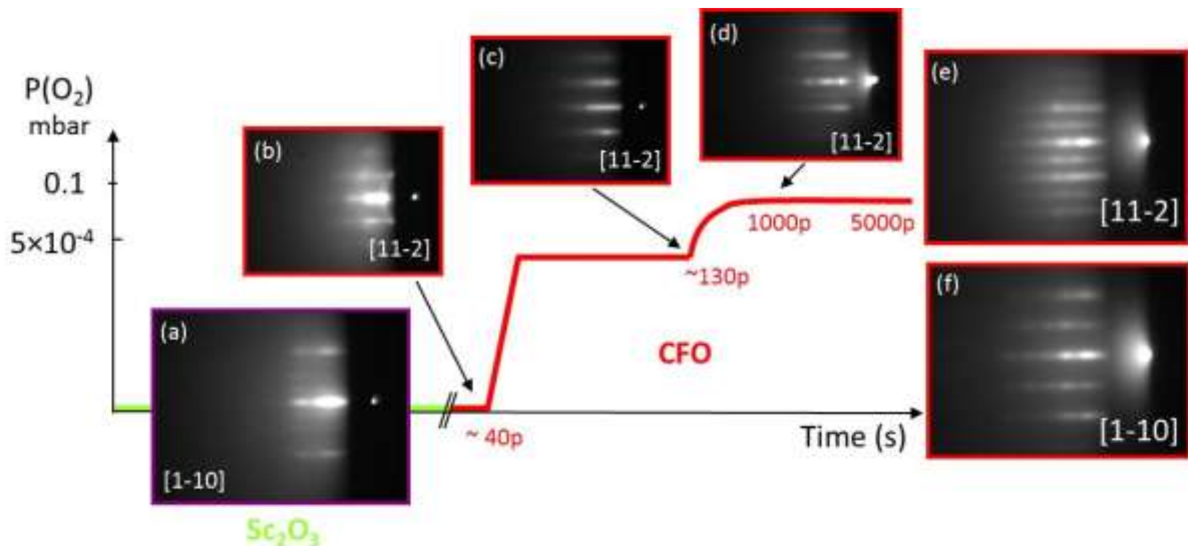

Figure V.5: RHEED patterns taken with an angle of 1.2° during and after growth of the CFO thin film: (a) of the Sc_2O_3 surface before CFO growth along [1-10]Si, (b) after deposition of 40p (~0.20 nm) of CFO under vacuum, and (c) after deposition of 130p (~0.65 nm) of CFO (d), after 1000 p (4.80 nm). ©and (f) patterns at the end of the deposition taken with an angle of 2°along [11-2]Siand [1-10]Si, respectively.

The streaks presents in the RHEED pattern shown in figure V.5.a attest the epitaxy and flatness of the Sc_2O_3 film. The three additional streaks between the most intense ones indicate a surface reconstruction, in agreement with previous studies reporting (4×4) reconstruction of Sc_2O_3 on Si(111) [GIU10, TAR10]. The rings and the diffuse halo appearing at the first stage (deposition under vacuum) of the CFO growth (figure V.5.b) indicate low crystallinity. But after introduction of oxygen, the crystallinity improves as indicates the clear streaky pattern with absence of the halo and rings (figure V.5.c). Then, after increasing the oxygen pressure up to 0.1 mbar, reflections at half positions appear (figure V.5.d). The streaks show modulation of the intensity along q_z at the end of the deposition, likely due to surface roughness as well as the higher RHEED angle (figure V.5.e and f).

V.2.3 AFM and XRD of $CoFe_2O_4$ and Sc_2O_3films on Si(111)

The surface morphology was characterized by AFM. The topographic images of the Sc_2O_3 and CFO surfaces are presented in figure V.6. (a) and (b) respectively. Both Sc_2O_3(figure 6.a) and CFO (figure 6.b) films have homogeneous and quite flat surfaces. The root-mean square (rms) roughness of Sc_2O_3 and CFO is 1.4 Å and 4.0 Å, respectively. The flatness of both surfaces is consistent with the RHEED patterns presented above (figure V.5.d and e).

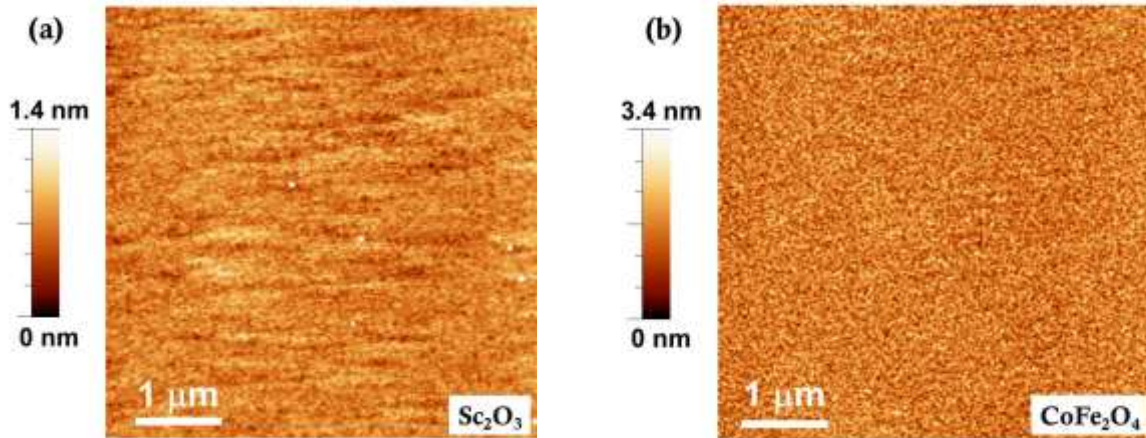

Figure V.6: AFM topographic images (5×5 μm^2) of (a) the Sc_2O_3 buffer and (b) the CFO film (t = 36 nm)/Sc_2O_3(t = 39 nm)/Si(111).

The crystallinity of the bilayer structure was characterized by XRD. Θ-2θ scans around symmetrical reflections and Φ–scans around asymmetrical reflections were measured. The diffraction peaks in the symmetrical θ-2θ scan (figure V.7.a) correspond to (111) reflections of CFO, Sc_2O_3, and Si, indicating that both CFO and Sc_2O_3 are fully (111) oriented along the out-of-plane with absence of secondary crystalline phases within the sensibility of the measurement. We have determined the out-of-plane lattice parameters of Sc_2O_3 and CFO from the angular position of Sc_2O_3(222) and CFO(333) peaks, using as a reference the positions of the Si(111) and Si(222) peaks, respectively. We obtain $d_{Sc2O3}(111) = 5.691 \pm 0.004$ Å and $d_{CFO}(111) = 4.852 \pm 0.004$ Å. These values are very close to corresponding interplanar distances in bulk, $d_{Sc2O3}(111)= 5.685$ Å and $d_{CFO}(111) = 4.845$ Å, indicating that both films are relaxed.

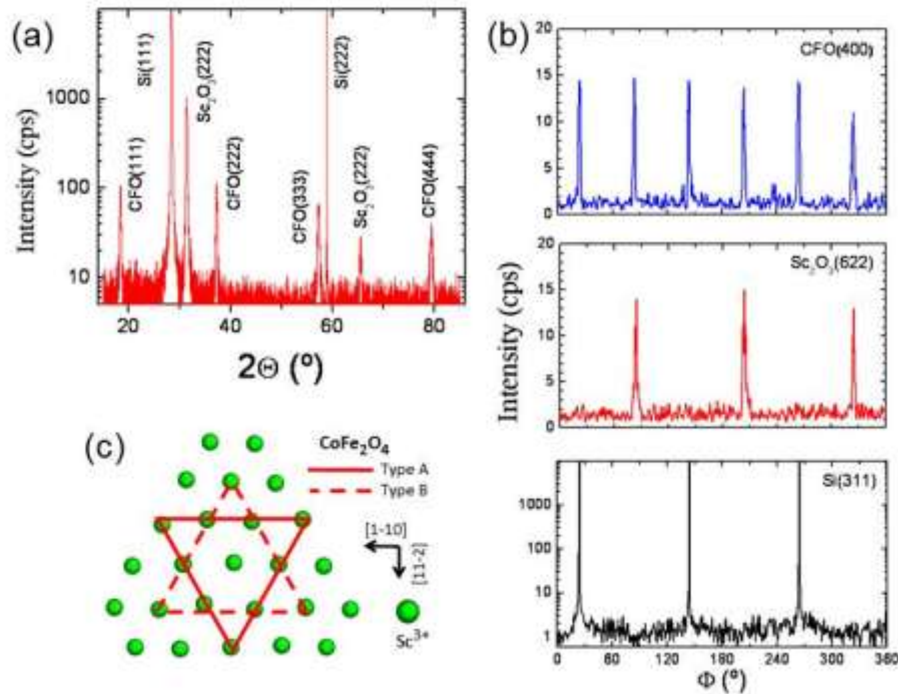

Figure V.7: XRD θ-2θ around symmetrical reflections (a) and Φ–scans around CFO(400), Sc_2O_3(622), and Si(311) reflections (b) of the CFO (t =36 nm)/Sc_2O_3/Si(111) sample. (c) Sketch of the A- and B-type crystal variants of CFO.

The Φ-scans around asymmetrical Si(311), Sc_2O_3(622) and CFO(400) reflections are presented in figure V.7.b. The three Sc_2O_3(622) peaks, 60° apart from the Si(311) ones, indicate that Sc_2O_3 presents single B-type crystal variant. *Ab initio* calculations attributed the stabilization of the B-type over the A configuration mainly to electrostatic interaction energies of the very ionic bixbyite oxide structure with the covalent Si(111) substrate [SCH08]. The Φ-scan around CFO(400) reflections confirms epitaxial growth, with six peaks indicating the coexistence of A- and B-type in-plane crystal variants, with fractions of about 50%. In a second sample with thinner CFO (t = 24 nm) the B-type variant was found to be slightly predominant (around 65%). The epitaxial relationships of A and B crystal variants correspond to [11-2]$CoFe_2O_4$(111)// [11-2]Sc_2O_3 (111)// [11-2]Si(111) and [-1-12]$CoFe_2O_4$(111)//[-1-12]Sc_2O_3 (111) //[11-2]Si(111), respectively.A top view schematic illustration of the matching of CFO(111) with A- and B-type variants on Sc_2O_3(111) is presented infigure.7.c. The presence of both CFO variants with close fractions on Sc_2O_3 buffer contrasts with the observation that, when CFO grows on $SrTiO_3$(111) substrates, the A-type variant is clearly minority or absent [YAN08, DIX09].

V.2.4 <u>HRTEM characterization</u>

The CFO (t = 24nm)/Sc_2O_3/Si(111) sample was prepared for TEM observation in cross section mode along the Si[11-2] zone axis. The low magnification view (figure V.8)reveals the thickness homogeneityof CFO and Sc_2O_3 films. The presence of an amorphous interfacial layer is clear at the Sc_2O_3/silicon interface, while the $CoFe_2O_4$/Sc_2O_3 interface is sharp. Below we present a detailed study of this interface to confirm the domain epitaxial matching between CFO and Sc_2O_3.

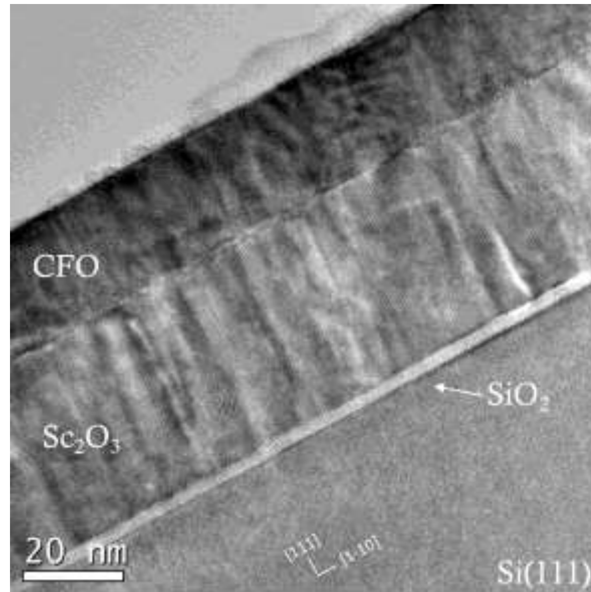

Figure V.8: Low resolution cross-sectional view of the t= 24nm $CoFe_2O_4$ thin film on Sc_2O_3/Si(111).

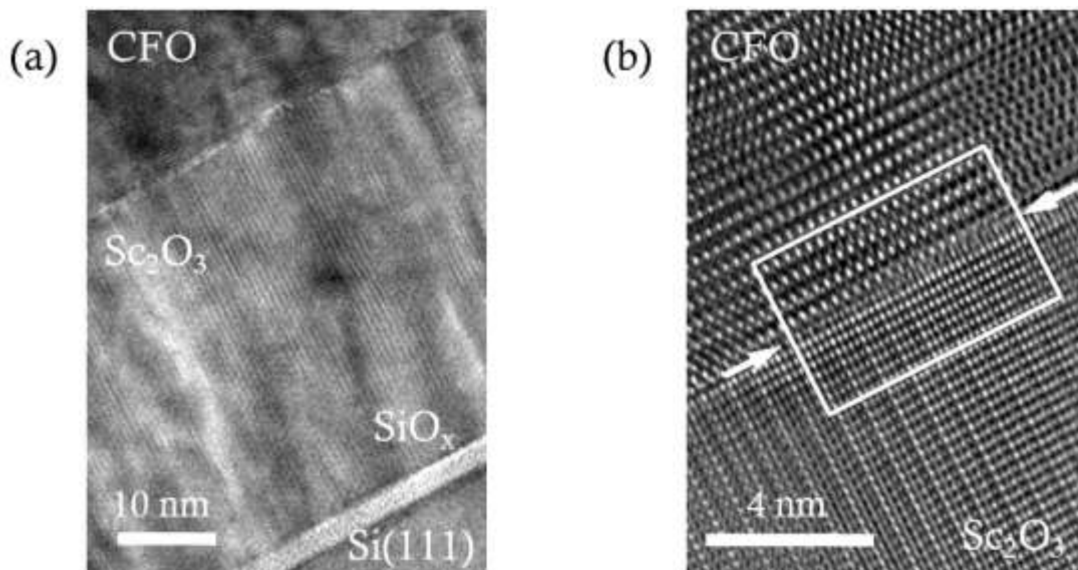

Figure V.9: (a) HRTEM image showing both interfaces. (b) Zoom around the CFO/Sc_2O_3 interface.

Figure V.9 shows an HRTEM view zooms around both interfaces. The CFO/Sc_2O_3 interface (indicated by white arrows in panel b) is abrupt and does not exhibit any trace of amorphous interfacial layer or secondary phases, while the Sc_2O_3/Si interface presents an amorphous interfacial layer of around 2.7 nm. This amorphous layer was probably formed by oxygen diffusion through the Sc_2O_3 buffer layer during the CFO deposition under 0.1 mbar oxygen pressure. Guo et al. reported the growth by PLD of ZnO on Si(111) buffered with MBE deposited Sc_2O_3film, observing that the initially SiO_x free interface was oxidized after growth of ZnO [GUO09].

The zoom around the CFO/Sc_2O_3 interface (marked by white arrows) in figure V.10.a shows the atomic matching along [111] direction. Columns of cations are well distinguished in this [1-12] zone axis picture. Dashed lines mark horizontal (111) and vertical (110) planes of CFO and Sc_2O_3. The bright spots in Sc_2O_3 correspond to Sc columns, and in the case of CFO film,

the brighter spots correspond to close Co and Fe columns with spots of lower intensity corresponding to single Fe columns. The sketch of the atomic columns is presented infigure.10.b, and the market rectangle at the lower part side of the HRTEM picture corresponds to the equivalent rectangles marked in figure V.10.a.

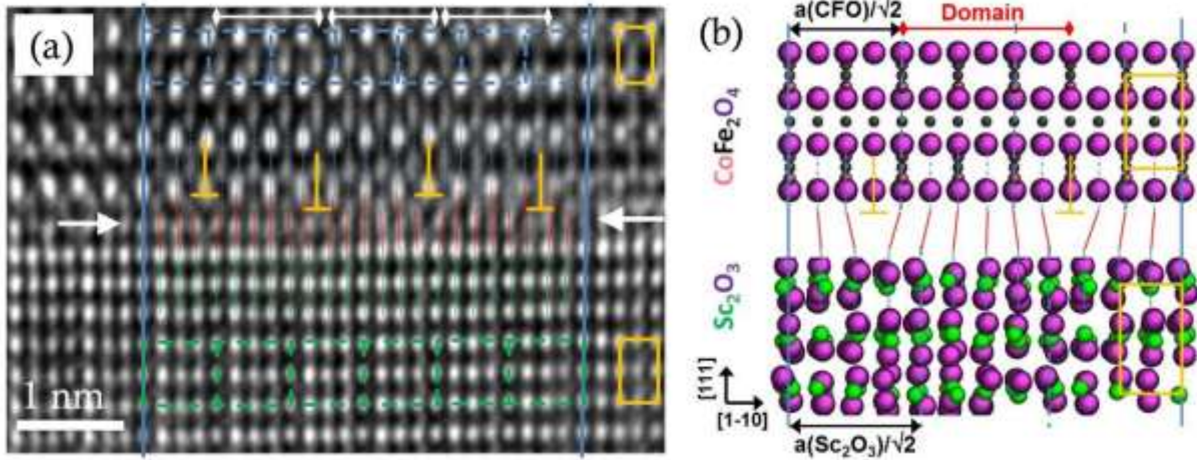

FigureV.10: HRTEM cross-sectional view along the Si[11-2] zone axis. (a) Zoom around the CFO/Sc_2O_3 interface (the zoomed area is marked in figure 8b). Dashed lines mark horizontal (111) and vertical (110) planes of CFO and Sc_2O_3. (b)Sketch of the atomic matching at the interface, including oxygen atoms. The rectangles at the right correspond to the equivalent rectangles marked in the right of panel a, and the lines ended with diamonds indicate 7/6 domains.

Detailed analysis of figure V.10.a permits to verify that the epitaxy of CFO on Sc_2O_3 occurs by domain matching. There is perfect matching of columns of cations along the solid lines drawn perpendicularly to the interface. In the indexed block delimited by two thick lines, the CFO film is separated by the 7 units marked by dashed lines, each unit being $d_{1-10}(CFO) = \frac{a_{CFO}}{\sqrt{2}}$, whereas in the Sc_2O_3 buffer they are separated by 6 equivalents units. Since there are four atomic columns in each unit cell of the respective materials, and there is a supplementary CFO unit cell with respect to Sc_2O_3 between the two lines, then there are four CFO supplementary planes along the 7/6 u.c. distance, constituting interfacial dislocations. This indicates a 7/6 DME, with m = 7(110) planes of CFO matching with n = 6(110) planes of Sc_2O_3. According to the definition introduced by Narayan and Larson [NAR03] each group of m = 7(110) planes of CFO or n = 6(110) planes of Sc_2O_3 constitutes a domain. Each domain with six atomic planes matching across the interface is shown with red lines ended with diamonds. The image shows clearly that dislocations around 9.9Å apart and composed by half CFO atomic planes, separate the domains.

The mismatch calculated for different domain configurations, presented above in table V.3, shows that the lower mismatch corresponds to m = 7 and n = 6 ($f_{m/n}$ = 0.55%), in agreement with the experimental observation. It is noted that a low percentage of 6/5 domains with a mismatch of $f_{6/5}$ = -2.2% could be present too, providing additional reduction of the strain energy. Because in figure V.10 only 7/6 domains are observed, we have analysed other zones along the interface aiming to find 6/5 domains.

Figure V.11 shows a zoom corresponding to a larger zone of the CFO/Sc_2O_3 interface and the corresponding Fourier filtered image to visualize easier the atomic planes (figure V11.b). In figure V.11.a the CFO/Sc_2O_3 interface is marked with two white arrows. Since dislocations are barely identified in the HRTEM picture, the FFT reconstruction picture is used to

emphasize the planes at the interface. Misfit dislocations are distinguished (figure V.11.b) and domains of different sizes are identified. They contain six or five consecutive $Sc_2O_3(110)$ planes as labelled on figure 11.b, and they are separated at the interface by half atomic planes of CFO (marked by the dislocation symbol ⊥). The FFT image shows three 7/6 domains but also two 6/5 domains, as expected considering the relaxed state of the films (Plastic relaxation is deduced considering the bulk value of the out-of-plane lattice parameter, measured by XRD).

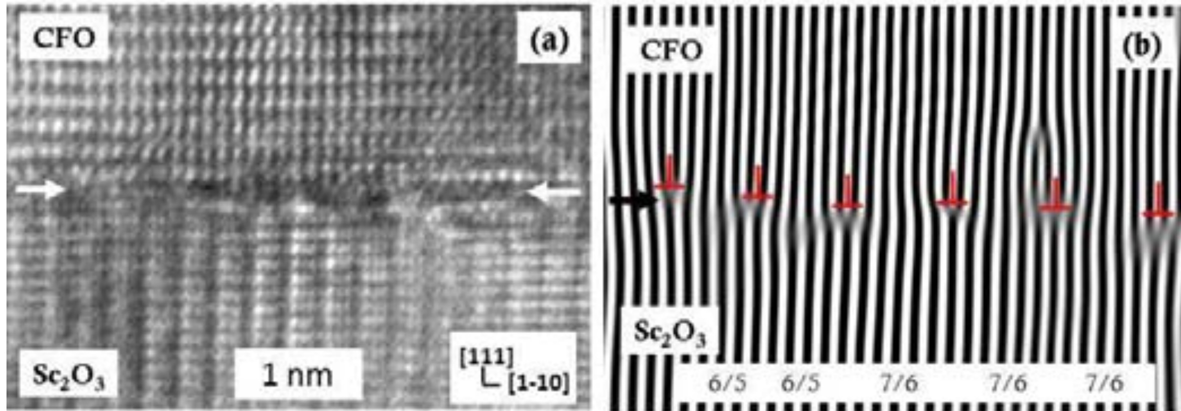

Figure V.11: (a) HRTEMof the CFO/ Sc_2O_3 interface, (b)and correspondingFast Fourier Transform (FFT)-reconstructed image. Labels at the bottom of (b) identify the 6/5 and 7/6 domains.

The edge geometry of dislocations (half extra planes of CFO) with a Burger vector $\vec{b} = \frac{1}{2}[1-10]_{Sc2O3}$ are observed in figure V.11.b. Dislocations are separated by a distance corresponding to the size of the domain. The width of the 7/6 domains is 10.4 Å (7 d_{CFO}), and the 6/5 domain are 8.8 Å wide, corresponding to 6 d_{CFO}. Then the introduction of 6/5 domains reduces the average spacing between interfacial dislocations. The average of the experimental distances between the interfacial dislocations measured is 9.8 Å, which is in perfect agreement with the theoretical spacing calculated previously (see table V.4).

V.2.5 Magnetic properties

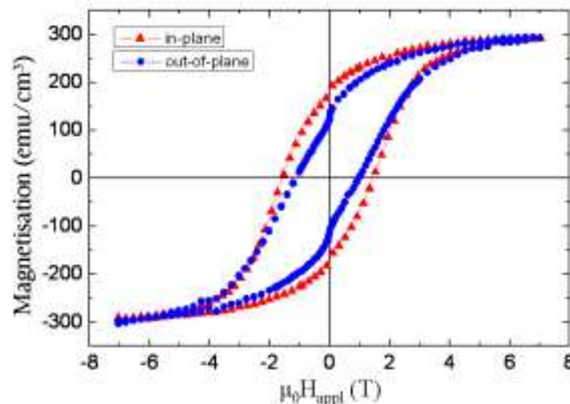

FigureV.12: Magnetization loops of the t_{CFO}=36 nm sample measured at 10k with the field applied in-plane along Si[1-10](triangles) and out-of-plane (circles).

Magnetization loops of the t = 36nm CFO film, measured at 10K, are plotted in figure V.12. Measurements were performed with the magnetic field applied in-plane along Si[1-10] (triangles) and out-of-plane (circles). The saturation magnetization of about 300 emu/cm^3 is below the bulk value (around 400 emu/cm^3), which is usual in CFO films deposited on non-spinel substrates as $SrTiO_3$(001) or MgO(001) [MA_10, YAN11]. Thus, the CFO films on Sc_2O_3/Si(111) present magnetization comparable to films on commonly used oxide single crystalline substrates. Figure V.12 also indicates that the [1-10] in-plane direction is easier magnetic axis than the out-of-plane direction, with the M_R[1-10]/M_R[111] remanences ratio around 1.4. The coercitive field when the field is applied along the in-plane direction (around 1.5T) is also higher than the out-of-plane direction (around 1T).

V.3 <u>$CoFe_2O_4$ on Y_2O_3 buffered Si(001)</u>

V.3.1 <u>Introduction</u>

The high potential of Y_2O_3 as high-k dielectric motivated its integration with silicon [KAN99, COP02, CHO02]. Yttria has a cubic bixbyite structure (figures V.1 and 2), and wide energy gap (5.1 eV) and high dielectric constant in a range of 10-18 [STE02]. The crystalline structure and electronic characteristics of Y_2O_3films are closely related to the bonding state between oxygen and yttrium atoms [CHI90-1]. The Y_2O_3 Young modulus is E_{Y2O3}= 150 Gpa, the Poisson ratio υ = 0.298 and the coefficient of thermal expansion is α=8.10^{-6}/K [IVA03, CHO97].Y_2O_3 is crystallograhically stable up to 2450°C and thermally stable with silicon up to 750°C [CHO03].

Lattice parameters of Y_2O_3 and Si are 10.604 Å and 5.431 Å, respectively. It suggests that epitaxy on silicon can occur with a matching of 1 u.c.Y_2O_3 / 2 u.c. Si, resulting in a mismatchf = -2.37%. Epitaxy has been confirmed on both Si(111) and Si(001), although only on Si(111) with the *a priori* expected cube-on-cube type epitaxial relationship. Epitaxy of Y_2O_3(111) on Si(111) was already achieved in 1989 [FUK89] by electron beam evaporation on HF etched Si(111), and on oxidised silicon [CHO01]. More recently, high quality Y_2O_3(111) films with atomically sharp interface with Si(111) were reported [NIE08]. However, these films presented coexistence of A- and B-type crystal variants (i.e., [11-2]Y_2O_3(111)//[11-2]Si(111) and [-1-12]Y_2O_3//[11-2]Si(111), respectively), being dominant the B-variant as the film increased in thickness. Single-crystalline Y_2O_3(111) films, with only presence of B-type orientation, can be obtained as demonstrated by Tarnawska et al. [TAR10]. In the case of deposition on Si(001) there is not "cube-on-cube" growth, changing the orientation of the films from Y_2O_3(111) to Y_2O_3(110) as the deposition temperature increases [CHO99]. The quality of these films is lower than the obtained on Si(111), but epitaxy of (110) oriented films was obtained by deposition at high substrate temperature on SiO_x/Si(001) [CHO97], using thus conditions similar that the used for YSZ epitaxy [chapter IV].

Epitaxy of CFO and Y_2O_3 is not evident considering lattice mismatch. The lattice parameters of CFO and $Y_2O_3$are 8.392 Å and 10.604 Å, respectively, resulting in a mismatch of -20.86%[(a_{CFO}- a_{Y2O3})/a $_{Y2O3}$)]. This excludes standard epitaxy but a mechanism of domain matching epitaxy as found in the case of Sc_2O_3 buffers can be considered. In the case of CFO on Y_2O_3 the mismatch can be reduced to -1.07% by domain matching with periodicity 5/4 (table V.3).

V.3.2 Thin film growth and in-situ characterization by RHEED

A sketch of the elaboration process is in figure V.13.Y_2O_3 thin films with different thickness (31.5, 3.0, and 1.8 nm) were grown by MBE on 4'' Si(111) wafers at IHP. Then, pieces around 10x5 mm were cut from the wafers and used to deposit CFO by PLD at ICMAB. We first describe the growth and properties of CFO (t = 26 nm) / Y2O3 (t = 31.5 nm) / Si(111) and later the fabrication of ultrathin CFO/Y_2O_3 heterostructures.

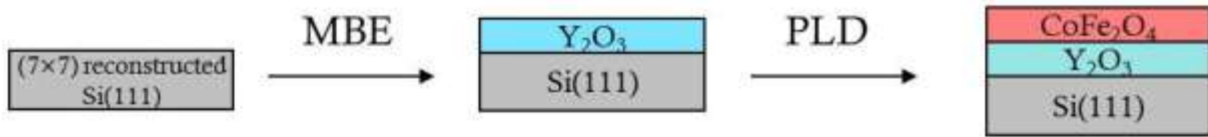

Figure V.13: Sketch of the elaboration of the CFO/Y_2O_3 thin films on Si(111).

The growth of CFO on Y_2O_3/Si(111) was carried out using similar deposition conditions that on Sc_2O_3 buffers. Deposition was under base pressure during the first 40 laser pulses (as in the case of Sc_2O_3), and then P(O_2) was fixed to ~5×10^{-4} mbar up to 500 pulses (it was 130 pulses in the case of Sc_2O_3), and then it was increased to 0.1 mbar (the total number of the pulses was 5000). The process is summarized in figure.V.14, where we include RHEED patterns of the Y_2O_3 surface and the CFO surface at several growth stages.

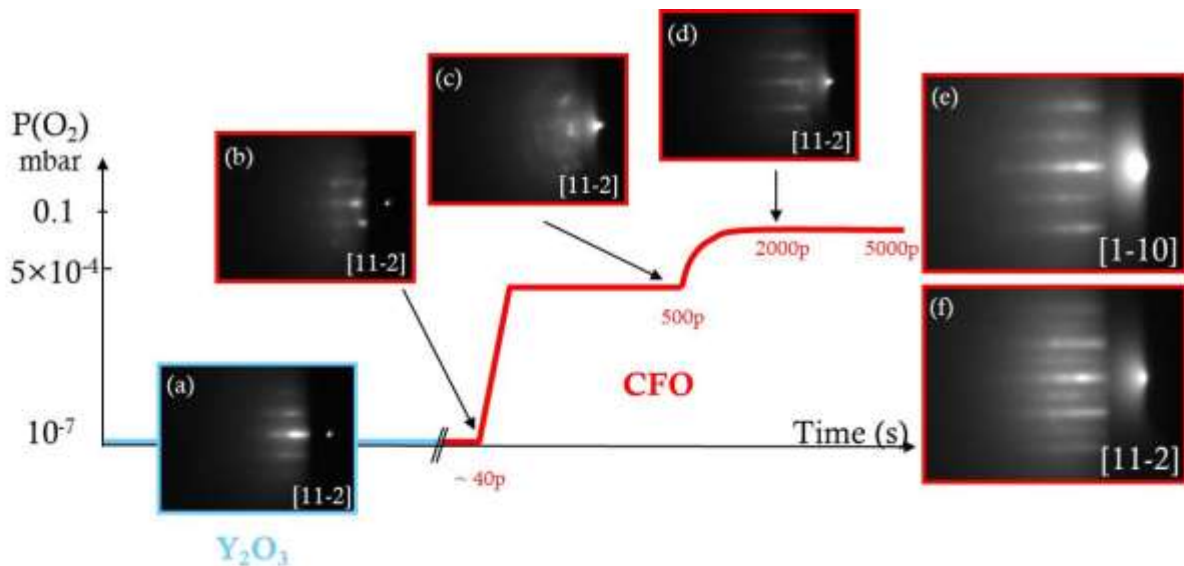

Figure V.14: RHEED patterns along [11-2]Si taken with an angle of 1.2°. (a) Y_2O_3 surface, (b) after 40p (t~ 0.24 nm) under vacuum, (c) after 500p (t ~ 2.6 nm) under low oxygen pressure, (d) after 2000p (t~10.4 nm) under 0.1 mbar. Patterns at the end of the deposition (5000p, t~ 26.0 nm) taken with an angle of 2°along $[1\text{-}10]_{Si}$(c) and $[11\text{-}2]_{Si}$ (f).

The streaks in the RHEED pattern along [11-2]Si(figure V.14.a) attest the epitaxy and flatness of Y_2O_3. The pattern changes quickly when CFO starts to grow. The rings and the diffuse halo appearing at the first stage of the CFO growth under vacuum (figure V.14.b) indicate low crystallinity. After increasing the oxygen pressureto 0.1 mbar, the streaky CFO pattern (figure V.14.d taken at 2000 p) attests an improved crystallinity.
Observing the RHEED patterns at the end of the CFO growth, it can be seen that streaks with characteristic spacing are found along [11-2]Si and [1-10]Si direction (figure V.14.e and f), attesting epitaxy of the film in spite of the large lattice mismatch with the bottom Y_2O_3 layer. In this pattern, the modulation of the intensity along the streaks (q_z direction) likely signals certain film roughness.

V.3.3 **AFM and XRD of $CoFe_2O_4$ and Y_2O_3 films on Si(111)**

The surface morphology of the Y_2O_3buffer and CFO film was analysed by AFM in dynamic mode. The topographic images of scanned 5×5 μm^2areas are presented in figure V.15 (a) and (b), respectively. Figure V.15.a shows a flat Y_2O_3 surface with the presence of bright spots likely resulting of the contamination due to exposure with ambient air. Figure V.15.b shows that the CFO film has homogeneous and quite flat surface (z scale is 3 nm). Morphology is granular, with grains that have a small lateral size of around 60 nm. Due to the small grain size, AFM tip size effects are important. The root-mean square (rms) roughness corresponding to the 1 ×1 μm^2 image (not shown here) is 4.3 Å. The moderately low roughness of the film surface is consistent with the RHEED patterns presented above in figures V.14.e and f, which were streaky instead display Bragg spots along Laue circles.

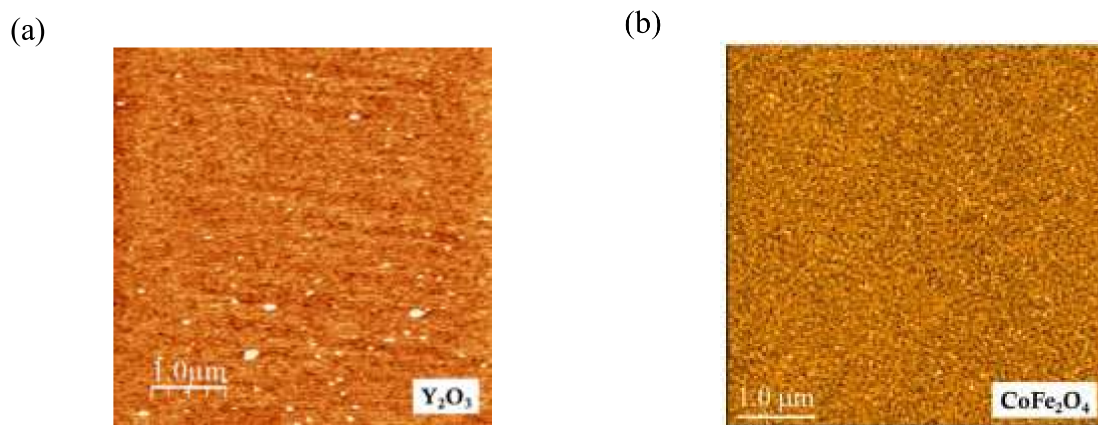

Figure V.15: AFM topographic images (5×5 μm^2) of (a) the Y_2O_3(t=31.5nm)buffer and (b) of the CFO(t=26nm) film.

The bilayer was characterized by XRD θ-2θ scans around symmetrical reflections, and Φ-scans were measured around asymmetrical reflections in order to determine the epitaxial relationships and the eventual presence of crystal variants. Figure V.16.a presents the symmetrical θ-2θ scan. The CFO, Y_2O_3, and Si diffraction peaks correspond to (111) reflections, indicating that both CFO and Y_2O_3 films are (111) oriented along the out-of-plane direction. There are also five narrow peaks, marked with asterisks that cannot be indexed as reflections from CFO, Y_2O_3 or Si. Their positions at 38.1°, 44, 3°, 64,4°, 77,4° and 81.1° as well as their relative intensity indicate that correspond to Ag (silver paste was used to glue the substrates to the heater and it remains on the sides of the substrates where it is not properly removed). Therefore, the CFO/Y_2O_3/Si(111) heterostructure only shows (lll) reflections from CFO, Y_2O_3, and Si, with absence of spurious crystalline phases.

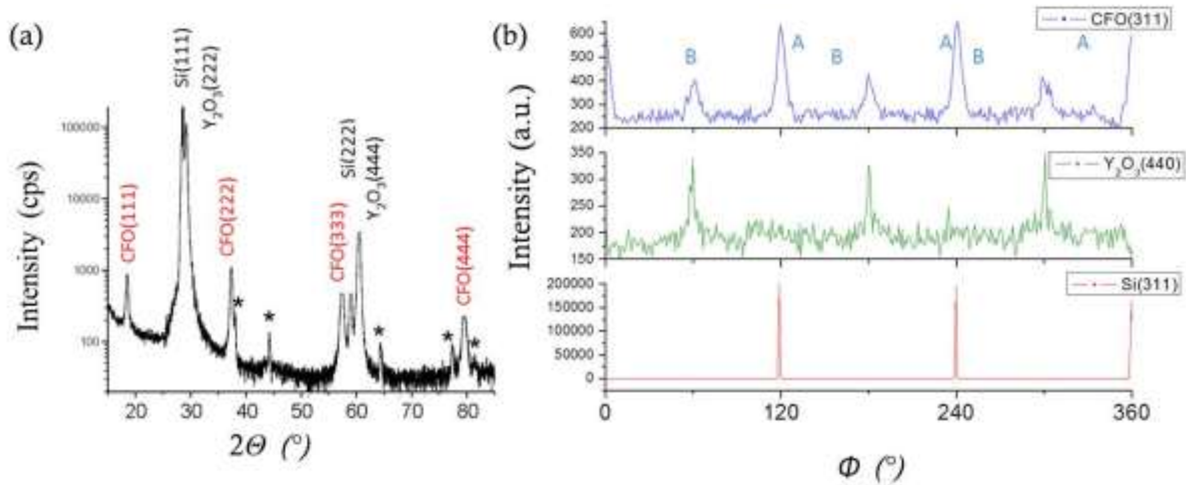

Figure V.16: XRD θ-2θ scan of symmetrical reflections (a) and Φ-scan around CFO(311), $Y_2O_3(311)$ and Si(311) reflections (b) of the CFO (t=26.0 nm)/Y_2O_3(t=31.5 nm) /Si(111) sample.

The out-of-plane lattice parameters of Y_2O_3 and CFO have been determined from the angular position of $Y_2O_3(222)$ and CFO(333) peaks, using as a reference the positions of the Si(111) and Si(222) peaks, respectively. We obtain d[Y_2O_3 (111)] = 6.126 Å+/-0.002 Åand d[CFO(111)] = 4.848 Å+/-0.004 Å. Comparing these experimental values with bulk ones d[Y_2O_3(111)] = 6.122 Å and d[CFO(111)] = 4.845 Å, it can be seen that lattice parameters have, bulk values signaling that both films are relaxed.

The Φ-scans around (311) for CFO, Y_2O_3, and silicon reflections are presented in figure V.16.b. The Φ-scan around CFO(311) reflections confirms epitaxial growth, with two sets of sharp peaks with three-fold symmetry indicating coexistence of A- and B-type in-plane crystal variants (peaks are labelled in the figure). The set with higher intensity has the same in-plane orientation than Si and is usually known as A-type orientation. The smaller intensity peaks 60° apart from the former set correspond to the same crystal structure of CFO, but rotated 180° in the plane, and is usually known as B-type orientation. Considering the intensity of both sets of peaks to roughly estimate the fraction population of the domains, we obtain 62.5% and 37.5% respectively.

The Φ-scans around Y_2O_3(311) presents a single B-type variant set of peaks with three fold symmetry confirming the epitaxial growth. This is in agreement with other samples fabricated at IHP [TAR10], and by other groups [NIE08, LIU10].Thus, the epitaxial relationships of the A and B type CFO crystal variants respect Y_2O_3 and Si correspond respectively to: [11-2]$CoFe_2O_4$(111)// [-1-12]Y_2O_3 (111) // [11-2]Si(111), and [-1-12]$CoFe_2O_4$(111)//[11-2]Y_2O_3 (111) //[11-2]Si(111).The top view schematic illustration of the matching of CFO(111) with A- and B-type variants on Y_2O_3(111) is identical to the one presented in figure V.16.c for CFO on Sc_2O_3. The majority of the CFO A-type variant on Y_2O_3 buffer contrasts with the previous observation of close fractions of variants or slight majority of B-type in CFO on Sc_2O_3 buffer, and the clear minority or absence of A-variant when CFO grows on $SrTiO_3$(111) substrates [YAN08, DIX09].

V.3.4 HRTEM characterization

The low resolution TEM picture (figure V.17.a) shows clear contrast between CFO and Y_2O_3 layers and Si substrate with strong brightness at the Y_2O_3/Si interface. The thickness of the CFO and Y_2O_3 layers are 26.0 and 31.5 nm, respectively. A HRTEM picture is presented infigure V.17.b. The crystalline order of both layers is evident in all the imaged region. The interfaces are abrupt and remarkably the Y_2O_3/Si(111) interface does not exhibit an interfacial layer. Then, the HRTEM picture confirms that the brightness at the interface observed in low resolution (figure V.17.a) is not caused by an amorphous interfacial layer. The origin of this interfacial contrast is discussed in chapter II, but what is critical to notice is that the characterization of the interface has to be done imperatively in high resolution. The Y_2O_3/Si and $CoFe_2O_4$/Y_2O_3 interfaces are studied in detail below, with FFT and geometrical phase analysis performed around both interfaces.

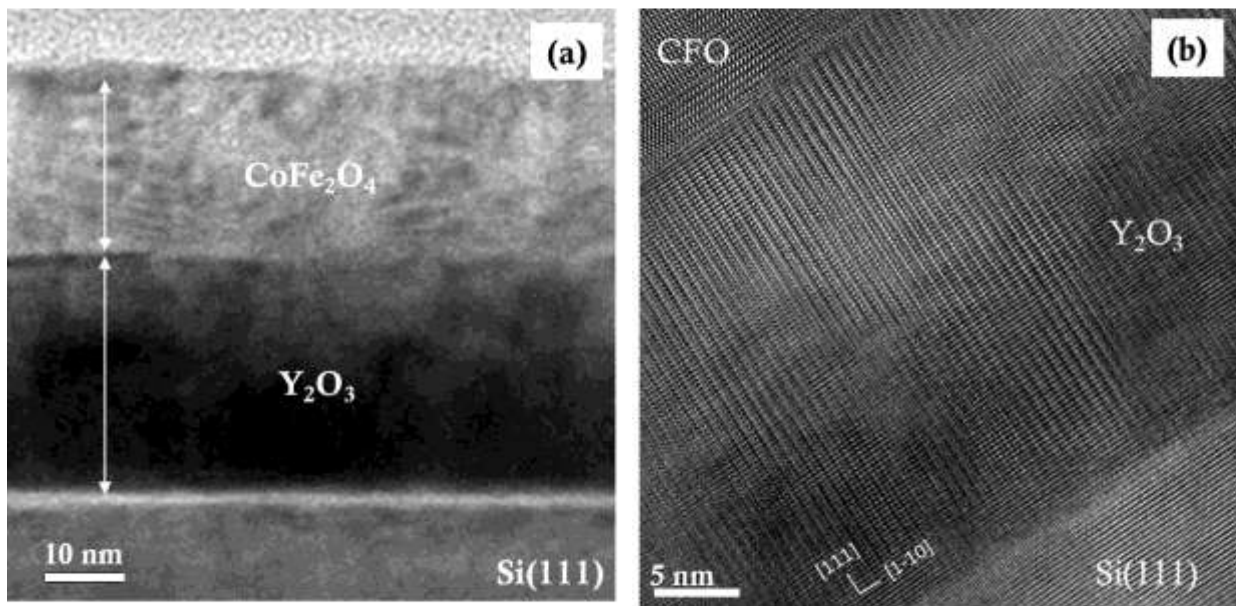

FigureV.17: (a) LR and (b) HRTEM cross-sectional views along the Si[11-2] zone axis of the CFO (t = 26 nm)/ Y_2O_3 (t=31.5 nm)/ Si(111) sample.

III.4.1 $CoFe_2O_4$/Y_2O_3 interface

Figure V.17.b confirms the epitaxial growth of CFO on Y_2O_3 in spiteof the large lattice mismatch of -20.86%. In figure V.18 we present a HRTEM image around the CFO/Y_2O_3 interface (marked by arrows). The picture evidences the homogeneity and high structural quality of the epitaxial CFO/Y_2O_3 heterostructure. The interface is abrupt and does not exhibit any sign of chemical interaction. The FFT pattern in the inset shows a well-defined rectangular array of spots reflecting the epitaxy of the oxide layers. The rectangular shape of the array reflects the larger spacing between atoms columns along the out-of-plane direction than along the in-plane direction.

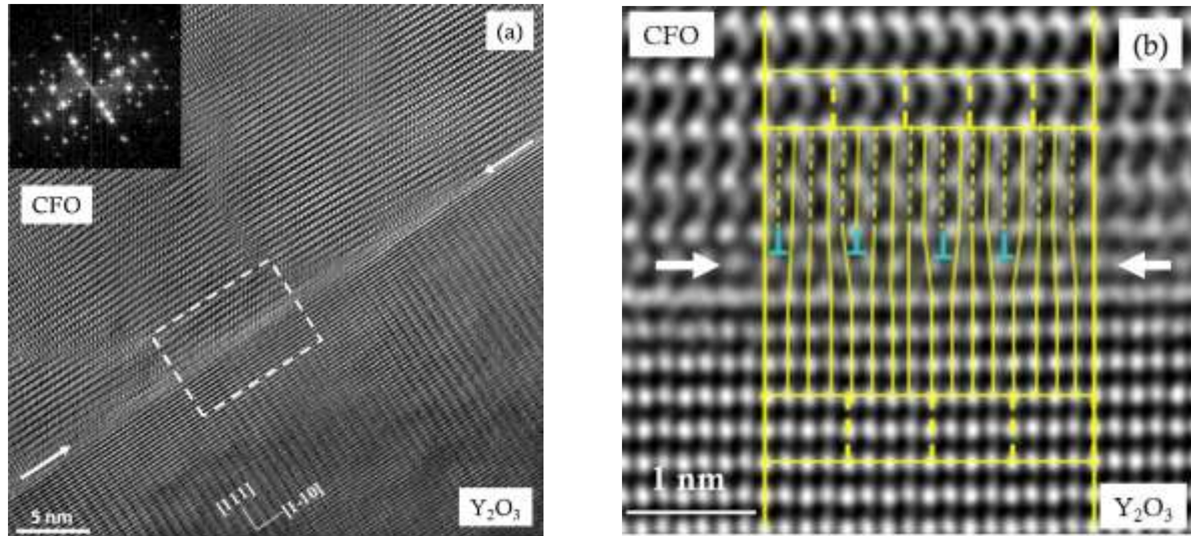

FigureV.18: (a) HREM cross-sectional view of $CoFe_2O_4$ / Y_2O_3 interface with the corresponding FFT in the inset. The marked region is zoomed in (b). Some dislocations can be appreciated, separating 5/4 domains.

The region around the interface marked with the dashed line is zoomed in figure V.18.b. The Fe atomic planes intercalated between the Fe-Co planes are not well observed here, differently from the HRTEM picture of the CFO film integrated on Sc_2O_3(figure V.10).In the zoom, yellow lines are drawn to visualize better the matching between CFO and Y_2O_3. It is seen that along the in-plane [1-10] direction, five CFO units, each $a_{CFO}/\sqrt{2}$ long, match with four Y_2O_3 units ($a_{Y2O3}/\sqrt{2}$ long). This matching gives to the lowest mismatch of -1.07% ($f_{r5/4}=(5d_{CFO}-4d_{Y2O3})/4d_{Y2O3}$). Since five CFO units match with four Y_2O_3 units and a CFO unit contains four atomic planes, there are four dislocations, marked with the symbol ⊥, formed by half extra plane of CFO. Then, in this zone of the interface, domains contains 5CFO (110) planes matching with $4Y_2O_3$ (110) planes; i.e. a 5/4 DMEbetween CFO and Y_2O_3, with a residual mismatch of -1.07%.

In order to investigate the eventual presence of other domains, in particular 4/3, a larger area of the CFO/Y_2O_3 interface was analysed. Figure V.19 shows the HRTEMpicture and the corresponding FFT-image reconstruction done to emphasize the planar arrangement and visualize easier dislocations along the interface.Figure V.19.b shows clearly dislocations formed by CFO extra half-planes, separating domains of varied size. The marked symbol ⊥ shows the edge geometry of dislocations with a Burger vector $\vec{b} = \frac{1}{2}[1\bar{1}0]_{Y2O3}$ as observed previously in figure V.11.b. Labels in the bottom of figure V.19.b indicate the values of each domain i.e. 5/4, 4/3, etc.

The most frequent domain contains four Y_2O_3 atomic planes continuous through the interface, and some others contain three atomic planes, indicating the majority of 5/4 domains over 4/3 ones. The percentage of 5/4 domains is higher than 75% in the region investigated, which is close to the 80% predicted (table V.4). This slight difference could be due to the low statistical data, but it has to be noted the presence of a 3/2 domain, which strongly compensates the compressive stress affecting the 5/4 domains. Domains extend to a low number of planes and thus their size is very small. The size of m/n domains is $n \times \frac{a_{Y2O3}}{4\sqrt{2}}$. Thus, 5/4, 4/3 and 3/2 domains extend along 7.5Å, 5.6Å, and 3.8Å respectively. These values agree well with the distance between dislocations which ranges from 3.0Å to 7.5Å (figure V.19.b).

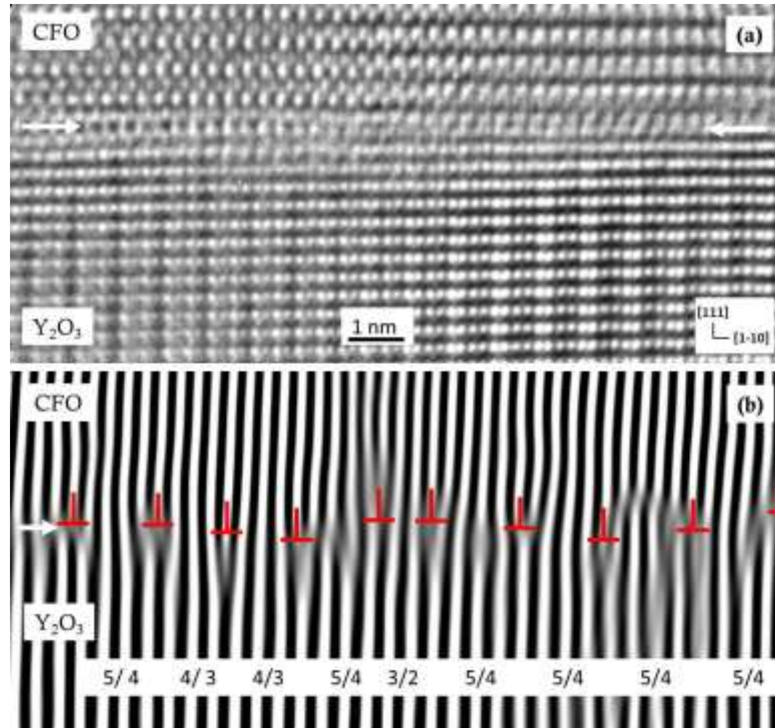

Figure V.19: (a) HRTEM image, and (b) reconstructed Fourier filtered image from the reflections corresponding to the in-plane periodicity of atomic planes, evidencingdislocations. Labels in the bottom of (b) indicates the sizes of each m/n domain (m=n+1).

V.3.4.2 Y_2O_3/Si interface

A HRTEM cross-section image of a region around the Y_2O_3/Si(111) interface is presented in figure V.20. The complete absence of SiO_x at the interface is highly remarkable. The number of crystalline oxides that can present atomically sharp interface with Si is low, and in most of the cases the interface is unstable under the conditions required for epitaxial growth of complex oxides as CFO. Figure V.20 demonstrates that Y_2O_3 (at least for a thickness t> 30 nm) presents atomically sharp interface with Si(111) after epitaxial growth of CFO.

In figure V.20 the crystalline planes in the Y_2O_3 film and the Si substrate are evident. The FFT in the inset where the brighter spots form a rectangular lattice is in agreement. The longer side parallel to the interface reflects the larger interplanar distance along the out-of-plane than along the [1-10] in-plane direction in both Si(111) and Y_2O_3(111). The additional three satellite peaks between the brighter spots along [1-10] are caused by the modulation of intensity between Y_2O_3 (110) planes.

Observation of the interface reveals minoritary regions presenting a certain disorder, but in general the crystalline order is very high with obvious coherence between atomic planes of substrate and film (see in figure V.20.b the zoom of the region marked with the dashed line). The drawn rectangles in figure V.20.b, one in the Y_2O_3 and two in the Si, are $d[1\text{-}10]=a/\sqrt{2}$ wide and $d[111]=a/\sqrt{3}$ high. They reflect the accommodation of one unit cell of Y_2O_3 on two units cells of Si. Since a_{Y2O3} is 10.604 Å and a_{Si} is 5.431Å, the mismatch is reduced to -2.37% ($1Y_2O_3$/ 2Si: -2.37%).

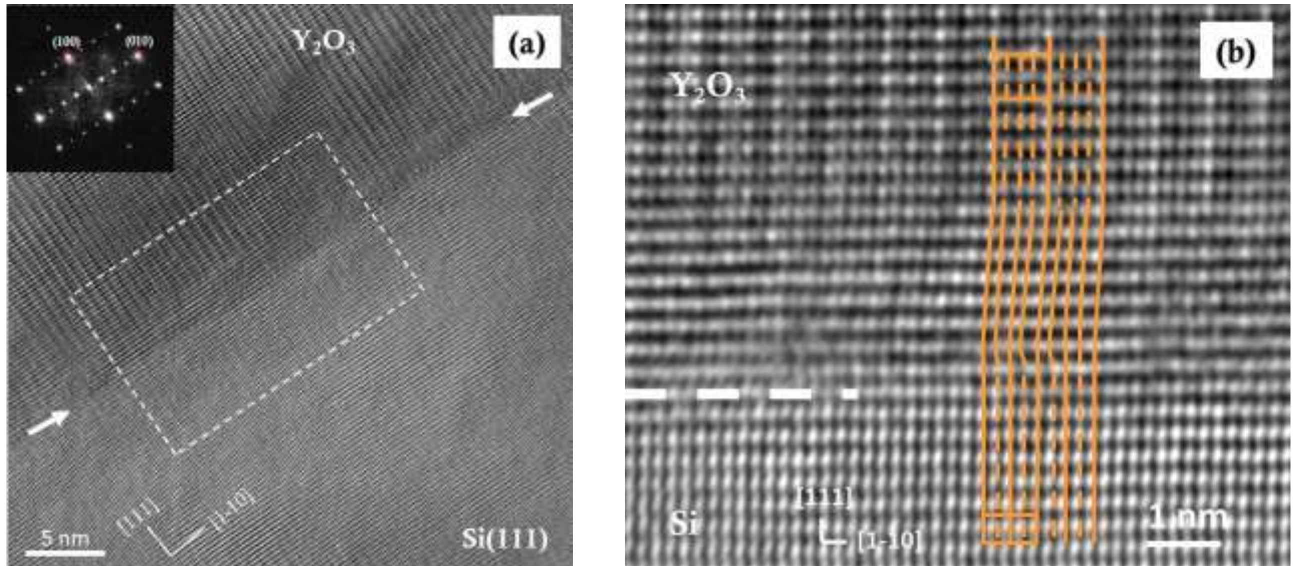

Figure V.20: (a) HRTEM cross-sectional view of the Y_2O_3/Si interface. The inset shows the corresponding FFT – image. (b) Zoom of the region marked in (a).

The vertical lines in figure V.20.b evidence the coherence of the interface. To detect misfit dislocations and to determine the strain of the film respect to the Si substrate, the GPA method, which measures local displacements and strain fields from the experimental HRTEM image, is very useful. Figure V.21 shows the in-plane strain map of the interfacial region shown in figure V.20.a, determined relatively to a reference zone on the silicon substrate. It indicates an homogeneous strain around -2.4% which corresponds to fully relaxation of Y_2O_3. Also, some interfacial dislocations shown by local deformation fields are well visualized, confirming the plastic relaxation of Y_2O_3.

(a)

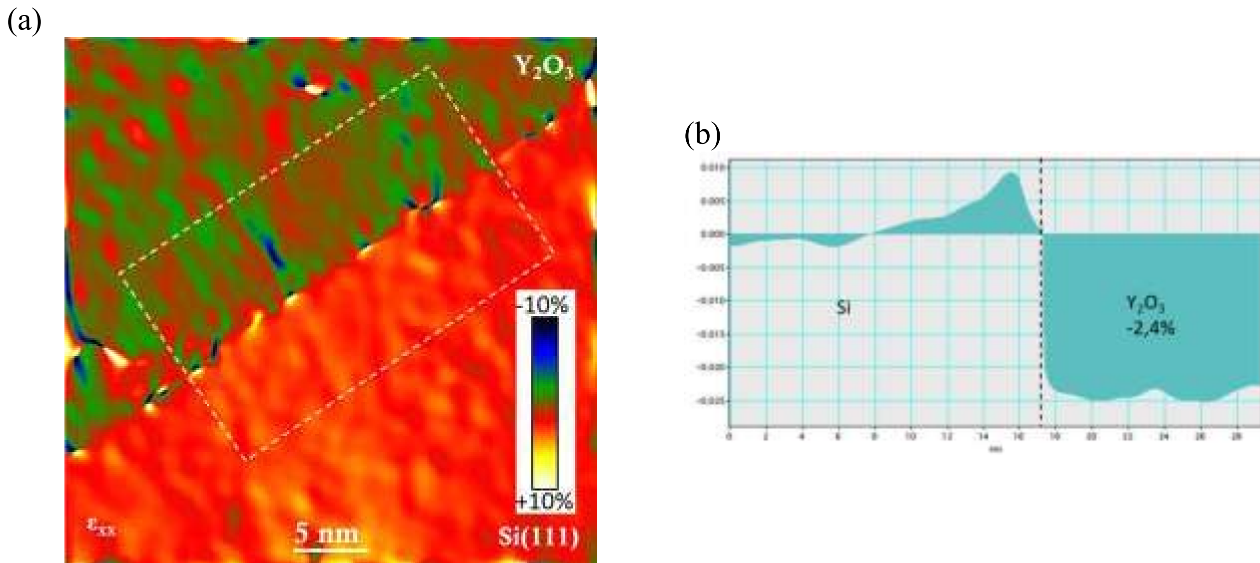

Figure 21: (a) In-plane strain map of the region shown in figure V.20.a.(b) Strain profile across the interface, obtained by averaging over the width of the marked rectangular region.

For completitude, we compare in figure V.22 the use of the GPA method and the Fourier filtered reconstruction of the HRTEM picture to visualize dislocations. The TEM image is a zoom from figure V.20, and the corresponding GPA and FFT-reconstructed images are in the

bottom panels, with the interface position indicated by white arrows. Some defective areas in the interface create contrast in the strain image, as well as distortions in the FFT image. However, the GPA image clearly shows the positions of misfit dislocations by a characteristic deformation at the interface with a symmetric double lobe shape. The FFT-reconstructed image shows the in-plane periodicity and confirms the presence of the dislocations (supplementary half-planes of Y_2O_3) detected in the deformation map.

Since the in-plane strain determined from figure V. 21 indicates fully relaxation we can verify if the experimental separation between dislocations is in agreement with the theoretical. The distance between the dislocations in a semi-coherent interface can be calculated from the in-plane interplanar distance of Y_2O_3 (d_{Y2O3}) and silicon (d_{Si}) with the formula $D= (d_{Y2O3}\times d_{Si})/|d_{Y2O3}-d_{Si}|$, where d_{Y2O3} and d_{Si} are the corresponding interplanar spacing of Y_2O_3 and Si along the interface. The spacing corresponding to a quarter of the distance between (110) planes for Y_2O_3, and to the half of the distance between (110) planes for silicon, are d_A= 1.874 Å and d_B=1.920 Å, respectively. Then the separation between dislocations in case of full relaxation is D_{Th}=7.9 nm. This value agrees perfectly with the determined experimentally.

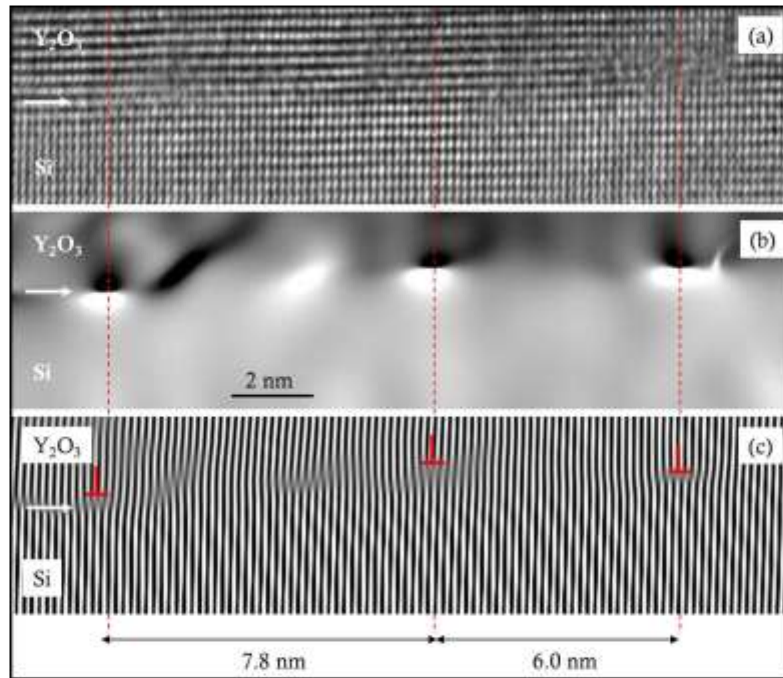

FigureV.22: (a)HRTEM image, corresponding in-plane strain map (b), and filtered image (c).

The separation between misfit dislocations in figure V.22 is not homogeneous. To evaluate the inhomogeneity a larger interfacial zone was analysed. Figure V.23 shows large coherence zones of around 10 nm, coexisting with other where dislocations are very close (even only 1.3 nm apart). In average the spacing between dislocations is around 7 nm.

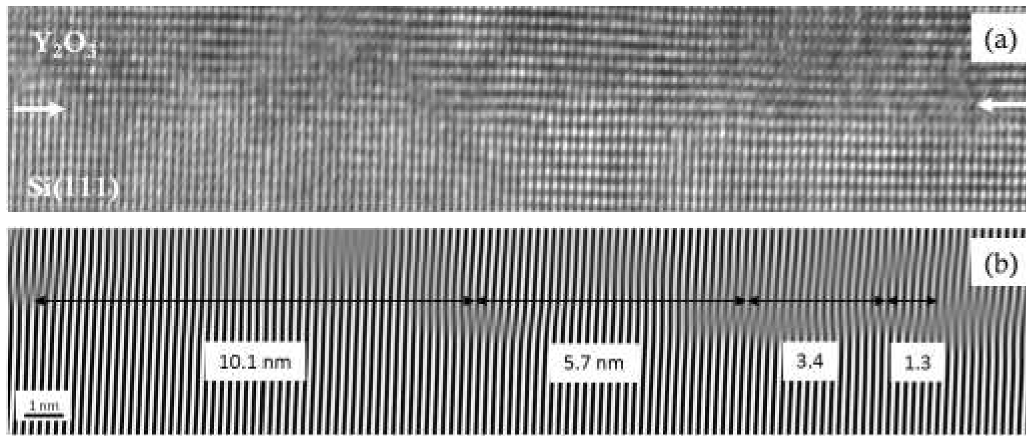

Figure V.23: (a)HRTEM image and,(b) reconstructed Fourier filtered picture.

V.3.5 <u>Magnetic properties</u>

The magnetization loop of the 26 nm CFO film measured at 10K is plotted in figure V.24. Measurement was performed with the magnetic field applied in-plane, along the [1-10] direction. The coercitive field is lower than 1T, and the saturation magnetisation of 273 ±10 emu/cm^3, which is below the bulk value (400 emu/cm^3). Similar reduced values are common in CFO films deposited on non-spinel substrates [MA_10, YAN11, SAN11]. On the other hand, the loop shows an evident shrinking at low field. This type of loop is very usual in spinel films, and it has been demonstrated recently that superposition of magnetic response from the bulk and surface islands causes shrinking [RIG09]. Thus, CFO films on Y_2O_3 buffered silicon present magnetisation comparable with films on common perovskite oxide single crystalline substrates, and to films on silicon buffered with scandium oxide (cubic bixbyite structure as Y_2O_3).

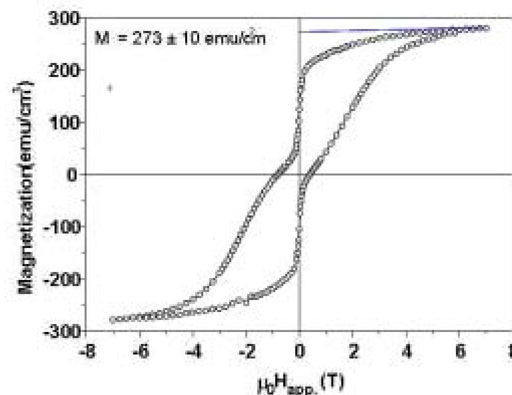

FigureV.24: Magnetisation loop of the t= 26 nm CFO film onY_2O_3/Si(111,) measured along the [1-10]direction at 10K.

V.3.6 <u>Ultrathin films of $CoFe_2O_4$ and Y_2O_3 on Si(111)</u>

The atomically sharp interface between Y_2O_3 and Si(111) in the $CoFe_2O_4/Y_2O_3$/Si(111) sample is an outstanding result that makes this heterostructure candidate for spin filter devices. The spin filter requires a CFO/buffer bilayer extremely thin to permit tunnel current, and the increase in thickness by the eventual presence of an

amorphous interfacial layer could do the heterostructure useless for tunnelling. To assess the potential of $CoFe_2O_4/Y_2O_3$/Si(111) for spin filter devices we prepared a series of samples to investigate: i) the epitaxy of CFO on ultrathin Y_2O_3 buffers; and ii) the stability of the interface between Si(111) and ultrathin CFO/Y_2O_3 bilayers.Two Y_2O_3/Si(111) wafers were prepared by IHP with Y_2O_3 thickness of 1.8 and 3.0 nm. On pieces of each of these wafers we prepared at ICMAB two series of samples depositing CFO films with thickness 46 nm, 23 nm, 2.2 nm and 1.5 nm.

We have to note that CFO/Y_2O_3 samples are not fabricated in a single process, but combining MBE at IHP and PLD at ICMAB. This can be a critical limitation since ultrathin oxide layers could be unstable under atmospheric conditions. Thus we first characterized the ultrathin Y_2O_3 by AFM at ICMAB; the measurement done several days after deposition at IHP. Figure 25shows the topographic 1×1 μm^2 images of the t = 1.8 nm (a) and t = 3 nm (b) film. Both samples present low roughness, with rms values of 2.3 Å and 2.9 Å, for the t = 1.8 nm and the t = 3.0 nm films respectively. Morphology shows grains with small and homogeneous lateral size around 30 nm in the t = 3.0 nm sample, that could correspond to two-dimensional islands. The relevant observation is that pinholes that could be formed by local oxidation of Si(111) are not observed within the lateral resolution of AFM detecting pits.

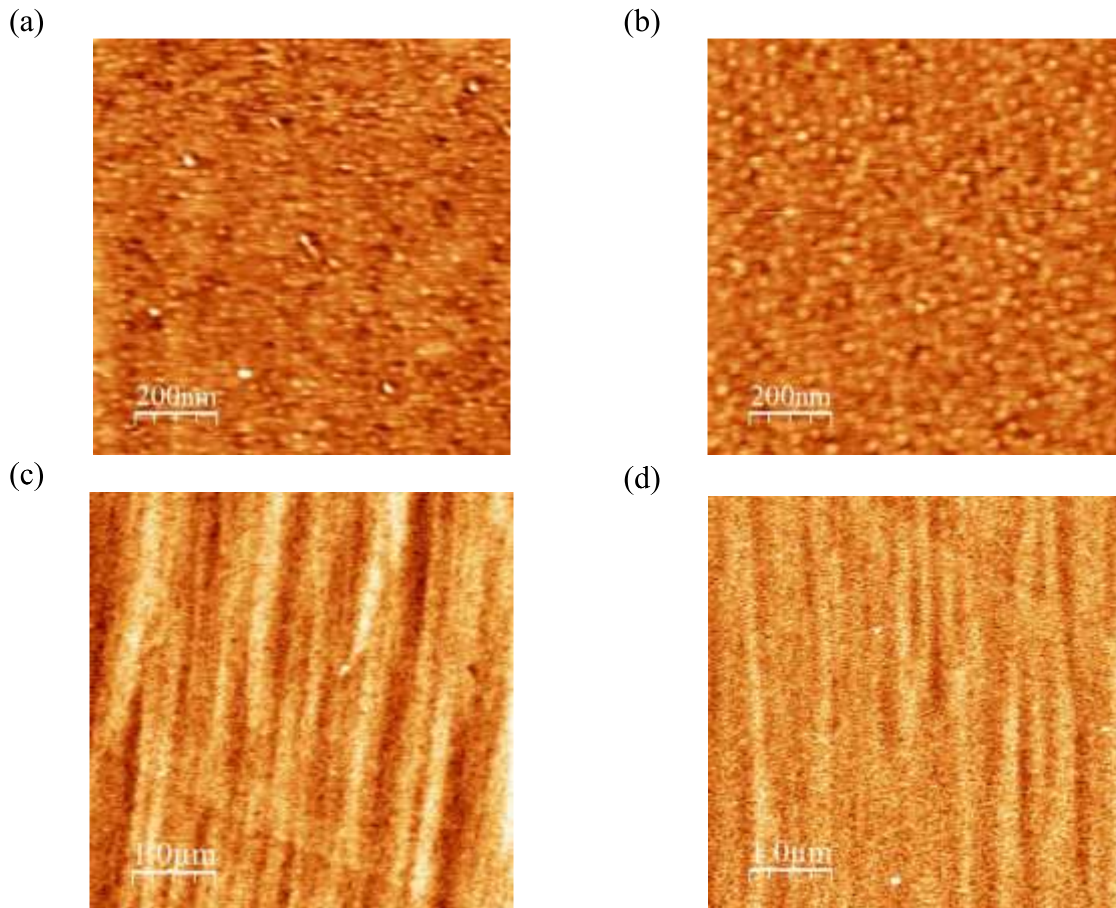

Figure V.25: AFM topographic images (1×1 μm^2) of Y_2O_3 buffer with thickness: t=1.8 nm (a) and 3.0 nm (b); and (5×5 μm^2) of the CFO film with thicknesses: t = 2 nm and 46 nm.

The CFO films were grown in 2-3 days after receiving the wafers form IHP. Relatively thick CFO films were deposited to confirm that crystalline growth is not degraded by the ultrathin thickness of the buffers. Figure 26 shows XRD θ-2θ scans the CFO films 23 and 46 nm thick on both ultrathin Y_2O_3 buffers. In addition of substrate peaks, only CFO (lll) reflections are evident. This confirms (lll) texture with no apparent differences respect the use of thick Y_2O_3 buffers. We note that all reflections (from film and substrate) are of lower intensity than in the scan corresponding to CFO on thick Y_2O_3 (figure V.16), but this is because diffractometers with different X-ray power were used. Scans in figure 26 were measured using the same power and the intensity of the CFO reflections scales with CFO thickness, andremarkably there are not significant differences in peak intensity depending on the Y_2O_3 thickness. To detect a possible influence on mosaicity, ω-scans (rocking curves) around CFO(222) were measured. The curves are plotted at the right of the corresponding θ-2θ scan, and the full-width at half-maximum (FWHM) is indicated. The FWHM values are in the 1.8 – 2.7º range, being the curves broader for the thinner Y_2O_3 buffer (for the same CFO thickness) and for the thinner CFO film (for the same Y_2O_3 thickness).

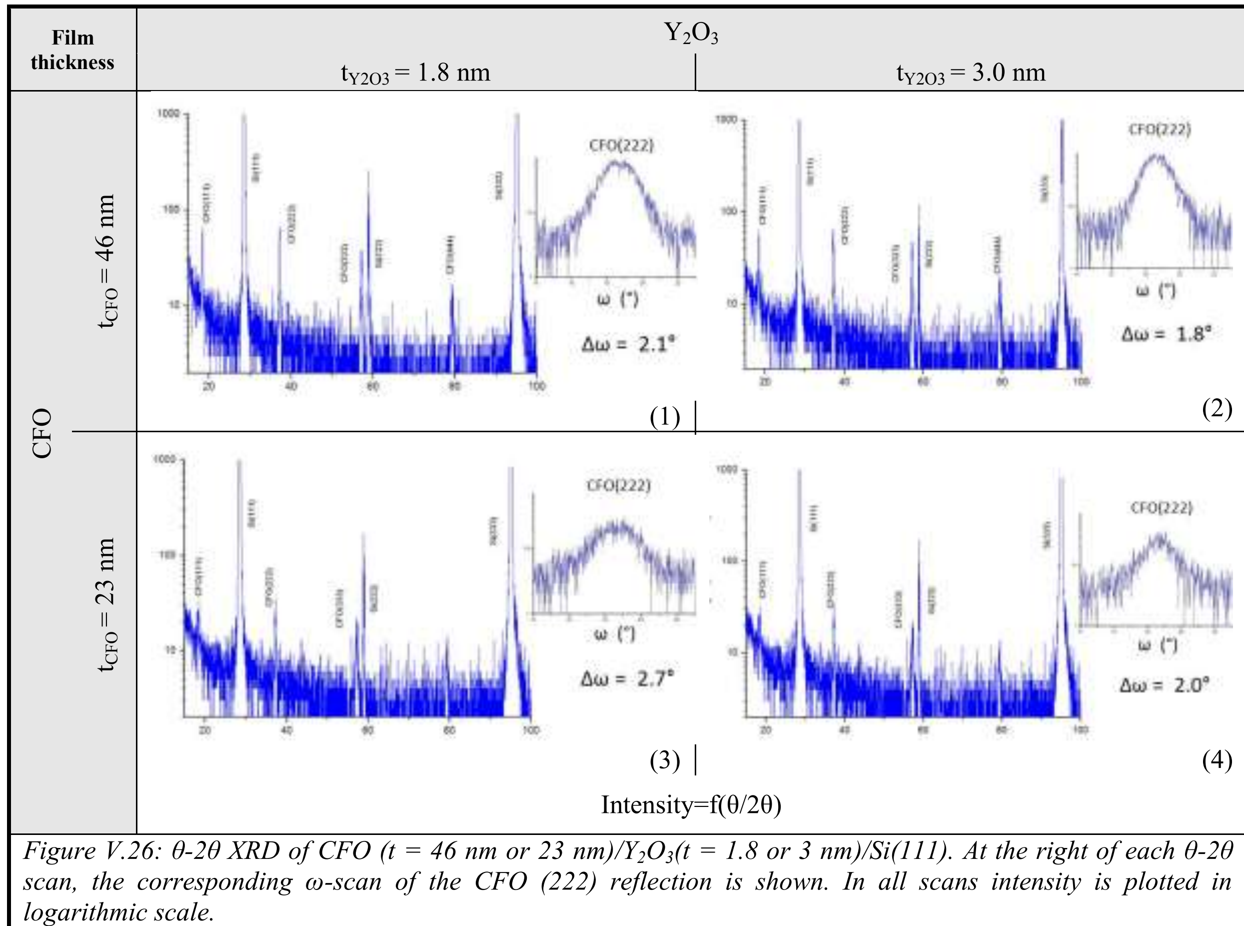

Figure V.26: θ-2θ XRD of CFO (t = 46 nm or 23 nm)/Y_2O_3(t = 1.8 or 3 nm)/Si(111). At the right of each θ-2θ scan, the corresponding ω-scan of the CFO (222) reflection is shown. In all scans intensity is plotted in logarithmic scale.

The eight samples of the series were characterized by AFM. All samples are very flat, with rms roughness in the 0.1 – 0.3 nm range, and with tendency to show granular-like morphology increasing CFO thickness. This is illustrated in the topographic images of the CFO films 46 and 1.5 nm thick grown on the 1.8 nm thick Y_2O_3 buffers shown in figure V.25. To compare the different samples we have plotted the rms values, calculated from 1x1 μm^2 scans, as a function of the CFO thickness (figure V.27). There is tendency to increase roughness with thickness, although rms is very low in all samples. It is noticeable that CFO

films on the thinnest Y_2O_3 buffers are not rougher, and indeed these samples are in general slightly flatter than the corresponding on the thicker buffer.

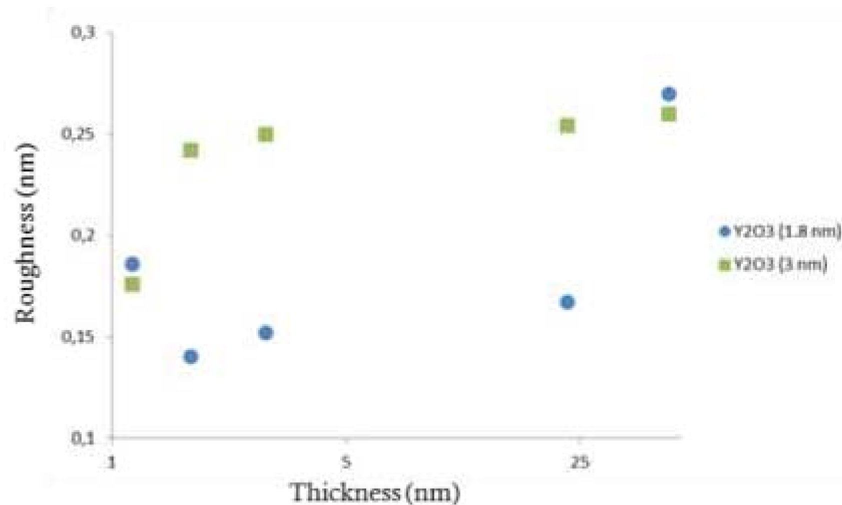

Figure V.27:Roughness (rms) of CFO filmsas a function of CFO thickness, and deposited on Y_2O_3buffers with thickness t= 1.8 or 3 nm. Data corresponding to the bare buffers are also indicated.

The ultrathin bilayers (the four samples having CFO thickness 2.2 or 1.5 nm) were characterized by HRTEM(in cross-section view). The sample preparation was challenging, as the crystalline structure of the materials was generally damaged by the process. For this reason, different preparation techniques were tried. In particular, a specimen was prepared with ion milling under cooling conditions (figure V.28.2), and other with bevel polishing without ion milling (figure V.28.4). Moreover, in other specimen prepared after deposition of a platinum protective layer,the interfacial layer was also present (figure II.21.4 of chapter II). More information and comparison of the different preparation techniques is detailed in Chap II.5.3.B.

Film thickness (nm)		Y_2O_3	
		t_{Y2O3} = 1.8 nm	t_{Y2O3} = 3 nm
CFO	t_{CFO} = 2.2 nm	(1)	(2)
	t_{CFO} = 1.5 nm	(3)	(4)

Figure V.28: HRTEM pictures (zone axis [11-2])of the ultrathin CFO/Y_2O_3samples.

In the four samples both CFO and Y_2O_3 layers, highly homogeneous in thickness, are perfectly observed. An amorphous interfacial layer (AIL) is present at the Y_2O_3/Si interface in all samples. It is noticeable that it is around 2.4 nm thick irrespective of the thickness of Y_2O_3 or CFO. We remark the absence of AIL when Y_2O_3 is not ultrathin, which implies that it has to be formed either from ambient exposure after growth at IHP, during CFO deposition, or by damage during cross section TEM specimen preparation. Considering the two first possibilities we would expect that AIL thickness dependent at least of Y_2O_3 thickness. We note also that CFO is heavily damaged during cross-section preparation (it appears mostly amorphous, whereas crystalline growth of CFO on ultrathin buffers is confirmed by XRD). These facts strongly signal that AIL can be formed by sample preparation. However, the AIL thickness is constant along the interfaces, whereas thickness variations are expected in case of amorphisation during preparation. Furthermore, the sample labelled (4) was totally prepared by mechanical methods (using tripod with the wedge technique) without ion-milling, which is the most critical step to cause amorphisation. Thus, in spite of the analysis of several samples and multiple cross-section specimens we cannot conclude if the ultrathin films were unstable during transport, during CFO growth, or damaged during TEM cross-section preparation.

V.4 Summary

We have demonstrated that spinel ferromagnetic CFO can be integrated with Si(111) using bixbyite A_2O_3 (A = Sc or Y) buffer layers. CFO grows epitaxially in spite of the huge lattice mismatch of around 15% (with Sc_2O_3) and 20% (with Y_2O_3). It occurs by the mechanism of domain matching epitaxy, and suggests opportunities of integration of other functional oxides with silicon by using highly mismatched buffer layers.

CFO films have single out-of-plane orientation and they are epitaxial, although with coexistence of A- and B- type crystal variants. The films are very flat, with rms roughness below 0.4 nm. They are ferromagnetic, with saturation magnetization similar to values reported for films deposited on perovskite substrates.

CFO films can be deposited on thick Y_2O_3 buffers without formation of an interfacial layer between Y_2O_3 and Si(111). It points to high potential of ultrathin CFO/Y_2O_3 bilayers for fabrication of spin filter devices. CFO has been deposited on ultrathin Y_2O_3 buffers, with no degradation of the epitaxy in comparison with the use of thick buffers. TEM characterization of CFO/Y_2O_3 ultrathin bilayers showed the presence of interfacial layers, although the study has not permitted concluding if the formation is caused by the CFO deposition or if it is an extrinsic effect (due to buffer air exposure or sample preparation).

Chapter VI

Conclusions and perspectives

This thesis presents an investigation of the $CoFe_2O_4$ integration with silicon, with attention to the requirement of the film to be used in a spin filter device. The thesis is focused on the growth of CFO thin films and buffer layers and their structural characterization, mainly using transmission electron microscopy (TEM).
In a parallel strategy, we have investigated different oxides as buffer layer. SrTiO3/Si(001) samples were fabricated by collaborators at INL-Lyon using molecular beam epitaxy (MBE). Similarly, collaborators at IHP-Frankfurt Oder fabricated Sc2O3/Si(111) and Y2O3/Si(111) samples. We used all these samples to grow CFO films by pulsed laser deposition (PLD) assisted with reflection high energy electron diffraction (RHEED). PLD was also used to deposit YSZ films on Si(001) and CFO/YSZ bilayers on Si(001).

Integration of CFO on Si(001) using SrTiO3 buffer layers
STO buffer layers permitted epitaxy of CFO, being the epitaxial relationships [100]$CoFe_2O_4$(001) // [100]$SrTiO_3$(001) // [110]Si(001). The CFO surface is homogeneous and moderately flat with a roughness of 0.5 nm. The microstructural study showed that the CFO/STO interface is sharp with roughness ~0.5 nm. The interface is commensurately crystalline with a CFO unit cell matching with 2 STO unit cells. Direct HRTEM measurements, GPA analysis and FFT-reconstructed image confirmed that CFO is relaxed on STO with presence of misfit dislocations formed by half-atomic planes of CFO, and separated by 2.5 nm. The amorphous interfacial layer (AIL) of 3.5 nm observed at the STO/Si interface could be due to oxygen diffusion through STO during the CFO deposition, although sample degradation during TEM specimen preparation was not discarded. A chemical analysis by EELS showed that the composition of CFO is the nominal at distance >10 nm of the interface. Composition profiles across the interfaces revealed Ti diffusion in the CFO film extending 8 nm deep. Ti diffusion in CFO is inhomogeneous and appears to be enhanced in regions where STO presents grain boundaries, which suggest that microstructural defects could enhance its diffusion. The films are ferromagnetic with saturation magnetization close to the value of bulk CFO.

Integration of CFO on Si(001) using YSZ buffer layers
CFO films grown on either CeO2/YSZ/Si(001) or YSZ/Si(001) are (111) oriented out-of-the plane. They are epitaxial with presence of four in-plane crystal domains and grow two-dimensionally presenting a flat surface with low roughness below 0.3 nm. The saturation magnetization is close to the bulk value. In order to fabricate ultrathin CFO/YSZ bilayers, we have investigated the mechanisms of epitaxy of YSZ on oxidized Si(001) covered with native SiOx. In-situ RHEED monitoring permits detecting in real time the onset of crystallization of

YSZ on SiOx/Si(001). Epitaxy occurs by local reduction of SiOx and lateral epitaxial growth after deposition of around 1 nm of YSZ. Ultrathin YSZ films with presence of around 1 nm of SiOx interfacial layer present high crystalline quality, whereas complete reduction of this layer in thicker YSZ films causes generation of defects close to the interface. The defective regions present in-plane lattice parameter intermediate between Si and the rest of the YSZ film, and thus can help to relief the stress associated to the interface between crystalline YSZ and Si(001).
Epitaxial CFO films with thicknesses in the 2-50 nm range were grown on Si(001) buffered with ultrathin YSZ buffers in a single process. Properties were similar to those of CFO on double CeO2/YSZ thick buffer layers. The interfacial SiOx layer became thicker but below 3 nm after deposition of the thicker CFO film, signalling a certain instability of the interface under conditions used for CFO deposition. Ultrathin CFO/YSZ heterostructures with a total thickness of 5 nm were fabricated, being the SiOx interface layer 2.4 nm. The total thickness above 7 nm appears to be excessive for their use in spin filter devices.

<u>Integration of CFO on Si(111) using Sc2O3 and Y2O3 buffer layers</u>
Bixbyte A2O3 (A = Sc or Y) buffer layers have permitted the integration of CFO with Si(111). CFO grows epitaxially in spite of the huge lattice mismatch of around 15% (with Sc2O3) and 20% (with Y2O3). CFO films have single (111) out-of-plane orientation with coexistence of A- and B- type crystal variants. The films are very flat, with rms roughness below 0.4 nm. They are ferromagnetic, with saturation magnetization similar to values reported for films deposited on perovskite substrates. Detailed TEM characterization has confirmed that epitaxy, unexpected considering the structural mismatch, occurs by the mechanism of domain matching epitaxy. Measurement of the domain size is in agreement with the theoretically expected for the mechanism of domain matching. CFO can be deposited on thick Y2O3 buffers without formation of an interfacial layer between Y2O3 and Si(111). It points to high potential of ultrathin CFO/Y2O3 bilayers for fabrication of spin filter devices. CFO has been deposited on ultrathin Y2O3 buffers, with no degradation of the epitaxy in comparison with the use of thick buffers. TEM characterization of CFO/Y2O3 ultrathin bilayers showed the presence of interfacial layers, although the study has not permitted concluding if the formation is caused by the CFO deposition or if it is an extrinsic effect (due to buffer air exposure or sample preparation).

<u>Perspectives</u>
The four buffer layers investigated in this thesis show different efficiency in its function of permitting CFO growth. For the final application of fabrication of a spin filter Y2O3 appears to be the good option and the next steps would be to confirm the stability of the Y2O3 interface when Y2O3 is ultrathin. For this purpose, fabrication of the bilayer in a single process would be desirable.
Ultrathin YSZ or bixbyite A2O3 buffer could have also potential for other applications with requirements less strict than the spin filter device. Since PLD is the usual technique to grow CFO films, ultrathin YSZ buffers can be the simplest option to integrate CFO with silicon. On the other hand YSZ, with thickness of tens or hundreds of nm, has been a popular buffer layer for other functional oxides. The fabrication process shown here, using in situ RHEED monitoring, could be used to obtain other functional oxides (thick or ultrathin) on ultrathin YSZ buffer layers.
The mechanism of domain matching epitaxy has permitted high quality CFO films on A2O3 buffers in spite of the huge lattice mismatch. This suggests opportunities of integration of other functional oxides with silicon by using highly mismatched buffer layers.

Appendix A
Transmission Electron Microscopy

A.1 Generalities

The transmission electron microscope allows the study of materials on an atomic scale. In comparison with optical microscopy, electrons have a smaller wavelength than photons, defined by: $\lambda = h/m\upsilon$ with h the Planck constant and m,υ the electron mass and speed. The electron wavelength is inversely proportional to the acceleration tension, and is theoretically λ= 0.00197 nm for a tension V= 300kV. A huge advantage of the magnetic lenses is that the focal length is tuneable with the current, and gives access to image and diffraction planes. However, the resolution obtained experimentally is limited by optical aberrations, and is defined by: $R=0.61\ \lambda/\alpha$ where λ is the radiation wavelength and α the effective angular opening of the objective lens depending principally on spherical aberration. There are two ways to raise the TEM resolution: increase the high tension or correct the optical aberrations. The first high tension TEM was developed in CEMES (1.5 et 3 MeV), but for economic and security reasons, now the improvements are focused on aberrations corrections and more coherent sources.
The interaction between electrons and matter is very hard, so it is important to keep the entire microscope under high vacuum, and to observe a very thin sample to allow the transmission through it.

A.1.1 Electron-matter interaction:

Interaction between the high energetic incident beam with sample can be described by several physical phenomenon resulting in different radiations. Indeed, a part of the beam can be absorbed, diffused or transmitted by the sample (figure A.1).

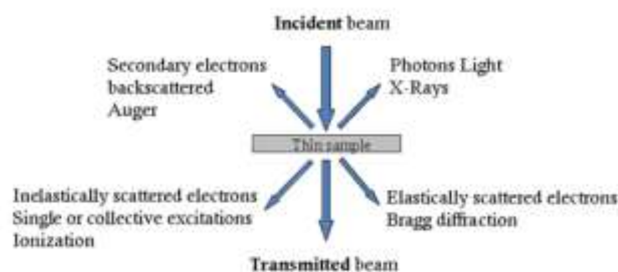

Figure A.1: Schematic illustration of the electron-matter interactions mechanisms.

These different mechanisms of reaction in the interaction electron/ matter result in a large panel of characterization techniques in a TEM used in different modes. The transmission electron microscope provides structural information with spatial resolution down to atomic dimensions by high resolution electron microscopy (HREM) and selected area electron diffraction (SAED). Chemical information is obtainable by energy-dispersive x-ray (EDX) spectroscopy and electron energy-loss spectroscopy (EELS).
The picture contrast depends on the transmitted beam resulting from elastic and inelastic diffusions. It is crucial to understand these processes of interaction in order to analyse and

interpret the TEM results. Furthermore, it allows to model different modes of TEM imagery. The linear momentum is conserved for both diffusions, while kinetic energy is only conserved by elastic interaction. Inelastic diffusion conserves the total energy and is confined in small angles of diffusion. A quantified energy is transmitted to atoms, where the electrons are excited.

A.1.2 Instrument

It is schematically composed by an electron gun, a column with magnetic lenses, and a CCD camera. These three stages have different vacuum levels and are separated by valves. The column is under secondary or ultra-high vacuum (10^{-6}-10^{-7} Torr) and the camera under secondary vacuum (10^{-5} Torr). The usual pumps used are the primary palette pump, the secondary oil diffusion pump and the turbo-molecular pump for higher UHV.

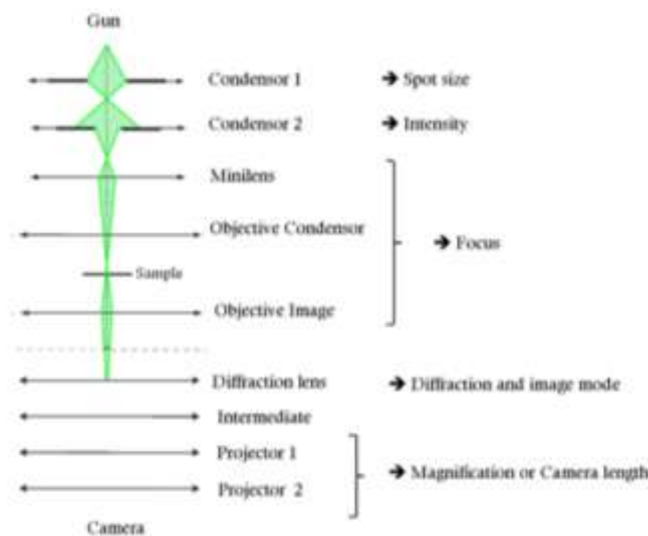

Figure A.2: Sketch of the lens system.

Gun:

There are two kinds of canon: the thermo-ionic source, and the field emission gun (FEG).
The thermo-ionic source is composed by a W or LaB_6 filament at the cathode, the Wehnelt and the anode. Electrons generated by heating the filament at extraction temperature are attracted by the anode. The role of the Wehnelt is to control de source emission with a variable negative potential. The optimum bias induces an intermediate current focalising the electrons in a cross-over between the cathode and the anode. The size of the cross-over determines the energy coherence of the electron source.
The cold FEG is composed by a tungsten crystal with a needle shape, and the electrons are extracted by tunnel effect through the electric field. This gun work under ultra-high vacuum (10^{-10} Torr), does not present a cross-over, and results in a highly spatially coherent beam and in a more energy coherent electron source without monochromation. Thermally assisted Schottky FEGs have a larger source size and energy spread, but they provide greater stability of beam current and lower noise.

Lenses:
The electromagnetic lenses present in the transmission electron microscopes are composed by a coil and polar pieces. Their huge advantage is their tuneable focal length with the applied current. Indeed, the magnetic field created in the polar pieces controls the electron trajectory.
The first stage of lenses is the condenser lens (C1) which determines the spot size reaching the sample. The second condenser lens (C2) determines the convergence of the beam over the sample, and then the screen intensity. A C2 diaphragm is used to determine the brilliance, the convergence angle and the electron source coherence (needed for high resolution imaging.
The objective lens is located on the sample level and its respective diaphragm is on the image focal plane of the lens. The eucentric position of the sample between the objective polar pieces allowing a symmetric configuration and homogeneous magnetic field is critical for the quality and reproducibility of the experiments.
The diffraction lens can be positioned on the object or focal plane of the objective lens in function of its excitation, and allows switching between the image mode and the diffraction mode.

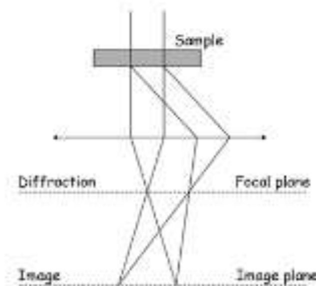

Figure A.3: Sketch of the optic modes in a TEM:
(a) diffraction mode, (b) image mode.

Then, the intermediary and projector lenses attend to spread the magnification given by the objective lens.

Aberrations:
There are different aberrations generated in the lens system responsible of a decrease of resolution:
-Spherical aberration: the electrons passing on the border of the lens (slow electrons) focalises before the electrons near the optical axis (quick electrons), resulting in a delocalisation. Cs corrector is critical for the study of surfaces and interfaces.
-Chromatic aberration: focal distance variation in function of the electrons length wave.
-Diffraction aberration: diffraction induced by the objective diaphragm.
-Astigmatism: the image of a punctual object is blurred.

A.2 Image contrast for structure analysis

The TEM imaging system is constituted by the system of magnetic lenses showed in figure II.11. The intermediate lens can magnify the first intermediate image or the first diffraction pattern by modulating its excitation. Then, it is possible to obtain images in the real space (image mode), and in the reciprocal space (diffraction mode).

The image contrast brought about by several mechanisms: mass contrast due to spatial separation between distinct atomic constituents, thickness of the sample due to the uniformity in sample thickness, diffraction contrast which is in the case of crystalline materials and phase contrast.

The contrast origin in a microscopy picture is related to the selected beam or radiation originated by the incident electron reaction with the sample using an objective diaphragm. Considering the sample and the geometry of the setup, it is important to notice that only a family of planes is oriented in diffraction condition (two beams).
In conventional microscopy, the amplitude contrast depends on the selected beam (transmitted or diffracted). While in high resolution electron microscopy, the contrast is related to the phase difference between the diffracted beams. Then, the interaction/interference between at least two diffracted beams constitutes the phase contrast.

For the phase contrast imaging mode, as it is based on the electron beam interference, the electron source used has to be coherent.
A small illumination aperture of the condenser diaphragm is normally used. The aperture of the objective diaphragm used in HREM mode is then larger than in CTEM in order to transfer high special frequencies, and its only purpose is to decrease the background by absorbing electron scattered at very large angles. The resolution is limited by the contrast-transfer function (CTF) caused by chromatic aberration and not by the objective aperture.

A.2.1 Amplitude contrast in conventional transmission electron microscopy (CTEM)

The bright-field mode (BF) with a centred objective diaphragm is the typical TEM imaging mode with which scattering contrast and diffraction contrast can be produced.
Unconventional types of contrast can be obtained by tilting the beam, changing the illumination cone, or selecting the scattered electrons on the focal plane of the objective lens. This last unconventional mode is the most widely used, and then it is commonly said that there are two types of amplitude contrast in conventional microscopy: The bright field mode (BF) using transmitted electrons and the dark-field mode (DF) formed by a diffracted beam. The objective diaphragm is used to select the electrons and change the observation mode.
In the dark-field mode, the primary beam is intercepted in the focal plane of the objective lens. Different ways of producing dark-field conditions are in use: shifted diaphragm, central beam-stop, and tilted primary-beam. Studying crystalline specimens, it is experimentally easy to shift the objective diaphragm, to select diffraction spots (but it introduces off-axis aberrations).

The image intensity is relied to the amplitude of the beams. *(Transmitted and diffracted)*
The amplitude for a diffracted beam ϕ_g for a reflection g is described as:

$$\phi_g = \frac{ai\pi}{\xi_g}\exp(-2\pi i\vec{K}.\vec{r})\exp(2\pi i\vec{k}.\vec{r})$$

Where "a" is the distance between the plans parallel to the sample surface, ξ_g is the extinction distance for the considered reflection g and $\vec{K}$ a vector from the reciprocal space. The extinction distance depends on the lattice parameters, the atomic number and the electron wavelength.

Considering interference between the transmitted beam noted "0" and the diffracted one noted "g", in the two beams approximation, the amplitude of both beams are coupled dynamically by:

$$\frac{d\phi_g}{dz} = \frac{\pi i}{\xi_g}\phi_0 + 2\pi is\phi_g$$

$$\frac{d\phi_0}{dz} = \frac{\pi i}{\xi_g}\phi_g$$

The resolved system equation given in dynamic diffraction books [WIL96] lead to:

$$I_g = |\phi_g|^2 = \left(\frac{\pi t}{\xi_g}\right)^2 \frac{\sin^2(\pi t s_{eff})}{(\pi t s_{eff})^2}$$

$$I_0 = 1 - I_g$$

Where « t » is the sample thickness, s_{eff} is the effective deviance from the Bragg condition (s_{eff} = s for large s).

An example of another configuration mode is the weak beam mode (WB) which provides a better diffraction contrast, and reveals the presence of defects in the atomic lattice. But further operating modes of a TEM exist resulting in specific contrast: Scanning TEM, electron diffraction modes, Lorentz microscopy…

Defects/dislocations:
The defects present in the crystal does not present the same diffraction conditions that the surrounding atoms. Then, a different contrast will reveal their presence in a long ordered structure. Defect appears as a dark contrast in the bright field imaging mode, while they are revealed by a bright contrast in a dark field mode. The Burger's vector of a dislocation can be determined by selecting the characteristic extinction g, where the reflector planes are not distorted by the dislocation and $\vec{g}.\vec{b} = 0$.

Coherent interfaces and stacking faults without long range strain fields form characteristic image contrast. The displacement of the thin film is characterized by a constant vector $\vec{u}$ relatively to the substrate. For columns passing through the interface, a phase factor $2\pi\vec{g}.\vec{u}$ can be introduced into the main and diffracted beam amplitudes. Then, when the diffraction vector $\vec{g}$ is perpendicular to the interface $\vec{g}.\vec{u} = 0$ and there is no interfacial contrast. For other values of $\vec{g}.\vec{u} \neq 0$, interference between waves from the film and the substrate gives a fringe pattern: a light or dark contrast.

Moiré figure:
The superposition of two crystals A and B with a slight different lattice parameter and/or slightly disoriented can result in interference fringes called Moiré fringes. This fringes can be observed in conventional and in high resolution microscopy. And result from the interaction of a diffracted beam by the crystal A and a diffracted beam from the crystal B.
The fringes distance is characteristic of the considered materials parameters d_A and d_B and of the disorientation angle β. In general and for cubic materials, the interfringe D, the angle α of the moirés, and the bisector β are express as:

$$D = \frac{d_A}{\tan\beta}\cos\arctan\left(\frac{d_A - d_B\cos\beta}{d_B\sin\beta}\right)$$
$$= \frac{d_A d_B\cos\beta}{\sqrt{(d_A - d_B\cos\beta)^2 + d^2{}_B\sin^2\beta)}}$$
$$et\alpha = \frac{\pi}{2} - \arctan\left(\frac{d_B - d_A\cos\beta}{d_A\sin\beta}\right) + \frac{\beta}{2}$$

For moirés having a pure translation: α=0 and D= $\frac{d_A d_B}{d_B - d_A} = \frac{d_A}{f}$ where f is the residual mismatch between A and B.

For moirés having a pure rotation: d_A=d_B, α= $\frac{\pi}{2}$, and D= $\frac{d_A}{2\sin\frac{\beta}{2}}$

Considering an epitaxial thin film presenting the same orientation than the substrate, the average misorientations angle is null. Then, the Moiré fringes can be considered as having a pure translation. In the case of a residual mismatch of 1 to 5%, the local variation of the lattice parameter is magnified by 20 to 100 times. The Moiré fringes can be used to evidence very small parameter difference between the film and the substrate.

A.2.2 Phase contrast in high resolution transmission electron microscopy (HREM)

In high resolution electron microscopy, the contrast observed is a phase contrast. This phase contrast comes from the difference of phase between the diffracted beams through the sample (minimum two beams).

The incident electron beam diffracted by the sample generates various diffracted beam with a phase difference, but after interference of these diffracted beams, their phase relation is conserved.

Amorphous materials do not diffract the electron beam, and almost all the incident beam is transmitted, providing a bright contrast. While crystalline samples generate a periodic fringe contrast which distance corresponds to the inter-reticular distance, while the position depends on the imagery conditions. The crystalline sample needs to be oriented in zone axis or high symmetry crystalline axis in relation to the incident beam projected along the optical axis of the microscope.

Considering the incident electron beam as a plane wave $\psi_0(\vec{r}) = \exp(2i\pi\vec{k}_0.\vec{r})$ with its wave vector $\vec{k}_0$, and the sample as a periodic potential; the wave function $\psi_f(\vec{r})$ forming the image contrast can be described as: $\psi_f(\vec{r}) = \sum_{\vec{g}} a_{\vec{g}}(z)\exp(i\varphi_{\vec{g}}(z))\exp(2i\pi(\vec{k}_0 + \vec{g}).\vec{r})$

In this expression $\vec{g}$ is the reciprocal space vector associated to each diffracted beam, and their respective amplitude and phase are $a_{\vec{g}}(z)$ and $\varphi_{\vec{g}}(z)$.

The fact that the resulting contrast is the sum of transmitted and diffracted plane waves is traduced. Furthermore, the amplitude of the signal depends on the sample thickness z, the crystalline potential and its orientation with respect to the incident beam.

The associated Fourier transform is $\tilde{\psi}_f(\vec{v}) = \exp(2i\pi k_0 z)\sum_{\vec{g}} a_{\vec{g}}(z)\exp(i\varphi_{\vec{g}}(z))\delta(\vec{v} - \vec{g})$, where the spatial frequency is $\vec{v}$. The square modulus of this function confers the diffraction diagram of the crystal.

The information function transfer $T(\vec{v})$ by the microscope can be described in the linear approximation. The wave function $\psi_i(\vec{r})$ in the image plane can be written in the Fourier space as: $\tilde{\psi}_i(\vec{\upsilon}) = T(\vec{v}).\psi_f(\vec{v})$

The transfer function of the microscope can be defined considering the phase shift introduced by the objective lens $X(\vec{v})$ which depends on the spherical aberration C_s and the defocalisation Δf.

$$T(\vec{v}) = G(\vec{v}).\exp(iX(\vec{v}))\ X(\vec{v}) = -(\pi\Delta f\lambda v^2 + \frac{1}{2}\pi C_s\lambda^3 v^4)$$

$G(\vec{v})$ is the sum function for all the $\vec{g}$ vectors selected by an objective diaphragm in the focal plane of the correspondent lens and contributing to the contrast.

Then, $\psi_i(\vec{r})$ in the image plane can be written in function of X and G:

$$\psi_i(\vec{r}) = \exp(2i\pi k_0 z)\sum_{\vec{g}} a_{\vec{g}}(z)\exp(i\varphi_{\vec{g}}(z))G(\vec{g})\exp(iX(\vec{g}))\exp(2i\pi\vec{g}.\vec{r})$$

And the image intensity being the square modulus of $\psi_i(\vec{r})$:

$I(\vec{r}) = \sum_{\vec{g}} a^2{}_{\vec{g}}(z)G(\vec{g})\ +\ \sum_{\vec{g}\neq\vec{0}} 2a^2{}_{\vec{0}}(z)a_{\vec{g}}(z)G(\vec{g})\cos[2\pi\vec{g}.\vec{r} + X(\vec{g}) + \varphi_{\vec{g}}(z) - \varphi_{\vec{0}}(z)]$ + non-linear terms

The first term is the constant contribution to the background signal, while the non-linear terms corresponds to an intermodulation. The linear terms corresponds to the information relied to atomic columns position.
Generally, the amplitude of the transmitted beam is higher than the diffracted ones, and the linear terms constitute the major party of the contrast. But non-linear terms can become preponderant for certain defocalisations as linear terms are affected by the phase shift X.

But this atomic phase contrast (depending on the atomic number and the specimen thickness) has to be converted into visible amplitude contrast: problem.
Then, for simplicity, the weak phase object (WPO) approximation is generally applied [REI84, CAR96]. The basic phase shift of a diffracted wave is π/2 with respect to the incident wave (in the Gaussian complex number plane). As a result, the scattering regions give a dark contrast on bright background which is called positive phase contrast.
A negative phase contrast where the atoms position appear bright on dark background, corresponding to negative phase shift - π/2 can be obtained in negative spherical aberration-corrected imaging (NCSI) [URB09] .

A.3 Some concepts definition

Spread function:
The presence of aberrations has the consequence that a point in the object plane is not imaged into a sharp point in the image plane, but rather into a point spread disc whose radius is given by the point spread function *R*, where the maximum has to be taken over the whole range of special frequencies contributing to the image.

$$R = \max\left|\frac{\partial\chi}{\partial g}\right| = \max\left|C_s\lambda^3 g^3 + Z\lambda g + ...\right|$$

Scherzer defocalisation:
For very thin foils (weak phase objects) it is considered that the transfer function is only constitute from its imaginary contribution. The higher contrast is obtained for a Scherzer defocalization depending on the microscope characteristics.

$$D_s = -1.2\sqrt{C_s \lambda}$$

Resolutionδ:
The microscope resolution is its faculty of separating two points on its image formatted from the object. The principal origin of the resolution limit is the presence of aberrations (chromatic and spherical).

Depth of image S:
The depth of image is defined by $S = \frac{\delta_s M}{\alpha'} = \frac{\delta_s M'}{\alpha_0}$, where α_0 is the objective aperture, and $\alpha' = \frac{\alpha_0}{M}$ denotes the angular aperture in the final image. A blurring of the image $\delta_s M$ will be observed at a high distance from the final image plane, describing the depth of image.

Depth of focus T:
The depth of focus T $< \frac{\delta_s}{\alpha}$ is defined by the axial distance between the two extreme points of the objective plan where the focalisation and the resolution is conserved. In thin specimens, the majority of the electrons are not scattered, while for thick specimens, the electrons are strongly scattered. Focusing at low magnifications sometimes becomes difficult owing to the large depth of focus.
In the case of HREM, the defocusing differences Δz changes the image intensity distribution. Indeed, if the specimen contains a periodicity, a diffraction maximum will be formed at $\sin\theta \approx \theta = \frac{\lambda}{\Lambda}$. The maxima and minima of the specimen periodicity Λ (and a special frequency $q = \frac{1}{\Lambda}$) will be reversed in contrast when the second term of the wave aberration W(θ) in caused by the defocusing Δz changes the phase of the diffracted beam by π. Setting $W(\theta) = \frac{\pi \Delta z \theta^2}{\lambda} \le \pi$ results in: $\Delta z < \frac{\lambda}{\theta^2} = \frac{\Lambda}{\theta}$.

Contrast Transfer Function (CTF):
The CTF for amplitude and phase specimens (Amplitude ACTF, Phase PCTF), where the imaging properties of an objective lens are described independently of any particular specimen structure was describes by Hansen and co-workers [HAN69].

In this thesis, HREM pictures were performed by two different accelerating voltages: 200 keV for the Tecnai and 300 keV for the Titan Cube (Zaragoza), and the CM30. The pictures obtained can seem different, but it principally results from the fact that different areas of the specimen are imaged. The sample thickness transparent to electrons increases with the microscope energy used. For the low-energy microscope, only the thinnest part of the foil is

available. Generally the quality of the image is better for higher thickness of the foil, so higher-energy microscope tends to image thicker layers. But the asset of the Tecnai is it spherical aberration corrector which avoid the atom delocalisation at interfaces [HAI98].

A.4 Incoherent imaging: Z-contrast by High Angular Annular Dark Field (HAADF)

The particularity of this technique is that it combines the structural and chemical information.
Indeed, the intensity of the high resolution picture is directly relied to the atomic number Z of the present elements [PEN83, NEL00].

The electrons scattered at high angles are detected by an annular DF detector, and the resulting pictures formed are incoherent (no interference caused by scattered waves resulting from zones next to the analysed one).
As heavy elements scatter the electrons at higher angle than light elements, the contrast will depends on the atomic number. Then, heavy elements appears with more contrast / or darker than light elements. Several approximations of the relationship of the image intensity and the element atomic number exist. The simpler one is the Rutherford dispersion where I is proportional to z^2[PEN99]. The limit of this comparative technique is that the atomic number of the present elements needs to differ to be differentiated.

A.5 Scanning TEM (STEM)

The scanning transmission electron microscope consists on working in a nanoprobe mode with a small probe size (<10nm) and scanne its position along a line or a rectangular surface [CRE69].

The advantages related to this mode are:
-the absence of chromatic aberrations (there is not an intermediate image formation but direct transfer of the information to the detector).
-the malleability of the electronic signal (brilliance, contrast..)
-the image is not rotated
-localisation of the nanobeam on the sample scanned in the spectroscopic analysis by EDXS and EELS.

Experimental configuration:
The sample has to be oriented in a perfect planar position, perpendicularly to the incident electron beam in order to study the profile across the interface without the influence of the diffusion depth measure in the sample.
It can be seen in the following figure that when the sample is tilted (b), the mixed elements detected could arise from a measure artefact and not from a real diffusion of elements. To avoid this limiting condition, it is important to orientate the sample in zone axis.

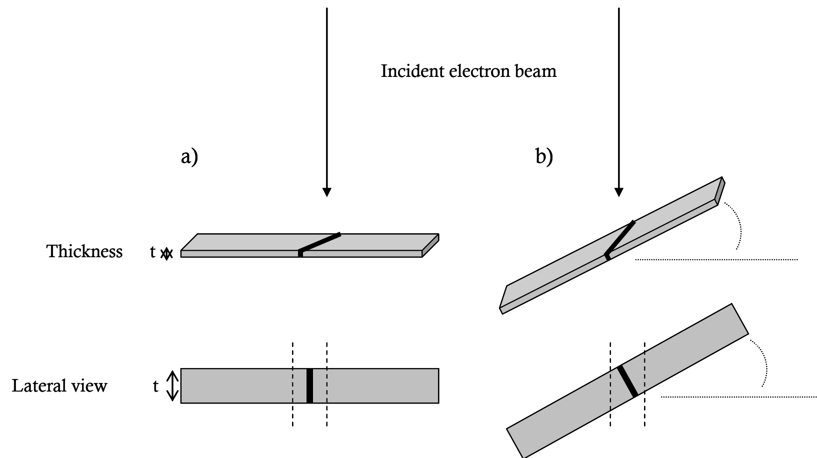

Figure A.4: (a) Sample oriented in the horizontal plane, (b) Sample tilted from the horizontal plane.

Furthermore, a s the thi ckness of the sample can c hange along the profile, a nd modify the intensity o f the signal, the a bsolute Ti intensity c annot be c ompared wi thout c hecking the thickness. In regions with different thickness, the relative intensities as Ti/O or Ti/Fe can be compared.

The S TEM-EELS experiments can b e don e in tree configurations of p robe siz e and step described by the following figure.

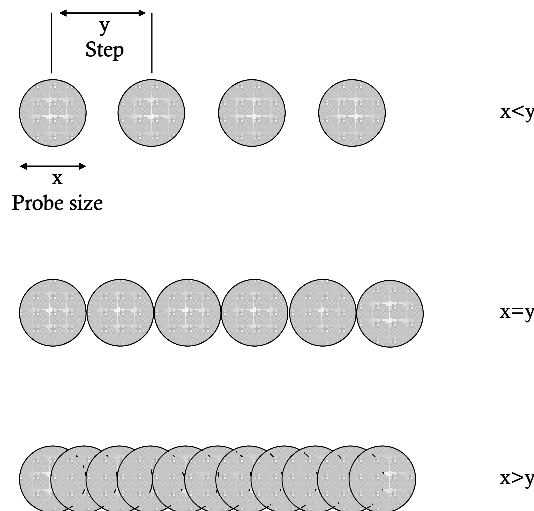

Figure A.5: Three possible configurations of probe size and step interval for STEM.

In the first case: x<y, the limiting parameter is the step size and the resulting profile is a non-continuous study. In order to obtain a continuous study, the chosen step “y” has to be equal or inferior to “x”. Theoretically, the case where x=y seems to be the more appropriate to have a continuous study, but will require a lon ger e xposition ti me versus surface pr obed, a nd the material can be da maged. The n, e xperimentally it c an be int eresting to wor k in the third condition: x>y, but it will depend on the sensibility of the studied material.
In all the results presented here, the probe size used was 1.5 nm with an inferior step size; and the incertitude of the measure is considered to be 2 nm.

A.6 <u>Effects of the sample preparation for TEM analysis</u>

All techniques employed in the preparation of samples for TEM introduces artefacts that can obscure subtle detail in the material being studied or could lead to misinterpretation. One significant cause of image degradation is surface amorphisation (top and bottom surface layers of TEM samples) [BAR93-99]. Measurements of surface damage on silicon produced during TEM sample preparation utilizing different techniques (cleaving, ion-milling, FIB) was investigated by J.P. McCaffrey et al [CAF01]. The thinnest damaged layer formed on a silicon surface was measured as 1.5 nm thick; while an optimized FIB sample preparation process results in the formation of a 22 nm thick damaged layer. For semi-conducting materials, cleaving and tripod wedge technique produces samples with the least surface amorphisation, followed by conventional ion milling, and focused ion beam (FIB) preparation.
As the cleaving and tripod wedge technique procedures are difficult to success and has a low reproducibility, the conventional sample preparation finished by ion-milling was used. Furthermore, this final surface polishing removes the damages induced during the mechanical polishing.

Particle energy and angle of beam incidence
The final preparation step consisting in ion-etching to electron transparency was widely investigated from the early 1950s by R.Castaing, P. Laborie and others [BAR93, CAF01, CAS53-62]. And particularly the effect of particle energy and species, angle of beam incidence, specimen type, specimen temperature, internal microstructure and surface topography was reviewed.

One effect of the ion-milling is the generation of an amorphous surface layer whose thickness increases with ion energy and angle of incidence. The principle of formation of the amorphous layer was proposed by D.G. Ivey et al. [IVE87]. The basic equation in transport theory determinates the damage function which is an expression for the energy dissipation per unit volume. The velocity, the path element and the differential scattering cross-section of the argon projectile and the density of atoms in the target are considered in a first-order collision phenomenon (or primary sputtering process). The sample can then present a local disorder region and many point defects associated with a degree of amorphisation which varies with the nature of the material. The damage level on the surface is often predicted from TRIM calculation (MC simulation) for non-crystalline matrices and MRLOWE [ROB89] for crystalline-matrices. The values of calculated thickness of amorphous layer display the same tendency to increase with increasing accelerating voltage and increasing the incident ion beam angle. Other models for ion-induced amorphisation have been proposed, but still far from satisfactory, especially for the low energy range [CAR91]. Schuhrke et al. reported a nominally linear dependence of the thickness of the amorphous layer produced by ion milling on the ion energy in a range from 2 to 9.5 kV. Their theoretical values (based on transport theory) are higher than the experimental ones, and this discrepancy was explained by the fact that the particles of the etching gas possess considerably lower energies than originally assumed in calculations [SCH92]. Molecular dynamics simulation of argon bombardment with intermediate energies (5-7 keV) predicted a damage region extended over 2.2-3.0 nm [MOO04]. A study by Barna et al. [BAR92] demonstrated the superior performance of a very low energy ion-mill developed by these authors where experimental data showed 2.5-5.0 nm rage of ion induced damage layers with 3-5 keV ion energies. Later, they summarized the published data of damage on silicon, particularly on the amorphous thickness produced by ions at different energies and angles of incidence. These same qualitative result leads to think

that ion-milled TEM samples can be improved by lowering both the ion accelerating voltage and the incident ion milling angle. Barna et al. also shows that lowering the ion energy also results in smoother interface between the amorphous region and the rest [BAR98].

Internal microstructure and surface topography

The rotation of the sample during the ion-milling process is critical to obtain an homogeneous sample surface [EBE08]. The rotation speed controls the milling length and frequency, and consequently the temperature local rise; but was not considered as relevant effect to be investigated.

Specimen temperature

It is also known that the internal structure and composition of the sample can be altered in this final preparation process. This was explained to be due by redeposition of the sputtered particles and atom diffusion promoted by the local heating of the thin foil. Few other studies have attempt direct measurements of the extent of surface damage and temperature elevation induced by ion-milling [KIM87, PAR07]. Then, cooling the sample with liquid nitrogen could improve the quality of the sample. But the low temperature can weak and break the sample, and act as a drawing power to fix impurities in it.

Specimen type and interfaces

The ion-milling thinning down rate can differ with the hardness of the materials. This difficult the preparation of cross-section samples presenting different tough compounds. Indeed, a similar thickness for all the parts of the foil is needed for the simultaneous observation of different materials, and especially to characterize their interface [DUN00, SEA05, KEL10].

Other parameters: single sector mode

The PIPS can be used in single canon geometry, allowing the milling of the same half side of the cross-section with both canons. This particular geometry was used when both parts of the cross-section break away before reaching the electron transparency. Then, it allows to protect at least one side from milling damage (shadowing). L. Dieterle et al. have investigated quantitatively the reliability and reproducibility of this preparation step, comparing with Monte-Carlo (MC) simulations. They have shown that single sector mode (associated with a small sputtering angle of 1.5-3°) enables the preparation of plane parallel regions with constant thickness alongside the epoxy (several μm). Then, this procedure facilitates a minimum of preferential thinning, especially well-suited for the cross-sectional preparation of inhomogeneous samples composed by materials that exhibit different sputtering yields [DIE11].

Protective coating/ Si amorphous layer

A different technique and arrangement was applied for the quantitative determination of the amorphised thickness dependence on ion energy. The basic idea is to cover, in-situ, the bombarded surface with a protective layer and then eliminate (as far as possible) oxidation and surface diffusion which occurs during the sample preparation. A metal film deposition is evaporated onto the freshly created surface, before finishing the ion-milling step and continued after the milling step (30 nm) [BAR98, BRI00].

In our study of integration of functional oxides on silicon, the sample preparation was challenging as it needed to consider all these preparation effects to found an appropriate preparation procedure.

Appendix B
Spectroscopies (EDXS, EELS)

A spectrometer can be added on a TEM in order to study the chemical nature of the sample. Several types of spectrometries exist, and are defined in function of the kind of collected radiation generated by the electron-specimen scattering.
Along their path through the specimen, many electrons undergo inelastic scattering. The incident beam is characterized by its intensity I_0, energy E_0 and wavelength λ_0 with a propagation direction described by its wave vector $k_0=1/\lambda_0$. After its interaction with the sample, the radiation can then loose some intensity, energy and change of direction. This energy transfer on the sample matter can be induced by potential energy of excitation, kinematic energy of ejected particles, thermal vibration energy, and induced defects energy. The relaxation process of the matter can lead to the emission of secondary radiation as characteristic X-rays, Auger electrons or light.

In this part, we will introduce two kinds of spectroscopies: EDXS and EELS detailed in several books and articles [CAR09, EGE09]. These techniques detect respectively photons or electrons generated by the inelastic interaction between the high energetic incident beam and the sample probed. The analysis methodology for each technique will be explained, and then, after a brief comparison with other techniques, the suited conditions for its use is discuss.

B.1 <u>Physical principle: Diffusion</u>

The inelastic interaction between electrons and atoms creates an excited state where an orbital electron acquires energy and goes from an internal orbital level to the band conduction level. The scattering phenomenon is accompanied with the creation of a characteristic photon witch energy corresponds to the energy difference between the two energy level considered on the electron transition. This quantified energy is characteristic of the probed element, allowing its identification.

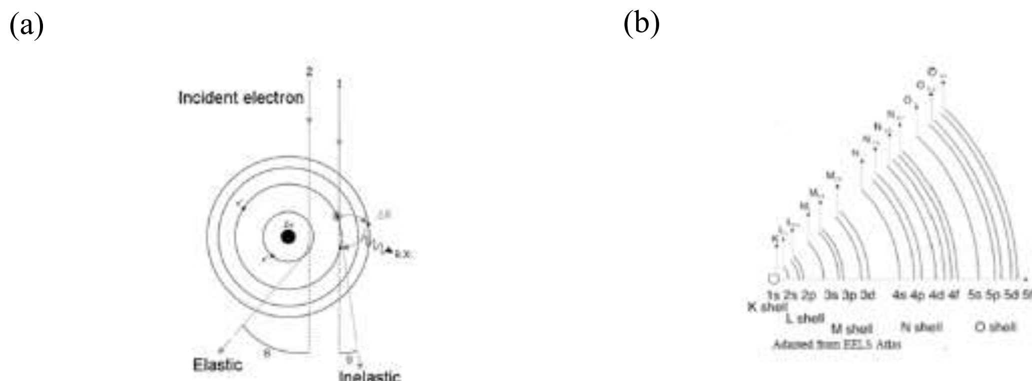

Figure B.1: (a) Electron diffusion mechanisms and (b) atom shell structure.

Elastic scattering:
The electron can lose a slight part of its energy due to the high mass difference with the atom. Generally it is considered that the monochromaticity of the beam is conserved ($\lambda \sim \lambda_0$, $k \sim k_0$). The radiation conserves its coherence by elastic diffusion. Individual atomic vibration (Debye effect) and collective oscillations of energy quantified states (phonons) with an energy range of 10^{-2} to 10^{-1} eV induces a thermal effect. Chemical effects can occur creating dissociation of atomic links with an energy transfer of 3-5 eV, and atomic displacement effect can produce an irradiation damage with an energy range of 15 to 30 eV.
The elastic scattering cross-section has behaviour proportional to Z^2/E_0^2 and is very small compared with that of other inelastic scattering events.

Inelastic scattering:
The inelastic interaction between the electron incident beam and the sample atoms is characterized by an energy transfer. Electron scattering from the valence or conduction band can produce collective excitation of free or quasi-free electrons with a quantified energy loss <50 eV called plasmons. Electron scattering from deep atomic levels (energy loss >50eV) generates the emission of characteristic X-ray radiations or secondary electrons (Auger electrons) in their desexcitement. Other electromagnetic radiation or phonons excitation can occur.
The inelastic scattering cross-section has behaviour proportional as Z/E_0^2 and is concentrated around several milliradians.

Cross-section:
A cross-section σ is defined considering a matter particle in a section S in the incident beam direction and a particular interaction. Several cross-sections can be defined for each particular interaction: differential diffusion cross-section, integrated diffusion cross-section, total diffusion cross-section. The surface of the cross-section can be measured calculating the ratio of the diffused intensity over the incident intensity.

B.2 Energy Dispersive X-ray Spectroscopy (EDXS)

B.2.1 Spectrometer and spectrum

An EDXS spectrometer can be added next to the TEM column. X-rays are collected by a photodiode detector Si(Li) or Ge and are transformed in electrons by a photoelectric effect, conserving the photons energy. The signal is amplified and analysed with an analytical or digital system. The signal obtained is energy filtered and the principal compromise is between the number of collected photons by unit time and their energy resolution. Then, the highest spatial resolution and the best analytical sensitivity cannot be achieved under the same experimental conditions.

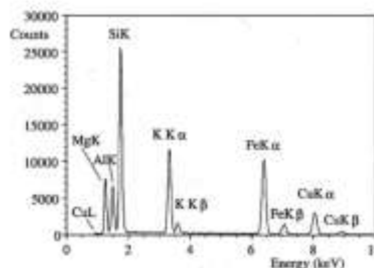

Figure B.2: EDXS spectrum.

The theoretical energy resolution of the detector increases as the square energy of the incident photon. In practice, the resolution achieved is 130eV for Si detectors measures with the Mn-K ray.

B.2.2 Intensity of the signal

The intensity of the signal I_A is $I_A = I_0 N_A \sigma_A$

I_A: is the number of photons per time unit resulting from the interaction with atoms of the element A.
I_0: incident intensity defined as the incident electron number per unit time and atom.
N_A: number of atoms of the same element A per volume unit.
σ_A: emission cross-section

The cross-section σ_A can be express by: $\sigma_A = \sigma.\omega.p$, where σis cross-section of the core levels, ω the desexcitementefficiencyper X-ray emission and p the emission probability of the considered ray.
For thin films, the emitted intensity of the ray A-Kα per surface unit is:

$$I_A = I_0(N/A)\ (\sigma.\omega.p)_A.c_A.R.\ \rho.t$$

σ: excitation cross-section of the K level
ω: desexcitement efficiency by X-Ray emission
p: emission probability of the Kα ray for the element A
R= <1: retro-diffusion factor
t: sample thickness
ρ: volumic mass of the sample
A: atomic mass
c_A: mass concentration
N: Avogadro number

Intensity measured by the detector is the intensity emitted by the concerned atom affected by physical factors due to the matrice (absorption, fluorescence) and due to instrumental factors (detection angle, detector efficiency).

$$I_A = I_0(N/A)\ (\sigma.\omega.p)_A.c_A.R.f(\chi)(1+f).\tau_A.\rho.t$$

f(χ): absorption function of the sample
(1+f): strengthening rate of florescenceby heavier atoms than *A*
τ_A: transmission factor of the spectrometer-detector system

Corrections for a very thin sample (t~10nm):
-Atomic number correction: expressed by R which depends on the energy loss, and of the mass function ρ: R~ 1
-Absorption correction: intensity of the emitted beam can be considered constant for very thin samples: $\chi_A.\rho.t<0.1$ and $f(\chi) \sim 1$. (χ_A: absorption factor of the characteristic ray for the element A)
-Fluorescence correction: the contribution on the A-Kα of the characteristic radiation of an element B heavier than A by fluorescence can be neglected if $\mu_A \rho t < 0.1$: (1+f) ~1, R~ 1, f(χ) ~1 and σ= constant.
μ_A: massic absorption coefficient of the characteristic ray of B exciting the fluorescence of the element A ($Z_B > Z_A$).

Considering theses correction factors for very thin samples as used in TEM, the measured intensity is:

$I_A = I_0\, k_A \tau_A\, c_A \rho\, t$ with $k_A = (N/A)\,(\sigma.\omega.p)_A$

IV.2.3 Quantification

The quantification of an element can be done in comparison with a test sample of known composition or theoretically determined if the physical parameters are well known (k_A, ρ, t). The Cliff-Lorimer method consisting in comparing the concentration of two elements is widely used. The intensity ratio between two elements A and B simultaneously measured is:

$$\frac{I_A}{I_B} = \frac{k_A \varepsilon_A}{k_B \varepsilon_B} \frac{c_A}{c_B}$$

And the ratio between the relatives concentration in the approximation for thin samples (independent from the: thickness, volumic mass, detection angle) is:

$$\frac{c_A}{c_B} = \frac{k_B \varepsilon_B}{k_A \varepsilon_A} \frac{I_A}{I_B} = k_{AB} \frac{I_A}{I_B} \text{ with } k_{AB} = \frac{k_B \varepsilon_B}{k_A \varepsilon_A}$$

The concentration ratio of two elements A and B imply the need to know the factor characteristics of the materials: "k factor method".
C_A and C_B are the weight fractions or atomic fractions. The k_{AB} factors can be estimated with physical and instrumental parameters, and some values are reported for particular element couples.
A test sample is needed to determine the Cliff-Lorimer k_{AB} factors and determine the quantitative composition. (It could be evaluated from the target powder as it composition is well known.)

Steps of the raw data analysis
First f all, the background is extracted (due to the braking radiation).
The intensity of identified picks can be compared with standards or reference spectrums for quantification, and the characteristic signal is quantified by integrating counts in peaks.
And then, k-factors are determined and a correction for absorption is done if necessary.

The limits of this analysis can be due to systematic or statistical errors.
-The approximation for very thin films needs to be verified for light elements and couples of heavy elements.
-The absorption correction depends on the emergence angle defined by the detector position. (the atomic number effect is increased by inclining the sample).
-The choice of the reference element is critical (it is better to choice a heavy major element).
- The low emission volume active leads counting slight rates. To compensate it, a long time measument is needed.
-The peack superposition can introduce supplementary errors if the deconvolution cannot be done.
The typical precision for heavy major elements (Z >10) is around 5-15%.

B.3 Electron Energy-Loss Spectroscopy (EELS)

The incident high energy electron beam changes its direction and losses some energy by an inelastic interaction with the sample. The study of this energy loss allows identifying

the present elements in the sample probe, and in some cases to determine the chemical kind of link between atoms. Furthermore, the thickness of the sample and other properties can be extracted, as electronic properties.

B.3.1 Spectrometer

An EELS spectrometer can be added to a TEM in order to collect the electrons transmitted by the sample and detect their energy. Two different configuration systems exist in function of their position with respect to the TEM column. Figure B.3 shows the first configuration of a system located under the column and deviating the signal at 90° with a magnetic sector. The second configuration "Ω filter" is integrated next to the column and contains 3 or 4 sectors.

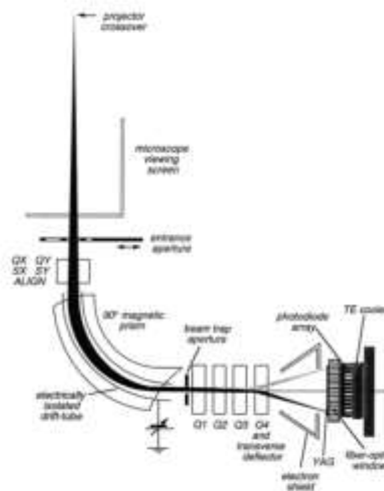

Figure B.3: Sketch of an EELS spectrometer.

B.3.2 Spectrum

The typical EELS spectrum is commonly described differentiating two principal regions: low loss (LL) and core loss (CL) energy losses (figure B.4). The Zero Loss Peak (ZLP) is generated when the electron beam is transmitted by the sample without losing energy. It also includes all elastically scattered electrons and also electrons with energy losses inferior to the energy resolution of the TEM. This peak is the more intense one, and is always observed. The Plasmon signal, next to the ZLP, corresponds to the collective electron excitation, but also contains interband transitions from the valence to the conductance band. Its shape depends on the probed material.

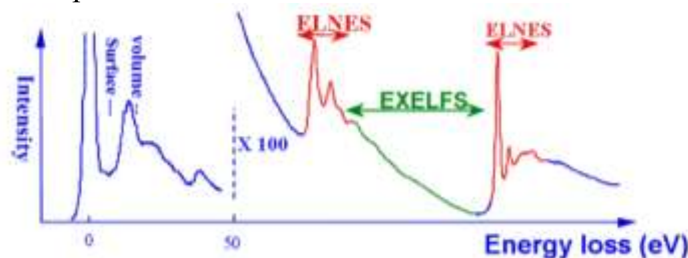

Figure B.4: Sketch of an EELS spectrum.

The high energy losses, above 50 eV, are related to internal electronic transitions. Theses core-levels excitations to the unoccupied Fermi levels lead to the edge like features with an onset energy corresponding to the lowest unoccupied state. An energy loss near edge structure (ELNES) zone or around 30eV is defined around each particular edge, presenting a high

intensity. Then, an extended energy loss fine structure (EXELFS) zone in the following electron-volts losses present an inferior intensity and represent the unoccupied state density under the Fermi level. The frequency and amplitude modulation of the EXELFS is related with the atomic arrangement around the excited atom. In addition, a background signal stemming from the low-loss events is superimposed in this high energy range.

B.3.3 Intensity of the signal

The intensity of the signal is the area of the portion of the spectrum after subtracting the background. The background is estimated with an extrapolation of the signal just before the edge pick by a law in $A\Delta E^{-r}$.

B.3.4 Quantitative analysis

The characteristic intensity of the signal S_A is related to the number of atoms per air unit in the volume probed:

$$S_A(\theta_c, \Delta E) = N_A . \sigma_A(\theta_c, \Delta E) I_0(\theta_c, \Delta E)$$

N_A: number of atoms of the element A present in the volume analysed.
$\sigma_A(\theta, \Delta E)$: diffusion cross-section of core-level excitation partially integrated on the collection angle θ_c and the energy loss window ΔE.
$I_0(\theta_c, \Delta E)$: intensity measured over the energy range ΔE in the collection angle θ_c.
$S_A(\theta_c, \Delta E)$: characteristic signal after the extraction of the background.

The concentration ratio of two elements A and B can be obtained, considering that the previous relation is verified for both elements detected on a spectrum.

$$\frac{N_A}{N_B} = \frac{S_A(\theta_c, \Delta E)}{S_B(\theta_c, \Delta E)} \frac{\sigma_B(\theta_c, \Delta E)}{\sigma_A(\theta_c, \Delta E)}$$

In our presented analysis, the same integrated energy windows where used respectively to extract the background and characteristic signal for different elements compared.

B.4 EELS/ EDXS comparison

Some studies report a comparison between both EDXS and EELS spectroscopies [LEA91, TIT89]. The table below summarizes advantages and drawbacks of both techniques.

Technique	Advantages	Drawbacks
EDXS	- more efficient for heavy elements - a direct evolution of the element composition - non-destructive (if beam not too focalised…) - Low background	-Needs a known sample and a high statistical measure (needing a sample stability) for quantification. - Presence of elements artefacts: Fe & Co (from polar pieces).
EELS	- Quantification -Highest spatial resolution and best analytical sensitivity -more efficient for light elements -diffusion is mainly concentrated on the direction of the electron beam propagation, what allows a more efficient detection. - can be localised with HRTEM observation, and the correlated to the structure - gives information of the elements boundaries, unoccupied state density, oxidation stage… - the sample thickness can be extracted	-Study of heavy elements not possible. -Overlapping of the signal for elements having similar energy threshold. -Extraction and interpretation.

Table B.1: Comparison of EDXS and EELS spectroscopies with its respective advantages and drawbacks [TIT89-99].

Appendix C
Other characterization techniques

C.1 Atomic Force Microscope (AFM)

The atomic force microscope (AFM) permits to probe the surface topology, scanning with extremely high resolution (typically around 0.1 Å in the vertical direction, and from atomic resolution to some nm in the lateral direction). The AFM is composed by a tip holded in a cantilever which scans the sample surface as shown in figure C.1.

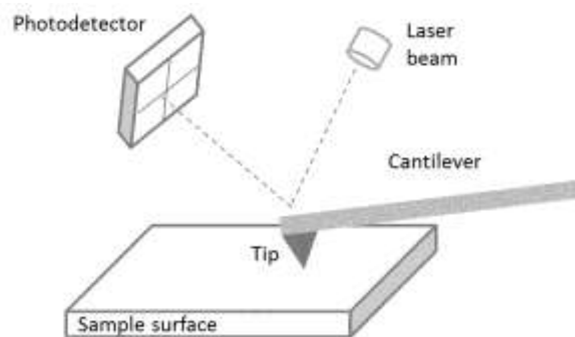

Figure C.1: Sketch of the principal components of an AFM.

The normal forces exerted from the surface to the tip generate a cantilever deflection proportional to the force. A laser beam pointed on the cantilever is reflected in a photodiode detector with four panels, which measures the deflection during the scanning process. The characterization of the surface topography can be done in three different modes: contact mode, non-contact mode, and tapping (intermittent/dynamic) mode. The higher force sensibility can be obtained in contact mode, but the measure is usually slow, it can be distorted in case of rough surfaces and the tip and the scanned surface can be damaged. While the tip mainteined at a distance from the surface in the non-contact mode allows conserving it intact, but the force detection and the resolution is reduced. The tapping mode, alternating the contact and non-contact modes, results to be a good compromise mode. The surface morphology of the samples studied in this thesis has been measured by tapping mode AFM.

C.2 Superconducting quantum interference device (SQUID)

A superconducting quantum interference device (SQUID) is a magnetometer used to measure very weak magnetic fields. It is composed by a superconductive loop where the critical current Ic under a magnetic flux Φ is measured. The flux variation created by a magnetic sample is detected. The electrical signal resulting from the induced voltage permits to determine the magnetization with a resolution of 10^{-7} emu.The magnetic measurements were performed at ICMAB using a SQUID system of Quantum Design. Measurements were done at 5 and 300 K, applying a magnetic field up to 7 T.

Appendix D
Thin film growth modes and interface

D.1 Thin film growth

Surfaces often change their form away from the simple "cleaved bond" bulk model. They are found to be highly dynamic regions, which readily rearrange or react, so that energy is often reduced by such processes as passivation, adsorption or reconstruction.
On the first step of the film deposition, atoms are adsorbed on the substrate surface creating an energetic equilibrium. Adatoms diffusion is dictated by kinetic energy, temperature, interfacial bonding, among other parameters. The possible growth mode can be discussed considering the surface tension of the substrate γ_S, the deposited material γ_d and their interface γ_i. The relationship between the surface tension can be written as: $\gamma_S = \gamma_d \cos\Theta + \gamma_i$ or $\cos\Theta = (\gamma_S + \gamma_i)/\gamma_d$. The adhesion coefficient is defined as: $\beta = \gamma_S + \gamma_d - \gamma i$, and the adhesion thermodynamic work needed to "remove the interfacial connection" is $W_{adh} = \sigma_s + \sigma_{d-} \sigma_i$, where σ_s, σ_{d} and σ_i are respectively the surface tension of the substrate, the deposited material, and the interface.

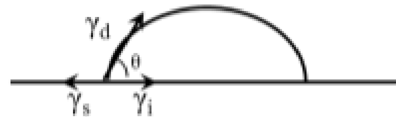

Figure D.1: Sketch of a droplet deposited on a substrate.

In this model, three-dimensional growth in the case of: $\cos\Theta<1$, $\gamma_S - \gamma_d - \gamma_i<0$, $\beta-2\gamma_d<0$ or $\gamma_S< \gamma_d+ \gamma_i$, and two-dimensional growth in the opposite case where the deposited material wets the surface: $\gamma_S - \gamma_d - \gamma_i>0$, $\beta-2\gamma_d>0$, or $\gamma_S> \gamma_d+ \gamma_i$.

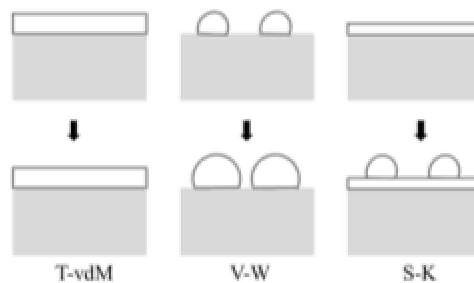

Figure D.2: Sketch of the three possible growth modes: Frank-van der Merwe (2D), Volmer-Weber (3D), and Stranski-Krastanov (2D +3D).

In addition, a combined two and three-dimensional growth in two steps is possible. Initially complete films are grown until a critical thickness, and the growth continues with the nucleation of islands.

D.1.1 Epitaxial growth

In the particular case of crystalline growth on a monocrystalline substrate, the epitaxy is defined by the long-range order of the crystalline lattice of the thin film in its whole

volume. The crystallographic relation between these two materials (A and B) is defined by matching of both lattices. The film can adopt the substrate lattice parameter by an elastic deformation, or conserve its own lattice parameter by a plastic deformation. Then, the epitaxy growth is described with two different modes: pseudomorphic or coherent growth (figure D.3.a) and relaxed growth (figure D.3.b).If the growth is not relaxed, the deformation is typically described by its two components: in-plane and out-of–plane. In the case of a pseudomorphic growth, the deposited material (A) or film is under tensile strain if $a_f < a_s$, and under compressive strain if $a_f > a_s$ (figure D.3.a).

(a)

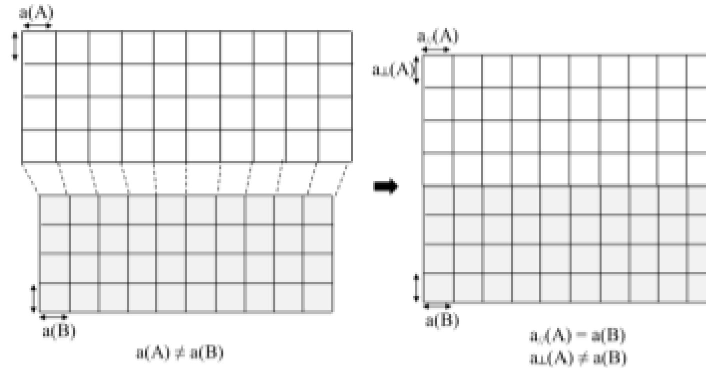

(b)

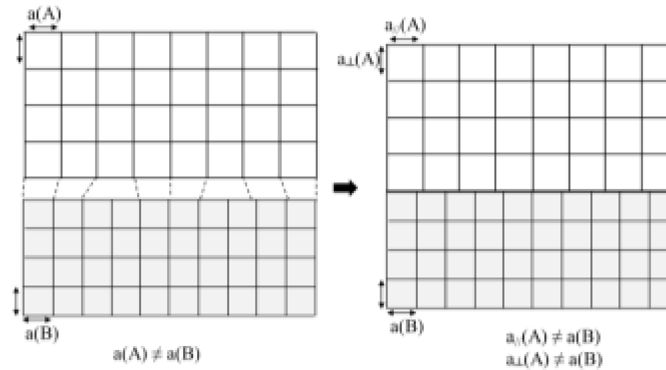

Figure D.3: Sketch of the epitaxial growth modes for different cubic materials: pseudomorphic (a), and relaxed (b).

The mismatch m between the thin film (a_f) and the substrate (a_s) is typically defined by $m = \frac{(a_f - a_s)}{a_s}$. It can also be define with respect to the film parameter $m' = \frac{(a_s - a_f)}{a_f}$. For very low mismatch $m = m'$. In this thesis, the mismatches values are calculated in function of the substrate parameter.

Other epitaxial growth techniques are possible and involve a lateral film growth. Lateral epitaxial overgrowth (LEO) consists on coating a film with a patterned mask as SiO_2 or silicon nitride, and pendeo-epitaxy (PE) consists on stripes etched through the film into the substrate constituting a pseudomask. The growth is not only vertically, along the c axis, but also laterally, perpendicularly to the c-axis, over the mask. The lateral growth can be several times faster than the growth along the c-axis. Ideally there should be no dislocations grow along the c-axis in the wing regions.

D.1.2 Elastic deformation

The mismatch presented between a deposited material and its substrate can originate an elastic deformation of the thin film. The accommodation of misfit across the interface can be partial and originate dislocations. The elastic deformation tends to disappear for thick films. As elastic energy is proportional to the thickness film, there is a critical thickness h_c from which the elastic strain relaxes and is converted into plastic misfit strain, generating misfit dislocations. The formation of islands can also allow the relaxation of a 2D film by a Stranski-Krastanov growth mode. The parameters involved are the difference between the two bulk lattice parameters, the thickness of the film, the geometry of the dislocations, and the bonding across the interface.

D.1.3 Plastic deformation

The plastic deformation appears from a critical thickness of the film, where the deposited material recovers its own lattice parameter by a relaxation introducing dislocations at the interface. A residual strain can remain for a partial relaxation of the film. The critical thickness can be calculated from the elastic constants and the mismatch, supposing equilibrium and that the substrate is not deformed. The plastic deformation is done by a shift of a part of a crystal with respect to another part of it. The crystalline continuity is conserved by this displacement of few lattices in a sliding/glide plane. Generally the sliding planes are the more compact planes in a crystal: (111) for a cfc. The linear defects created are dislocations characterized by the Burgers vector $\vec{b}$.

D.1.4 Critical thickness h_c

In pseudomorphic heteroepitaxy, the mismatch of lattice constants originates a strain energy stable until a critical thickness h_c. Above this thickness, dislocations are generated at the interface, and the film relaxes. The concept of critical thickness was introduced by Frank and Van der Merwe, based on energy considerations and limited for systems with moderate misfits(<4%): $h_c = 0.1\frac{a_0}{f}$, where a_0 is the bulk lattice of the substrate and f is the misfit ($f=(a_f-a_s)/a_s$). The minimum energy to generate dislocations corresponds to the interfacial energy [MER62].

Applying this model to both epitaxial domain matching interfaces of $CFO/Y_2O_3/Si(111)$, the critical thickness of Y_2O_3 on Si is 4.57 nm, and the CFO critical thickness on Y_2O_3 is then 5.76 nm. The thickness of the films studied in chapter V are both superior to the critical ones calculated. Then, the presence of interfacial dislocations is consistent with this model.

The same critical thickness is given by Matthew and Blakeslee using a force balance approach [MAT70-75].

$$h_c = \frac{b}{8\pi f}\frac{(1-\upsilon\cos\theta)}{(1+\upsilon)\cos\lambda}\left(\ln\frac{h_c}{b}+1\right)$$

In addition, a very different critical thickness was obtained by People and Bean using the energy minimisation approach [PEO85].

$$h_c \approx \frac{1}{16\sqrt{2\pi}}\left(\frac{1-\upsilon}{1+\upsilon}\right)\frac{b2}{af2}\ln\frac{h_c}{b}$$

The major difference between these two models is the dependence in 1/f or $1/f^2$.

(1) (2)

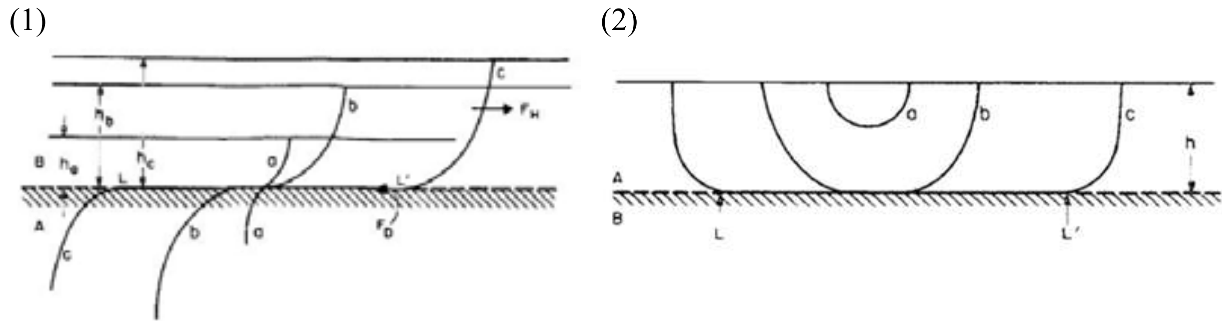

Figure D.4: Sketch of the nucleation and growth of a threading dislocation (1), and of a half-loop dislocation. The dislocation growth process is detailed in three steps: in a coherent interface (a), critical interface (b), and an incoherent interface (c) [PEO85].

And the concept of critical thickness was even questioned by S.M.Hu, as the dislocation density could gradually increase with the thickness [HU_91].

Marée proposed another formula relying the critical thickness h_c, the Burger's vector $\vec{b}$, the mismatch m, the Poisson's coefficient υ, and the dislocation parameter α (4 for semiconductors) [MAR87].

$$m\mathrm{h}_c = \frac{b}{8\pi(1+\upsilon)} \ln\alpha \frac{h_c}{b}$$

This calculus is only satisfied for semiconductors, and then the Matthews formalism is preferred.
Some dislocation concepts are presented above (part D.3), and mechanisms of generation and multiplication of dislocations were studied by other groups [CHI90-2, GIL94] and summarized by V.I. Vdovin [VDO99].

D.2 <u>Interface microstructure</u>

There are three types of interfaces: coherent, semi-coherent and incoherent. The major difference between them concerns the surface energy $\gamma_{interface}$ which can be decomposed with a chemical and a structural component: $\gamma_{interface} = \gamma_{chem} + \gamma_{struct}$.
A coherent interface arises when two crystals match perfectly at the interface plane conserving a continuity of the two lattices across the interface. The structure is then conserved and new chemical bonds are created between the two materials. The coherent interfacial energy needed for the creation of this interface is then $\gamma_{chemical}$.
For larger misfits a strain is originated and it becomes energetically unfavourable to conserve a coherent interface $\gamma_{semi\text{-}coherent\ interface} = \gamma_{chem} + \gamma_{st}$. Misfit dislocations appears then in a semi-coherent interface. The semi-coherent interfacial energy range is 200-500 mJ/m^2. When the mismatch increases, the dislocation spacing in the interface decreases. For small values of mismatch, the density of dislocations is roughly proportional to the structural contribution to the interfacial energy. For increasing misfits values up to 0.25, γ_{st} increases less rapidly and the dislocation spacing decreases. The associated strain field tends to overlap and annul each other.
An incoherent interface takes place for larger misfits, where a dislocation appears every few interplanar spacings with poor fit, and overlap with others. Typically, the interplanar distances differ more than 25% do not allow a good matching. Then the structural contribution is very large on the incoherent interfacial energy (500-1000 mJ/m^2).

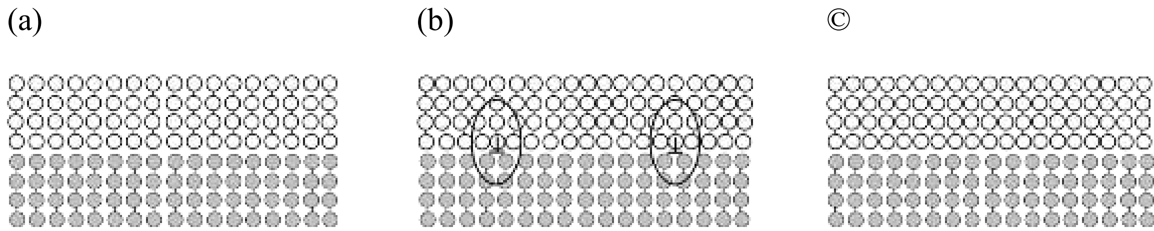

Figure D.5: Schematic drawing of: (a) a coherent interface, (b) a semicoherent interface, and (c) an incoherent interface. Adapted from [GUT97].

In a coherent interface (figure D.5), the lattice mismatch is entirely accommodated by straining the lattice of the film. There is an atomic continuity between both materials along the interface, resulting in a periodicity parallel to the interface. Semicoherent interfaces are characterized by coherent regions separated by misfit dislocations ⊥. The misfit dislocations accommodate the lattice mismatch partially or completely. The lattice in the bulk of the film is not strained if the misfit dislocations accommodate the entire lattice mismatch, and the distance between mismatch dislocations can be calculated. Incoherent interfaces match two rigid connected lattices and are not periodic parallel to the interface. Incoherent interfaces can also be interpreted as an extreme case of a semicoherent interface in which the displacement field of the misfit dislocation vanishes, that is the dislocation core of the misfit dislocation is completely delocalised.

Defaults in semi-coherent and incoherent interfaces as vacancies can allow diffusion mechanisms. Then it seems critical to obtain coherent interfaces to avoid diffusion and the creation of new phases. Thus, for a given diffusion coefficient, the incoherent interface moves fastest, while the coherent one are more stable. Becker's model describes the coherent interface: the surface energy is proportional to the square of concentration gradient:
$\gamma = (dC/dx)^2$.

D.3 <u>Dislocations</u>

A dislocation is a line defect where an atomic plane sliding over an adjacent one, originated by plastic deformation in a single crystal under a critical shear stress. There are two types of dislocation geometry: edge and screw dislocations. The model of a simple cubic lattice assumes that the bonds can be represented as flexible springs between adjacent columns [DOU08, HIR68, HUL01]. Dislocations are characterized by the Burgers vector $\vec{b}$, which is normal to the line of the dislocation for an edge dislocation, and parallel to the line of the dislocation for a screw dislocation. In most general cases, a dislocation line has a mixed edge and screw character. A dissociation of this dislocation decreases its energy, and increases its mobility. The dislocation propagation takes place orthogonally to the dislocation line. The dislocations with the same line sense but opposite Burgers vector or alternatively with opposite line sense but opposite Burgers vector, are physical opposites and can annihilate each other to restore the perfect crystal. Other, called pile-up dislocation can slide and stack in a microstructural defect as grain boundaries, generating a strain zone able to fissure. The dislocation study in the active areas of devices seems critical and complementary to strain characterization. Formation and influence of interfacial dislocations in thin films microstructure and ferroelectric properties has been investigated [ALP04, MAT74b, NAR02, TRU02, ZHE 06]. It has been found that the hysteresis loop for $BaTiO_3$ films is strongly dependent on the type and density of interfacial dislocations. Controlling the formation of dislocation could then enhance or reduce coercitive field and remanent polarization [LI_08].

The Burgers vector can be determined by dark field imaging mode selecting different diffracted beams, and FFT-reconstructed image from the correspondent in-plane spots allows to localise interfacial dislocations.

The magnitude of length b of the smaller vector for a centered cubic cell $\vec{b} = \frac{1}{2} < 111 >$ is:

$$b = \sqrt{(\frac{a^2}{4} + \frac{a^2}{4} + \frac{a^2}{4})} = \frac{a\sqrt{3}}{2}$$

Similarly, in a faced centered cubic structure, $\vec{b} = \frac{1}{2} < 110 >, b = a/\sqrt{2}$.

The misfit m equals the strain ε of the film if the lattice mismatch is only accommodated by straining the film lattice (coherent interface). If the lattice mismatch is fully accommodated by misfit dislocations, the average distance d_{MD} between the misfit dislocations is:

$$d_{MB} = |\overrightarrow{b_{MB}}| \frac{1}{m}$$

$\overrightarrow{b_{MB}}$ is the Burgers vector component of the misfit dislocations, which is parallel to the interface, and $m=(a_s-a_f)/a_s$.

The theoretical distance between dislocations in a semicoherent interface can be calculated from the smallest atomic spacing of the A and B materials (film and substrate) along the interface, d_A and d_B respectively. The lattice mismatch induces the matching of nd_A with $(n+1)d_B$ for $d_A>d_B$. There will be an extra B plane with respect to A every D step, originating a misfit dislocation.

$$nd_A = (n+1)d_B$$
$$nd_A = nd_B + d_B$$
$$nd_A - nd_B = d_B$$
$$n(d_A - d_B) = d_B$$

$$n = \frac{d_B}{(d_A - d_B)}$$

The misfit dislocation step D at the interface of a relaxed thin film on a substrate can be calculated from the in-plane interplanar distances d_A and d_B:

$$D = \frac{d_A d_B}{|d_A - d_B|}$$

d_A and $d_B$are the smallest interplanar spacing along the interface, then corresponds to a fraction of the interplanar distance calculated directly from the lattice parameter.

Ie: CFO: $d_A = \frac{1}{4} d(001)$; $d_B = \frac{1}{3} d(110)$; STO: $d_A = \frac{1}{2} d(001)$…

The dislocation step can be expressed in function of the materials mismatch ($m = (a_f-a_s)/a_s$):

$$D = \frac{100}{m}$$

It can be noted that even if the mixted (edge and screw) dislocationis the most common configuration, pure edge dislocation can be considered in epitaxial systems where a small lattice mismatch induces dislocations at the interface.

Scientific contributions

Publications list:

1- *Mechanisms of epitaxy and defects at the interface in ultrathin YSZ films on Si(001)*
P. de Coux, R. Bachelet, C. Gatel, B. Warot-Fonrose, J. Fontcuberta and F. Sánchez
Cryst. Eng. Comm. 14, 7851-7855 (2012).

2- *Domain matching epitaxy of ferromagnetic $CoFe_2O_4$ thin films on Sc_2O_3/Si(111)*
F. Sánchez, R. Bachelet, P. de Coux, B. Warot-Fonrose, V. Skumryev, L. Tarnawska, P. Zaumseil, T. Shroeder and J. Fontcuberta
Appl. Phys. Lett. 99, 211910(2011).

3- *Flat epitaxial ferromagnetic $CoFe_2O_4$ films on buffered Si(001)*
R. Bachelet, P. de Coux, B. Warot-Fonrose, V. Skumryev, J. Fontcuberta and F. Sánchez
Thin solid films 519, 5726-5729 (2011).

4- *$CoFe_2O_4$/ buffer layer ultrathin heterostructures on Si(001)*
R. Bachelet, P. de Coux, B. Warot-Fonrose, V. Skumryev, J. Fontcuberta and F. Sánchez
J. Appl. Phys. 110, 086102 (2011).

Oral communications: (presenting author is underligned)

1- *Integration of ferrimagnetic $CoFe_2O_4$ on Si(111) buffered with Y_2O_3: epitaxial growth and sharp interfaces*
P. de Coux, B. Warot-Fonrose, R. Bachelet, V. Skumryev, J. Fontcuberta, L. Tarnawska, P. Zaumseil, T. Schroeder, F. Sánchez
European Materials Research Society (MRS) Spring Meeting, Strasbourg (France), 2013.

2- *Two-dimensional growth and properties of magnetoelectric $BaTiO_3$-$CoFe_2O_4$ epitaxial bilayers on $SrTiO_3$(001) and Si(001)*
F. Sánchez, I. Fina, N. Dix, R. Bachelet, M. Scigaj, P. de Coux, B. Warot-Fonrose, C. Kanamadi, L. Fàbrega, J. Fontcuberta
Invited talk, The 7th International Conference on Advanced Materials, ROCAM, Brasov, Rumanía, 2012.

3- *Integration of ferromagnetic spinel oxide on silicon using structurally-compatible γ-Al_2O_3 nanometric epitaxial buffer-layer*
R. Bachelet, F. Sánchez, P. de Coux, B. Warot-Fonrose, V. Skumryev, G. Niu, B. Vilquin, G. Saint-Girons, G. Hollinger, J. Fontcuberta
European Materials Research Society (MRS) Spring Meeting, Strasbourg, France, 2012.

4- *Epitaxy of ferroelectric $BaTiO_3$ and ferrimagnetic $CoFe_2O_4$ on Si(001)*
F. Sánchez, P. de Coux, R. Bachelet, N. Dix, I. Fina, C. Carrillo, L. Fàbrega, V. Skumryev, B. Warot-Fonrose, J. Fontcuberta
European Materials Research Society (MRS) Spring Meeting, Strasbourg, France, 2012.

5- *Integration of functional oxides with semiconductors*
R. Bachelet, F. Sánchez, P. de Coux, B. Warot-Fonrose, V. Skumryev, G. Niu, B. Vilquin, G. Saint-Girons, G. Hollinger, J. Fontcuberta.
Invited talk, Collaborative Conference on Crystal Growth (3CG), Orlando, December 2012.

6- *Integration of ferromagnetic spinel oxide on silicon using ultrathin structurally-compatible epitaxial buffer-layer*
R. Bachelet, F. Sánchez, P. de Coux, B. Warot-Fonrose, V. Skumryev, G. Niu, B. Vilquin, G. Saint-Girons, G. Hollinger, J. Fontcuberta.
Material Research Society (MRS) Fall meeting- Boston- November 2012.

7- *Epitaxy of ferroelectric $BaTiO_3$ and ferromagnetic $CoFe_2O_4$ on Si(001)*
F. Sánchez, P. de Coux, R.Bachelet, N.Dix, I.Fina, C.Carrillo, L.Fàbrega, V.Skumryev, B. Warot-Fonrose, J. Fontcuberta
European Material Research Society (E-MRS), Spring Meeting, Strasbourg, France, May 2012.

8- *Integration of ferromagnetic spinel oxide on silicon using structurally-compatible γ-Al_2O_3 nanometric epitaxial buffer-layer*
R. Bachelet, F. Sánchez, P. de Coux, B. Warot-Fonrose, V. Skumryev, G. Niu, B. Vilquin, G. Saint-Girons, G. Hollinger, J. Fontcuberta.
European Material Research Society (E-MRS), Spring Meeting, Strasbourg, France, 2012.

9- *Integration of ferrimagnetic $CoFe_2O_4$ and ferroelectric $BaTiO_3$ with Si(001)*
F. Sánchez, R. Bachelet, N. Dix, P. de Coux, I. Fina, C. Carrillo, B. Warot-Fonrose, L. Fàbrega, V. Skumryev, J. Fontcuberta
Materials Research Society (MRS) Fall Meeting, Boston, USA, 2011.

10- *Integration of functional complex oxides with silicon*
F. Sánchez, R. Bachelet, P. de Coux, B. Warot-Fonrose, N. Dix, I. Fina, C. Carrillo, L. Fàbrega, V. Skumryev, L. Tarnawska, P. Zaumseil, T. Schroeder, J. Fontcuberta
Barcelona Nanotechnoloy Cluster – Bellaterra (BNC-b) Meeting, Bellaterra, 2011.

11- *Microstructural characterization of epitaxial nanometric $CoFe_2O_4$/YSZ films on Si(001)*
P. de Coux, R. Bachelet, B. Warot-Fonrose, V. Skumryev, J. Fontcuberta and Florencio Sánchez
European Materials Research Society (EMRS) Spring Meeting, Nice, France, 2011.

12- *Epitaxial ferromagnetic $CoFe_2O_4$(111) films on CeO_2/YSZ/Si(001)*
P. de Coux, B. Warot-Fonrose, R. Bachelet, V. Skumryev, J. Fontcuberta, F. Sánchez
European Materials Research Society (EMRS) Spring Meeting, Strasbourg, France, 2011.

13- *Integration of nanometric spinel oxides with silicon*
P. de Coux, R. Bachelet, B. Warot-Fonrose, J. Fontcuberta and Florencio Sánchez
« Journée des doctorants du CEMES » (SEMEC), Toulouse, France, 2011.

14- *Integration of nanometric spinel oxides with silicon : challenges and strategies*
P. de Coux, R. Bachelet, B. Warot-Fonrose, J. Fontcuberta and Florencio Sánchez
« Journées de l'Ecole Doctorale Science de la Matière » (JED), Laboratoire de Chimie de Coordination LCC-CNRS, Toulouse, France, May 2011.

15- *Structural properties of epitaxial ferromagnetic $CoFe_2O_4$ films on Si(001)*
P. de Coux, R. Bachelet, B. Warot-Fonrose, V. Skumryev, J. Fontcuberta and Florencio Sánchez
« Journées EELS » (JEELS): Les Diablerets, Switzerland, 2011.

16- *Integration of Functional Complex Oxides with Silicon*
F. Sánchez, R. Bachelet, P. de Coux, B. Warot-Fonrose, N. Dix, I. Fina, C. Carrillo, L. Fàbrega, V. Skumryev, L. Tarnawska, P. Zaumseil, T. Schroeder, J. Fontcuberta
Consolider Nanoselect Meeting, Sant Feliu de Guixols, 2011.

17- *Microstructural characterization of YSZ on Si(001) and its use as buffer layer for the integration on functional oxides*
P. de Coux, R. Bachelet, B. Warot-Fonrose, V. Skumryev, J. Fontcuberta and Florencio Sánchez
TEM-UCA: "Transmission Electron Microscopy of Catalytic Materials and Nanoparticles", European Summer Workshop, Cadiz, Spain, 2010.

Posters list:

1- *Domain Matching Epitaxy of ferromagnetic $CoFe_2O_4$ on Si(111) buffered with A_2O_3 (A=Sc, Y)*
P. de Coux, B.Warot-Fonrose, R. Bachelet, V. Skumryev, L.Tarnawska, P. Zaumseil, T. Shroeder, J.Fontcuberta and Florencio Sánchez
XVème Colloque Louis Néel, Tours, France, 2013.

2- *Domain Matching Epitaxy of ferromagnetic $CoFe_2O_4$ on Si(111) buffered with A_2O_3 (A=Sc, Y)*
P. de Coux, B.Warot-Fonrose, R. Bachelet, V. Skumryev, L.Tarnawska, P. Zaumseil, T. Shroeder, J.Fontcuberta and Florencio Sánchez
Nanoselect annual meeting, Costa Brava, Spain, 2012.

3- *Microstructural characterization and chemical analysis of epitaxial nanometric YSZ films on Si(001)*
P. de Coux, R. Bachelet, B. Warot-Fonrose, J. Fontcuberta and Florencio Sánchez
12ème Colloque de la Société Française de Microscopie (SFMU) Strasbourg,France, 2011.

4- *Integration of nanometric spinel oxides with silicon : challenges and strategies*
P. de Coux, R. Bachelet, B. Warot-Fonrose, J. Fontcuberta and Florencio Sánchez
«Journées de l'Ecole Doctorale Science de la Matière » JED, 2011.

5- *Microstructural characterization of epitaxial ferromagnetic $CoFe_2O_4$(111) films on CeO_2/YSZ/Si(001)*
P. de Coux, R. Bachelet, B. Warot-Fonrose, J. Fontcuberta and Florencio Sánchez
XIII^{ème}Colloque Louis Néel 2010 « Couches minces et nanostructures magnétiques », 2010.

6- *Epitaxial ferromagnetic $CoFe_2O_4$(111) films on Si(001) buffered with ultrathin YSZ layers*
P. de Coux, R. Bachelet, B. Warot-Fonrose, V. Skumryev, J. Fontcuberta, F. Sánchez
17th Workshop on oxides electronics (WOE), Awaji, Japan, 2010.

7- *Integration of nanometric spinel oxides on buffered silicon*
P. de Coux, R. Bachelet, B. Warot-Fonrose, J. Fontcuberta and Florencio Sánchez
« Journée des doctorants du CEMES »(SEMEC), 2010.

Acknowledgments

This thesis was made in collaboration between the CEMES in Toulouse and the ICMAB in Barcelona. During this period, I had the great pleasure to workin constant interaction and collaboration with a list of people from different institutes who made possible the work presented here.

First of all, I would like to express my gratitude to my supervisors Dr. Bénédicte Warot-Fonrose and Florencio Sánchez Barrera, to have leaded and supported me during this adventure. They have contributed to my scientific and personal evolution with great patience over this period.

I thank all the jury members for evaluating this thesis, in particular Luis A. Morellón Alquézar for accepting to preside the jury, and Francesca Peiró Martínez and Yves Dumont for assessing this work.

I want to devote my gratitude to certain colleagues and collaborators that have contributed in the elaboration of thin films and in the characterization analysis. I have particularly to thank Romain Bachelet for its thin film work and its strong implication in my training in thin films growth and RHEED characterization. I also want to thank particularly Christophe Gatel for his precious contribution to obtain and analyze HRTEM characterizations. I want to address a particular acknowledgement to Jacques and Cathy Crestou, for their kind explanations, advices and company in the sample preparation for TEM; and to Florent Houdellier for the TEM trainings and high disponibility to step in(and for not being too hard when I made an air entry….).

I thank Prof. Vassil Skumryev for the magnetic measurements and the technicians of the AFM service of the ICMAB for the performance oftopographic measurements. And I want to specially thank Sébastien Joulié for its disposal to perform STEM-EDXS experiments, even if it is not reflected in this manuscript.

No matter the order of reference, I have to thank L. Tarnawska, P. Zaumseil, T. Shroeder, and all the group of the IHP of Frankfurt for providing A_2O_3 (A=Sc, Y) buffers on Si(111). And the group of the INL of Lyon for those of $SrTiO_3$ on Si(001).

I would like to express my gratitude to the "Ecole Doctorale Sciences de la Matière" (EDSDM), and in particular to Michel Caffarel and Soraya Berkouk, for their guidance in this project, far more than the thesis.
I thank also the invaluable help of the administrative personnel of both universities, and in particular Sandra Germinano and Albert Girao who made possible this cotutelle UPS-UAB.
A special thanks to Jordi Sort and Javier Rodríguez Viejo, respectively coordinator and tutor of the thesis. And I would like to express my gratitude to my Godfather Jérémy Grisolia for its kind foster.

This work was made in the framework of a BDI ICMAB/CNRS scholarship, and I would like to thank the proved confidence of these two institutions by their financing. I also want to acknowledge the University Paul Sabatier of Toulouse for attributing me a mobility grant (ATUPS).

Moreover, I would like to express my gratitude to all the laboratories members for sharing places and moments unforgettable for me.
I want to address a particular acknowledgement to Jacques Crestou, Christophe Gatel, Florent Houdellier, Nico Dix, Xavi Martí and Jaume Roqueta for their explanation about material science or transmission electron microscopy with such passion. I learned a lot about your knowledge and person, and every discussion with you has brought me lots of motivation and provides me more questions (and sometimes answers….).
I spent great moments with all the PhD students and post-docs. I want to thank particularly Elsa Javon for her disposal to take a break (between scientific and theater classes) and continue discussing about anything, including about work! And for making be laugh everytime she loses her keys or anything else…. I would like to thanks warmly Mayerling for her contagious smileand happiness, and all the Spanish invasors for contributing to the CEMES ambience. I particularly thank the all the friends who spent a week-end in Espot, the Basque country or the Mediterranean coast, and of course, Robin, the best flatmate!

And most of all, thanks to my family, who has given me the support and constancy during this period filled with emotion.

References

AFA07 V. V. Afanas'ev et al., *Electronic structure of silicon interfaces with amorphous and epitaxial insulating oxides: Sc_2O_3, Lu_2O_3, $LaLuO_3$,* Microelectronic Engineering **84**, 2278–2281 (2007).

AGU97 R. Aguiar et al., *Effects of wavelength, deposition rate and thickness on laser ablation deposited YSZ films on Si(001)*,Thin Solid Films **304**, 225 (1997).

AKA05 D. Akai et al., *Ferroelectric properties of sol-gel delivered epitaxial Pb(Zrx,Ti1−x)O_3 thin films on Si using epitaxial γ-Al_2O_3 Layers*, Appl. Phys. Lett. **86**, 202906 (2005).

ALP04 S.P. Alpay et al., *Can interface dislocations degrade ferroelectric properties?*, Appl. Phys. Lett., **85**, 11 (2004).

BAC08 R. Bachelet, et al., *Reversible growth-mode transition in $SrRuO_3$ epitaxy*, Appl. Phys. Lett. **98**, 151916 (2008).

BAC11 R. Bachelet, et al., *$CoFe_2O_4$/buffer layer ultrathin heterostructures on Si(001)*, J. Appl. Phys. **110**, 086102 (2011).

BAR93 D.J. Barber, *Radiation damage in ion-milled specimens: characteristics, effects and methods of damage limitation*, Ultramicroscopy **52**, 101-125, (1993).

BAR94 T. Bardal, et al., *Initial stages of epitaxial growth of Y-stabilized ZrO_2 thin films on a-SiOx/ Si(001) substrates*, J. Appl. Phys. **75**, 2902 (1994).

BAR98 A.Barna et al., *Amorphisation and surface morphology development at low-energy ion milling*, Ultramicroscopy, **70**, 161-171 (1998).

BAR99 A.Barna et al., *TEM sample preparation by ion milling/amorphisation*, Micron **30**, 267-276 (1999).

BEN90 J. Benedicte et al., *Specimen Preparation for Transmission Electron Microscopy of Materials-II* Mater. Res. Soc. Symp. Proc. **199**, 189 (1990).

BER90 M.A. Berding et al., *Cleavage energies in semiconductors,* J. Appl. Phys. 67, 10 (1990).

BHU03 M.N.K. Bhuiyan et al., *Study of epitaxial $SrTiO_3$ (STO) thin films grown on Si(001)-2×1 substrates by molecular beam epitaxy*, Appl. Surf. Sc. **216**, 590-595 (2003).

BIB01 Bibes et al., *Nanoscale Multiphase Separation at $La_{23}Ca_{13}MnO_3SrTiO_3$ Interfaces*, Phys. Rev. Lett. **87**, 067210 (2001).

BIB12 M. Bibes, *Nanoferronics is a winning combination*, Nat. Mater. **11**, 354 (2012).

BOJ03 N.A. Bojarczuk et al., *Epitaxial silicon and germanium on buried insulator heterostructures and devices,* Appl. Phys. Lett. **83**, 5443 (2003).

BOZ55 R.M. Bozoth et al., *Anisotropy and magnetostriction of some ferrites*, Phys. Rev. **99**, 1788 (1955).

BRI00 M.R. Brickey and J.L. Lee, *New technique for successful thermal barrier coating specimen preparation for transmission electron microscopy*, Microsc. Microanal. **6**, 231-236, (2000).

CAF91 J.P. McCaffrey, *Small-angle cleavage of semiconductors for transmission electron microscopy*, Ultramicroscopy **38**, 149-157 (1991).

CAF97 J.P. McCaffrey et al., *Transmitted color and interfaces fringes for TEM sample preparation of*

silicon, Micon **29**, 139-144 (1997).

CAF98 J.P.Mc Caffrey and J. Hulse, *Transmitted color and interference fringes for TEM sample preparation of silicon*, Micron, **29**, 139-144, (1998).

CAF01 J.P.Mc Caffrey et al., *Surface damage formation during ion-beam thinning of samples for transmission electron microscopy*, Ultramicroscopy **87**, 97-104 (2001).

CAR96 D.B. Williams and C.B. Carter, *Transmission electron microscopy*, Specimen preparation, Plenum Press (1996).

CAS53 R.Castaing et al., C.R. Acad. Sc. (1953).

CHE05 C.P. Chen et al., *Thin single-crystal Sc_2O_3 films epitaxially grown on Si(111) structure and electrical properties,* J. Cryst. Growth **278**, 638-642 (2005).

CHI90-1 W.Y. Ching and Y.N. Xu, *Electronic and optical properties of yttria,* Phys. Rev. Lett., **67**, 895 (1990).

CHI90-2 D. Chidambarrao et al., *Effect of peierls barrier and epithreading dislocation orientation on the critical thickness in heteroepitaxial structures*, Appl. Phys. Lett., **57**, 10 (1990).

CHO97 S. C. Choi et al., *Epitaxial growth of Y_2O_3 films on Si(100) without an interfacial oxide layer,* Appl. Phys. Lett. **71**, 7 (1997).

CHO99 M.-H. Cho et al., *Structural transition of crystalline Y_2O_3 film on Si(111) with substrate temperature,* Thin Solid Films, **349**, 266-269 (1999).

CHO01 M.-H. Cho et al., *Epitaxial Y_2O_3 films grown on oxidized Si(111) surface,* J. Appl. Phys. **89**, 3 (2001).

CHO02 M.-H. Cho et al., *Epitaxial Y_2O_3 film growth on an oxidized Si surface,* Thin Solid Films, **402**, 38-42, (2002).

CHO03 M.H. Cho et al., *Thermal stability of epitaxial Pt films on Y_2O_3 in a metal-oxide-Si structure,* Appl. Phys. Lett., **83**, 23 (2003).

CHR08 H.M. Christen and G.Eres, *Recent advances in pulsed-laser deposition of complex oxides*, J. Phys. Condens. Matt., 264005 (2008).

COP00 M. Copel et al., *Structure and* stability of ultrathin zirconium oxide layers on Si(001), Appl. Phys. Lett. **76**, 436 (2000).

COP02 M.Copel, et al., *Characterization of silicates/Si(001) interfaces,* Appl. Phys. Lett., **81**, 22 (2002).

COP10 M.Copel, et al., *Stability of terbium scandate on Si(001),* Appl. Phys. Lett., **97**, 182901 (2010).

COW81 J.M. Cowley, *Diffraction physics*, ed. North-Holland Publising, Amsterdam (1981).

CRE69 A.V. Crewe et al, *A simple scanning electron microscope,* Rev. Sci. Inst. **40**, 241-246 (1969).

DAT94 Dat et al., *Polycrystalline $La_{0.5}Sr_{0.5}CoO_3/PbZr_{0.53}Ti_{0.47}O_3/La_{0.5}Sr_{0.5}CoO_3$ ferroelectric capacitors on 128icroscopy silicon with no polarization fatigue*, Appl. Phys. Lett. **64**, 2673 (1994).

DEK09 M.Dekkers et al., *Ferroelectric properties of epitaxial Pb(Zr, Ti)O_3 thin films on silicon by control of crystal orientation*, Appl. Phys. Lett. **95**, 012902 (2009).

DEK10 M. Dekkers et al., *Ferroelectric properties of epitaxial Pb(Zr, Ti)O_3 thin films on silicon by control of crystal orientation*, Appl. Phys. Lett. **95**, 012902 (2010).

DIE03 A.C. Diebold et al., *Thin dielectric film thickness determination by advanced transmission electron microscopy*, Microsc. Microanal. **9**, 493-508 (2003).

DIE11 L. Dieterle et al., *Optimized Ar^{+}-ion milling procedure for TEM cross-section sample preparation*, Ultramicroscopy **111**, 1636-1644, (2011).

DIX09 N. Dix et al., *Critical limitations in the fabrication of biferroic $BiFeO_3$-$CoFe_2O_4$ columnar nanocomposites due to bismuth loss,* Chem. Mater. **21**, 1375-1380 (2009).

DOU08 J. Douin, *Mécanique des milieux continus. Introduction à la plasticité des matériaux.*, Diderot multimédia (2008).

DUN00 R.E. Dunin-Borkowski, *The development of Fresnel contrast analysis, and the interpretation of mean inner potential profiles at interfaces*, Ultramicroscopy **83**, 193-216 (2000).

EAG90 D.J. Eaglesham and M. Cerullo, *Dislocation-free Stranski-Krastanow growth of Ge on Si(100)*, Phys. Rev. Lett., **64**, 1943 (1990).

EAS07 R. Eason, *Pulsed laser deposition of thin films: application-led growth of functional materials*, Wiley (2007).

EBE08 E. Eberg et al, *Comparison of TEM specimen preparation of perovskite thin films by tripod polishing and conventional ion milling*, J. Electron Microscopy **57**, 175-179 (2008).

EGE96 Egerton R. F., *Electron Energy Loss Spectroscopy in the Electron Microscopy* (Plenum, New-York, 2nd ed., 1996).

EGE09 R.F. Egerton, *Electron energy-loss spectroscopy in the TEM*, Rep. Prog. Phys. **72**, 016502 (2009).

EST08 S. Estradé, et al., *Cationic and charge segregation in $La_{2/3}Ca_{1/3}MnO_3$ thin films grown on (001) and (110) $SrTiO_3$*, Appl. Phys. Lett. **93**, 112505 (2008).

FIS06 T. Fissel, et al., *Interface formation during molecular beam epitaxial growth of neodymium oxide on silicon*, J. Appl. Phys. **99**, 074105 (2006).

FOE11 M. Foerster et al., *Distinct magnetism in ultrathin epitaxial $NiFe_2O_4$ films on $MgAl_2O_4$ and $SrTiO_3$ single crystalline substrates*, Phys. Rev. B **84**, 144422 (2011).

FON99-1 J. Fontcuberta et al., *Tunable epitaxial growth of magnetoresistive $La_{2/3}Sr_{1/3}MnO_3$ thin films*, J. Appl. Phys. **85**, 4800 (1999).

FON99-2 J. Fontcuberta, et al., *Epitaxial growth of magnetoresistive (00h), (0hh), and (hhh) $La_{2/3}Sr_{1/3}MnO_3$ thin films on (001)Si substrates*, Appl. Phys. Lett. **74**, 1743 (1999).

FOR90 D.K. Fork et al., *Epitaxial yttria stabilized zirconia on hydrogen terminated Si by pulsed laser deposition*, Appl. Phys. Lett. **57**, 1137 (1990).

FUK89 H. Fukumoto et al., *Heteroepitaxial growth of Y_2O_3 film on silicon,* Appl. Phys. Lett. **55**, 360, (1989).

FUK11 Fukamachi et al., *Effect of stress engineering on the electrical properties of $BaTiO_3$ thin films*, Jpn. J. Appl. Phys. **50**, 09NA03 (2011).

GAT04 C. Gatel, *Elaboration et étude d'un système hybride oxyde ferrimagnétique/métal non magnétique/ oxyde ferrimagnétique*, Thesis (2004).

GIA99 L.A. Giannuzzi et al., *A review of focused ion milling techniques for TEM specimen preparation*, Micron **30**, 197-204 (1999).

GIL94 V.T. Gillard et al., *Role of dislocation blocking in limiting strain relaxation in heteroepitaxial films*,

J. Appl. Phys. **76**, 11 (1994).

GIU10 A. Giussani et al., *A novel engineered oxide buffer approach for fully lattice matched SOI structures,* New J. Phys. **12**, 093005 (2010).

GUE01 C. Guerrero et al., *Growth and characterization of epitaxial ferroelectric $PbZr_xTi_{1-x}O_3$ thin film capacitors with $SrRuO_3$ electrodes for non-volatile memory applications*, Solid State Electron **45**, 1433 (2001).

GUO09 W. Guo et al., *Epitaxial ZnO films on (111) Si substrates with Sc_2O_3 buffers layers,* Appl. Phys. Lett. **94**, 122107 (2009).

GUT87 G. Gutekunst et al., *Atomic structure of epitaxial Nb-Al_2O_3 interfaces I. Coherent regions.*, Phil. Mag. A **75**, 5, 1329-1355 (1997).

HAE04 J.H. Haeni et al., *Room-temperature ferroelectricity in strained $SrTiO_3$*, Nature, **430**, 758-761 (2004).

HAI98 M.Haider et al., *A spherical-aberration-corrected 200kV transmission electron microscope*, Ultramicroscopy **75**, 53-60 (1998).

HAN69 Z. Angew, *Problems of image interpretation in electron microscopy with linear and nonlinear transfer,* Phys. 27, 125 (1969).

HE_05 F.He et al., *Interfacial reaction in the growth of epitaxial $SrTiO_3$ thin films on (001) Si substrates*, J. Appl. Phys. **97**, 104921 (2005).

HIR68 J.P. Hirth et al., *Theory of dislocations*, Mc Graw-Hill, New York (1968).

HON05 M. Hong et al., *High-quality nanothickness single-crystal Sc_2O_3 film grown on Si(111),* Appl. Phys. Lett. **87**, 251902 (2005)

HU_81 S.M.Hu, *Misfit dislocations and critical thickness of heteroepitaxy*, J.Appl. Lett. **69**, 11 (1991).

HU_00 G. Hu et al., *Structural tuning of the magnetic behaviour in spinel-structure ferrite thin films*, Phys. Rev. B, **62**, R779 (2000).

HU_03 X. Hu et al., *The interface of epitaxial $SrTiO_3$ on silicon: in-situ and ex-situ studies*, Appl. Phys. Lett. **82**, 2 (2003).

HUL01 D. Hull et al., *Introduction to dislocations*, fourth ed.Butterworth-Heinemann (2001).

HER04 G. Herranz, *Growth mechanisms and functionalities of epitaxial metallic ferromagnetic oxide thin films*, PhD Thesis (2004).

HUB96 H.J. Hubbard et al., *Thermodynamic stability of binary oxides in contact with silicon*, J. Mater. Res. **11**, 2757 (1996).

HYD06 PhD thesis of J.M. Hydrick, (2006).

HYT98 MJ. Hytch, et al., *Quantitative measurement of displacement and strain fields for HREM micrographs*, Ultramicroscopy **74**, 131-146 (1998).

INI10 K. Iniewski, *CMOS processors and memories*, Series: Analog circuits and signal processing, Ed. Springer VI, 382 (2010).

ITO03 D. Ito et al., *Ferroelectric properties of $YMnO_3$ epitaxial films for ferroelectric-gate field-effect transistors*, J. Appl. Phys., **93**, 5563 -5567 (2003).

KAN99 Sung-Kwan Kang et al., *Interfacial reactions in the thin film Y_2O_3 on chemically oxidized Si(001)*

substrate systems, Thin Solid Films, **353**, 8-11, (1999).

KEE98 McKee et al., *Direct $SrTiO_3$ on Si (001): the first five* monolayers, Phys. Rev. Lett. **81**, , 3014-3018, (1998).

KIG02 T. Kiguchi, et al., *Role of Ultrathin SiO_x Layer for epitaxial growth of YSZ/SiO_x/(001)Si Thin Films*, J. Ceram. Soc. Jpn. **110**, 338 (2002).

KIG03 T. Kiguchi et al., *Role of ultrathin SiO_x layer on epitaxial YSZ/SiO_x/Si thin film*, Integr. Ferroelectric. **51**, 51 (2003).

KIG05 T. Kiguchi, et al., *High-temperature in situ cross-sectional transmission electron microscopy investigation of crystallization process of yttrium-stabilized zirconia/Si and yttria-stabilized zirconia/SiO_x/Si thin films*, J. Mater. Res. **20**, 1878 (2005).

KIM87 M.J. Kim et al., *TEM specimen heating during ion beam thinning: microstructural instability*, Ultramicroscopy **21**, 327-334 (1987).

KIM01 Y.W. Kim, *Artifacts in sample preparation of transmission electron microscopy*, Materials and materials International **7**, 499-504 (2001).

KIM03 J.H. Kim et al., *Epitaxial colossal magnetoresistive $La_{0.67}(Sr,Ca)_{0.33}MnO_3$ films on Si*, Appl. Phys. Lett. **82**, 4295 (2003).

KIN00 A .I. Kingon et al., *Alternative dielectrics to silicon dioxide for memory and logic devices*, Nature **406**, 1032-1038 (2000).

KLE05 D.O. Klenov et al., *Extended defects in epitaxial Sc_2O_3 films grown on (111) Si,* Appl. Phys. Lett., **86**, 051901 (2005).

KLI05 R.F.Klie et al., *Atomic resolution STEM analysis of defects and interfaces in ceramic materials*, Micron **36**, 219-231 (2005).

KRO11 J.A. Krogstad et al., *Effect of yttria content on the zirconia unit cell parameters*, J. Am. Ceram. Soc. **94**, 4548-4555 (2011).

KUM03 M. Kumar et al., *Epitaxial growth of high quality ZnO :Al film on silicon with a thin γ-Al_2O_3 buffer layer*, J. Appl. Phys. 93, 3837 (2003).

KUM10 D.P.Kumah et al., *The atomic structure and polarization af strained $SrTiO_3$/Si*, Appl. Phys. Lett **97**, 251902(2010).

KWO00 J. Kwo et al., *High ε gate dielectrics Gd_2O_3 and Y_2O_3 for silicon,* Appl. Phys. Lett., **77**, 1 (2000).

LAC11 B. Lacroix et al., *Crystal defects and related stress in Y_2O_3 thin films: origin, modeling, and consequence on the stability of the C-type structure*, Phys. Rev. B 84, 014104 (2011).

LEA91 R.D. Leapman et J.A. Hunt, *Comparison of detection limits for EELS and EDXS,* Microsc. Microanal. Microstruct. **2**, 231-244 (1991).

LI_93 Q. Li et al., *Epitaxial $YBa_2Cu_3O_7{-}y$ bolometers on micromachined windows in silicon wafers*, Appl. Phys. Lett. **62**, 2428 (1993).

LI_03 H. Li et al, *Two-dimensional growth of high quality strontium titanate thin films on Si*, J. Appl. Phys., **93**, 4521-4526, (2003).

LI_04 Q. Li, et al., *Heteroepitaxy of high-quality Ge on Si by nanoscale Ge seeds grown through a thin layer of SiO_2,* Appl. Phys. Lett. **85**, 1928 (2004).

LI_08 Y.L. Li et al., *Influence of interfacial dislocations on hysteresis loops of ferroelectric films*, J. Appl.

Phys. **104**, 104110 (2008).

LIU08 W.R. Liu et al., *Domain matching epitaxial growth of high-quality ZnO film using Y_2O_3 buffer layer on Si(001)*, Crystal Growth & Design, 9, 239-242 (2008).

LIU10 C.H. Liu et al., *Structural properties of ultra-thin Y_2O_3 gate dielectrics studied by X-ray diffraction (XRD) and X-ray photoelectron spectroscopy (XPS),* IEEE 4244-3544 (2010).

LEE91 Lee et al., *Monolithic 77 K dc SQUID magnetometer*, Appl. Phys. Lett. **59**, 3051 (1991).

LEE02 H.N. Lee et al., *Ferroelectric $Bi_{3.25}La_{0.75}Ti_3O_{12}$ Films of Uniform a-Axis Orientation on Silicon Substrates*, Science **296**, 2006 (2002).

LOC06 J.P. Locquet et al., *High-K dielectrics for the gate stack*, J. Appl. Phys. **100**, 051610 (2006).

LU_96 Lu et al., *Large magnetotunneling effect at low magnetic fields in micrometer-scale epitaxial $La_{0.67}Sr_{0.33}MnO_3$ tunnel junctions*, Phys.Rev. B **54**, R8357 (1996).

LUD04 U. Lüders et al., *Self-organized structures in $CoCr_2O_4(001)$ thin films: Tunable growth from pyramidal clustersto {111} fully faceted surface*, Phys. Rev. B **70**, 045403 (2004).

LUD06 U. Lüders et al., *$NiFe_2O_4$: A versatile spinel material brings new opportunities for spintronics*, Adv. Mat. **18**, 1733-1736 (2006).

MA_10 J.X. Ma et al., *A robust approach for the growth of epitaxial spinel ferrite films,* J. Appl. Phys. **108**, 063917 (2010).

MAH90 J. E. Mahan et al., *A review of the geometrical fundamentals of reflection high-energy electron diffraction with application to silicon surfaces*, J. Vac. Sci. Technol. A. 8, 5 (1990).

MAR87 P.M. Marée, et al., *Generation of misfit dislocations in semiconductors*, J. Appl. Phys. **62**, 11 (1987).

MAR94 M.R.Marks et al, *A high-quality cross-sectional transmission electron microscope specimen preparation technique for structural and interfacial property studies in microelectronic packaging,* Microelectron. Reliab., **35**, 807-815 (1995).

MAR10 L.W. Martin et al., *Advances in the growth and characterization of magnetic, ferroelectric, and multiferroic oxide thin films*, Mat. Sc. And Eng. R. **68**, 89-133 (2010).

MAR12 L.W. Martin and R. Ramesh., *Multiferroic and magnetoelectric heterostructures*, Acta Mater. **60**, 2449 (2012).

MAT70 J.W. Matthews et al., *Accommodation of misfit across the interface between crystals of semiconducting elements or compounds*, J. Appl. Phys. **41**, 3800 (1970).

MAT74 J.W. Matthews et al., *Defects associated with the accommodation of misfit between crystals*, J. Vac. Sci. Technol., **12**, 1 (1974).

MAT74b J.W. Matthews, *Defects in epitaxial multilayers*, J. Cryst. Growth., **27**, 118-125 (1974).

MAT75 J.W. Matthews, *Defects associated with the accommodation of misfit between crystals*, J. Vac. Sci. Technol. **12**, 126 (1975).

MAY07 J.Mayer et al., *TEM sample preparation and FIB-Induced damage*, MRS Bulletin **32**, 400-407 (2007).

MEC99 L.Méchin et al., *The direct growth of $SrTiO_3(100)$ layers on silicon (100) substrates; application as a buffer layer for the growth of $DyBa_2Cu_3O_{7-\delta}$ thin films*, Physica C **324**, 47-56(1999).

MER62 J.W. van der Merwe, *Crystal interfaces. PartII. Finite overgrowths*, J. Appl. Phys. **34**, 1 (1062).

MER06 C. Merckling et al., *Pseudomorphic molecular beam epitaxy growth of γ-Al_2O_3(001) on Si(001) and evidence for spontaneous lattice reorientation during epitaxy*, Appl. Phys. Lett. **89**, 232907 (2006).

MI_08 S.B. Mi et al., *Atomic structure of the interface between $SrTiO_3$ thin films and Si(001)* substrates, Appl. Phys. Lett **93**, 101913 (2008).

MIS77 R.K. Mishra et al., *Surface energy of spinel*, J. Appl. Phys. **48**, 4576 (1977).

MI_08 S.B. Mi et al., *Atomic structure of the interface between $SrTiO_3$ thin films and Si(001) substrates*, Appl. Phys. Lett. **93**, 101913 (2008).

MOO88 J.S. Moodera et al., *Electron-spin polarization in tunnel junctions in zero applied field with ferromagnetic barriers*, Phys. Rev. Lett. **61**, 637 (1988).

MOO04 M.C. Moore et al., *Structural and sputtering effects of medium energy ion bombardment of silicon*, Nucl. Instr. And Meth. In Phys. Res. B **225**, 241-255 (2004).

MOO10 J.S. Moodera et al., *Frontiers in spin-polarized tunneling*, Phys. Today **63**(4), 46 (2010).

MOR91 H. Mori et al., *Epitaxial growth of $SrTiO_3$ films on Si(100) substrates using a focused electron beam evaporation method*, Jap. J. Appl. Phys. **30**, 1415-1417 (1991).

NAR92 J. Narayan et al., *Epitaxial growth of TiN films on (100) silicon substrates by laser physical vapor deposition,* Appl. Phys. Lett.**61**, 1290 (1992).

NAR95 J. Narayan et al., US patent n° 5, 406, 123 (April 11, 1995).

NAR02 J. Narayan, *Formation of misfit dislocations in thin film hétérostructures*, J. Appl. Phys., **92**, 12 (2002).

NAR03 J. Narayan and B.C. Larson, *Domain epitaxy: A unified paradigm for thin film growth,* J. Appl. Phys. **93**, 1 (2003).

NAV10 A. Navrotsky, *Thermodynamics of solid electrolytes and related oxide ceramics based on the fluorite structure,* J. Mater. Chem. **20**, 10577-10587 (2010).

NEL00 P. Nellist and S.J. Pennycook, *Advanced in imaging and electron physics*, Ed Academic Press (2000).

NIE08 C.W. Nieh et al., *Nanometer thick single crystal Y_2O_3 films epitaxially grown on Si(111) with structures approaching perfection,* Appl. Phys. Lett. **92**, 061914 (2008).

NIU09 G. Niu et al., *Molecular beam epitaxy of $SrTiO_3$ on Si(001): Early stages of the growth and strain relaxation*, Appl. Phys. Lett. **95**, 062902 (2009).

NIU11-1 G. Niu et al., *Epitaxy of $BaTiO_3$ thin film on Si(001) using a $SrTiO_3$ buffer layer,* Microelectronics Engineering **88**, 1232-1235 (2011).

NIU11-2 G. Niu, et al., *Direct epitaxial growth of SrTiO3 on Si (001): Interface, crystallization and IR evidence of phase* transition, Thin Solid Films **517**, 5722–5725 (2011).

NIU11-3 G. Niu, et al., *Heteroepitaxy of $SrTiO_3$thin films on Si (001) using different growth strategies: Toward substratelike quality*, J. Vac.Sci.Technol. B 041207, 1-5 (2011).

NOR06 G.J. Norga et al., *Solid phase epitaxy of $SrtiO_3$ on (Ba, Sr)O/Si(100): The relationship between oxygen stoeichiometry and interface stability*, J. Appl. Phys., **99**, 084102 (2006).

PAR07 Y.M. Park et al., *Measurement and estimation of temperature rise in TEM sample during ion*

milling, Ultramicroscopy **107**, 663-668, (2007).

PEN83 S. J. Pennycook and D. McMullan, *A new high-angle annular detector for STEM*, Ultramicroscopy **11**(4) 315-320 (1983).

PEN99 S.J. Pennycook and P.D. Nellist, *Impact of Electron Microscopy on Material research*, Ed. Kluver Academic, Dordrecht (1999).

PEO85 R. People and J.C. Bean, *Calculation of critical layer thickness versus lattice mismatch for Ge_xSi_{1-x}/Si strained-layer heterostructures*, Appl. Phys. Lett. **47**, 3 (1987).

PER09 P. Perna et al., H*igh Curie temperature for $La_{0.7}Sr_{0.3}MnO_3$ thin films deposited on CeO_2/YSZ-based buffered silicon substrates*, J. Phys. Cond. Matter, **21**, 306005 (2009).

PRA05 A.K. Pradhan et al., *Integration of epitaxial colossal magnetoresistive films onto Si(001) using $SrTiO_3$ as a template layer*, Appl. Phys. Lett. **86**, 012503 (2005).

PRA08 A.K. Pradhan et al., *Magnetic properties of $La_{0.6}Sr_{0.4}MnO_3$ thin films on $SrTiO_3$ and buffered Si substrates with varying thickness*, J. Apl. Phys. **103**, 023914 (2008).

RAM07 A.V. Ramos et al., *Room temperature spin filtering in epitaxial cobalt-ferrite tunnel barriers*, Appl. Phys. Let. **91**, 122107 (2007).

RAM08 A.V. Ramos et al., *Influence of oxidation on the spin-filtering properties of $CoFe_2O_4$ and the resultant spin polarization*, Phys. Rev. B. **78**, 180402 (2008).

RAI11 R.C. Rai et al., *Optical and electronic properties of $NiFe_2O_4$ thin films*, Appl. Phys. A, 00339 (2011).

REI84 L. Reimer, *Transmission Electron Microscopy, physics of image formation and microanalysis,* (1984).

REI10 J. Reiner et al., *Crystalline oxides on silicon*, Adv. Mater. **22**, 2919-2938 (2010).

RIG09 F. Rigato et al., *The magnetization of epitaxial nanometric $CoFe_2O_4$(001) layers,* J. Appl. Phys. **106**, 113924 (2009).

RIG10 F. Rigato et al., *Andreev reflection in 134ilms134agnetic $CoFe_2O_4$ spin filters*, Phys. Rev. B **81**, 174415 (2010).

RIJ07-1 Guus Rijnders and Dave H. A. Blank, I*n situ diagnostics by high-pressure RHEED during PLD*, Edited by Robert Eason (Chapter 4).

RIJ07-2 Guus Rijnders and Dave H. A. Blank, *Pulsed laser deposition of thin films: applications-led growth of functional materials*, Edited by Robert Eason (Chapter 8).

ROB89 M.T. Robinson, *Slowing-down time of energetic atoms in solids*, Phys. Rev. B, **40**, 10717 (1989).

RON11 Rondinelli and Spaldin, *Structure and properties of functional oxide thin 134ilms: Insights from electronic-structure calculations*, Adv. Mater. **23**, 3363-3381 (2011).

ROS91 F.M. Ross and W. M. Stobbs, *A study of the initial stages of the oxidation of silicon using the Fresnel Method*, Philos. Mg. A **63**, 1-36 (1991).

SAM90 G. A. Samara, *Low-temperaturedielectric properties of candidate substrates for high-temperature superconductors: $LaAlO_3$ and ZrO_2: 9.5mol % Y_2O_3*, J. Appl. Phys. 68, 4214 (1990).

SAN11 F. Sanchez et al., *Domain matching epitaxy of ferrimagnetic $CoFe_2O_4$ thin films on Sc_2O_3/Si(111),* Appl. Phys. Lett. **99**, 211910 (2011).

SCH92 T. Schuhrke et al., *Investigation of surface amorphisation of silicon wafers during ion-milling*, Ultramicroscopy **41**, 429-433 (1992).

SCH02 D.G. Schlom and J.H. Haeni, *A thermodynamic approach to selecting alternative gate dielectrics*, MRS Bull. **27**, 198 (2002).

SCH08 T. Schroeder et al., *Engineering the semiconductor/oxide interaction for stacking twin suppression in single crystalline epitaxial silicon (111)/ insulator/ Si(111) heterostructures,* New J. Phys. **10**, 113004 (2008).

SCH09 A. Schaefer, et al., *Growth of praseodymium oxide on Si(111) under oxygen-deficient conditions*, Phys. Rev. B **80**, 045414 (2009).

SCI13 M. Scigaj et al., *Ultra-flat $BaTiO_3$ epitaxial films on Si(001) with large out-of-plane polarization*, Appl. Phys. Lett. **102**, 112905 (2013).

SEA05 M.P.Seah et al., *An accurate semi-empirical equation for sputtering yields I: for argon ions*, Surf. Interface Anal., **37**, 444-458 (2005).

SIM04 Simon et al., *Diffusion and segregation effects in doped manganite titanate heterostructures*, Appl. Phys. Lett. **84**, 3882 (2004).

SPA05 Spaldin and Fiebig, *The Renaissance of Magnetoelectric Multiferroics*, Science **309**, 391 (2005).

STE02 S. Stemmer et al., *Reactions of Y_2O_3films with (001) Si substrates and with polycrystalline Si capping layers,* Appl. Phys. Lett. **81**, 4 (2002).

STE04 S. Stemmer, *Thermodynamic considerations in the stability of binary oxides for alternative gate dielectrics in complementary metal-oxide-semiconductors*, J. Vac. Sci. Tecnol. B **22**, 791 (2004).

STU69 M.D. Sturge et al., *Magnetic behavior of cobalt in garnets, II. Magnetocrystalline anisotropy and ferrimagnetic resonance of cobalt-doped yttrium iron garnet,* Phys. Rev. **180**, 413-423 (1969).

SUD97 S. Suder et al., *Thin solid film sample preparation by small-angle cleavage for transmission electron microscopy*, Thin Solid Films **304**, 157-159, (1997).

TAC60 M. Tachiki et al., *Origin of the magnetic anisotropy energy of cobalt ferrite*, Prog. Theoret. Phys. (Kyoto) **23**, 1055 (1960).

TAM98 Toyokazu Tambo et al., *Molecular beam epitaxy of $SrTiO_3$ films on Si(100)-2×1 with SrO buffer layer*, Jap. J. Appl. Phys. **37**, 4454-4459 (1998).

TAR10 L. Tarnawska et al., *Single crystalline Sc_2O_3/Y_2O_3 heterostructures as novel engineered buffer approach for GaN integration on Si(111),* J. Appl. Phys. **108**, 063502 (2010).

TAT09 S. Tateno et al., *The advanced ion-milling method for preparation of thin film using ion slicer: application to a sample recovered from diamond-anvil cell*, Rev. Sci. Instrum. **80**, 013901 (2009).

TEO09 V.S. Teodorescu et al., *Fast and simple specimen preparation for TEM studies of oxide films deposite don silicon wafers*, Microsc. Microanal. **15**, 15-19 (2009).

TIA06 H.F. Tian et al., *Interface of epitaxial $SrTiO_3$ on silicon characterized by transmission electron microscopy, electron energy loss spectroscopy, and electron holography*, Phys. Rev. B **73**, 075325 (2006).

TIT89 J.M. Titchmarsh, *Comparison of high spatial resolution in EDX and EELS analysis,* Ultramicroscopy **28**, 347-351 (1989).

TIT99 J. M. Titchmarsh, *EDX spectrum modeling and multivariate analysis of sub-nanometer segregation*,

Micron **30**, 159-171 (1999).

TRU02 E.M. Trukhanov et al., *Influence of the misfit-dislocation screw component on the formation of the threading dislocations in semiconductor hétérostructures*, Semiconductors, **36**, 3 (2002).

TOK95 E. Tokumitsu et al., *Crystalline quality and electrical properties of $PbZr_xTi_{1-x}$ thin films prepared on $SrTiO_3$-covered Si substrates*, Jap.J. Appl. Phys. **34** , 5202-5206 (1995).

TRA96 Trajanovic et al., *Growth of colossal magnetoresistance thin films on silicon*, Appl. Phys. Lett. **69**, 1005 (1996).

TRT98 V. Trítk, et al., *Room-temperature epitaxial growth of $CeO_2(001)$ films on YSZ buffered Si(001) substrates*, J. Crystal Growth **192**, 175 (1998).

TRT99 V. Trtik et al., *Influence of laser-ablation plume dynamics on the room-temperature epitaxial growth of CeO_2 on silicon*, Appl. Phys. A, **69**, S815 (1999).

URB09 K.W. Urban et al., *Negative spherical aberration ultrahigh-resolution imaging in corrected transmission electron microscopy*, Phyl. Trans. R. Soc. A, **367**, 3735-3753 (2009).

VIS95 R. D. Vispute et al., *High quality epitaxial aluminium nitride layers on sapphire by pulsed laser deposition*, Appl. Phys. Lett. **67**, 1549 (1995).

VDO99 V.I. Vdovin, *Misfit dislocations in epitaxial hétérostructures: mechanisms of generation and multiplication*, Phys. Stat. Sol. **171**, 239 (1999).

WAK00 N. Wakiya, et al., *Heteroepitaxial growth of $Ce0_2$ thin film on Si(001) with an ultrathin YSZ buffer layer*, Thin Solid Films **371**, 211 (2000).

WAK02 N. Wakiya et al., *Orientation Control and Properties of Pb(Zr, Ti)O3 Thin Films Deposited on Ni–Zn-Ferrite for Novel Ferroelectric/Ferromagnetic Memory Applications*, Jpn. J. Appl. Phys. **41**, 7242 (2002).

WAK04 N. Wakiya et al., *Stress induced magnetization for epitaxial spinel ferrite films through interface engineering*, Appl. Phys. Lett. **85**, 1199 (2004).

WAN00 S.J. Wang et al., *Epitaxial growth of yttria-stabilized zirconia oxide thin film on natively oxidized silicon wafer without an amorphous layer*, Semicond. Sci. Technol. **15**, 836-839 (2000).

WAN01 S.J.Wang et al., *Epitaxial Y-stabilized ZrO_2 films on silicon: Dynamic growth process and interface structure*, Appl. Phys. Lett. **80**, 2541 (2001).

WAR01 B. Warot-Fonrose, *Elaboration et croissance de bicouches Co/NiO épitaxiées sur MgO(001), (110) et (111) - Influence de l'orientation du substrat sur la microstructure - Relation structure-magnétisme*, Thèse (2001).

WEI02 Y. Wei et al., *Mechanism of cleaning Si(001) surface using Sr or SrO for the growth of crystalline SrTiO3 films*, J.Vac. Sci. Technol. B **20**, 1402-1406, (2002).

WIL96 D. B. William and C.B. Carter, *X-Ray Spectrometry*, Transmission Electron Microscopy, a textbook for Material Science (Plenum, New-York, 1996).

WILOO P.R. Willmott and J.R. Huber, *Pulsed laser vaporization and deposition*, Rev. Mod. Phys. 72, (2000).

WIL01 G.D. Wilk et al., *High-k gate dielectrics: Current status and materials properties considerations*, J. Appl. Phys. **89**, 5243 (2001).

YAN08 L. Yan et al., *Nanogrowth twins and abnormal magnetic behavior in $CoFe_2O_4$ epitaxial films,* J. Appl. Phys. **104**, 123910(2008).

YAN11 H.Yanagihara et al., *Perpendicular magnetic anisotropy in* $CoFe_2O_4$*(001) films epitaxially grown on MgO(001),* J. Appl. Phys. **109**, 07C122 (2011).

YON10 G.J.Yong et al., *Thermal stability of* $SrTiO_3/SiO_2/Si$ *interfaces at intermediate oxygen pressures*, J. Appl. Phys. 108, 033502 (2010).

YU_00 Z.Yu et al., *Epitaxial perovskite thin films grown on silicon by molecular beam epitaxy*, J. Vac. Sci. Technol B **18**(3), 0734-211 (2000).

YU_04 Z. Yu et al., *Advances in heteroepitaxy of oxides on silicon*, Thin Solid Films 462-463, 51-56 (2004).

ZHA98 H.Zhang, *What limits the application of TEM in the semiconductor industry?*, Thin Solid Films **320**, 77-85 (1998).

ZHA10 Y.Zhang et al., *The electrical and switching properties of a metal-ferroelectric* $(Bi_{3.15}Nd_{0.85}Ti_3O_{12})$*-insulator* ($Y_2O_3$*-stabilized* ZrO_2)*-silicon diode*, Appl. Phys. Lett. **97**, 103501 (2010).

ZHE97 T.S. Zheleva, et al., *Dislocation density reduction via lateral epitaxy in selectively grown GaN structures*, Appl. Phys. Lett. **71**, 2472 (1997).

ZHE06 Y. Zheng et al., *Simulation of interface dislocations effects on polarization distribution of ferroelectric thin films*, Appl. Phys. Let., **88**, 092903 (2006).

ZHO07 Zhou et al., *Effects of the substrate temperature and oxygen pressure on the magnetic properties and structures of* $CoFe_2O_4$ *thin films prepared by pulsed-laser deposition*, Appl. Surface Sc. **253**, 7456-7460 (2007).

ZUB11 Zubko et al., *Interface Physics in complex oxide heterostructures*, Annu. Rev. Cond. Mat. Phys. **2**, 141 (2011).